UNIVERSITÀ DEGLI STUDI DI PISA
Facoltà di Scienze Matematiche, Fisiche e Naturali
Scuola Galileo Galilei
Dottorato in Scienze Chimiche - XXI Ciclo.

PhD Thesis

Computational simulation of the excited states dynamics of azobenzene in solution.

Candidato
Teresa Cusati

Relatore
Prof. **Maurizio Persico**

Revisore esterno
Prof. **Saulo A. Vázquez R.**

Pisa, Gennaio 2009.

Ai miei genitori che mi hanno dato ogni giorno la loro vita con ogni piccolo gesto. A mio fratello Orlando.

"Tutti abbiamo i nostri sogni, pensò. L'unica differenza è che alcuni lottano e non rinunciano a realizzare il proprio destino, a costo di affrontare qualunque rischio, mentre altri si limitano a ignorarli, timorosi di perdere quel poco che hanno. E così non potranno mai riconoscere il vero scopo della vita...
Arriva un momento nella vita in cui non rimane altro da fare che percorrere la propria strada...
I sogni sono fatti di tanta fatica. Forse, se cerchiamo di prendere delle scorciatoie, perdiamo di vista la ragione per cui abbiamo cominciato a sognare e alla fine scopriamo che il sogno non ci appartiene più. Se ascoltiamo la saggezza del cuore il tempo infallibile ci farà incontrare il nostro destino...Ricorda: Quando stai per rinunciare, quando senti che la vita è stata troppo dura con te, ricordati chi sei. Ricorda il tuo sogno."

Il delfino. Sergio Bambaren

E proprio perché ricordo il mio sogno dedico questa tesi anche a te Alejandro...il mio angelo, il mio amore...mi Tus...

Index

List of Figures

List of Tables

Part I

INTRODUCTION

Introduction

Azobenzene and its derivatives are molecules very often used to construct photomodulable materials and molecular devices. The main characteristic of this kind of molecules is the efficient and reversible $trans \rightarrow cis$ photoisomerization, that occurs in either sense, without secondary processes. A peculiar advantage is that the *trans* isomer absorbs more strongly in the UV, at ∼320 nm, and the *cis* one in the visible, around 450 nm. Therefore, using the appropriate wavelength, one can convert either isomer into the other one.

Among the most important applications we can mention optical memories and switches, nanotechnology and molecular machines, many of which are based on the large variation of geometry that the photoisomerization can induce [1–15]. A very recent and "funny" application of azobenzenic compounds and their isomerization processes is the synthesis and employment of the "nanoworms", by Sasaki et al [16]. The authors have synthesized a nanovehicle that takes advantage of the $cis-trans$ photoisomerization of an azobenzene chromophore to generate an inch-worm-like motion on a surface (see Figure 1). The photoisomerization of the azobenzene chassis produces the bending of the worm.

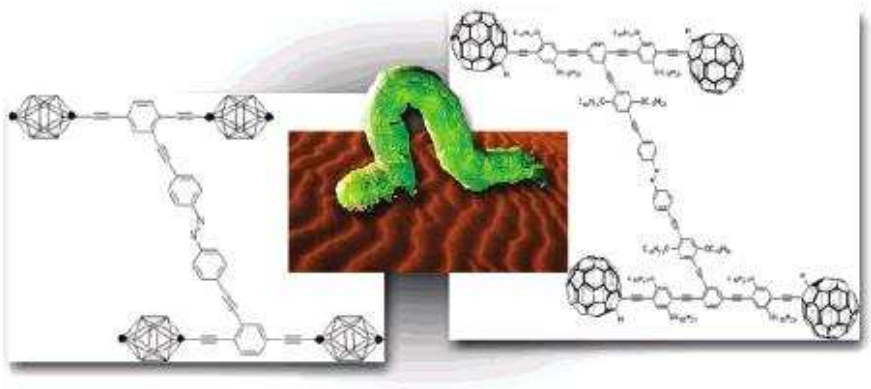

Figure 1: Scheme of a nanovehicle ("nanoworm") synthesized with a new photoactive moity, employing an azobenzene chassis. Figure taken from ref. [16].

When an azobenzene sample is exposed to the radiation, it reaches a photostationary state: the composition (*trans* with respect to *cis*) depends on the competition between the photoisomerization and the $cis \rightarrow trans$ thermal relaxation. In this process, what matters are the wavelength and the irradiance of exciting light, the $\Phi_{cis \rightarrow trans}$ and $\Phi_{trans \rightarrow cis}$ quantum yields, and the thermal relaxation kinetic constant. The photoisomerization quantum yields Φ=(number of isomerized molecules)/(number of absorbed photons)

depend on the wavelength: $\Phi_{cis\rightarrow trans} \approx 50\%$ and $\Phi_{trans\rightarrow cis} \approx 25\%$ for the $n \rightarrow \pi^*$ excitation; $\Phi_{cis\rightarrow trans} \approx 40\%$ and $\Phi_{trans\rightarrow cis} \approx 15\%$ for the $\pi \rightarrow \pi^*$ excitation. It is clear that knowing how the photoisomerization quantum yield is affected when azobenzene is inserted in chemical environments where some geometrical constraints are imposed, is important to develop such technologies. For some applications, it is also useful to estimate the response times, that find a lower limit in the azobenzene photodynamics in supramolecular environments.

The photoisomerization mechanism of azobenzene has been debated, during the last decades, because of the peculiar wavelength dependence of the quantum yields and because at least two standard possibilities exist: N=N double bond torsion and N inversion. This fundamental interest and the wealth of potential applications have stimulated a long record of experimental studies [1, 5, 6, 8, 13, 17–20]. Under the theoretical point of view, it is important to assess the potential energy surfaces and the molecular dynamics that follows the optical excitation. Our research group has performed simulations of the photodynamics of azobenzene molecule [21] by mixed quantum-classical methods [22]. Such simulations have been successful in explaining the dependence of the quantum yield on the excitation wavelength. However, our simulations have been conducted on the isolated azobenzene molecule, while almost all the experimental data have been obtained in condensated phase. In particular, Diau's group has shown a strong dependence of the excited states dynamics on the solvent viscosity [6].

The general aim of this work is to study the excited state dynamics of azobenzene in solution, specifically to simulate its transient spectra, in order to produce data directly comparable with the experiments. In particular, we shall study the reorientation of the transition dipole moment during the excited state relaxation, in order to understand the time resolved fluorescence anisotropy measurements obtained by the group of Diau and collaborators [6]. This research will also permit to study the reorientation of the whole molecule, which leads to alignment of an azobenzene sample in a polarized laser field.

This PhD Thesis will be organized in three main parts, each one composed of two chapters. In the first Chapter we shall describe the photoisomerization process and the experimental work on the reaction mechanism. The second Chapter describes an ab initio study of the transition dipole moment for the forbidden $n \rightarrow \pi^*$ transition of *trans*-azobenzene, considering the vibrational motions that contribute to the oscillator strength, and focussing on the most effective ones, i.e. those of lowest frequency. The second part contains a preliminary study of the photodynamics. Chapter 3 presents the reparameterization of the semiempirical AM1 hamiltonian, to be used for the semiclassical dynamics simulations. Chapter 4 describes the simulations of the photoprocesses for a molecule in vacuo, and in two solvents of different viscosity, implicitly described by Brownian nuclear trajectories. The last part is dedicated to the study of the explicit inclusion of the solvent effects on the photodynamics of azobenzene, choosing methanol and ethylene glycol as representative solvents. In Chapter 5 we discuss the determination of the solute-solvent interaction parameters, that will be used to carry out the semiclassical dynamics of azobenzene in solution with a QM/MM method. The simulations and their results will be described in the last Chapter.

Part II

PHOTOISOMERIZATION OF AZOBENZENE

Chapter 1

Photochemistry of azobenzene

1.1 Isomer structures of azobenzene

The *trans*-azobenzene (TAB) geometry in its ground electronic state has been debated for a long time because the phenyl rings can easily rotate out of the plane of the CNNC group, and because such rotations may be favoured in certain environments (solutions, crystal structure, mesophases etc). Many experimental and theoretical studies have found either planar (C_{2h}) or twisted (C_2 or C_i) structures [23–39]. The matter has been reviewed by Briquet et al, who concluded in favour of the C_{2h} planar structure, at least for the isolated molecule, on the basis of accurate ab initio calculations [39].

For *cis*-azobenzene (CAB), an X-Ray Diffraction study [40] shows a non planar structure with C_2 symmetry, with a CNNC dihedral angle near to 8° and the phenyl rings rotated by 53.3° with respect to the plane defined by the NNC atoms. This conformation can be explained considering the steric hindrance of phenyl rings that would be very near if they were in the same plane. Ab initio and DFT calculations confirm the rotated structure for CAB [30, 41] with NNCC angles of ≈ 55°.

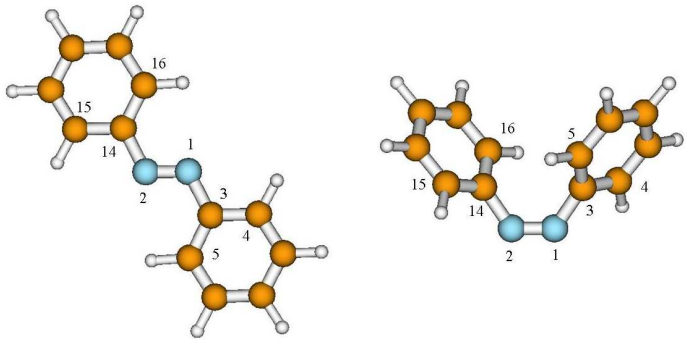

Figure 1.1: Conformation of *trans*- and *cis*-azobenzene with the relative numbers of the principal atoms.

1.2 Spectroscopic features of azobenzene

The steady-state UV-visible spectra of both azo-isomers in solutions are featured with two absorption bands that represent, respectively, the $S_0 \rightarrow S_1$ and a superposition of the $S_0 \rightarrow S_2$, $S_0 \rightarrow S_3$ and $S_0 \rightarrow S_4$ transitions. In the visible region, the $S_0 \rightarrow S_1$ transition corresponds to a perpendicular electronic excitation from the non bonding n orbital of the N atom to the antibonding π^* orbital with the maximum intensity near 440 nm for both isomers. For the *trans*-isomer with C_{2h} symmetry, this electronic transition is strictly forbidden. The two related orbitals, n and π^*, have A_u and B_u symmetries, respectively, therefore the state symmetry is B_g. Since the dipole components have ungerade symmetry, at the equilibrium geometry the transition dipole vanishes. The $\pi \rightarrow \pi^*$ transition, at about 320 nm, is of B_u symmetry, so it is allowed and strong.

For the *cis*-isomer, that belongs to the C_2 point group, both the $n \rightarrow \pi^*$ transition ($\lambda_{max} \simeq 440$ nm) and the $\pi \rightarrow \pi^*$ one ($\lambda_{max} \simeq 280$ nm) have B symmetry. As usual, the former is weak and the latter is relatively strong. However, compared with those of TAB, the $n \rightarrow \pi^*$ band of CAB is stronger by almost a factor of three, and the $\pi \rightarrow \pi^*$ is weaker.

1.3 Photoisomerization mechanism

In Table 1.1 we show several values of quantum yields obtained by different groups in a variety of conditions, along 50 years of research. Although the different origin of these values does not guarantee a perfect consistence of the data, it is possible to individuate two trends: the $\Phi_{cis-trans}$ quantum yield is always greater than the $\Phi_{trans-cis}$ one, and both of them, especially the second one, are larger if the excitation occurs in the $n \rightarrow \pi^*$ band. The former observation can be explained by taking into account the relative stability of the two isomers: CAB is 12 kcal/mol higher in energy than TAB [42] and the potential energy curve of the excited state is more favorable to the $cis \rightarrow trans$ conversion than to the $trans \rightarrow cis$ one. The dependence of the quantum yield with the initial excited state is a clear violation of Kasha's rule.

The photodynamics of azobenzene has stimulated a wealth of experimental and theoretical work, because of its peculiar violation of Kasha's rule and the related debate on the photoisomerization mechanism. Originally, two pathways were proposed: N=N double bond torsion and N inversion, respectively when the excitation wavelength falls into the $n \rightarrow \pi^*$ band or into the $\pi \rightarrow \pi^*$ one [1, 47, 49, 52, 53]. This view is supported by the observation of a wavelength dependent quantum yield of the photoisomerization process. Recently, the symmetric NNC bending has been suggested to be important in the decay of excited *trans*-azobenzene, because the crossing between the S_0 and S_1 PESs can also be reached along this internal coordinate [6,54]. In Figure 1.2, the different isomerization mechanisms discussed in the literature are shown. Some theoretical works [32,34,38,54,55] show that the inversion way is viable only in the S_1 state ($n \rightarrow \pi^*$ transition), and the torsional one is energetically preferred both in S_1 and in S_2. A conical intersection between the PESs corresponding to S_0 and S_1 is placed in correspondence with the minimum of S_1, at the rotamer geometry (with the CNNC dihedral angle near to 95°). This shape of the potential energy surfaces has been confirmed by several theoretical studies [34, 38, 54]. Semiempirical calculations done by our group have reproduced with sufficient accuracy the features of the PESs and of the conical intersection, although some recent ab initio results (those of Diau's and Orlandi's groups [6, 38, 54, 55]) were not available when the

Table 1.1: Experimental quantum yields for the photoisomerization of azobenzene in different solvents, and computational simulation results for the isolated molecule (TSH = Trajectories with Surface Hopping, FMS = Full Multiple Spawning wavepacket dynamics).

excitation band	solvent polarity	solvent viscosity	$\Phi_{trans\rightarrow cis}$	$\Phi_{cis\rightarrow trans}$	Ref.
$n \rightarrow \pi^*$	low	low	0.21-0.28	0.40-0.56	[43–48]
	medium	low	0.24-0.26	0.58-0.69	[46]
	high	low	0.31	0.46	[46]
	protic	low	0.20-0.36	0.42-0.63	[45, 46, 49, 50]
	low	high	0.18	0.60	[44]
	protic	high	0.23-0.42	0.53	[44]
	TSH simulation, without solvent		0.33±0.03	0.61±0.03	[21]
	FMS simulation, without solvent		0.46±0.08	0.68±0.11	[51]
$\pi \rightarrow \pi^*$	low	low	0.09-0.13	0.40-0.44	[43–48]
	medium	low	0.12	0.40	[46, 48]
	high	high	0.16	0.35	[46, 48]
	protic	low	0.10-0.22	0.30-0.50	[45, 46, 49, 50]
	low	high	0.05	0.40	[44]
	protic	high	0.03-0.05	0.50	[44]
	TSH simulation, without solvent		0.15±0.02	0.48±0.03	[21]

reparameterization was done (see Section 3.3). It was then possible to carry out more complete studies of the PESs, showing that the conical intersection found for the torsion of the N=N double bond (rotamer) and the symmetric bending NNC belong to the same crossing seam, that can be reached from the Franck-Condon region by different combinations of the two internal motions.

In the simulations performed for the isolated molecule, four cases have been considered: the $cis \rightarrow trans$ and $trans \rightarrow cis$ isomerizations, and the $n \rightarrow \pi^*$ and $\pi \rightarrow \pi^*$ excitations [21, 51, 56]. The results obtained from the simulations of the isolated molecule show that the torsional pathway is dominant in all four cases and the results are in agreement with the experimental ones: the computed quantum yields are close to the higher limit in the range of experimental values for non polar and low viscosity solvents. The quantum yields are determined by the competition between the excited state decay and the advancement along the reaction coordinate (dihedral angle CNNC). Although both coordinates are considered important in the decay, only the first one conduces to the isomerization: the photoisomerization via inversion would need an asymmetric bending motion. The simulations show that most of the excited molecules decay before the torsion angle attains the value of 90°, i.e. before reaching the middle point of the isomerization pathway. The earlier the molecule decays, the lower is the probability of isomerizing, but the inertia can drive the molecule to overcome the barrier in the S_0 PES. In the case of $\pi - \pi^*$ excitation, the molecules convert very rapidly to S_1. At this point they have more

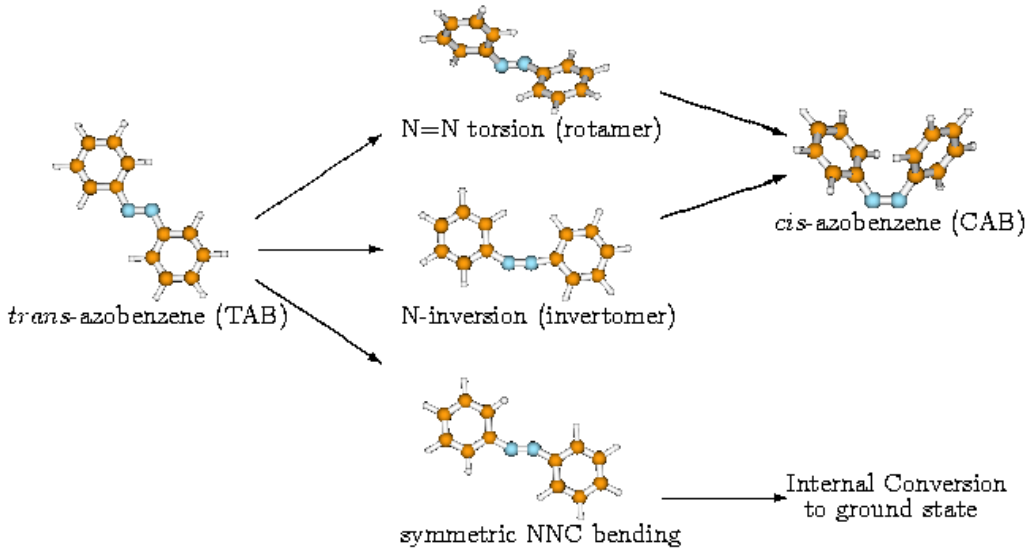

Figure 1.2: Photoisomerization mechanisms of azobenzene.

energy than in the case of direct excitation to S_1, and decay faster to the ground state. The excess energy is mainly concentrated in the symmetric bending motion. The large oscillations along this coordinate in the S_1 PES permit to reach the intersection with S_0, so that the $S_1 \rightarrow S_0$ decay can occur when the molecule is still at the beginning of the isomerization pathway ("early decay"). In the decay of both excited states (S_1 and S_2) there is a combination of the torsional and bending motions, but the molecules excited to S_2 exhibit stronger bending oscillations and earlier decay, which explains the smaller photoisomerization quantum yield obtained in this case.

1.4 Fluorescence anisotropy

Time-resolved spectroscopy is the most powerful experimental tool to study the photochemical dynamics. It has provided important information about the photoisomerization mechanism of azobenzene. In the last year, the researchers have monitored spectroscopically the dynamics of the $n \rightarrow \pi^*$ state of TAB by different time resolved techniques, i.e. differential absorption [2–4], fluorescence [5,6], IR and Raman [5,7] and photoionization [8]. In almost all cases, one finds more than one time scale of the excited state decay, which cannot be represented by a simple exponential function. In particular, a short component (0.1-0.4 ps) and a slower one (1-3 ps) have been individuated.

Among the experimental techniques applied to study the $n \rightarrow \pi^*$ excited state of TAB, we have mentioned the time resolved fluorescence spectroscopy. In these experiments, the fluorescence light is polarized, if the transition dipole moment maintains the memory of its original orientation. In other words, the direction of the transition dipole relative to the emission ($\vec{\mu}_f$) has a preferential relationship with the one relative to the absorption

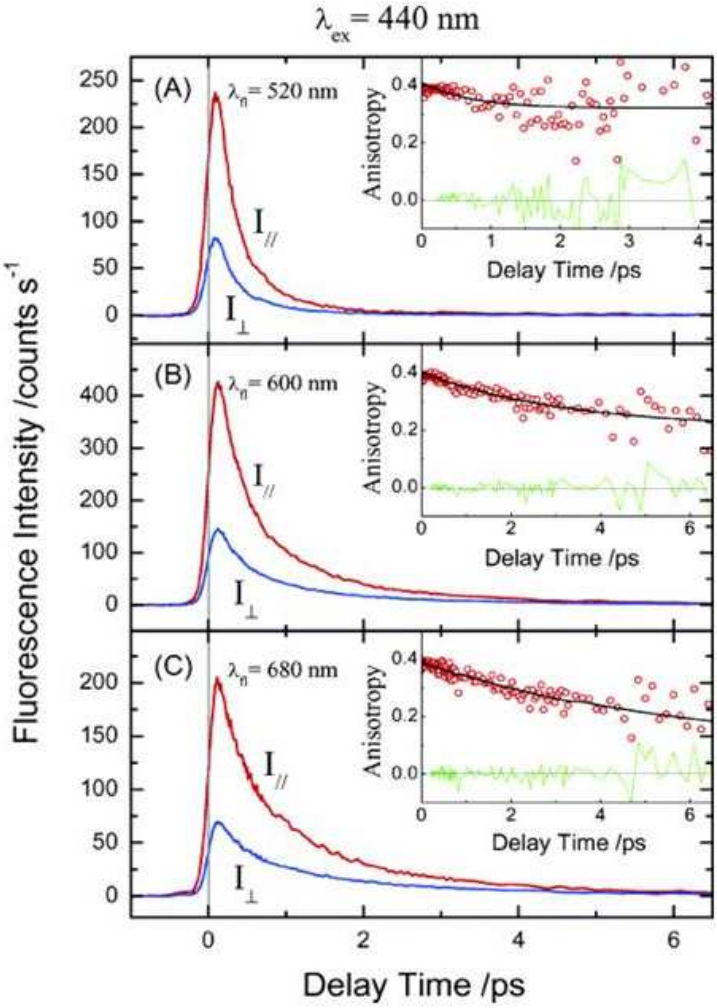

Figure 1.3: Polarized femtosecond fluorescence up-conversion transients of TAB in hexane with excitation at $\lambda_{ex} = 440$ nm and detection at different λ_{fl} with both parallel and perpendicular polarization as indicated [6].

($\vec{\mu}_a$). This occurs if the excited molecule has no time to rotate to a random orientation before emitting. In this case, the $n \rightarrow \pi^*$ absorption and emission of TAB involve the same pair of states. Before emitting, the molecule cannot undergo an overall rotation the lifetime of the excited state is of the order of one picosecond. However, in such a short time the molecule can undergo important geometrical changes. Thus, the direction of $\vec{\mu}_f$ can change and the fluorescence polarization decays in time. Then, measuring the polarization changes it is possible to obtain information about the internal motions of the molecule before emission.

In the experimental work by Diau and coworkers [6], the system response in two solvents with different viscosity is analyzed. It is observed how both the fluorescence intensity and anisotropy decay in time, and this decay is fitted with different exponential functions. In hexane, the fluorescence intensity presents two decay times, the shorter one (0.6-1.7

ps), associated with the anisotropy decay and the faster one(0.15-0.33 ps), with constant anisotropy. In a more viscous solvent (ethylene glycol) the fluorescence decay becomes slower and is represented by three times: 0.35-0.65 ps, 3.1-3.6 ps, and ∼20ps, the last one with a small weight (3%). The anisotropy decay is negligible, being only associated with the last component. In both solvents, the anisotropy tends to a non null value for long times, confirming the fact that the change of the $\vec{\mu}$ orientation it is not due to the overall rotation of the molecule. Based on these results, Diau and coworkers propose that two mechanisms are active in the decay of the $n \rightarrow \pi^*$ excited state. In particular, the torsion around the N=N double bond would be the slow motion, responsible for the fluorescence decay and strongly inhibited by the viscous solvent. The fast decay would mainly be due to the symmetric NNC bending motion, that is less likely to alter the direction of $\vec{\mu}_f$.

However, the experiments do not provide detailed information about the direction of the transition dipole moment in the absorption. The polarization changes provide a clue about the internal motion of the molecule before emission, but a theoretical determination of the dependence of the dipoles on the internal coordinates, and a simulation of the excited state dynamics, would shed more light on this problem.

Chapter 2

Oscillator strength and polarization of the forbidden $n \longrightarrow \pi^*$ band of *trans*-azobenzene

In this chapter, we present a computational study of the $n - \pi^*$ transition, focussing on its oscillator strength and polarization. We shall take into account the anharmonicity of the most important vibrational modes, the effect of a finite temperature and that of a polar solvent. The direction of the transition dipole moment is also determined, as a first step towards a theoretical interpretation of the time resolved fluorescence anisotropy measurements by Chang et al [6]. As we have seen in Chapter 1, these experiments provide precious data about the photodynamics of the $n - \pi^*$ excited TAB. The solvent viscosity is shown to slow down the decay of fluorescence, and even more the decay of its anisotropy. In order to relate these observations to the geometrical and electronic relaxation processes, one needs to know the direction of the dipole moment associated with the absorption/emission of a photon, and how it changes along the most important internal coordinates.

As we have mentioned in Chapter 1, the equilibrium geometry of the molecule of TAB probably has a C_{2h} symmetry, and the $n - \pi^*$ transition is forbidden, i.e. the transition dipole moment is null. For this reason, the determination of the direction of the transition dipole $\vec{\mu_a}$ that is responsible of the $n - \pi^*$ absorption band is not a trivial problem. Of course, to tackle the problem of the fluorescence anisotropy and its decay, one must know first of all the direction of $\vec{\mu_a}$. The idea will be to individuate the vibrational modes that modify the molecular geometry so as to generate a non vanishing transition dipole moment to permit the transition. The most important coordinates will be those that produce a greater moment, having larger amplitude and more influence on the electronic structure.

2.1 Oscillator strength

This study is based on the general expression for the total oscillator strength of an electronic band, in the Born-Oppenheimer approximation:

$$f = \frac{2}{3} \sum_{v,v'} P_{0v} \Delta E_{0v',1v} \mu^2_{0v',1v} \tag{2.1}$$

Here v and v' are the vibrational quantum numbers of the ground and excited states, respectively. The associated vibronic states will be indicated as $|\psi_0\chi_{0v}\rangle$ and $|\psi_1\chi_{1v'}\rangle$. $\Delta E_{0v,1v'}$ is the transition energy of the $0v \rightarrow 1v'$ subband, and $\vec{\mu}_{0v,1v'}=\langle\psi_0\chi_{0v}|\vec{\mu}|\psi_1\chi_{1v'}\rangle$ is the corresponding transition dipole moment. P_{0v} is the population of the initial state $|\psi_0\chi_{0v}\rangle$.

For a polyatomic molecule, Eq. 2.1 contains a double summation over a very large number of vibrational states. In fact, v' spans a wide range, especially when the ground and excited state equilibrium geometries differ noticeably, as in the case of azobenzene. The number of important terms in the v summation depends on the P_{0v} factors, i.e. on the temperature and on the ground state vibrational frequencies. To simplify the expression of the oscillator strength, the first approximation is introduced: $\Delta E_{0v,1v'} \approx \Delta E_{0,1}$. With this approximation we neglect the differences between the individual transition energies, replacing them with the vertical transition energy (closure approximation):

$$f \cong \frac{2}{3}\Delta E_{0,1}\sum_{v,v'} P_{0v}\mu^2_{0v',1v} = \frac{2}{3}\Delta E_{0,1}\sum_{v} P_{0v}\langle\psi_0\chi_{0v}|\vec{\mu}^2_{0,1}|\psi_1\chi_{1v'}\rangle \tag{2.2}$$

where, $\vec{\mu}_{0,1} = \langle\psi_0|\vec{\mu}|\psi_1\rangle$ is the electronic transition dipole moment.

Moreover, a second approximation has been applied. It consist on assuming an harmonic potential for the ground state, writing the wavefunctions χ_{0v} in terms of the normal coordinates:

$$Q_r = \sum_r L_{\alpha,r}\rho_\alpha \tag{2.3}$$

where

$$\rho_\alpha = (X_\alpha - X_{0,\alpha})m_\alpha^{1/2} \tag{2.4}$$

where X_α are the cartesian coordinates of atoms, $X_{0,\alpha}$ their equilibrium values, and m_α the associated masses. Together with the harmonic approximation, we introduce a linear approximation for the transition dipole, which is also valid for small displacements $X_\alpha - X_{0,\alpha}$:

$$\vec{\mu}(Q) = \sum_r \left(\frac{\partial\vec{\mu}_{01}}{\partial Q_r}\right)_{\mathbf{Q}=0} Q_r \tag{2.5}$$

where $\mathbf{Q}$ is the collection of the normal coordinates Q_r. Only the non-symmetric coordinates yield non vanishing terms in the summation, since, for the totally symmetric coordinates, $(\partial\vec{\mu}_{01}/\partial Q_r)_{\mathbf{Q}=0}$. In this way, the expression of the oscillator strength breaks up into a sum of contributions, one for each normal coordinate and for each cartesian component $\mu_{0,1,\lambda}$ of the $\vec{\mu}_{0,1}$ transition dipole:

$$f \cong \frac{2}{3}\Delta E_{0,1}\sum_{\lambda} S_\lambda \tag{2.6}$$

with

$$S_\lambda = \sum_r \left(\frac{\partial\mu_{0,1,\lambda}}{\partial Q_r}\right)^2_{\mathbf{Q}=0}\left[\sum_{v_r} P_{v_r}\langle\chi^{(r)}_{v_r}|Q^2_r|\chi^{(r)}_{v_r}\rangle\right] \tag{2.7}$$

Here, v_r and $\chi_{v_r}^{(r)}$ are the quantum number and the wavefunction for the r-th normal mode, while λ numbers are the cartesian components of the $\vec{\mu}_{0,1}$ vector. P_{v_r} is the probability factor for the r-th mode, with $P_{0v} = \prod_r P_{v_r}$. In the harmonic approximation we have:

$$P_{v_r} = e^{-v_r \hbar\omega_r / K_B T} / (1 - e^{-v_r \hbar\omega_r / K_B T}) \tag{2.8}$$

and

$$\langle \chi_{v_r}^{(r)} | Q_r^2 | \chi_{v_r}^{(r)} \rangle = \hbar\omega_r^{-1} \left(v_r + \frac{1}{2} \right) \tag{2.9}$$

With a little algebra we obtain:

$$S_\lambda = \sum_r \frac{\hbar}{2\omega_r} \frac{(1 + e^{\hbar\omega_r / K_B T})}{(1 - e^{\hbar\omega_r / K_B T})} \left(\frac{\partial \mu_{0,1,\lambda}}{\partial Q_r} \right)^2_{\mathbf{Q}=0} \tag{2.10}$$

The partial derivative $\frac{\partial \mu_{0,1,\lambda}}{\partial Q_r}$ is the limit for Q_r tending to zero of the incremental ratio $\mu(Q_r)/Q_r$, where all the displacements Q_s along the normal coordinates with $s \neq r$ are null. In fact we are interested in the changes of the transition dipole moments for finite displacements Q_r, and more precisely, for a displacement of the order of $Q_r^{tp} = (\hbar/\omega_r)^{1/2}$. This value coincides with the turning point of the wavefunction of the vibrational level with $v = 0$, i.e., the point where the potential is equal to the zero point vibrational energy:

$$\frac{1}{2}\omega_r^2 Q_r^2 = \frac{1}{2}\hbar\omega_r \Rightarrow Q_r^{tp} = \left(\frac{\hbar}{\omega_r} \right)^{1/2} \tag{2.11}$$

The derivatives can be evaluated numerically by computing $\vec{\mu}_{0,1}$ at small values of the Q_r coordinates. We have chosen to compute $\vec{\mu}_{0,1}$ at $Q_r^{tp} = (\hbar/\omega_r)^{1/2}$, i.e. the classical turning point, because here we have the maximum of the integrand in the matrix element $\langle \chi_0^{(r)} | Q_r^2 | \chi_0^{(r)} \rangle$. Then, in the expression 2.10, we approximate:

$$\frac{\hbar}{2\omega_r} \left(\frac{\partial \mu_{0,1,\lambda}}{\partial Q_r} \right)^2_{\mathbf{Q}=0} \cong \left[\mu_{0,1,\lambda}^2 \right]_{Q_r = Q_r^{tp}} \tag{2.12}$$

In this way we avoid the numerical inaccuracies associated with the finite differences approximation of the derivative, and we partially take into account the higher order terms in the expansion of $\vec{\mu}_{0,1}$ as a function of Q_r.

2.1.1 TAB geometry and vibrational analysis.

As we already mentioned in the Chapter 1, some experimental and computational results [33, 35, 39] indicate that the equilibrium geometry of TAB is not planar, because of the easy rotation of the phenyl rings around the N-C bonds. However, the most accurate studies [35,38,39] favour a planar C_{2h} structure. In this work, and as a first step, we have optimized the TAB geometry and obtained the vibrational frequencies with three methods: DFT with the B3LYP functional and the 6-31G* basis set, MP2 with the same basis set, and again DFT B3LYP/6-31G* within the PCM representation of a polar solvent (in this case ethanol, with a dielectric constant of 24.55). The geometry we have obtained is planar and compares well with experimental data and accurate computational results. Also, the 6-31G* basis yields geometries in good agreement with the 6-311G* ones, so we have used the smaller basis to determine the PES and to perform the normal coordinate analysis,

and the larger one to calculate the transition dipole moments and the excitation energies, by the TD-DFT method. Our results are collected in Table 2.1 for comparison.

Table 2.1: Main geometrical parameters of *trans*-azobenezene, obtained with different methods. The DFT calculations make use of the B3LYP functional. Distances in Å, angles in degrees.

	6-31G* basis set			6-311G* basis set			
Parameters	DFT	MP2	PCM	DFT	MP2	PCM	Exp. [35]
r_{NN}	1.260	1.279	1.262	1.253	1.272	1.255	1.260
r_{NC}	1.419	1.422	1.419	1.418	1.421	1.418	1.427
r_{CC}	1.398	1.398	1.399	1.395	1.400	1.396	1.399
∠NNC	114.8	113.5	115.1	115.2	113.8	115.5	113.6
∠NCC	124.8	124.8	124.9	124.7	124.7	124.8	124.7
∠CNNC	180.0	180.0	180.0	180.0	180.0	-179.9	180.0

To summarize, the results labelled as "DFT" are based on the B3LYP/6-31G* ground state PES and normal coordinates, with TD-DFT/6-311G* transition quantities computed at B3LYP/6-31G* geometries; the "MP2" label means that the normal coordinate treatment has been done at MP2/6-31G* level, and the ground state energies have also been recomputed with the same method, at the B3LYP/6-31G* geometries while the transition dipole moments at the B3LYP/6-311G*; and the "PCM" label refers to PCM-B3LYP/6-31G* normal coordinates and energies, with PCM-TD-DFT/6-311G* transition properties [57, 58], still at B3LYP/6-31G* geometries.

2.1.2 Low temperature limit.

If we assume the low temperature (T near to absolute zero) or high frequency limit ($\hbar\omega_r >> K_B T$), such that only the vibrational ground state (v=0) is populated, the expression of S_λ further simplifies to:

$$S_\lambda = \sum_r \frac{\hbar}{2\omega_r} \left(\frac{\partial \mu_{0,1,\lambda}}{\partial Q_r} \right)^2_{\mathbf{Q}=0} \tag{2.13}$$

After the geometry optimization, the frequencies and the normal modes of TAB have been calculated, considering again the three methods described above. The frequencies and the contributions to S_x, S_y and S_z in the low temperature limit according to eqs. 2.6 and 2.13 are shown in Table 2.2. The cartesian frame is body fixed and referred to the equilibrium geometry of TAB (see Fig. 2.1). The x axis coincides with the N-N one, the y axis lies on the molecular plane, and the z axis is the C_2 symmetry axis.

The S_0 and S_1 states of TAB are of A_g and B_g symmetry, respectively. Modes with A_g and B_g symmetry yield vanishing transition dipole moments, because of the presence of an inversion center. Therefore only the ungerade modes are active: the A_u modes contribute to S_x and S_y, and the B_u modes to S_z. In fact, the B_u modes, that retain the planarity of TAB, contribute very little to the oscillator strength. There are 66 normal modes: 11 A_u, 22 B_u, 23 A_g and 10 B_g.

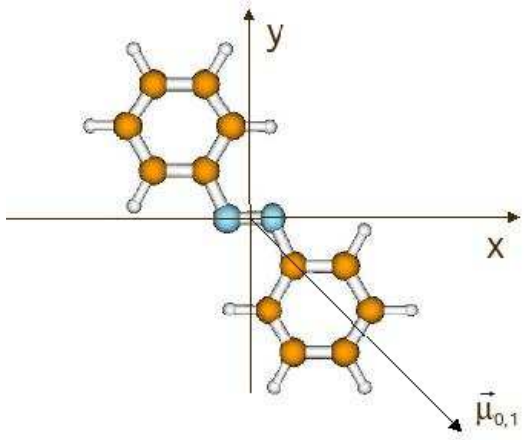

Figure 2.1: Reference coordinate system for *trans*-azobenzene (TAB) and $n-\pi^*$ transition dipole vector $\vec{\mu}_{01}$.

Table 2.2: Normal mode analysis and contributions to the oscillator strength in the low temperature limit. All the A_u and B_u modes with frequencies below 700 cm^{-1}, and the A_g and B_g ones below 500 cm^{-1} are listed. We give the squared transition dipole x, y components for the A_u modes, and the z component for the B_u ones.

		ω_r (cm^{-1})			$\mu^2_{0,1,x}$,$\mu^2_{0,1,y}$ (10^{-5} a.u.) or $\mu^2_{0,1,z}$ (10^{-8} a.u.)		
r	SYMM	DFT	MP2	PCM	DFT	MP2	PCM
1	A_u	26.1	11.9	21.4	839,1507	1970,3633	1980,3356
2	A_u	64.3	61.4	66.1	241,458	289,578	384,694
3	B_u	86.4	86.7	91.1	324	361	144
4	B_g	106.9	57.8	91.5	-	-	-
5	A_g	223.6	227.3	221.5	-	-	-
6	B_g	258.6	234.5	248.6	-	-	-
7	A_g	307.3	307.4	306.6	-	-	-
8	A_u	309.1	297.9	308.8	582,991	681,1220	1073,1750
9	A_u	419.6	396.3	418.3	99,116	107,132	187,224
10	B_g	422.8	397.0	421.0	-	-	-
11	B_g	492.2	455.9	489.4	-	-	-
12	B_u	530.6	532.6	529.5	225	256	529
13	B_u	547.0	546.8	545.1	36	49	4
14	A_u	560.9	475.2	560.5	645,1177	142,246	1202,2126
15	A_g	627.2	625.5	619.5	-	-	-
16	B_u	633.0	632.3	626.0	225	256	225
19	A_u	705.8	572.3	703.5	57,169	808,1760	98,288

Table 2.3: Normal mode analysis and contributions to the oscillator strength in the low temperature limit, in the DFT calculations. For the A_u modes, we give the squared transition dipole x, y components, and for the B_u ones, the z component. The A_g and B_g modes with frequencies below 500 cm^{-1} are listed.

r	SYMM.	ω_r (cm^{-1})	μ_x^2 (10^{-5} a.u.)	μ_y^2 (10^{-5} a.u.)	μ_z^2 (10^{-8} a.u.)
1	A_u	26.1	839	1507	-
2	A_u	64.3	241	458	-
3	B_u	86.4	-	-	324
4	B_g	106.9	-	-	-
5	A_g	223.6	-	-	-
6	B_g	258.6	-	-	-
7	A_g	307.3	-	-	-
8	A_u	309.1	582	991	-
9	A_u	419.6	99	116	-
10	B_g	422.8	-	-	-
11	B_g	492.2	-	-	-
12	B_u	530.6	-	-	225
13	B_u	547.0	-	-	36
14	A_u	560.9	645	1177	-
16	B_u	633.0	-	-	225
19	A_u	705.8	57	169	-
21	A_u	800.2	13	91	-
22	B_u	839.7	-	-	49
23	A_u	864.2	190	267	-
27	A_u	952.7	6	2	-
28	A_u	984.6	22	100	-
31	A_u	1006.4	1	29	-
32	B_u	1017.7	-	-	64
35	B_u	1048.7	-	-	256
37	B_u	1108.5	-	-	441
39	B_u	1184.6	-	-	1681
40	B_u	1191.2	-	-	4
43	B_u	1262.4	-	-	529
44	B_u	1343.2	-	-	100
46	B_u	1368.4	-	-	121
49	B_u	1500.1	-	-	64
51	B_u	1534.4	-	-	36
53	B_u	1639.4	-	-	49
55	B_u	1656.4	-	-	400
57	B_u	3185.1	-	-	16
60	B_u	3195.8	-	-	1
61	B_u	3207.0	-	-	36
63	B_u	3218.1	-	-	16
66	B_u	3235.0	-	-	529

Table 2.4: Normal mode analysis and contributions to the oscillator strength in the low temperature limit, in the MP2 calculations. For the A_u modes, we give the squared transition dipole x, y components, and for the B_u ones, the z component. The A_g and B_g modes with frequencies below 500 cm^{-1} are listed.

r	SYMM.	ω_r (cm^{-1})	μ_x^2 (10^{-5} a.u.)	μ_y^2 (10^{-5} a.u.)	μ_z^2 (10^{-8} a.u.)
1	A_u	11.9	1970	3633	-
2	B_g	57.8	-	-	-
3	A_u	61.4	289	578	-
4	B_u	86.7	-	-	361
5	A_g	227.3	-	-	-
6	B_g	234.5	-	-	-
7	A_u	297.9	681	1220	-
8	A_g	307.4	-	-	-
9	A_u	396.3	107	132	-
10	B_g	397.0	-	-	-
11	B_g	455.9	-	-	-
12	A_u	475.2	142	246	-
13	B_g	492.3	-	-	-
14	B_u	532.6	-	-	256
15	B_u	546.8	-	-	49
16	A_u	572.3	808	1706	-
18	B_u	632.3	-	-	256
21	A_u	742.9	0	0	-
22	A_u	835.0	244	398	-
24	B_u	843.9	-	-	49
26	A_u	879.1	2	12	-
28	A_u	893.5	2	0	-
30	A_u	903.3	8	154	-
32	B_u	1023.9	-	-	49
35	B_u	1060.4	-	-	225
37	B_u	1122.6	-	-	484
39	B_u	1203.8	-	-	1521
40	B_u	1213.2	-	-	9
43	B_u	1280.0	-	-	484
44	B_u	1352.2	-	-	144
47	B_u	1477.2	-	-	49
49	B_u	1508.8	-	-	64
52	B_u	1543.3	-	-	36
53	B_u	1656.5	-	-	16
56	B_u	1668.9	-	-	400
57	B_u	3223.0	-	-	16
61	B_u	3242.2	-	-	64
63	B_u	3250.7	-	-	4
66	B_u	3264.0	-	-	576

Table 2.5: Normal mode analysis and contributions to the oscillator strength in the low temperature limit, in the PCM calculations. For the A_u modes, we give the squared transition dipole x, y components, and for the B_u ones, the z component.The A_g and B_g modes with frequencies below 500 cm^{-1} are listed.

r	SYMM.	ω_r (cm^{-1})	μ_x^2 (10^{-5} a.u.)	μ_y^2 (10^{-5} a.u.)	μ_z^2 (10^{-8} a.u.)
1	A_u	21.4	1980	3356	-
2	A_u	66.1	384	694	1
3	B_u	91.1	-	-	144
4	B_g	91.5	-	-	-
5	A_g	221.5	-	-	-
6	B_g	248.6	-	-	-
7	A_g	306.6	-	-	-
8	A_u	308.8	1073	1750	-
9	A_u	418.3	187	224	1
10	B_g	421.0	-	-	-
11	B_g	489.4	-	-	-
12	B_u	529.5	-	-	529
13	B_u	545.1	-	-	4
14	A_u	560.5	1202	2126	1
16	B_u	626.0	-	-	225
19	A_u	703.5	98	288	-
21	A_u	800.0	22	150	-
22	B_u	832.2	-	-	100
23	A_u	863.5	355	500	1
27	A_u	954.8	16	5	1
29	A_u	988.7	30	153	1
30	B_u	1007.5	-	-	144
32	A_u	1010.6	3	20	1
35	B_u	1042.6	-	-	225
37	B_u	1103.7	-	-	361
39	B_u	1176.3	-	-	1444
40	B_u	1180.0	-	-	49
43	B_u	1256.8	-	-	729
44	B_u	1338.6	-	-	49
46	B_u	1364.1	-	-	196
49	B_u	1493.5	-	-	100
51	B_u	1528.5	-	-	36
53	B_u	1631.6	-	-	25
55	B_u	1647.9	-	-	441
57	B_u	3147.3	-	-	16
61	B_u	3163.5	-	-	49
63	B_u	3171.0	-	-	16
66	B_u	3192.1	-	-	729

From the tables here presented, it is apparent that the z component is always negligible and for this reason we shall pay more attention to the A_u coordinates. We are interested in the lowest frequency normal modes, which have the largest zero point amplitude and produce the most important contributions to the transition dipole moment. With all three methods, the lowest frequency is the symmetric torsion of the phenyl groups around the N-C bonds. Its symmetry is A_u and a deformation along this coordinate produces a C_2 structure. According to the DFT calculations, the next frequency is associated with the torsion of the N=N double bond, again an A_u mode, and the third one with the antisymmetric NNC bending (B_u symmetry). The fourth mode is the antisymmetric torsion of the phenyl groups (B_g symmetry). A deformation along this coordinate produces a C_i structure (see Figure 2.2). The frequency ordering of the low frequency modes obtained by MP2 calculations is different, because the potential for the phenyl torsion is shallower.

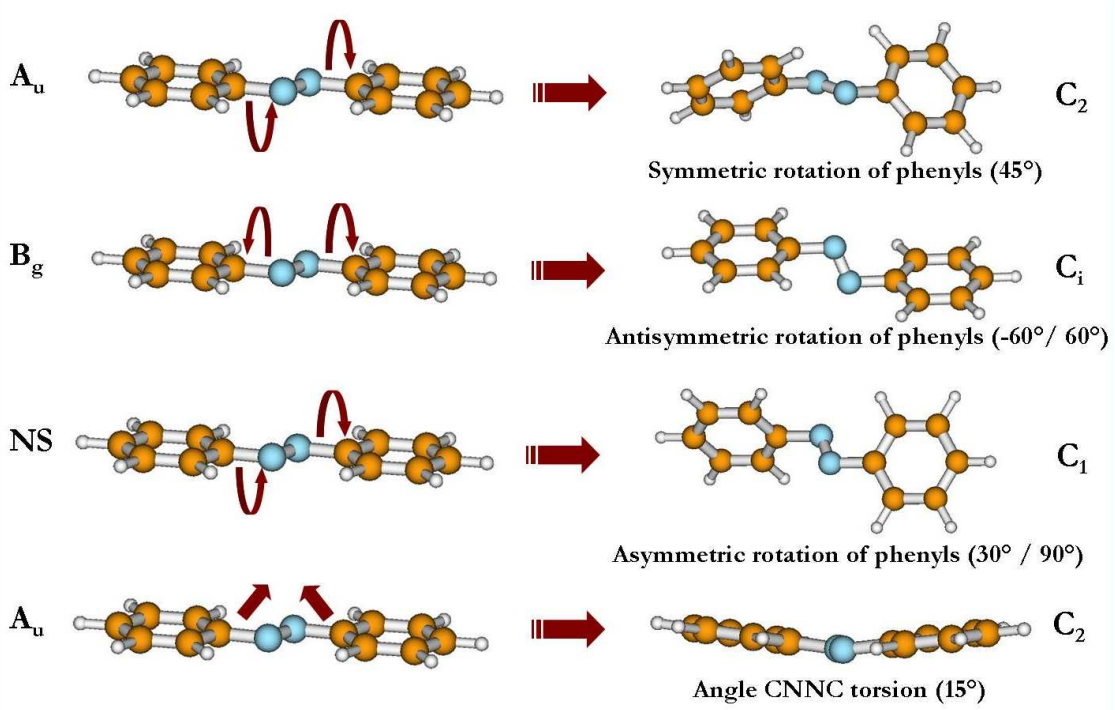

Figure 2.2: Schematization of the different molecular motions related to the lowest frequency modes.

The $n-\pi^*$ vertical excitation energy, computed at the TD-DFT/6-311G* level at DFT, MP2 and DFT-PCM geometries are shown in Table 2.7. Experimental values reported in the literature are shown in Table 2.6. The vapour phase spectra show the $n-\pi^*$ absorption maximum at 2.82 eV [59]. Non polar solvents bring about a red shift, which is offset in the polar or protic ones. The oscillator strengths have been measured in vapour phase, and show a modest increase with temperature: 0.0071 at 472 K and 0.0077 at 599 K. In solution larger values were found, especially with polar solvents. The accuracy of these data is rather low, with relative errors of the order of 10%. In particular, the vapour phase data rely on the determination of the vapour pressures, which is in turn based on absorption measurements for the $\pi - \pi^*$ band.

Table 2.6: Vertical transition energies $\Delta E_{0,1}$ (from the absorption maximum) and oscillator strengths f for the $n-\pi^*$ band of *trans*-azobenzene in vapour phase and various solvents.

solvent	$\Delta E_{0,1}$ (eV)	f	Ref.
vapour, 472 K	2.82	0.0071[a]	[59]
vapour, 599 K	2.82	0.0077[a]	[59]
n-hexane	2.77	0.0100[a]	[5]
n-hexane	2.77	0.0100[b]	[60]
cyclohexane	2.77	0.0096[b]	[45]
cyclohexane	2.77	0.0100[b]	[61]
iso-octane	2.77	0.0095[b]	[43]
DMSO	2.79	0.0110[b]	[62]
methanol	2.79	0.0103[b]	[63]
ethylene glycol	2.82	0.0129[b]	[60]

[a] f value given in the literature reference.
[b] f value inferred by us from the available spectra.

Table 2.7: Vertical transition energies $\Delta E_{0,1}$, oscillator strengths f and the angle of the transition dipole α for the $n-\pi^*$ band of *trans*-azobenzene, obtained from the calculation with the three methods: DFT, MP2 and PCM, at low and room temperature.

		(T = 0 K)		(T = 298 K)	
Method	$\Delta E_{0,1}$ (eV)	f	α	f	α
DFT	2.56	0.0024	53.4	0.0150	53.3
MP2	2.63	0.0040	54.0	0.0672	53.7
PCM	2.60	0.0047	52.8	0.0385	52.5

In the low temperature limit, the computed oscillator strengths, based on the data of Table 2.6, are of the right order of magnitude, but underestimated. MP2 yields a value in better agreement with the experimental data than DFT, and the PCM result, which is larger, reproduces the trend found in polar solvents (see Table 2.7).

In the other hand, we are interested in the direction of the transition dipole moment. Since the $\mu_{0,1,z}$ component is practically negligible, the transition dipole moment lies in the molecular plane. Therefore, its direction can be simply expressed as the angle between the transition dipole vector and the N-N axis. For almost all of the A_u coordinates the $\mu_{0,1,x}$ and the $\mu_{0,1,y}$ components have opposite signs: the exceptions (one mode in the DFT treatment and two in the MP2 and PCM ones) correspond to almost negligible contributions to the oscillator strength. Then, we can define the average angle between the N-N axis (x direction) and the transition dipole moment on the basis of the squares of the two components:

$$\alpha = arctg\left(\sqrt{\frac{S_y}{S_x}}\right) \tag{2.14}$$

2.1.3 Finite temperature.

At room temperature for the low frequency modes, the vibrational levels are very near, and then, not only the vibrational ground level is populated. Since three of the normal modes that promote the $n - \pi^*$ absorption have frequencies well below K_BT (i.e. 210 cm^-1, at room temperature), the low temperature approximation is not tenable. We have therefore applied eq. (2.10), instead of (2.13), with $T = 298$ K.

The f values obtained in this way, shown in Table 2.7, are overestimated, especially by the MP2 and PCM methods. The reason is that the harmonic approximation for the potential and the linear approximation for the transition dipole are not valid for large amplitude deformations. In particular, for the Q_1 mode (phenyl torsion) the $\mu_{0,1,\lambda}$ functions deviate from linearity towards lower values. Moreover, in certain cases the true potential rises steeper than the harmonic one.

We have therefore studied the dependence of the $U(\mathbf{Q})$ potential energy function and of the $\vec{\mu}_{0,1}$ transition dipole on the most important internal coordinates, as we shall detail in the next section. On the basis of such data, we have computed the average of the oscillator strength by classical statistics, as described in section 2.3.

2.2 Potential energy and transition dipole functions.

In Table 2.8 we report the four lowest frequency coordinates. The fourth one has not been considered till now because of its B_g symmetry. However, the rotations of the phenyl groups are largely independent from each other, so a purely symmetric motion (Q_1) is not to be expected, even under mild external perturbations (collisions or solute-solvent interactions).

Table 2.8: Internal motions of lowest frequency (largest amplitude).

NORMAL MODE	DFT ω_r	MP2 ω_r	PCM ω_r	MOTION
1 (A_u)	26.1	11.9	21.4	Symmetric rotation of phenyls
2 (A_u)	64.3	61.4	66.1	Torsion around NN double bond
3 (B_u)	86.4	86.7	91.1	Antisymmetric bending NNC
4 (B_g)	106.9	57.8	91.5	Antisymmetric rotation of phenyls

The most important internal coordinate, for the promotion of the $n \rightarrow \pi^*$ absorption, is the symmetric torsion of the phenyl groups, which corresponds to the first normal mode, Q_1. The associated frequency is very low, so the zero point vibrational motion has a large amplitude, the related transition dipole is also large (see Table 2.2), and its effect is further amplified at finite temperatures. The antisymmetric torsion is also a low frequency coordinate (Q_4, i.e. the fourth normal mode in the DFT and PCM treatments, and the second in the MP2 one), but it does not contribute to f for symmetry reasons. However,

the phenyl groups are able to rotate almost independently, so we have decided to take into account both of their torsional angles (φ_1 and φ_2) in the statistical averaging. Another important contribution arises from the torsion of the N=N double bond (Q_2), i.e. the dihedral angle $\theta = \angle\text{CNNC} - 180°$. It corresponds to the mode with frequency between 61 and 66 cm^{-1} in the three treatments.

Therefore, we have computed $U(Q)$ and $\mu_{0,1,\lambda}(Q)$ as functions of φ_1, φ_2 and θ, by optimizing all of the other internal coordinates. We have then represented these functions analytically, taking care of their symmetry properties. For arbitrary geometries, we need to redefine the body fixed frame and therefore the $\mu_{0,1,\lambda}$ components. The x axis is still coincident with the N-N one, and the z axis is defined with reference to the $\vec{R}_{NN}$, $\vec{R}'_{NC}$ and $\vec{R}''_{NC}$ vectors, i.e. the relative positions of the atoms of the C′N′N″C″ group: N″ vs. N′, C′ vs. N′, and C″ vs. N″, respectively. We first orthogonalize $\vec{R}'_{NC}$ and $\vec{R}''_{NC}$ with respect to $\vec{R}_{NN}$, and we normalize them, whence the $\vec{A}$ and $\vec{B}$ unit vectors that lie on the C′N′N″ and N′N″C″ planes. The vector $\vec{R}_{NN} \wedge (\vec{A} - \vec{B})$, after normalization, is the z axis. For a more detailed information see the Appendix A.

Then, we have run three kinds of calculations, hereafter called "1D", "2D" and "3D", with $N_x = 1$, 2 and 3, respectively. The 1D calculations only consider the symmetric rotation of the phenyl groups, with angles $\varphi_1 = \varphi_2$, thus dealing with C_2 geometries only. The 2D calculations consider the independent rotations of both phenyl groups. Finally, for the 3D calculations we also include the torsion of the dihedral angle CNNC (θ), which is a key coordinate in the photoisomerization mechanism and in the fluorescence depolarization process. The Q_3 coordinate (antisymmetric NNC bending) has not been included in the classical statistical treatment, because of its negligible effect on the oscillator strength.

2.2.1 Symmetry considerations.

The symmetry considerations are important for two basic reasons: they are useful to obtain a complete map of the quantities under study without the need to do the calculations of all points, allowing us to save computer time. Moreover, they are used to understand the behavior of the function plotted and they are necessary to impose the correct sign pattern to the dipole functions, that are affected by the sign arbitrariness of the electronic wavefunctions. In the 3D calculations we consider the variation of the angles φ_1 and φ_2 (independent phenyls rotation) and θ (CNNC angle torsion). Our aim is to represent the potential energy function as

$$U(\varphi_1, \varphi_2, \theta) = U_{min}(\varphi_1, \varphi_2) + \frac{K(\varphi_1, \varphi_2)}{2}[\theta - \theta_{min}(\varphi_1, \varphi_2)]^2 \tag{2.15}$$

where $U_{min}(\varphi_1, \varphi_2)$ is the minimum of the potential energy as a function of θ, $K(\varphi_1, \varphi_2)$ is the force constant and $\theta_{min}(\varphi_1, \varphi_2)$ is the equilibrium angle. The three parameters are determined from three potential energy values computed at θ=-15°,0° and 15°. The dipole components are represented as

$$\mu_\lambda(\varphi_1, \varphi_2, \theta) = \mu_\lambda(\varphi_1, \varphi_2, 0) + \left(\frac{\partial \mu_\lambda}{\partial \theta}\right)_{\varphi_1,\varphi_2,0} \theta + \left(\frac{\partial^2 \mu_\lambda}{\partial \theta^2}\right)_{\varphi_1,\varphi_2,0} \frac{\theta^2}{2} \tag{2.16}$$

where $\mu_\lambda(\phi_1, \phi_2, 0)$ is the transition dipole moment corresponding to the 2D case, with θ=0°, while its derivatives are computed from the dipole values at θ=0 and ±15° (we shall drop the electronic indices 0,1 from the transition dipole, from now on). The U and

μ_λ functions are determined for a grid of φ_1, φ_2 points and for the three different values of θ (0,and $\pm 15°$), with constrained geometry optimizations at the DFT/6-31G* level. Energies and dipoles are then computed according to the three procedures (DFT, MP2 and PCM). In this way, we easily obtain the 12 parameters U_{min}, K, θ_{min}, $\mu_\lambda(\varphi_1, \varphi_2, 0)$, $\left(\frac{\partial \mu_\lambda}{\partial \theta}\right)_{\varphi_1,\varphi_2,0}$ and $\left(\frac{\partial^2 \mu_\lambda}{\partial \theta^2}\right)_{\varphi_1,\varphi_2,0}$ ($\lambda = x, y, z$) for each pair of φ_1, φ_2 values. The above 12 functions of φ_1, φ_2 are fitted by two-dimensional cubic splines [64]:

$$f_{ij}(\varphi_1, \varphi_2) = \sum_{r,s=0}^{3} A_{rs,ij}(\varphi_1 - \varphi_{1,i})^r (\varphi_2 - \varphi_{2,j})^s \tag{2.17}$$

where $\phi_{1,i}$ $\phi_{2,j}$ are the nodes of a suitably chosen grid and f_{ij} is the interpolating polynomial for the $[\phi_{1,i},\phi_{1,i+1}]$, $[\phi_{2,j},\phi_{2,j+1}]$ cell. The $A_{rs,ij}$ coefficients are chosen by a least squares fit of the computed values. We were able to choose a number of cells such that the deviations of the spline functions from the ab initio data was quite negligible (more details can be found in Appendix B).

For the 2D calculations we only need the values of U and μ_λ at θ=0, with variable φ_1 and φ_2: this is just a subset of the data needed in the 3D case.

The symmetry properties of the 12 functions of φ_1 and φ_2 can be expressed in terms of selection rules for the matrix elements of the electronic hamiltonian and of the dipole moment, and for their derivatives with respect to φ_1, φ_2 (or equivalently, respect to φ_+ and φ_-, where $\varphi_\pm = (\varphi_+ \pm \varphi_-)/2$ and θ. The selection rules are valid for particular points or subspaces of the φ_1, φ_2 and θ space, where at least one symmetry element is conserved. Since we only deal with abelian groups, the same rules that apply to the first derivative also hold for all the odd ones, and similarly the second derivative (or the function itself, in the case of the transition dipole matrix elements) is representative of the even ones. Notice that the θ coordinate, at all the geometries we deal with, has the same symmetry as φ_+ (symmetric torsion of the phenyl groups), and therefore gives place to the same rules. From such rules, one can deduce the equivalence of different regions of the φ_1, φ_2 plane. We can limit ourselves to consider the interval $-\pi/2 \leq \varphi_1 \leq \pi/2$ and the same for φ_2, because of the obvious periodicity associated with the torsion of the phenyl groups. This is shown as a square in Fig. 2.3. The points with $\varphi_1 = \varphi_2$ (φ_+ axis) have C_2 symmetry, those with $\varphi_1 = -\varphi_2$ (φ_- axis) have C_i symmetry, and those with $\varphi_1 = 0$ or $\varphi_1 = \pm\pi/2$ and one of the same values for φ_2 have C_s symmetry. Combinations of these subgroups give place to the C_{2h} point group for $\varphi_1 = \varphi_2 = 0$ or $|\varphi_1| = |\varphi_2| = \pi/2$. The symmetry rules that apply at these special geometries are given in the Tables 2.9-2.13. The square in Fig. 2.3 can be partitioned into eight triangles by the φ_1, φ_2 and $\varphi_\pm$ axes. Triangles having a common side on the φ_1 axis or on the φ_- one, are equivalent by symmetry. Line segments connecting the C_s or C_{2h} special points are also subject to equivalence rules, as shown in Fig. 2.3. As a results, the energy and the transition dipole are only computed in the first quadrant of the (φ_-, φ_+) plane, i.e. the shaded area in Fig. 2.3.

In Tables 2.9, 2.10 and 2.11, 2.12 2.13, the symmetry consideration are shown for the energy, force constant, equilibrium angle, transition dipoles and their derivatives. It is possible to observe, for each symmetry group, the values of the function and its derivatives with respect to φ_1, φ_2, φ_+ and φ_- and crossed derivatives. The symmetry group C_s corresponds to the molecule with a geometry where the phenyl rings are one perpendicular respect to the other one (0°/90°). The group C_i corresponds to the TAB molecule with a geometry where the phenyl rings are rotated with equal and opposite sign angle (i.e. $30°/-30°$). The group C_2 correspond to the TAB with a geometry where the

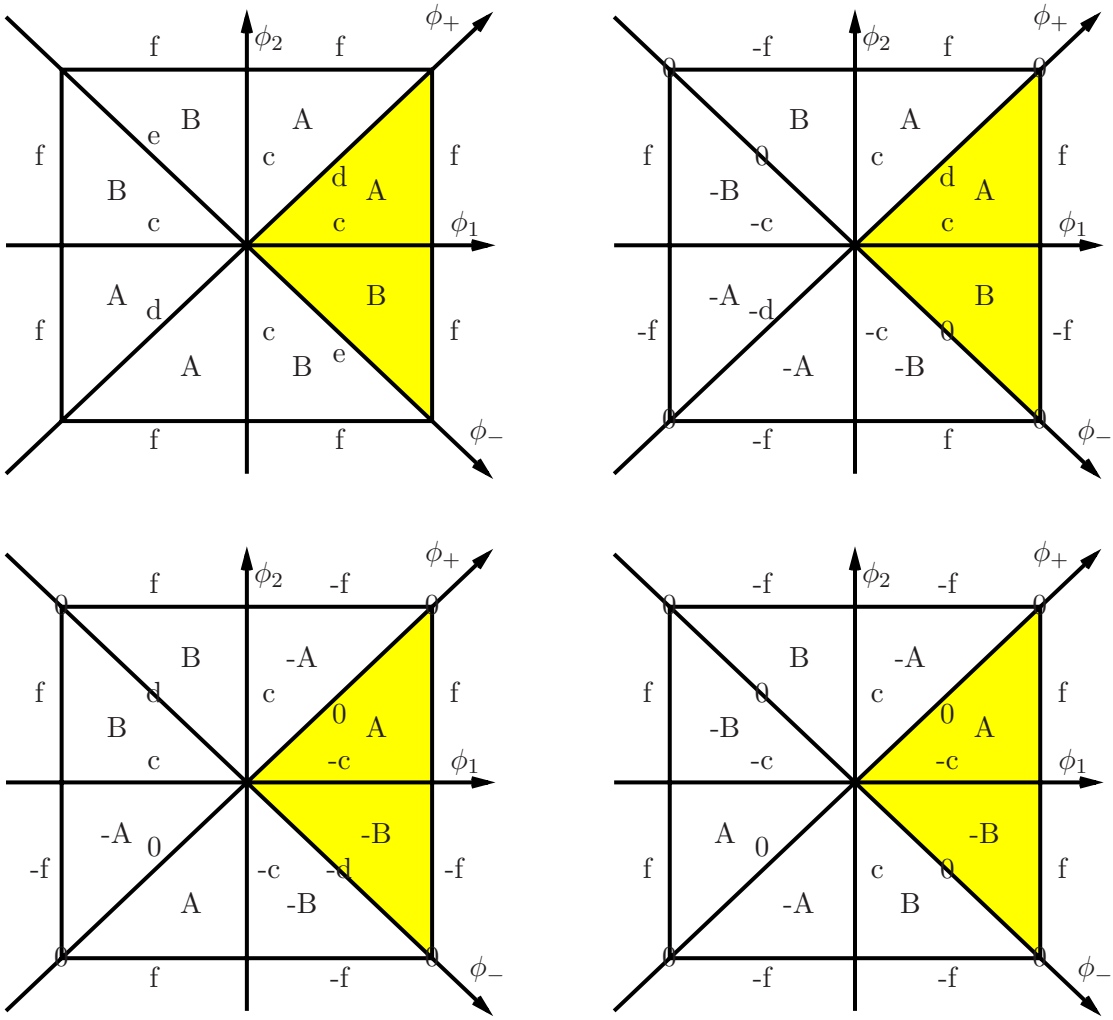

Figure 2.3: Symmetry patterns for the U_{min}, K and $\left(\frac{\partial \mu_{x,y}}{\partial \theta}\right)$ functions (left upper panel) for the θ, $\mu_{x,y}$ and $\left(\frac{\partial^2 \mu_{x,y}}{\partial \theta^2}\right)$ components of the transition dipole (right upper panel), for the $\left(\frac{\partial \mu_z}{\partial \theta}\right)$ component of the transition dipole moment (left lower panel) and for the $\left(\frac{\partial^2 \mu_z}{\partial \theta^2}\right)$ component (right lower panel). Capital letters (A, B) indicate values in triangular regions, and small letters (c, d, e, f) indicate values on segments. The square in the two figures represents the $-\pi/2 \leq \varphi_1 \leq \pi/2$ and $-\pi/2 \leq \varphi_2 \leq \pi/2$ intervals. The corners and the center of the square are points of C_{2h} symmetry. The mid-points of the sides have C_s symmetry. The points on the φ_+ axis have C_2 symmetry and those on the φ_- axis have C_i symmetry.

both phenyl rings are rotated with the same angle (i.e. 30°/30°). Finally, the C_{2h} group corresponds to the planar TAB molecule.

In Figures 2.4 and 2.5 we show the three functions that define the PES, U_{min}, K and θ_{min}, the three components of the transition dipole and their first and second derivatives

Table 2.9: Symmetry groups for the several function under study in this work, considering the geometries belonging to the C_s, C_i, C_2 or C_{2h} point groups.

GROUP	ψ_0	ψ_1	φ_1	φ_2	φ_+	φ_-	θ	$\mu_{x,y}$	μ_z
C_s	$A^{'}$	$A^{''}$	$A^{''}$	$A^{''}$	$A^{''}$	$A^{''}$	$A^{''}$	$A^{'}$	$A^{''}$
C_i	A_g	A_g	-	-	A_u	A_g	A_u	A_u	A_u
C_2	A	B	-	-	A	B	A	B	A
C_{2h}	A_g	B_g	-	-	A_u	B_g	A_u	B_u	A_u

Table 2.10: Symmetry selection rules for the potential energy U_{min}, force constant K and equilibrium angle θ_{min}, valid at geometries belonging to the C_s, C_i, C_2 or C_{2h} point groups. U_{min} and K follow the same rules as $U(\varphi_1, \varphi_2, 0)$, given in the upper part of the Table. θ_{min} depends on $\left(\frac{\partial U}{\partial \theta}\right)_{\theta=0}$, whose symmetry rules are given in the lower half.

GROUP	$\frac{\partial U}{\partial \varphi_1}$	$\frac{\partial U}{\partial \varphi_2}$	$\frac{\partial^2 U}{\partial \varphi_1 \partial \varphi_2}$	$\frac{\partial U}{\partial \varphi_+}$	$\frac{\partial U}{\partial \varphi_-}$	$\frac{\partial^2 U}{\partial \varphi_+ \partial \varphi_-}$
C_s	0	0	$\neq 0$	0	0	$\neq 0$
C_i	$\neq 0$	$\neq 0$	0	0	$\neq 0$	0
C_2	$\neq 0$	$\neq 0$	0	$\neq 0$	0	0
C_{2h}	0	0	0	0	0	0
GROUP	$\frac{\partial U}{\partial \theta}$	$\frac{\partial^2 U}{\partial \theta \partial \varphi_{1,2}}$	$\frac{\partial^3 U}{\partial \theta \partial \varphi_1 \partial \varphi_2}$	$\frac{\partial^2 U}{\partial \theta \partial \varphi_+}$	$\frac{\partial^2 U}{\partial \theta \partial \varphi_-}$	$\frac{\partial^3 U}{\partial \theta \partial \varphi_+ \partial \varphi_-}$
C_s	0	$\neq 0$	0	$\neq 0$	$\neq 0$	0
C_i	0	$\neq 0$	0	$\neq 0$	0	$\neq 0$
C_2	$\neq 0$	$\neq 0$	0	$\neq 0$	0	0
C_{2h}	0	$\neq 0$	0	$\neq 0$	0	0

whit respect to θ, all of them as contour plots in the φ_1,φ_2 plane. These results were obtained by the DFT method, but the MP2 and PCM ones are qualitatively similar. The U_{min} plot shows that the torsion of the two phenyl groups is substantially independent up to about 60°, which correspond to 4 kcal/mol, resulting in almost circular contours. Even at 90°, the energy required for the simultaneous torsion of both phenyl rings is about twice that of one ring. The deviation θ of the CNNC equilibrium angle from the planarity nowhere exceeds 2.3°, and its force constant K remains around 0.017 kcal mol^{-1} deg^{-2} = 56 kcal mol^{-1} rad^{-2}, showing that this coordinate is rather stiff and the N=N double bond is not much affected by the phenyl torsions.

The plots of the μ_x and μ_y components of the transition dipole (right panel in the Fig. 2.4) present a nodal line along the φ_- axis, and two more that cross the first one: all these sign changes are determined by symmetry (the same holds for θ_{min}). The principal node along φ_- axis arises in a natural way from the change in the function sign, as a consequence of the symmetry properties taken into account (showed in Figure 2.3 and explained previously). The secondary nodes arise indirectly, as a consequence of the symmetry features that provoke their presence: in each case, the function is zero

Table 2.11: Symmetry selection rules for the x, y and z components of the $n-\pi^*$ transition dipole moment, valid at geometries belonging to the C_s, C_i, C_2 or C_{2h} point groups.

GROUP	$\mu_{x,y}$	$\frac{\partial \mu_{x,y}}{\partial \varphi_{1,2}}$	$\frac{\partial^2 \mu_{x,y}}{\partial \varphi_1 \partial \varphi_2}$	$\frac{\partial \mu_{x,y}}{\partial \varphi_+}$	$\frac{\partial \mu_{x,y}}{\partial \varphi_-}$	$\frac{\partial^2 \mu_{x,y}}{\partial \varphi_+ \partial \varphi_-}$
C_s	0	$\neq 0$	0	$\neq 0$	$\neq 0$	0
C_i	0	$\neq 0$	0	$\neq 0$	0	$\neq 0$
C_2	$\neq 0$	$\neq 0$	$\neq 0$	$\neq 0$	0	0
C_{2h}	0	$\neq 0$	0	$\neq 0$	0	0
GROUP	μ_z	$\frac{\partial \mu_z}{\partial \varphi_{1,2}}$	$\frac{\partial^2 \mu_z}{\partial \varphi_1 \partial \varphi_2}$	$\frac{\partial \mu_z}{\partial \varphi_+}$	$\frac{\partial \mu_z}{\partial \varphi_-}$	$\frac{\partial^2 \mu_z}{\partial \varphi_+ \partial \varphi_-}$
C_s	$\neq 0$	0	$\neq 0$	0	0	$\neq 0$
C_i	0	$\neq 0$	0	$\neq 0$	0	$\neq 0$
C_2	0	$\neq 0$	0	0	$\neq 0$	$\neq 0$
C_{2h}	0	$\neq 0$	0	0	0	$\neq 0$

Table 2.12: Symmetry selection rules for the first derivative of x, y and z components of the $n-\pi^*$ transition dipole moment, valid at geometries belonging to the C_s, C_i, C_2 or C_{2h} point groups.

GROUP	$\frac{\partial \mu_{x,y}}{\partial \theta}$	$\frac{\partial^2 \mu_{x,y}}{\partial \theta \partial \varphi_{1,2}}$	$\frac{\partial^3 \mu_{x,y}}{\partial \theta \partial \varphi_1 \partial \varphi_2}$	$\frac{\partial^2 \mu_{x,y}}{\partial \theta \partial \varphi_+}$	$\frac{\partial^2 \mu_{x,y}}{\partial \theta \partial \varphi_-}$	$\frac{\partial^3 \mu_{x,y}}{\partial \theta \partial \varphi_+ \partial \varphi_-}$
C_s	$\neq 0$	0	$\neq 0$	0	0	$\neq 0$
C_i	$\neq 0$	$\neq 0$	$\neq 0$	0	$\neq 0$	0
C_2	$\neq 0$	$\neq 0$	$\neq 0$	$\neq 0$	0	0
C_{2h}	$\neq 0$	0	$\neq 0$	0	0	0
GROUP	$\frac{\partial \mu_z}{\partial \theta}$	$\frac{\partial^2 \mu_z}{\partial \theta \partial \varphi_{1,2}}$	$\frac{\partial^3 \mu_z}{\partial \theta \partial \varphi_1 \partial \varphi_2}$	$\frac{\partial^2 \mu_z}{\partial \theta \partial \varphi_+}$	$\frac{\partial^2 \mu_z}{\partial \theta \partial \varphi_-}$	$\frac{\partial^3 \mu_z}{\partial \theta \partial \varphi_+ \partial \varphi_-}$
C_s	0	$\neq 0$	0	$\neq 0$	$\neq 0$	0
C_i	$\neq 0$	$\neq 0$	$\neq 0$	0	$\neq 0$	0
C_2	0	$\neq 0$	$\neq 0$	0	$\neq 0$	$\neq 0$
C_{2h}	0	$\neq 0$	$\neq 0$	0	$\neq 0$	$\neq 0$

along the φ_- axis and also it should be zero at the points [$\varphi_1 = \pm 90$, $\varphi_2 = 0$] and [$\varphi_1 = 0$, $\varphi_2 = \pm 90$]. Consequently, at these points there is a change in the sign of the considered function. Then, nodal lines that link these pairs of points appear, namely, between [$\varphi_1 = 90$, $\varphi_2 = 0$] and [$\varphi_1 = 0$, $\varphi_2 = -90$] and between [$\varphi_1 = -90$, $\varphi_2 = 0$] and [$\varphi_1 = 0$, $\varphi_2 = 90$]. As a consequence, the transition dipole remains small in the region with φ_- between 40° and 60°. In general, for a given value of φ_+, the transition dipole is maximum at $\varphi_- = 0$. The maximum is more pronounced when $\varphi_+ > 30°$. As we shall see, inclusion of the φ_- coordinate (Q_4) in the calculations results in a decrease of the computed oscillator strength. The μ_z function has two nodes, along the φ_+ and φ_- axis, so it remains very small in a wide region around the potential energy minimum. The two important components, μ_x and μ_y, have very similar plots, except for their sign and a

Table 2.13: Symmetry selection rules for the second derivative of x, y and z components of the $n-\pi^*$ transition dipole moment, valid at geometries belonging to the C_s, C_i, C_2 or C_{2h} point groups.

GROUP	$\frac{\partial^2\mu_{x,y}}{\partial\theta^2}$	$\frac{\partial^3\mu_{x,y}}{\partial\theta^2\partial\varphi_{1,2}}$	$\frac{\partial^4\mu_{x,y}}{\partial\theta^2\partial\varphi_1\partial\varphi_2}$	$\frac{\partial^3\mu_{x,y}}{\partial\theta^2\partial\varphi_+}$	$\frac{\partial^3\mu_{x,y}}{\partial\theta^2\partial\varphi_-}$	$\frac{\partial^4\mu_{x,y}}{\partial\theta^2\partial\varphi_+\partial\varphi_-}$
C_s	0	$\neq 0$	0	$\neq 0$	$\neq 0$	0
C_i	0	$\neq 0$	0	$\neq 0$	0	$\neq 0$
C_2	$\neq 0$	$\neq 0$	$\neq 0$	$\neq 0$	0	0
C_{2h}	0	$\neq 0$	0	$\neq 0$	0	$\neq 0$
GROUP	$\frac{\partial^2\mu_z}{\partial\theta^2}$	$\frac{\partial^3\mu_z}{\partial\theta^2\partial\varphi_{1,2}}$	$\frac{\partial^4\mu_z}{\partial\theta^2\partial\varphi_1\partial\varphi_2}$	$\frac{\partial^3\mu_z}{\partial\theta^2\partial\varphi_+}$	$\frac{\partial^3\mu_z}{\partial\theta^2\partial\varphi_-}$	$\frac{\partial^4\mu_z}{\partial\theta^2\partial\varphi_+\partial\varphi_-}$
C_s	$\neq 0$	0	$\neq 0$	0	0	$\neq 0$
C_i	0	$\neq 0$	0	$\neq 0$	0	$\neq 0$
C_2	0	$\neq 0$	0	0	$\neq 0$	$\neq 0$
C_{2h}	0	0	0	0	0	$\neq 0$

scaling factor ($\mu_y/\mu_x \simeq -1.35$). This is why treatments based on different probability distributions, e.g. the normal coordinates approximation with $T = 0$ K or $T = 298$ K, yield practically the same angle $\alpha \simeq 53^\circ$ between the dipole vector and the N-N axis.

The plots of the second derivatives with respect to θ of the transition dipole components are similar to those of the corresponding dipole functions. The first derivative of the x and y components show two similar plots, without nodes and an almost constant ratio ($\mu'_y/\mu'_x \simeq$ -1.33), close to that between μ_y and μ_x. The functions increase with the torsional angles faster along φ_+ axis than the φ_- one. The first derivative of the z component has a nodal line along φ_+ axis. In the other hand, the second derivatives show the same features of the transition dipole moment function (as we have mentioned before for the symmetry rules of these functions), but their values are very small. In this case we observe a node along φ_+ axis for the x and y components, but an opposite sign respect to the dipole functions. The scaling factor is lightly greater respect to the function and its first derivative ($\mu''_y/\mu''_x \simeq 1.50$). The z component presents again two nodes along the φ_+ and φ_- axis.

The DFT, MP2 and PCM results are compared in Figs. 2.6, 2.7, 2.8 and 2.9. In the first figure we see three cuts of the functions that define the PES, along the φ_1, φ_+ and φ_- coordinates. In all three cases the MP2 treatment lowers the torsional barrier, and the solvent effect (PCM calculation) goes in the same direction. The relative magnitude of the difference between the DFT and MP2 potentials is especially important for small angles, and this is why the MP2 frequencies for the Q_1 and Q_4 modes are much lower than the DFT ones, although overall the potential energy curves are rather similar. This also explains the failure of the harmonic approximation in the calculation of the oscillator strength, based on MP2 data. MP2 calculations with larger basis sets have been done by Briquet et al [39], who have also reviewed the work of other authors. Basis sets with added diffuse functions (such as 6-31+G* and 6-31++G**) favour non planar geometries, with phenyl torsion angles as large as 20° for the equilibrium geometry. However, further extensions of the basis set, in particular the addition of more polarization functions, restore the planarity. Upgrading the correlation treatment to MP4 also tends to stabilize

the planar geometry. Within the MBPT treatments, our choice (MP2/6-31G*) seems to be a reasonable compromise between accuracy and computational cost. The force constant functions show a moderate and similar dependence on φ_1 and φ_2, with all three methods. The deviation of the CNNC dihedral from planarity (θ_{min}) is larger with the PCM treatment and smaller with the MP2 one, with respect to DFT.

Figure 2.7 shows a consistent enhancement of the transition dipole, due to the solvent effect, without alteration of the μ_y/μ_x ratio. The same features are observed in the Figures 2.8 and 2.9 for the first and second derivatives with respect to the torsional angle θ, conserving again the μ'_y/μ'_x and μ''_y/μ''_x ratios. The $n-\pi^*$ transition dipole can be interpreted as a result of mixing with the allowed $S_0 \rightarrow S_2$ ($\pi-\pi^*$) transition. The computed oscillator strength for the $S_0 \rightarrow S_2$ transition, at DFT level, is 0.77 (at the equilibrium geometry, without vibrational treatment). By comparing with measurements in n-hexane solution, that yield f =0.51-0.59 [5, 60], we see that the TD-DFT method slightly overestimates the $\pi-\pi^*$ oscillator strength. The computed transition energy is 3.72 eV, so the energy difference with respect to the $n-\pi^*$ transition is $\Delta E_{12} = 1.15$ eV. In a perturbation treatment, the $n-\pi$ transition dipole $\vec{\mu}_{01}$ due to a given distortion of the molecular geometry is connected to the $\pi-\pi^*$ one, $\vec{\mu}_{02}$, by:

$$\vec{\mu}_{01} = \vec{\mu}_{02} V_{12}/\Delta E_{12} \tag{2.18}$$

where V_{12} is the interaction between the excited states due to the vibronic coupling. The DFT value of μ_{02} is 2.91 a.u. and, for small φ_+ angles where the linear approximation is valid, we find $\partial\mu_{01}/\partial\varphi_+ = 0.025$ a.u./deg. The interaction V_{12} is then about $0.010\varphi_+$ eV (angles in degrees). A validation of the vibronic model comes from the orientation of the $\vec{\mu}_{02}$, which lies on the molecular plane and makes an angle of 55.0° with the N-N axis, very close to the average computed for the $\vec{\mu}_{01}$ vector. According to the PCM calculations, the solvent effect increases μ_{02} to 3.22 a.u. and decreases ΔE_{12} to 0.94 eV. On the basis of eq. (2.18), these changes are perfectly consistent with the increase in $\partial\mu_{01}/\partial\varphi_+$, which is 0.033 a.u./deg at PCM level. However, we notice that the gas phase maximum of the $\pi-\pi^*$ band corresponds to $\Delta E_{02} = 4.12$ eV [59], so ΔE_{12} is about 1.30 eV, slightly larger than the computed value. The $\pi-\pi^*$ oscillator strength, as noted above, is instead smaller than the computed one. Finally, ΔE_{12} does not decrease noticeably in polar solvents (from 1.14 eV in n-hexane [5, 60] to 1.10 eV in methanol [63] or 1.05 eV in ethylene glycol [60]). Therefore, it is reasonable to conclude that the $n-\pi^*$ transition dipole is slightly overestimated by our TD-DFT calculations, and even more by the PCM treatment.

2.3 Statistical treatment of the torsional coordinates.

The contribution to the oscillator strength of anharmonic internal coordinates is based on classical statistics, as justified by the low frequency associated with such modes. We maintain the closure approximation on which Eq. (2.2) is based, and we substitute the quantum mechanical density $\sum_v P_{0v} |\chi_{0v}|^2$ by the classical Boltzmann expression. The contribution to S_λ of the anharmonic modes $\mathbf{Q}^{(anharm)}$ is therefore

$$S_\lambda^{(anharm)} = \frac{\int \mu_\lambda^2(\mathbf{Q}^{(anharm)}) e^{U(\mathbf{Q}^{(anharm)})/K_B T} d\mathbf{Q}^{(anharm)}}{\int e^{U(\mathbf{Q}^{(anharm)})/K_B T} d\mathbf{Q}^{(anharm)}} \tag{2.19}$$

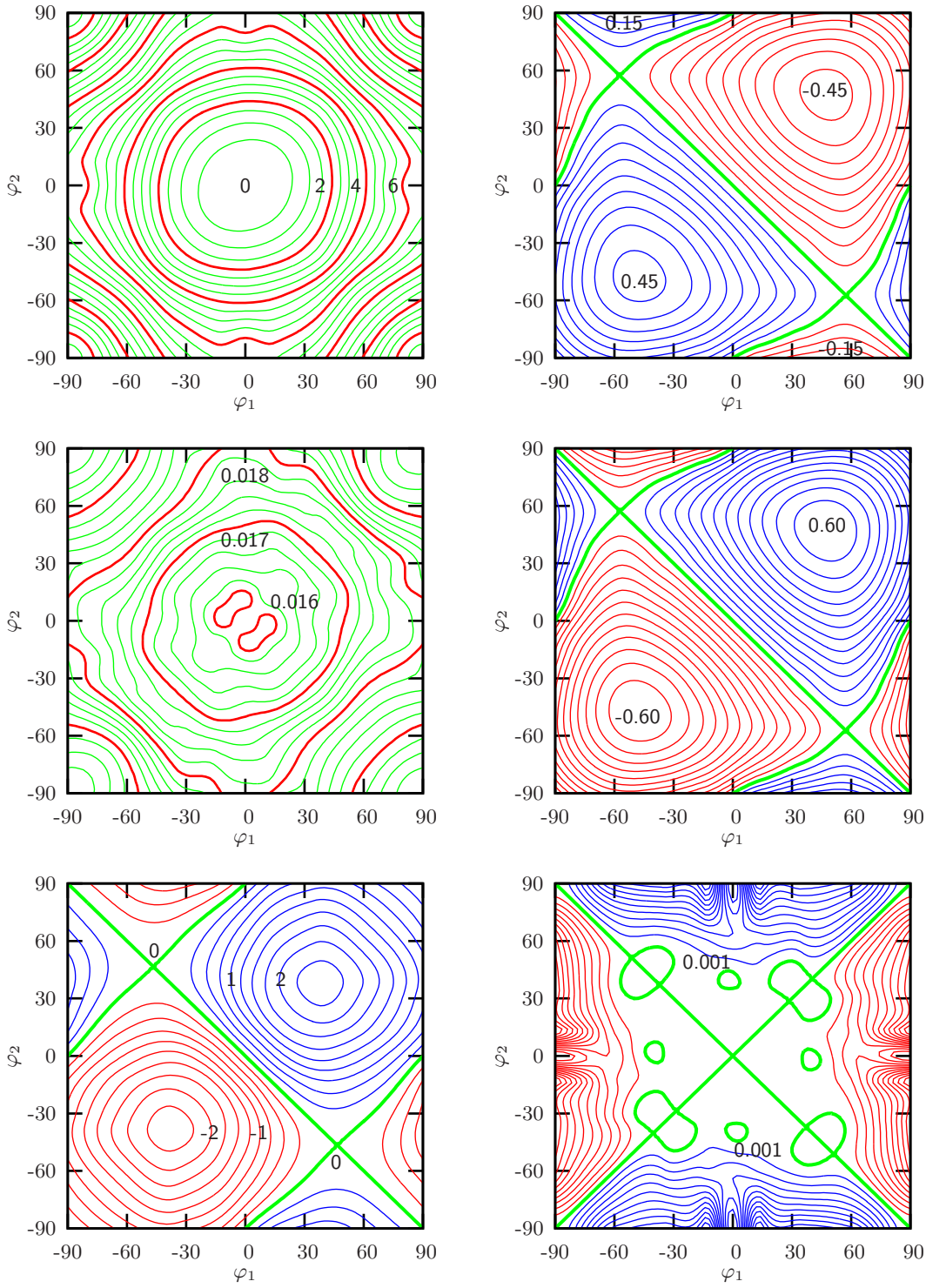

Figure 2.4: PES parameters (left panels) and transition dipole functions (right panels) according to the DFT treatment. δ is the distance between the contour lines (the labels are function values). Upper panel: U_{min} (δ=0.5 kcal/mol, and 2 kcal/mol between thick lines); $\mu_x(\varphi_1, \varphi_2, 0)$ (δ=0.05 a.u.). Middle panel: K (δ=0.0002 kcal mol^{-1} deg^{-2}, and 0.001 kcal mol^{-1} deg^{-2} between thick lines); $\mu_z(\varphi_1, \varphi_2, 0)$ (δ=0.001 a.u.). Lower panel: θ_{min} (δ=0.25°, the thicker dashed lines are nodes of the function); $\mu_y(\varphi_1, \varphi_2, 0)$ (δ=0.05 a.u.).

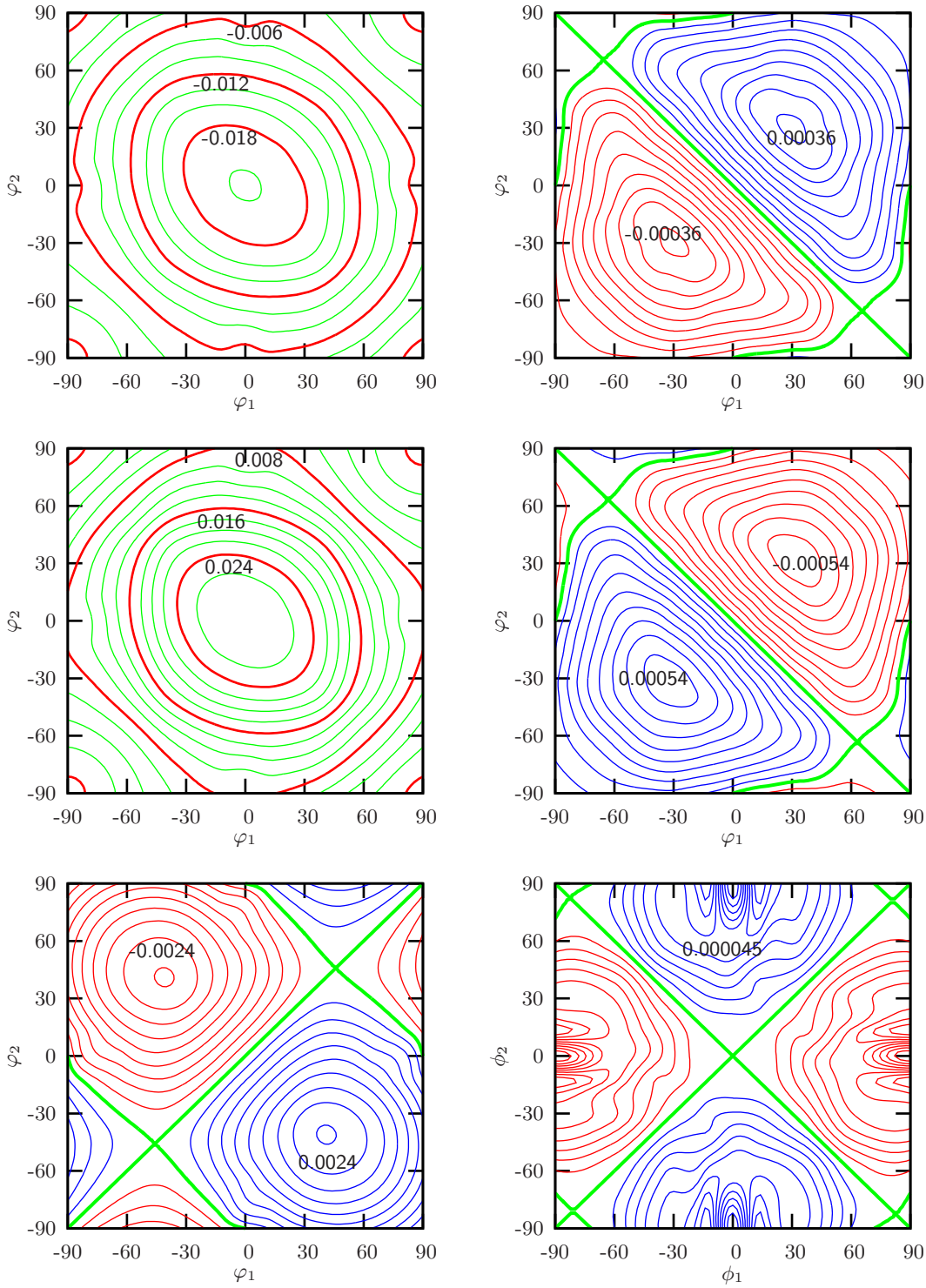

Figure 2.5: First derivative (left panels) and second derivative (right panels) of the transition dipole moment function, according to the DFT treatment. δ is the distance between the contour lines (the labels are function values). Upper panel: $\frac{\partial \mu_x}{\partial \theta}$ (δ=0.006 and δ=0.002 a.u between thick lines); $\frac{\partial^2 \mu_x}{\partial \theta^2}$ (δ=0.004 a.u between thick lines). Middle panel: $\frac{\partial \mu_y}{\partial \theta}$ (δ=0.008 and δ=0.002 a.u between thick lines); $\frac{\partial^2 \mu_y}{\partial \theta^2}$ (δ=0.006 a.u between thick lines). Lower panel: $\frac{\partial \mu_z}{\partial \theta}$ (δ=0.0003 a.u between thick lines); $\frac{\partial^2 \mu_z}{\partial \theta^2}$ (δ=0.000009 a.u between thick lines).

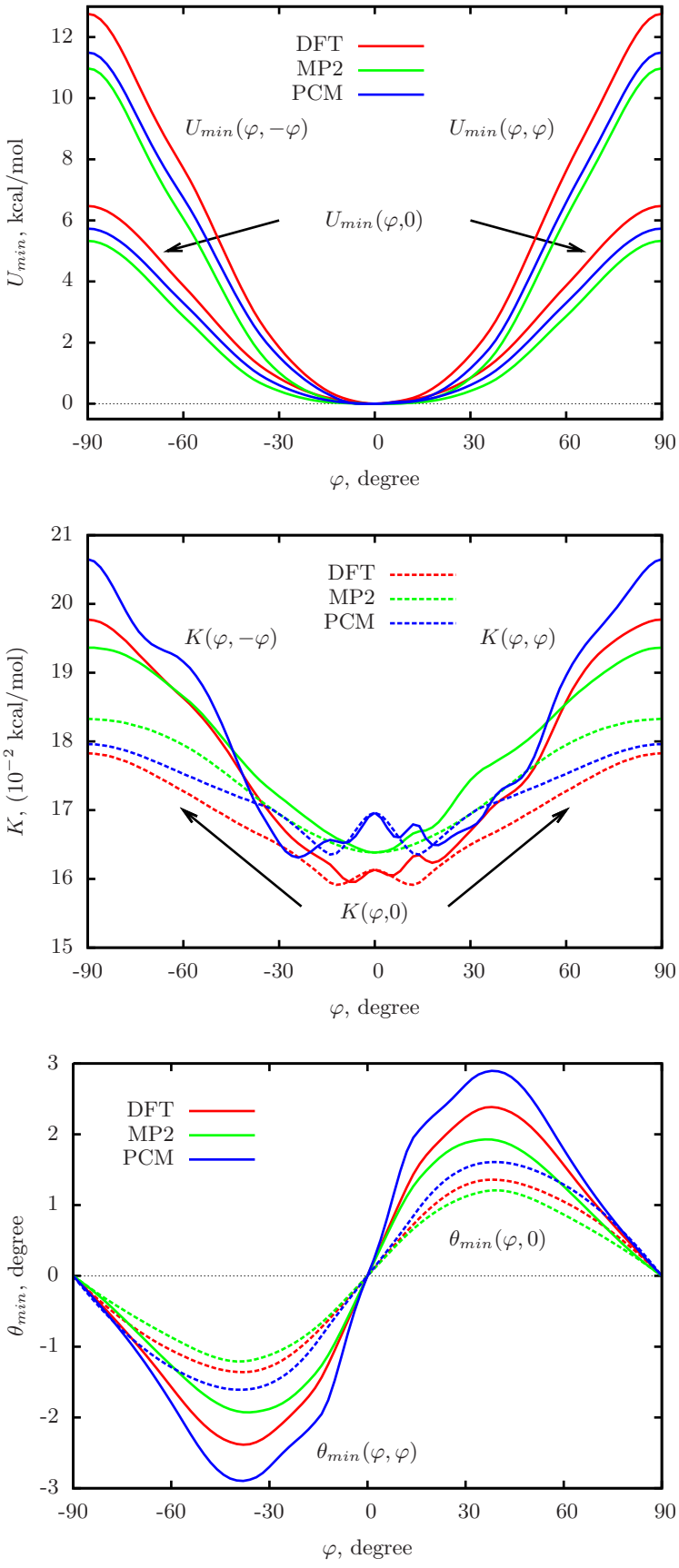

Figure 2.6: Torsional potential for the phenyl rings, force constant and equilibrium angle computed by DFT, MP2 and PCM methods. U_{min}, K and θ_{min} are given as a function of φ_1, with φ_2 =0, for the whole range $-90° \leq \varphi \leq 90°$. For a sake of clarity, U_{min} and K as a function of φ_+ is only given for $\varphi_+ \geq 0$ and as a function of φ_-, for $\varphi_- \leq 0$. $\theta_{min}(\varphi,\varphi)$ is also given for the whole range $-90° \leq \varphi \leq 90°$; full lines for $K(\varphi,\varphi)$, $K(\varphi,-\varphi)$ and $\theta_{min}(\varphi,\varphi)$, dashed lines for $K(\varphi,0)$ and $\theta_{min}(\varphi,0)$.

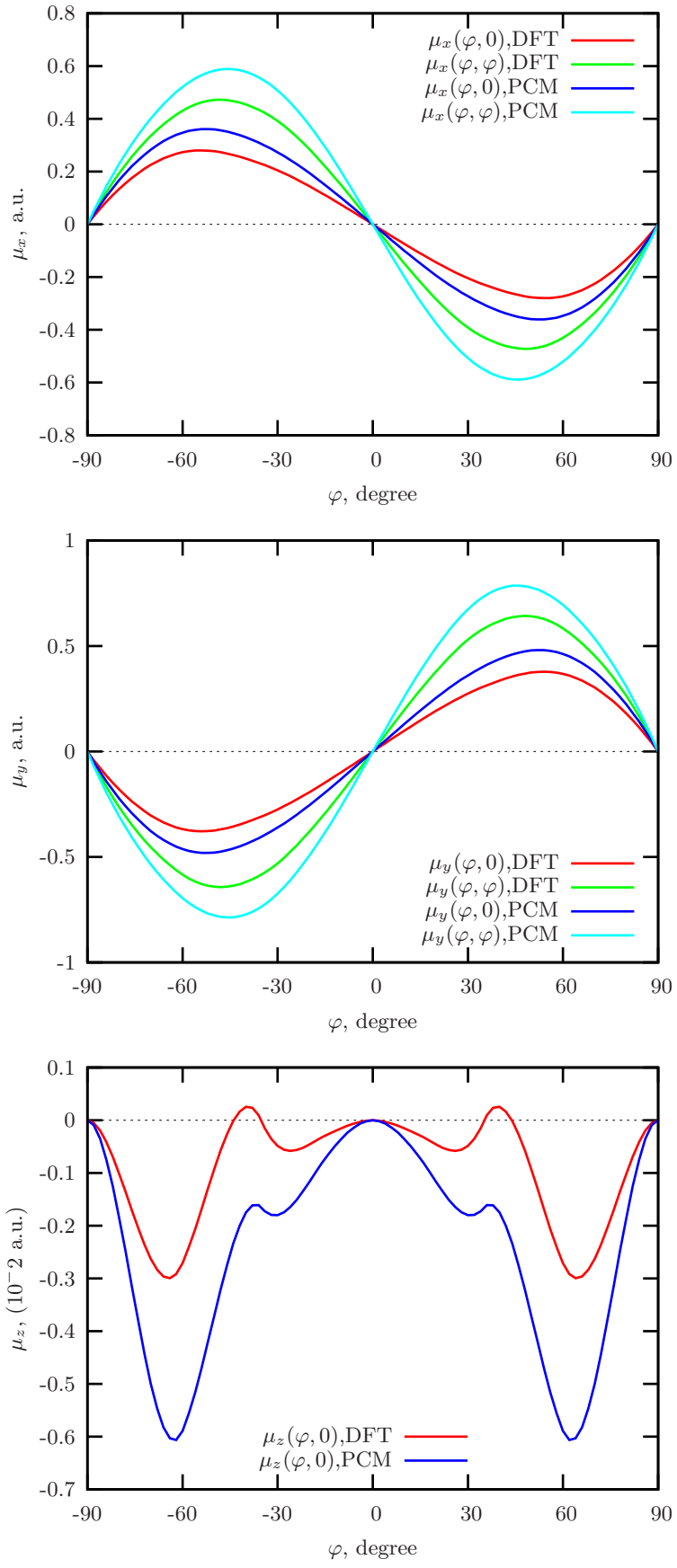

Figure 2.7: μ_x, μ_y and μ_z for the torsion of phenyl rings, computed by DFT, MP2 and PCM methods. The functions are given as a function of φ_1, with φ_2 =0, or $\varphi_1 = \varphi_2$ for the whole range $-90° \leq \varphi \leq 90°$.

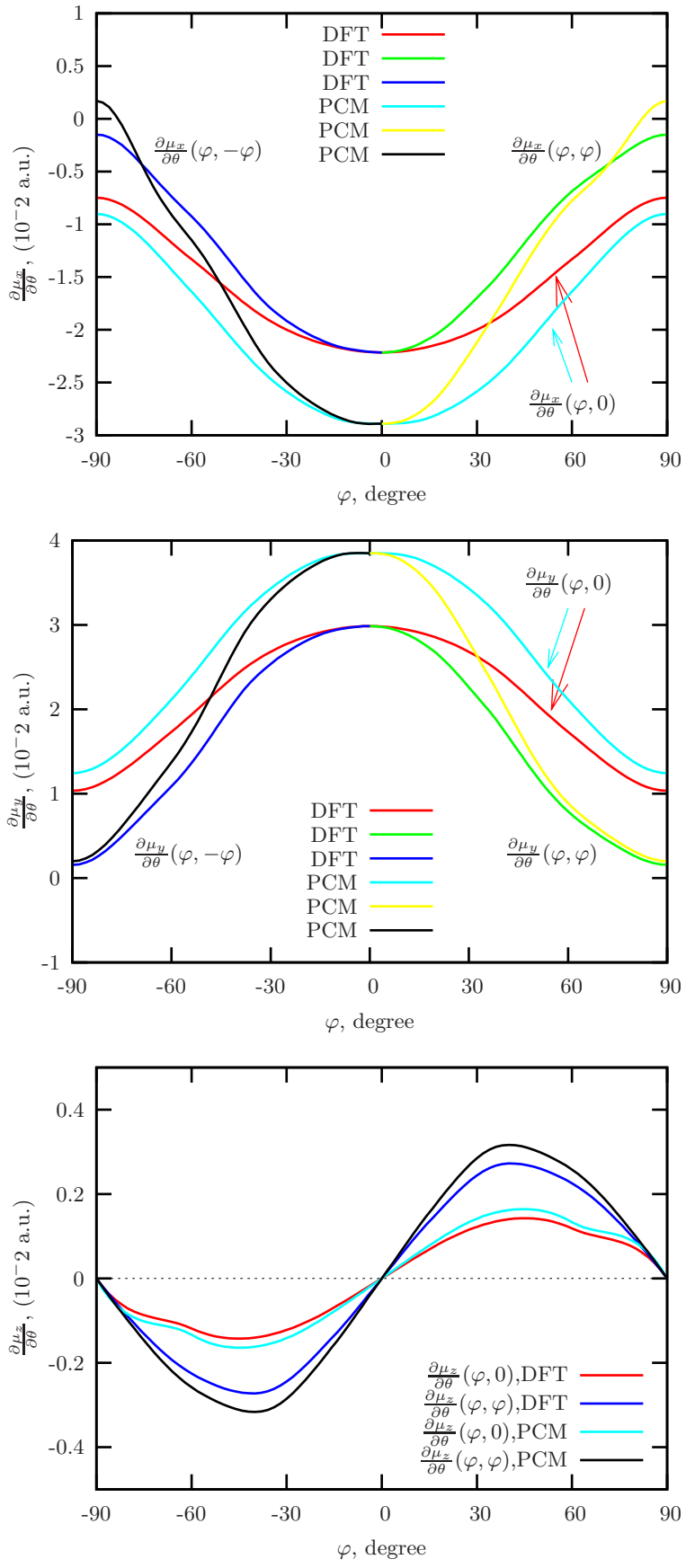

Figure 2.8: $\frac{\partial \mu_x}{\partial \theta}$, $\frac{\partial \mu_y}{\partial \theta}$ and $\frac{\partial \mu_z}{\partial \theta}$ for the torsion of phenyl rings, computed by DFT, MP2 and PCM methods. $\frac{\partial \mu_x}{\partial \theta}$, $\frac{\partial \mu_y}{\partial \theta}$ and $\frac{\partial \mu_z}{\partial \theta}$ are given as a function of φ_1, with $\varphi_2 = 0$ (and as a function of $\varphi_1 = \varphi_2$ in the case of $\frac{\partial \mu_z}{\partial \theta}$), for the whole range $-90° \leq \varphi \leq 90°$. For a sake of clarity, $\frac{\partial \mu_x}{\partial \theta}$ and $\frac{\partial \mu_y}{\partial \theta}$ as a functions of φ_+ is only given for $\varphi_+ \geq 0$ and as a function of φ_-, for $\varphi_- \leq 0$.

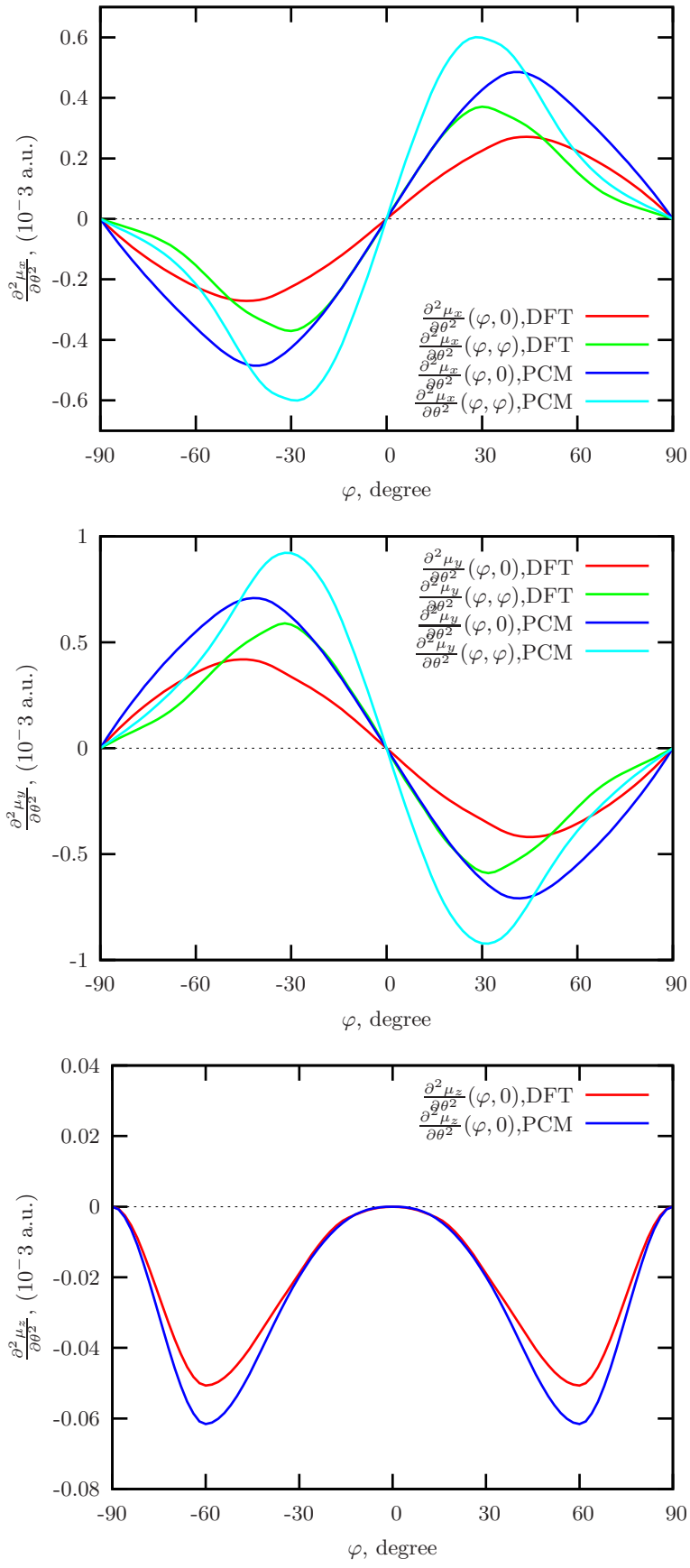

Figure 2.9: $\frac{\partial^2\mu_x}{\partial\theta^2}$, $\frac{\partial^2\mu_y}{\partial\theta^2}$ and $\frac{\partial^2\mu_z}{\partial\theta^2}$ for the torsion of phenyl rings, computed by DFT, MP2 and PCM methods. The functions are given as a function of φ_1, with φ_2 =0, or $\varphi_1 = \varphi_2$ for the whole range $-90° \leq \varphi \leq 90°$.

Table 2.14: Oscillator strength f for the $n-\pi^*$ transition of *trans*-azobenzene, and average angle α (degrees) between the N-N axis and the transition dipole vector, computed with the 1D, 2D and 3D procedures, based on DFT, MP2 and PCM data. T=298 K.

		DFT		MP2		PCM	
	contributions	f	α	f	α	f	α
1D	anharm.[a] (Q_1)	0.0076		0.0115		0.0165	
	harmonic[b] ($Q_2 - Q_{66}$)	0.0033		0.0043		0.0055	
	total	0.0109	53.4	0.0159	53.6	0.0220	52.8
2D	anharm.[a] (Q_1, Q_4)	0.0065		0.0085		0.0142	
	harmonic[b] (Q_2, Q_3, $Q_5 - Q_{66}$)	0.0033		0.0043		0.0055	
	total	0.0098	53.4	0.0129	53.7	0.0197	52.9
3D	anharm.[a] (Q_1, Q_2, Q_4)	0.0089		0.0107		0.0177	
	harmonic[b] (Q_3, $Q_5 - Q_{66}$)	0.0018		0.0024		0.0033	
	total	0.0108	53.2	0.0131	53.4	0.0211	52.8

To this we shall add $S_\lambda^{(harm)}$, computed as in eq. (2.10), with the sum running only over the harmonic modes $\mathbf{Q}^{(harm)}$.

We applied the above scheme in three variants. First ("1D" case) we considered as the anharmonic coordinate Q_1, i.e. φ_+, and we made use of the $\mu_\lambda(\varphi_1, \varphi_1, 0)$ functions. Second ("2D" case), we added the Q_4 mode, and the dipole functions where $\mu_\lambda(\varphi_1, \varphi_2, 0)$. Finally, the "3D" case considered the anharmonic coordinates Q_1, Q_2 (i.e. θ) and Q_4, with the full $\mu_\lambda(\varphi_1, \varphi_2, \theta)$ functions defined in the previous section.

The results are shown in Table 2.14 for a fixed temperature (T = 298 K). The anharmonic and harmonic contributions reported in Table 2.14 confirm that the φ_+ coordinate (symmetric phenyl torsion, Q_1) is by far the most effective in promoting the $n - \pi^*$ absorption, its contribution ranging from 70% to 90% of the total. The φ_- coordinate (antisymmetric phenyl torsion, Q_4), that is ineffective by itself, lowers the average oscillator strengths if it is included in the anharmonic treatment, because it gives access to geometries with low values of the transition dipole (see previous section and Fig. 2.4). The difference between the 2D and 3D results shows that the contribution of the N=N torsional coordinate (θ, or Q_2), which ranges between 10% and 22%, is always larger when treated anharmonically. This is at least partly due to the small displacement θ_{min} in the equilibrium position of this coordinate, that is associated with a torsion of the phenyl groups, and is neglected in the harmonic treatment: the deviation of the CNNC group from planarity causes a further increase of the transition dipole.

Overall, the DFT results compare well with the experimental f values obtained in non polar solvents (see Table 2.6). The MP2 results tend to overestimate f, although the inclusion of φ_- in the anharmonic treatment brings to a better agreement with experiment. The PCM results correctly show an increase in f, due to the effect of polar solvents, but definitely overestimate it, for the reasons seen at the end of the previous section.

Table 2.15: Oscillator strength as a function of the temperature, based on DFT, MP2 and PCM methods, and considering 1D, 2D and 3D calculations.

	DFT			MP2			PCM		
T (K)	1D	2D	3D	1D	2D	3D	1D	2D	3D
200	0.0082	0.0076	0.0084	0.0129	0.0105	0.0108	0.0175	0.0160	0.0172
220	0.0088	0.0080	0.0089	0.0135	0.0110	0.0113	0.0185	0.0168	0.0181
240	0.0093	0.0085	0.0094	0.0141	0.0115	0.0118	0.0194	0.0176	0.0189
260	0.0099	0.0089	0.0099	0.0148	0.0120	0.0123	0.0203	0.0183	0.0197
275	0.0103	0.0093	0.0102	0.0152	0.0123	0.0126	0.0210	0.0189	0.0202
290	0.0106	0.0096	0.0106	0.0156	0.0127	0.0130	0.0217	0.0194	0.0208
298	0.0109	0.0098	0.0108	0.0159	0.0129	0.0131	0.0220	0.0197	0.0211
310	0.0111	0.0100	0.0110	0.0162	0.0131	0.0134	0.0225	0.0201	0.0215
330	0.0117	0.0104	0.0114	0.0168	0.0136	0.0138	0.0234	0.0208	0.0222
360	0.0124	0.0110	0.0121	0.0176	0.0142	0.0144	0.0246	0.0217	0.0231
380	0.0129	0.0114	0.0125	0.0181	0.0146	0.0148	0.0254	0.0223	0.0237
400	0.0134	0.0118	0.0129	0.0187	0.0150	0.0151	0.0261	0.0230	0.0243

2.3.1 Temperature effects

As we have mentioned in Section 2.1.2, the oscillator strengths of azobenzene have been measured in vapour phase, and show a modest increase with temperature: 0.0071 at 472 K and 0.0077 at 599 K [59]. However, the accuracy of this results is rather low.

In Table 2.15 and Figure 2.10 the results of oscillator strength as a function of the temperature are shown. In our case, all methods predict an increase of the oscillator strength with higher temperatures. In relative terms, this increment is about the same by the DFT, MP2 and PCM treatments: according to 3D data, it is about 32% of the 298 K value, in going from 200 to 400 K. This shows that the small differences in the shape of the potentials have little influence on the dependence of f on the temperature. The average direction of the $n - \pi^*$ transition dipole remains practically the same in all treatments, with an angle of 53° with respect to the N-N axis. In this way the dipole vector is almost parallel to the N-C bonds, and to the long axis of the inertial ellipsoid.

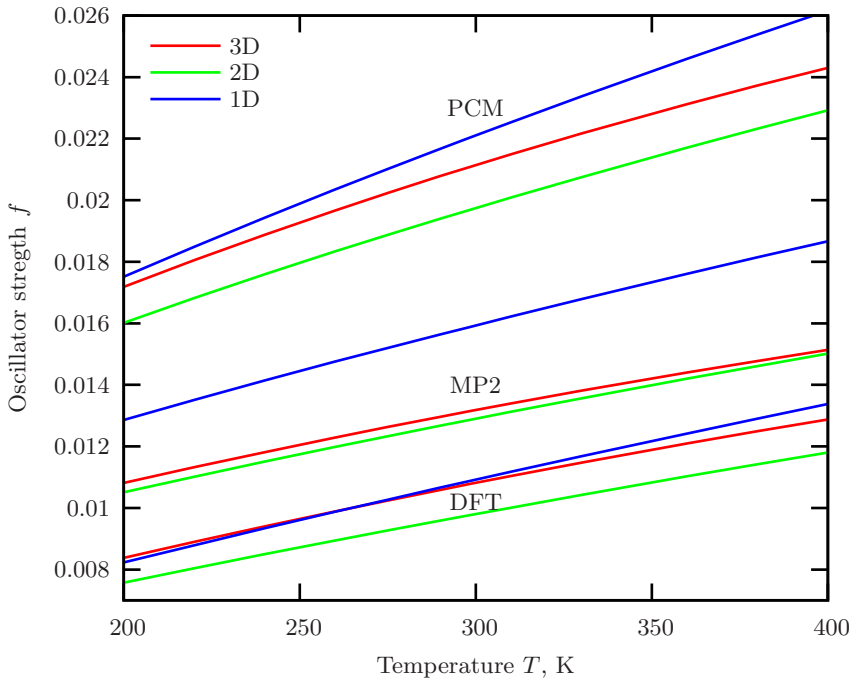

Figure 2.10: Oscillator strength f as a function of temperature, computed by the 1D, 2D ad 3D calculations, and based on DFT, MP2 and PCM results.

Part III

MOLECULAR DYNAMICS

Chapter 3

Semiempirical Model

The simulation of the excited state dynamics in large chemical systems can be done with mixed quantum-classical methods, such as Surface Hopping, whereby the nuclear motion is represented by classical trajectories. In fact, these techniques have been already applied by our group to the photoisomerization of azobenzene and its derivatives [21,51,56,65,66]. The trajectory methods can be combined with a "direct" or "on the fly" calculation of all the electronic quantities that are needed, i.e. the electronic energies, their gradients, the transition dipoles and the nonadiabatic couplings. The direct strategy may be a very convenient alternative to preparing in advance analytic expressions of the above electronic quantities as functions of the internal coordinates. In fact, the fitting of ab initio or experimental data by means of analytic functions can be quite a hard job, especially when several internal coordinates undergo important changes during the process under study, i.e. when the reaction pathway is far from being uniquely defined. Further problems arise when conical intersections between the electronic PES are present.

However, the direct methods can be quite expensive, since an electronic calculation is needed at every time step. The total computational cost scales linearly with the number of trajectories and with the time length of the simulated process. In order to reduce the burden of the electronic calculations, we have resorted to semiempirical methods. In this chapter we describe some modifications of the standard semiempirical procedures we have introduced, to describe the photochemical processes.

In the past decades the semiempirical molecular orbital (MO) methods have been used widely in different computational studies. Semiempirical approaches are normally formulated within the same conceptual framework as ab initio methods, but they neglect many smaller integrals to speed up the calculations. In order to compensate the errors caused by the approximations considered, empirical parameters are introduced into the remaining integrals and calibrated against reliable experimental or theoretical reference data. This strategy can only be successful if the semiempirical model retains the essential physics to describe the properties of interest. Provided that this is the case, the parameterization can account for all other effects in an average sense, and it is then a matter of validation to establish the numerical accuracy of a given approach. Semiempirical methods serve as efficient computational tools which can yield fast quantitative estimates for a number of properties [67].

Compared with ab initio or density functional methods, semiempirical calculations are faster, typically by several orders of magnitude, but they are also less accurate, with errors that are less systematic and thus harder to correct. Hence, there remains the need to

improve semiempirical methods with regards to their accuracy and range of applicability, without compromising their computational efficiency. In addition, there is the need to develop new algorithms in order to exploit modern computer architectures and to extend semiempirical calculations to ever larger molecules.

Semiempirical MO methods are parametrized to reproduce experimental reference data (or if it is possible, accurate high-level theoretical predictions as substitutes of experimental data). The reference properties are the best selected such that they are representative for the intended applications. The quality of semiempirical results is strongly influenced by the effort put into the parameterization.

3.1 Semiempirical methods

Semiempirical treatments in quantum chemistry are defined with the following specifications:

a) *Theoretical approach.*
A big number of actual semiempirical methods are based on Molecular Orbital theory (MO) and they need a minimum basis set. Only the valence electrons are treated explicitly.

b) *Integrals approximation.*
There exists three levels of approximations: CNDO (complete neglect of the differential overlap), INDO (partial neglect of the differential overlap) and NDDO (neglect of the diatomic differential overlap). In the CNDO approximation only the two-electron integrals are considered and all the bicentric coulombic interactions $\langle \mu\mu \mid \nu\nu \rangle$ are treated as if they involved only the s orbitals. The INDO approximation is similar to the previous one, but in this case the exchange integrals $\langle \mu\nu \mid \mu\nu \rangle$ are considered, for which the atomic orbitals are centered on the same atom. In the more elaborated NDDO approximation all the monocentric integrals and the bicentric ones $\langle \mu_A\nu_A \mid \lambda_B\sigma_B \rangle$ are included (where ν_A is an atomic orbital belonging to the atom A).

c) *Integral evaluation.*
For each kind of approximation, the integrals are determined from experimental data, calculated from analytic formulas or obtained from parametric expressions.

d) *The parameterization.*
The parameterizations employed in semiempirical methods have as the principal aim to reproduce reference data. The quality of the semiempirical results is strongly influenced by the care taken in carrying out the parameterization.

A well known class of semiempirical methods, employed in the study of the ground state potential surfaces, are the different parameterizations of the MNDO model [68]. The MNDO model is based on the NDDO integral approximation and it employs a real atomic orbital minimum basis (AO) for the valence electrons. The molecular orbitals (MO) are obtained by solving the SCF equations, where the superposition of atomic orbitals is neglected. For a closed shell system, using a matrix expression, we have:

$$\mathbf{FC} = \mathbf{C}\varepsilon \tag{3.1}$$

$$|\varphi\rangle = |\chi\rangle\,\mathbf{C} \tag{3.2}$$

where $\mathbf{F}$ is the Fock matrix, ε is the diagonal matrix of the MO energies, and $|\chi\rangle$ and $|\varphi\rangle$ are the row vectors that represent the atomic and molecular orbitals, respectively. The $\mathbf{C}$ matrix is orthogonal. For A or B atoms, the Fock matrix elements can be written as:

$$F_{\mu_A\nu_A} = h_{\mu_A\nu_A} + \sum_{\lambda_A,\sigma_A} P_{\lambda_A\sigma_A}\left[\langle\mu_A\nu_A \mid \lambda_A\sigma_A\rangle - \frac{1}{2}\langle\mu_A\lambda_A \mid \nu_A\sigma_A\rangle\right] + \sum_B \sum_{\lambda_B,\sigma_B} P_{\lambda_B\sigma_B}\langle\mu_A\nu_A \mid \lambda_B\sigma_B\rangle \tag{3.3}$$

$$F_{\mu_A\nu_B} = h_{\mu_A\nu_B} - \frac{1}{2}\sum_{\lambda_A,\sigma_B} P_{\lambda_A\sigma_B}\langle\mu_A\lambda_A \mid \nu_B\sigma_B\rangle \tag{3.4}$$

where $h_{\mu\nu}$ and $P_{\mu\nu}$ are the one-electron hamiltonian matrix and the density matrix elements, respectively. Then, the total energy E_{tot} can be obtained as the sum of electronic energy E_{HF} and nucleus-nucleus repulsion energy E_{AB}^{core}:

$$E_{\mathrm{HF}} = \frac{1}{2}\sum_{\mu\nu} P_{\mu\nu}(h_{\mu\nu} + F_{\mu\nu}) \tag{3.5}$$

$$E_{tot} = E_{\mathrm{HF}} + \sum_{A<B} E_{AB}^{core} \tag{3.6}$$

The following interactions and parameters are included in the MNDO model:

1) One-electron monocentric integrals, $h_{\mu_A\nu_A}$, approximated in this way:

$$h_{\mu_A\nu_A} = U_\mu\delta_{\mu_A\nu_A} - \sum_{B\neq A} Z_B\langle\mu_A\nu_A \mid s_B s_B\rangle$$

where U_μ is a parameter that represents the AO energy χ_μ of atom A. U_μ is obtained from spectroscopic data. The second term of the expression written above represents the electrostatic nucleus-electron attraction (where Z_B is the core charge of B and s_B is an s type AO centered at B).

2) One-electron bicentric orbitals $h_{\mu_A\nu_B}$, (not considering the index A and B), can be expressed as:

$$h_{\mu\nu} = \frac{1}{2}S_{\mu\nu}(\beta_\mu + \beta_\nu)$$

where β_μ is an empirical parameter, that depends on the atom and the orbital and $S_{\mu\nu}$ is the superposition between orbitals χ_μ and χ_ν.

3) Two-electron monocentric repulsive integrals $\langle\mu_A\nu_A \mid \lambda_A\sigma_A\rangle$. These integrals are all represented by empirical parameters. In the case that s and p orbitals are used, only 5 atomic parameters will be necessary.

4) Repulsive two-electron bicentric integrals $\langle \mu_A \nu_A \mid \lambda_B \sigma_B \rangle$. Their evaluation is done by electrostatic considerations and it involves the exponent ζ, that depends on the atom and the orbital. When the distance between A and B tends to zero, $\langle \mu_A \nu_A \mid \lambda_B \sigma_B \rangle$ converges to the corresponding monocentric integral.

5) Bicentric core-core repulsions E_{AB}^{core} are constituted of an electrostatic term $E_{AB}^{coul} = Z_A Z_B \langle s_A s_A \mid s_B s_B \rangle$ and an additional term E_{AB}^{eff}. The last one possesses an exponential repulsive form an it represents the Pauli exchange repulsion. It contains up to four empirical parameters.

The MNDO model, in its standard applications (MNDO, AM1,PM3,PM5 [68–73]), has been parameterized by the use of the Hartree-Fock wavefunction (HF), with respect to the ground state properties, with particular emphasis on the organic molecules. This fact presents two principal consequences:

1) Configuration Interaction calculations (CI) do not represent an improvement with respect to the HF method (although they are essential for a correct representation of the ground and excited states, especially when the bond breaking occurs).

2) The excited states are often obtained with the CIS method (single excitations), where the ground state is represented by the HF wavefunction.

A method for the calculation of electronic states employed in a direct dynamics scheme should satisfy the following requirements: (a) all the electronic states considered in the dynamics should be treated on the same footing; (b) the method should behave correctly for all nuclear configurations that are explored in the dynamics, namely in the case of bond breaking, state degeneracies and multiconfigurational states. This is not the case of the CIS wavefunctions.

3.2 Floating occupation molecular orbitals and CI choice

Good representation of homolytic bond breaking and a balanced description of the ground and excited states comes from a CI procedure based on orbitals obtained from SCF calculation with fractional and floating occupation numbers [21, 22, 65, 66, 74]. The CI space is often chosen with the CAS criterium (Complete Active Space). In the ab initio framework, the same problems are usually tacled by the State Average - CASSCF method, i.e. by minimizing variationally the mean energy of several states. However, this method requires high computational costs, because of the calculations of more CI roots and the simultaneous optimization of the orbitals. Our group has implemented the method of fractional and floating occupation numbers in the MOPAC program [22], and we will proceed to describe it.

In order to introduce a variable orbital occupation, the method considers the population of each orbital distributed along the energy axis according to a gaussian function centered at the corresponding Fock eigenvalue, without separating a priori the space of molecular orbitals into occupied and virtuals ones. Then, for the n-th orbital with energy ε, the electronic distribution function is:

$$g_i(\varepsilon) = \frac{\sqrt{2}}{\sqrt{\pi}\omega} e^{-(\varepsilon-\varepsilon_i)^2/2\omega^2} \tag{3.7}$$

such that:

$$\int_{-\infty}^{\infty} g_i(\varepsilon)d\varepsilon = 1 \tag{3.8}$$

Instead of the form 3.7 one can use different kinds of functions (e.g. a lorentzian or a cubic spline bell-shaped function).The amplitude of the orbital energy range ω is an arbitrary parameter while the occupation numbers are given for each SCF step following the expression:

$$O_i = \int_{-\infty}^{\varepsilon_F} g_i(\varepsilon)d\varepsilon \tag{3.9}$$

where ε_F indicates the Fermi level energy obtained by imposing that the sum of occupation numbers be equal to the total electron number (N):

$$N = \sum_i \int_{-\infty}^{\varepsilon_F} g_i(\varepsilon)d\varepsilon \tag{3.10}$$

For all orbitals with energy much lower than the Fermi level ($\varepsilon_F - \varepsilon >> \omega$) the occupation number is $O_i \simeq 2$. The virtual orbitals with high energy will have O_i null. With this occupation numbers we construct the new density matrix used for the SCF interactions. Thus, it is possible to obtain a better representation of virtual orbitals nearest to the Fermi level, that are involved in the description of the lowest energy excited states. Moreover, we can describe the elongation of bonds, considering that the involved orbitals in the two fragments adopt occupation numbers near to 1, thus representing in a correct way the homolytic dissociation. Another advantage is that, in presence of degeneracy, the degenerated orbitals are treated in the same way, having the same occupation number. This is an important condition needed to reproduce the degeneracy of states in a truncated CI. On the other hand, this method has the disadvantage that it produces an SCF energy without physical meaning, depending on the electron fraction distributed on the virtual orbitals and thus on the amplitude ω. A CI calculation is necessary to obtain the electronic energies and wavefunctions. When carrying out dynamics calculation that consider large geometrical changes, the fractional occupation would result essential for a correct description of certain reaction paths. The introduction of the floating occupation requires important modifications to the method for the calculation of the gradient of the CI energy. This is important for the geometry optimization and for the classical trajectory calculations [22].

In a CI calculation, the orbitals can be partitioned into active, inactive and virtual ones. The blocks involving doubly occupied inactive orbitals in the one- and two-particle density matrices of the CI wavefunctions are the same as in the closed shell HF calculation. As a consequence, only the two-electron integrals involving four active orbitals are needed. In our case, the active space must formally coincide with that of the orbitals with floating occupation. Within this space, we perform a full transformation of the two-electron integrals from the atomic to the molecular basis. However, it is not necessary to run a CAS-CI, and some of the formally active orbitals may not be involved in the excitations. Normally, one chooses the active space as small as possible, to reduce the computational effort. In fact, a large CI calculation is not necessary, because in the semiempirical framework the dynamic correlation effects are taken into account primarily by the parameterization. The minimal active space includes all the orbitals whose occupation depends on the electronic state and on the geometry (here

considering states and geometries that are accessible in the process under study). For organic molecules, usually one considers the n and π MOs of higher energy and the lowest π^* ones.

In State Average CASSCF calculations, different stationary points for the averaged energy may exist, and one may switch from a solution to another one during a PES scan or a geometry optimization. This may be a problem in trajectory calculations and in geometry optimizations, because it generates discontinuities in the PESs. In particular, such irregularities in the PES make very hard to conserve the total energy during the integration of a trajectory. Besides the non-linear nature of SCF problems, there are two specific reasons for this behaviour: one is the possible occurrence of a state switching (the states that are optimized are not the same at different geometries), and the second one is an exchange between active and non-active MOs. The former source of PES discontinuities is eliminated in our floating occupation SCF, because there is no explicit reference to a given set of electronic states to be optimized. The second one remains: in some cases, the orbital energies can change with the molecular geometry, so that an active MO, with floating occupation, swaps its position with a virtual or a doubly occupied one. This exchange may take place across a very small variation of the internal coordinates, and an abrupt change in the CI energies and wavefunctions then occurs. The tendency of the SCF procedure to optimize with greater care the orbitals with a larger occupation number may contribute to the suddenness of the switch. To eliminate this problem, one may be forced to enlarge the active space, beyond the minimum required to describe the electronic states of interest.

3.3 Reparameterization of the semiempirical hamiltonian for azobenzene

In a previous work our group determined a set of parameters for the AM1 semiempirical hamiltonian, that described rather well the first four singlet PES of azobenzene. As described in Chapter 1, these parameters were employed in the first simulation of the photoisomerization of an isolated azobenzene molecule, that was able to reproduce the experimental quantum yields for the $cis \rightarrow trans$ and $trans \rightarrow cis$ conversion, and offered an explanation of the violation of Kasha's rule [21]. The simulations yielded S_1 lifetimes for the *trans* isomer, that agree with the shorter components found in measurements, but underevaluate the longer components [21,66]. The disagreement can be due to the solvent effects (that were neglected in those simulations), to drawbacks of the surface hopping method, or to inaccuracies in the potential energy surfaces.

We have therefore decided to proceed to a new optimization of the semiempirical parameters. A better accuracy is expected, since we can exploit new high quality ab initio data that have been published in the meantime [38,54,55]. Moreover, we have realized the importance of the torsional modes of the phenyl groups around the C-N single bonds (see chapter 2), that was overlooked in our previous work. The reparameterization has been based on experimental data and on the results of ab initio calculations.

The optimization of the semiempirical parameters consists on the following steps:

(A) Determination of a set of "target" values $V_{t,i}$ (energy differences, internal molecular coordinates and others) taken from experimental results or ab initio calculations, that should be reproduced by the semiempirical calculations;

(B) Choice of the semiempirical method, namely choice of the type of Hamiltonian

(MNDO, AM1, PM3, etc), active space of the molecular orbitals, MO energy width parameter w, CI subspace;

(C) Choice of the starting semiempirical parameters (generally they are the standard ones) and partition of the parameters in two subsets: those that will not be modified and those that will be optimized;

(D) Semiempirical calculation of all quantities $V_{s,i}$ corresponding to the "target" values $V_{t,i}$, yielding results that depend on a given set of parameters $\mathbf{P}$;

(E) Determination of the function to minimize, that is:

$$F(\mathbf{P}) = \left[\sum_i \left(\frac{V_{s,i}(\mathbf{P}) - V_{t,i}}{V_{t,i}}\right)^2 W_i\right]\left[\sum_i W_i\right]^{-1} \tag{3.11}$$

where the weights W_i are chosen according to the importance and accuracy of the associated target values.

(F) Application of an optimization algorithm to determine new tentative values of the parameters $\mathbf{P}$.

Points (D), (E) and (F) are repeated until convergence of the optimization.

We can now examine our choices. Among the "target" values, we have considered the excitation energies of TAB and CAB, some energy differences between remarkable points of the potential energy surfaces, and a set of geometrical parameters. The tables 3.1 3.2, 3.3 and 3.4 report the "target" values and those obtained semiempirically with the best set of parameters, and the weights W_i. When possible, we have used values that were measured in vapour phase: in fact, we shall eventually take into account the solvent effects in an explicit way, using a QM/MM strategy (see Chapter 5). For the excited PES, the most accurate calculations are the CASPT2 ones by the group of Bologna (Gagliardi et al [55] and Cembran et al [38]). Very good values for the excitation energy were also determined by the Coupled Cluster method [37].

In the following tables we use some acronyms to indicate particular geometries. Besides TAB and CAB (*trans*- and *cis*-azobenzene), we have:

- ROT = rotamer: dihedral angle CNNC near to 90°;
- INV = invertomer: one of the two angles NNC near to 180°;
- PlanINV = planar invertomer: both phenyl groups are on the plane formed by the atoms CNNC;
- PerpINV = perpendicular invertomer: the phenyl group attached to the nitrogen atom that undergoes the inversion, is perpendicular to the CNNC plane, while the other one is on the plane.

Some items in the Tables 3.1 and 3.2 need to be explained.

- Vertical excitation energies, $\Delta E(S_0 - S_n)$ are deduced, when possible, from the absorption spectra in vapour phase [59, 75], namely, from the wavelength λ_{max} where the maximum molar extinction coefficient is found. The bands are well defined for TAB S_1 (^1B_g), TAB S_2 (^1B_u), CAB S_1 (^1B) and CAB S_4 (^1B). The states TAB S_3 (^1A_g) and TAB S_4 (^1B_u) are very near in energy to S_2 but they have very small oscillator strengths, thus their bands are not evident in the spectrum. The best ab initio calculations put them a fraction of eV above S_2 [8, 32, 37, 76]. The states CAB S_2 (^1B) and S_3 (^1A) probably correspond to the shoulder extended from 4.4 to 4.8 eV, next to the more intense band that we attribute to S_4: two computational works confirm this interpretation [37, 76].

Table 3.1: Target values and semiempirical results obtained with the optimized parameters and the CI space of 82 determinants. Energies in eV, given as differences from TAB S_0 (except for the excitation energies of CAB).

	value target $V_{t,i}$	value semiemp. $V_{s,i}$	error $V_{s,i} - V_{t,i}$	relative error (%)	weigth W_i
TAB, $\Delta E(S_0 - S_1)$	2.8200	2.7993	-0.0207	0.733	8/11
TAB, $\Delta E(S_0 - S_2)$	4.1200	4.4583	0.3383	8.211	8/11
TAB, $\Delta E(S_0 - S_3)$	4.2000	4.8339	0.6339	15.092	2/11
TAB, $\Delta E(S_0 - S_4)$	4.2000	4.8774	0.6774	16.129	2/11
TAB, $\Delta E(S_0 - T_1)$	1.7000	1.5812	-0.1188	6.988	1/11
TAB, $\Delta E(S_0 - T_2)$	2.2000	2.7958	0.5958	27.082	1/11
CAB, $\Delta E(S_0 - S_1)$	2.9200	2.8737	-0.0463	1.584	8/10.5
CAB, $\Delta E(S_0 - S_2)$	4.6000	5.4091	0.8091	17.589	2/10.5
CAB, $\Delta E(S_0 - S_3)$	4.6000	4.9040	0.3040	6.609	2/10.5
CAB, $\Delta E(S_0 - S_4)$	5.1700	5.5161	0.3461	6.695	8/10.5
CAB, $\Delta E(S_0 - T_1)$	2.1000	1.5590	-0.5410	25.762	1/10.5
ΔE(CAB-TAB), S_0	0.5500	0.5871	0.0371	6.742	2/3
ΔE 90° phenyl rotat. TAB S_0	0.5000	0.3777	-0.1223	24.468	1/3
PerpINV S_0	1.5500	1.9132	0.3632	23.435	4/15
PerpINV S_1 (geom. S_0)	2.7500	3.0655	0.3155	11.472	4/15
PerpINV S_2 (geom. S_0)	4.5500	5.2794	0.7294	16.030	4/15
PerpINV S_3 (geom. S_0)	6.8000	5.4679	-1.3321	19.590	2/15
PlanINV S_0	2.1000	2.1439	0.0438	2.088	1/15
TS ROT S_0	1.7000	2.0842	0.3842	22.597	4/13
TS ROT S_1 (geom. S_0)	2.5300	2.4827	-0.0473	1.871	4/13
TS ROT S_2 (geom. S_0)	2.9100	3.2208	0.3108	10.679	2/13
TS ROT S_3 (geom. S_0)	4.4800	5.8981	1.4181	31.654	1/13
TS ROT S_4 (geom. S_0)	4.4800	6.6287	2.1487	47.962	2/13
Min. S_1 planar (TAB)	2.2700	2.3369	0.0669	2.948	4/5
S_0 (geom min. S_1 planar)	1.0200	0.6445	-0.3755	36.815	2/5
PlanINV S_1	3.3000	2.8994	-0.4006	12.139	4/5
Conic Intersec. $S_0 - S_1$ ROT	2.2700	2.2132	-0.0568	2.502	8/9
Conic Intersec. $S_0 - S_1$ TAB	3.3000	2.9592	-0.3408	10.328	8/9
Min. S_2 ROT	2.3000	3.1495	0.8495	36.936	2/9
Min. T_1 ROT	1.2500	1.0866	-0.1634	13.074	1/2
S_0 (geom. min. T_1 ROT)	1.5000	1.3842	-0.1158	7.722	1/2

Table 3.2: Target values and semiempirical results obtained with the optimized parameters and the CI space of 94 determinants. Energies in eV, given as differences from TAB S_0 (except for the excitation energies of CAB).

	value target $V_{t,i}$	value semiemp. $V_{s,i}$	error $V_{s,i} - V_{t,i}$	relative error (%)	weigth W_i
TAB, $\Delta E(S_0 - S_1)$	2.8200	2.8291	0.0091	0.323	8/11
TAB, $\Delta E(S_0 - S_2)$	4.1200	4.3696	0.2496	6.057	8/11
TAB, $\Delta E(S_0 - S_3)$	4.2000	4.7143	0.5143	12.245	2/11
TAB, $\Delta E(S_0 - S_4)$	4.2000	4.7340	0.5340	12.714	2/11
TAB, $\Delta E(S_0 - T_1)$	1.7000	1.6144	-0.0856	5.035	1/11
TAB, $\Delta E(S_0 - T_2)$	2.2000	2.6645	0.4645	21.114	1/11
CAB, $\Delta E(S_0 - S_1)$	2.9200	2.8932	-0.0268	0.918	8/10.5
CAB, $\Delta E(S_0 - S_2)$	4.6000	5.4397	0.8397	18.254	2/10.5
CAB, $\Delta E(S_0 - S_3)$	4.6000	4.8634	0.2634	5.727	2/10.5
CAB, $\Delta E(S_0 - S_4)$	5.1700	5.5335	0.3635	7.030	8/10.5
CAB, $\Delta E(S_0 - T_1)$	2.1000	1.5709	-0.5291	25.195	1/10.5
ΔE(CAB-TAB), S_0	0.5500	0.6080	0.0580	10.548	2/3
ΔE 90° phenyl rotat. TAB S_0	0.5000	0.3964	-0.1036	20.715	1/3
PerpINV S_0	1.5500	1.9330	0.3830	24.710	4/15
PerpINV S_1 (geom. S_0)	2.7500	3.0869	0.3369	12.249	4/15
PerpINV S_2 (geom. S_0)	4.5500	5.3021	0.7521	16.531	4/15
PerpINV S_3 (geom. S_0)	6.8000	5.4821	-1.3179	19.381	2/15
PlanINV S_0	2.1000	2.1626	0.0626	2.981	1/15
TS ROT S_0	1.7000	2.1069	0.4069	23.935	4/13
TS ROT S_1 (geom. S_0)	2.5300	2.5042	-0.0258	1.021	4/13
TS ROT S_2 (geom. S_0)	2.9100	3.2409	0.3309	11.372	2/13
TS ROT S_3 (geom. S_0)	4.4800	5.9038	1.4238	31.782	1/13
TS ROT S_4 (geom. S_0)	4.4800	6.6507	2.1707	48.453	2/13
Min. S_1 planar (TAB)	2.2700	2.3613	0.0913	4.024	4/5
S_0 (geom min. S_1 planar)	1.0200	0.6545	-0.3655	35.838	2/5
PlanINV S_1	3.3000	2.9238	-0.3762	11.400	4/5
Conic Intersec. $S_0 - S_1$ ROT	2.2700	2.2355	-0.0345	1.521	8/9
Conic Intersec. $S_0 - S_1$ TAB	3.3000	2.9559	-0.3441	10.428	8/9
Min. S_2 ROT	2.3000	3.1750	0.8750	38.045	2/9
Min. T_1 ROT	1.2500	1.1105	-0.1395	11.163	1/2
S_0 (geom. min. T_1 ROT)	1.5000	1.3985	-0.1015	6.766	1/2

- For the triplets, we have adopted as target values the averages of several experimental and computational data, that cover the following ranges: 1.57-2.09 eV for TAB T_1 [32, 38, 76, 77] and 2.10-2.83 eV for TAB T_2 [32, 76, 78]. In the case of CAB, we only have two calculated values for T_1: 1.83 eV [32] and 2.20 eV [38].
- The energy difference between CAB and TAB has been measured in *n*-heptane (0.51±0.06) [42], while most of the calculated values for the isolated molecule are slightly higher (0.55-0.69 eV) [32, 36, 55, 79–81]. We have chosen the value 0.55 eV, which is compatible with the PES computed by Gagliardi et al [55] and very near to the experimental value.
- Concerning the rotation of the phenyl groups around the N-C bonds, there is some uncertainty. Our previous work (see ref. [82] and chapter 2), based on DFT and MP2 calculations, shows a barrier for the simultaneous torsion of both groups, equal to 0.5 eV (C_{2h} geometry with torsion angles of 90°). Our study was directed to calculate the oscillator strength for the forbidden $n \rightarrow \pi^*$ transition and we found good agreement with the experiment. On the other hand, preliminary calculations show that a good reproduction of torsional potential using semiempirical methods is quite difficult. For this reason, we gave a little weight to this target value and we introduced an ad hoc correction after the optimization of the parameters (see below).
- Configuration interaction calculations, with geometries optimized at CASSCF level [32, 79], show that the transition state (TS) between CAB and TAB has a perpendicular invertomer geometry (PerpINV). The experimental values of activation energy for the conversion CAB→TAB should be referred to this geometry. In nonpolar solvents, the activation ΔH is 1 eV [83–87], i.e., 1.55 eV with respect to the TAB. Two more saddle points have been individuated, by geometry optimizations: the rotamer (ROT) [32, 38, 79] and the planar invertomer (PlanINV) [32, 79]. Target values were assigned to these geometries according to computational results of previous studies: for the ground state of TS-ROT we used data from the ref. [32] and for its excited states from the ref. [55]. For the ground and excited states of PerpINV, ref. [32]. At a semiempirical level, for TS-ROT we performed a saddle point search, while for PerpINV and PlanINV we individuated two constrained minima, fixing one of the two NNC angles at 180°.
- The optimization of the internal coordinates in the S_1 PES, keeping a planar geometry TAB type, decreases the energy by 0.55 eV [6, 38]. Combining these data with the experimental vertical excitation energy, the target value of 2.27 eV is obtained. From ref. [38] we infer the energy difference $S_0 - S_1$ at the same geometry (1.25 eV), which puts the energy of S_0 equal to 1.02 eV.
- For the invertomer (PlanINV) in the S_1 state (one of the NNC angles fixed at 180°), we have chosen a value of 0.48 eV above the vertical excitation energy, as a compromise between two rather different theoretical values: 0.20 e 0.86 eV respectively, from refs. [6] and [32].
- The S_0 and S_1 surfaces present one crossing seam [21, 66]. The lowest energy point (conical intersection $S_0 - S_1$ ROT) coincides with the minimum of the S_1 PES. Its energy has been determined by Cembran et al [38] in 2.03 eV with respect to TAB. Considering that in their calculations the vertical transition energy for TAB and CAB is underestimated by 0.2-0.3 eV, we took a target value of 2.27 eV for the conical intersection. The crossing seam can also be reached by keeping a planar geometry of TAB type, deformed for the symmetric opening of the two angles NNC, as shown by Diau [6]: in this case, the energy is little higher than the vertical excitation one (near

to 3.3 eV).
- The energy value of the minimum of S_2 has been taken with some approximation from the potential energy curves of Gagliardi et al [55] (in the corresponding figure of this reference, the identification of the states is not clear).
- The minimum of the T_1 state (rotamer), as well as the energy of S_0 at the same geometry, have been determined by Cembran et al [38].

Concerning the target values of internal coordinates relative to critical points of the PESs, we note that the internal consistence of such data is important. In fact, the dynamical behavior depends on the small differences of the optimal geometries, between ground and excites states, or between isomers and transition states. For this reason, we have employed, whenever possible, the work of Cembran et al [38], that provides data about several different geometries. The calculation level, CASSCF with a large active space, guarantees a good agreement with the experimental data for the ground state of TAB [27, 28, 31, 35] and CAB [40].

- As indicated above, we have used the data of ref. [38] for the geometries TAB S_0, CAB S_0, TS ROT S_0, planar minimum S_1 (TAB) and conical intersection $S_0 - S_1$ ROT.
- The geometries PlanINV and PerpINV S_0 were taken from our previous CASSCF calculations [32]. We have corrected the distances and the bond angles, considering the differences found with respect to the results of Cembran et al [38] for the TAB and CAB geometries. For the PlanINV and PerpINV geometries, the two R_{NC} bond distances are different: the longer one, indicated by (1), is relative to the sp^2 nitrogen, while the shorter one, indicated as (2), concerns the nitrogen undergoing inversion.
- The geometry of the $S_0 - S_1$ conical intersection of TAB, obtained by symmetric opening of the NNC angles, has been calculated by Diau [6]. The values of R_{NN} and R_{NC} have been corrected by comparison between the data of Diau and those of Cembran et al [38], for the geometry of the minimum of planar S_1.
- For the geometry PlanINV S_1 there exists only one previous calculation [32]. This result has not been corrected, because of the lack of more accurate data for similar geometries in the same state to compare with.

The choice of the semiempirical method to be used and the starting parameters for the optimization (points B and C in the reparameterization procedure, see above) has been done by trial-and-error, taking also into account the "robustness" of the calculation procedure. Moreover, we have taken advantage of previous reparameterizations, having as target the electronic states of benzene, using the AM1 [88] and PM3 [89] Hamiltonians.

Concerning to the "robustness" of the method, we observe that the CI calculation is based on an active space of molecular orbitals, that have variable occupation numbers at the SCF level. It is very important that the active space does not undergo sudden variations with the gradual changes of the geometry; in other words, we want to avoid the switching of two orbitals, as described at the end of section 3.2. It is possible to influence the composition of the active space and then to improve the "robustness" of the calculation, acting on three kinds of parameters:
- The extension of the active space, namely, how many orbitals (N_{act}) and how many electrons belong to it.
- The parameter w (orbitalic energy amplitude): if w is much less than the difference between the Fermi level and the energy of the lowest active orbital, the last one has an occupation number of almost 2, as the underlying inactive orbitals; possible exchanges

Table 3.3: Target values of internal coordinates and semiempirical results obtained with the optimized parameters of azobenzene and the CI space of 82 determinants. Distances in Å and angles in degrees.

	Target value $V_{t,i}$	Semiemp. value $V_{s,i}$	error $V_{s,i} - V_{t,i}$	relative value (%)	weight W_i
TAB, R_{NN}	1.243	1.2771	0.0341	2.746	1/5
TAB, R_{NC}	1.422	1.4368	0.0148	1.041	1/5
TAB, ∠NNC	115.1	117.9	2.7780	2.414	3/5
CAB, R_{NN}	1.242	1.2541	0.0121	0.972	1/6.1
CAB, R_{NC}	1.435	1.4506	0.0156	1.088	1/6.1
CAB, ∠NNC	122.4	125.8	3.3596	2.745	3/6.1
CAB, ∠NNCC	62.0	60.4	-1.5842	2.555	1/6.1
CAB, ∠CNNC	4.2	0.7	-3.4857	82.992	0.1/6.1
TS ROT S_0, R_{NN}	1.304	1.2941	-0.0099	0.758	1/8
TS ROT S_0, R_{NC}	1.370	1.3952	0.0252	1.841	1/8
TS ROT S_0, ∠NNC	122.2	128.4	6.2387	5.105	3/8
TS ROT S_0, ∠CNNC	85.3	91.0	5.7294	6.717	3/8
PerpINV S_0, R_{NN}	1.233	1.2391	0.0061	0.492	1/6
PerpINV S_0, $R_{\mathrm{NC}}(1)$	1.425	1.4380	0.0130	0.915	1/6
PerpINV S_0, $R_{\mathrm{NC}}(2)$	1.318	1.3911	0.0731	5.546	1/6
PerpINV S_0, ∠NNC(1)	116.0	125.9	9.9442	8.573	3/6
PlanINV S_0, R_{NN}	1.247	1.2447	-0.0023	0.184	1/6
PlanINV S_0, $R_{\mathrm{NC}}(1)$	1.424	1.4418	0.0178	1.247	1/6
PlanINV S_0, $R_{\mathrm{NC}}(2)$	1.354	1.3937	0.0397	2.929	1/6
PlanINV S_0, ∠NNC(1)	118.0	126.3	8.2761	7.014	3/6
Min. S_1 planar (TAB), R_{NN}	1.253	1.2598	0.0068	0.544	1/5
Min. S_1 planar (TAB), R_{NC}	1.366	1.4072	0.0412	3.017	1/5
Min. S_1 planar (TAB), ∠NNC	128.8	132.3	3.5329	2.743	3/5
PlanINV S_1, R_{NN}	1.309	1.2348	-0.0742	5.669	1/6
PlanINV S_1, $R_{\mathrm{NC}}(1)$	1.403	1.4036	0.0006	0.045	1/6
PlanINV S_1, $R_{\mathrm{NC}}(2)$	1.360	1.3824	0.0224	1.644	1/6
PlanINV S_1, ∠NNC(1)	118.7	141.1	22.3826	18.856	3/6
Con. Int. $S_0 - S_1$ ROT, R_{NN}	1.261	1.2669	0.0059	0.466	1/14
Con. Int. $S_0 - S_1$ ROT, R_{NC}	1.397	1.4131	0.0161	1.149	1/14
	1.371	1.3977	0.0267	1.949	1/14
Con. Int. $S_0 - S_1$ ROT, ∠NNC	117.3	128.0	10.6858	9.110	3/14
	136.0	139.5	3.5382	2.602	3/14
Con. Int. $S_0 - S_1$ ROT, ∠CNNC	94.0	96.2	2.1544	2.292	3/14
Con. Int. $S_0 - S_1$ ROT, ∠NNCC	25.9	9.2	-16.7420	64.641	1/14
	18.8	9.1	-9.7048	51.621	1/14
Con. Int. $S_0 - S_1$ TAB, R_{NN}	1.1950	1.2345	0.0395	3.309	1/5
Con. Int. $S_0 - S_1$ TAB, R_{NC}	1.3260	1.3895	0.0635	4.789	1/5
Con. Int. $S_0 - S_1$ TAB, ∠NNC	156.6	158.0	1.4000	0.894	3/5

Table 3.4: Target values of internal coordinates and semiempirical results obtained with the optimized parameters of azobenzene and the CI space of 94 determinants. Distances in Å and angles in degrees.

	Target value $V_{t,i}$	Semiemp. value $V_{s,i}$	error $V_{s,i} - V_{t,i}$	relative value (%)	weigth W_i
TAB, R_{NN}	1.243	1.2799	0.0369	2.965	1/5
TAB, R_{NC}	1.422	1.4342	0.0122	0.857	1/5
TAB, ∠NNC	115.1	117.8	2.6850	2.333	3/5
CAB, R_{NN}	1.242	1.2537	0.0117	0.942	1/6.1
CAB, R_{NC}	1.435	1.4515	0.0165	1.153	1/6.1
CAB, ∠NNC	122.4	125.5	3.1206	2.550	3/6.1
CAB, ∠NNCC	62.0	63.2	1.2104	1.952	1/6.1
CAB, ∠CNNC	4.2	0.3	-3.9414	93.843	0.1/6.1
TS ROT S_0, R_{NN}	1.304	1.2944	-0.0096	0.733	1/8
TS ROT S_0, R_{NC}	1.370	1.3950	0.0250	1.828	1/8
TS ROT S_0, ∠NNC	122.2	128.4	6.1972	5.071	3/8
TS ROT S_0, ∠CNNC	85.3	91.4	6.1189	7.173	3/8
PerpINV S_0, R_{NN}	1.233	1.2391	0.0061	0.493	1/6
PerpINV S_0, $R_{\mathrm{NC}}(1)$	1.425	1.4377	0.0127	0.890	1/6
PerpINV S_0, $R_{\mathrm{NC}}(2)$	1.318	1.3912	0.0732	5.553	1/6
PerpINV S_0, ∠NNC(1)	116.0	125.9	9.9521	8.579	3/6
PlanINV S_0, R_{NN}	1.247	1.2454	-0.0016	0.132	1/6
PlanINV S_0, $R_{\mathrm{NC}}(1)$	1.424	1.4408	0.0168	1.178	1/6
PlanINV S_0, $R_{\mathrm{NC}}(2)$	1.354	1.3935	0.0395	2.917	1/6
PlanINV S_0, ∠NNC(1)	118.0	126.2	8.2112	6.959	3/6
Min. S_1 planar (TAB), R_{NN}	1.253	1.2598	0.0068	0.545	1/5
Min. S_1 planar (TAB), R_{NC}	1.366	1.4072	0.0412	3.017	1/5
Min. S_1 planar (TAB), ∠NNC	128.8	132.3	3.5320	2.742	3/5
PlanINV S_1, R_{NN}	1.309	1.2348	-0.0742	5.670	1/6
PlanINV S_1, $R_{\mathrm{NC}}(1)$	1.403	1.4037	0.0007	0.050	1/6
PlanINV S_1, $R_{\mathrm{NC}}(2)$	1.360	1.3824	0.0224	1.645	1/6
PlanINV S_1, ∠NNC(1)	118.7	141.1	22.3831	18.857	3/6
Con. Int. $S_0 - S_1$ ROT, R_{NN}	1.261	1.2668	0.0058	0.459	1/14
Con. Int. $S_0 - S_1$ ROT, R_{NC}	1.397	1.4131	0.0161	1.150	1/14
	1.371	1.3975	0.0265	1.935	1/14
Con. Int. $S_0 - S_1$ ROT, ∠NNC	117.3	128.0	10.7301	9.148	3/14
	136.0	139.5	3.5095	2.581	3/14
Con. Int. $S_0 - S_1$ ROT, ∠CNNC	94.0	96.1	2.1173	2.252	3/14
Con. Int. $S_0 - S_1$ ROT, ∠NNCC	25.9	9.4	-16.5335	63.836	1/14
	18.8	9.2	-9.5815	50.965	1/14
Con. Int. $S_0 - S_1$ TAB, R_{NN}	1.1950	1.2302	0.0352	2.942	1/5
Con. Int. $S_0 - S_1$ TAB, R_{NC}	1.3260	1.3777	0.0517	3.895	1/5
Con. Int. $S_0 - S_1$ TAB, ∠NNC	156.6	156.9	0.3267	0.209	3/5

Table 3.5: Semiempirical parameters characterizing the AM1 and PM3 methods.

Parameters	Description
U_s, U_p	monocenter and one-electron integrals of p and s orbitals
β_s, β_p	bicenter and one-electron resonance integrals of p and s orbitals
ξ_s, ξ_p	s and p Slater atomic orbital exponent
α_A	core-core repulsion of atom A
$\alpha_{A,B}$	core-core repulsion between atoms A and B
G_{ss},G_{sp} G_{pp},$G_{pp'}$	two-electron monocenter repulsion integral between $s-s$, $s-p$ $p-p$ and $p-p'$ orbitals
H_{sp}	two-electron monocenter exchange integral between $s-p$ orbitals
K_{nA}	gaussian multiplier of core-core repulsion
L_{nA}	gaussian exponent of core-core repulsion
M_{nA}	gaussian center of core-core repulsion

between active and inactive orbitals will be rather gradual, except in extreme cases. The same thing is valid for the highest active orbital, if its occupation number is near to zero. However, a small parameter w involves fast variation of the occupation number and then changes in the orbital shape, when their energies are near to the Fermi level.

- In order to control the composition of the active space, we have implemented a procedure that allows the use of different semiempirical parameters in the SCF and CI calculations. We observe that the energies and the wavefunctions of the states depend directly on the set of parameters used in the CI calculation. However, considering that a truncated configuration basis is used, the shape of the orbitals also influences the results. For this reason, also the parameters used in the SCF calculation have an effect, although indirect. In our case, we have fixed the parameters β_S and β_P for the carbon atoms to high values, for the SCF calculation only, with the idea of increasing the separation between the occupied and virtual orbitals of the phenyl groups. In this way, we try to control the number of aromatic π and π^* orbitals belonging to the active space.

Several optimization trials have brought to the following choices. Among the two standard parameterizations (AM1 [90] and PM3 [69–72]), for which the optimized parameters of benzene were available, AM1 has given better results. Then we have used: for H, the standard parameters of AM1; for C, those optimized for benzene [88], and for N, we have optimized all parameters, except those of the core potential (α, K_I, L_I, M_I, see Table 3.5 for their meaning). All the final parameters are reported in Table 3.6. The parameters β_S and β_P used for the C atoms in the SCF calculation are -38 and -35 eV, respectively. The magnitude associated with the orbitalic energy is $w = 0.10$ hartree. The

Table 3.6: Semiempirical parameters used in the calculation for azobenzene, considering a CI with 82 determinants. The parameters of carbon had been already optimized for the benzene molecule [88]. The parameters for hydrogen are the standard ones in the AM1 method [90], as well as those of the nitrogen core potential (α, K_I, L_I, M_I). The other parameters of nitrogen have been optimized. The units are indicated in the table (the K_I parameters are dimensionless).

parameter	unit	N_{std}	N_{opt}	C_{std}	C_{opt}	H
U_{SS}	eV	-71.860000	-68.388062	-52.028658	-49.536242	-11.396427
U_{PP}	eV	-57.167581	-56.045018	-39.614239	-33.722927	
β_S	eV	-20.299110	-11.018709	-15.715783	-13.797578	-6.173787
β_P	eV	-18.238666	-19.591942	-7.719283	-10.113264	
G_{SS}	eV	13.590000	16.667653	12.230000	12.492690	12.848000
G_{SP}	eV	12.660000	11.470530	11.470000	11.571701	
G_{PP}	eV	12.980000	13.339308	11.080000	12.017613	
G_{P2}	eV	11.590000	10.242204	9.840000	7.923532	
H_{SP}	eV	3.140000	1.794342	2.430000	2.739211	
ζ_S	bohr^{-1}	2.315410	2.169870	1.808665	1.412377	1.188078
ζ_P	bohr^{-1}	2.157940	1.917021	1.685116	1.749266	
α	Å^{-1}	2.947286	2.947286	2.648274	2.626199	2.882324
K_1		0.025251	0.025251	0.011355	0.011355	0.122796
K_2		0.028953	0.028953	0.045924	0.045924	0.005090
K_3		-0.005806	-0.005806	-0.020061	-0.020061	-0.018336
K_4			-0.001260	-0.001260		
L_1	Å^{-2}	5.000000	5.000000	5.000000	5.000000	5.000000
L_2	Å^{-2}	5.000000	5.000000	5.000000	5.000000	5.000000
L_3	Å^{-2}	2.000000	2.000000	5.000000	5.000000	2.000000
L_4	Å^{-2}			5.000000	5.000000	
M_1	Å	1.500000	1.500000	1.600000	1.600000	1.200000
M_2	Å	2.100000	2.100000	1.850000	1.850000	1.800000
M_3	Å	2.400000	2.400000	2.050000	2.050000	2.000000
M_4	Å	2.650000		2.650000		

active space includes 12 orbitals, 6 formally occupied and 6 virtuals (i.e., 12 electrons). For a more restricted orbital set the CI space is complete (CAS-CI), i.e., it includes all the determinants obtained distributing the electrons in the orbitals, with a total spin $S_z = 0$. The CAS-CI orbital set includes three occupied and one virtual orbitals (two lone pairs, one π and one π^*). Moreover, in the CI space we included all the single excitations from the 6 occupied orbitals to the 6 virtual ones of the active space. In total, there are 82 determinants.

As we shall see in the next chapters, the explicit inclusion of the solvent molecules and their interaction with the solute (in our case the azobenzene molecule) in some cases perturbs the molecular orbitals, and brings about a considerable alteration of the active space. For this reason we have decided to increase the CI space (only for the dynamics calculations of azobenzene in solution), considering an active space with 13 orbitals (from the 28-th to the 40-th), 7 formally occupied and 6 virtual (namely, 14 electrons). In this case all the single excitations from the 7 occupied orbitals to the 6 virtual ones are included. In total, there will be 94 determinants. As seen in the tables 3.1 3.2, 3.3 and 3.4, the results obtained with 82 or 94 determinants are almost exacly the same.

All semiempirical calculations were executed with the MOPAC program [91], in the development version modified by our group. In order to optimize the parameters we have applied the simplex method, combined with the simulated annealing, as described in the Appendix A.

3.3.1 Inclusion of the torsional potentials

As already found in the previous reparemeterization [21], the optimization of the parameters could not eliminate a wrong feature of the calculated potentials, namely that the equilibrium NNC angles are too large and the inversion barrier of the nitrogen is too small. For this reason we have added the same potential energy term to all the electronic PESs, with the following expression:

$$U_{ang}(\theta,\alpha_1,\alpha_2) = P_1 \left[cos\left(\pi\frac{\alpha_1 - P_2}{\pi - P_2}\right) + 1\right] \left[cos\left(\pi\frac{\alpha_2 - P_2}{\pi - P_2}\right) + 1\right] \frac{P_3 + cos(2\theta)}{P_3 + 1} \quad (3.12)$$

Here and in the following, θ is the CNNC dihedral angle, α_1 and α_2 are the NNC angles. The parameter P_1 is an energy, in eV, P_2 is an angle and corresponds to the minimum of U_{ang}, and P_3 is a dimensionless constant. The dependence of U_{ang} on the dihedral angle CNNC vanishes if one of the NNC angles is near to 180°, as it must. The three parameters P_I have been optimized together with the semiempirical ones. In Table 3.7 we present the optimized set.

Table 3.7: Parameters that define the added potentials U_{ang} and U_{ph}.

parameter	unit	value
P_1	eV	-0.382809
P_2	degrees	82.172261
P_3		13.416564
P_4	eV	0.0949700
P_5		-0.660000

At the same time, a less important correction has been introduced to obtain a good torsional potential of phenyl groups. This added term has the form:

$$U_{ph}(\theta,\alpha_1,\alpha_2,\phi_1,\phi_2) = P_4 \frac{P_5 - cos\theta}{P_5 + 1} (1 + cos\alpha_1)\,(1 + cos\alpha_2)\,(sin^2\phi_1 + sin^2\phi_2) \quad (3.13)$$

Here we define ϕ_1 and ϕ_2 as torsion angles of the two phenyl groups; for each ring, the associated ϕ_i angle is given by $(\angle \mathrm{NNC_1C_2} + \angle \mathrm{NNC_1C_6} - \pi)/2$. The parameters P_4 and P_5 have been determined after the optimization of the semiempirical parameters. P_4 is an energetic factor and P_5 modulates the dependence of the angle $\theta \equiv$ CNNC. Before the addition of the U_{ph} potential, in the CAB isomer the C-N bond torsional potential is too strong, so at equilibrium we have $\phi = 46°$, while experimentally one finds 62° [40]. Viceversa, for TAB the torsional potential of the phenyl groups is too weak. In order to give a positive contribution to the torsional potential for TAB and a negative one for CAB, we take $P_4 > 0$ and $P_5 < 1$. We have determined P_4 and P_5 considering the torsional barriers for TAB, the equilibrium geometry of CAB, and the energetic difference CAB-TAB. The chosen values are in the Table 3.7. The semimepirical results of Tables 3.1 3.2, 3.3 and 3.4 were obtained with the addition of the potentials U_{ang} and U_{ph}.

In Figure 3.3.1 we show the different geometry configurations of azobenzene taken into account for the reparameterization procedure. The semiempirical results, obtained with the optimized parameters, are shown in the Tables 3.1, 3.2, 3.3 and 3.4. The vertical excitation energies can be compared with the experimental and ab initio ones. For the S_1 state ($n \rightarrow \pi^*$ transition) we obtained a nearly exact transition energy. The ab initio calculations used as reference for the optimization of the parameters [38, 55] are not as accurate: the errors are -0.32 eV for TAB and -0.21 eV for CAB. For the $\pi \rightarrow \pi^*$ singlet with the most intense absorption band (S_2 for TAB and S_4 for CAB), we have errors of about 0.34-0.35 eV. The semiempirical calculations seem to give results with the same accuracy for the most part of the ground state PES and the lowest excited singlets. Also the geometries are well reproduced. The most important errors are associated with the NNC angle of rotamers and invertomers, namely the transition states in S_0 and S_1; probably the added potential U_{ang} does not correct completely the drawbacks of the semiempirical calculation at these geometries. It is also possible that the ab initio data used as reference were not so accurate. It is important to consider the good reproduction of the conical intersection geometries $S_0 - S_1$.

The figures 3.2 and 3.3 shows the potential energy curves for the inversion and torsion mechanisms, with geometries optimized in S_0 or in S_1. It is important to notice that S_0 and S_1 potential curves are in good agreement with the most accurate ones, while the S_2 state is a bit too high.

3.3.2 Transition dipoles and absorption spectra.

The target values that are used in the reparameterization procedure are more or less directly connected with the PESs rather than with the electronic wavefunctions. Some features of the wavefunctions, of basic importance for the dynamics, are strictly dependent on the eigenvalues: for instance, the phase and mixing properties of the two states that share a conical intersection. However, the risk of computing the "right energy for the wrong wavefunction" is real. In the reparameterization procedure, the only safeguard against this risk is to require the right symmetry of the electronic wavefunctions, when applicable.

In this section, we show that the computed transition dipoles, a property directly related with the semiempirical wavefunctions, are in rather good agreement with the ab initio ones (see chapter 2) and reproduce the experimental absorption spectra. In Figure 3.4 we present the absorption spectrum of TAB and CAB, and in the Figures 3.5 and 3.6 the contributions due to the transitions to S_1 ($n - \pi^*$) and to S_2, S_3, and S_4 ($\pi - \pi^*$).

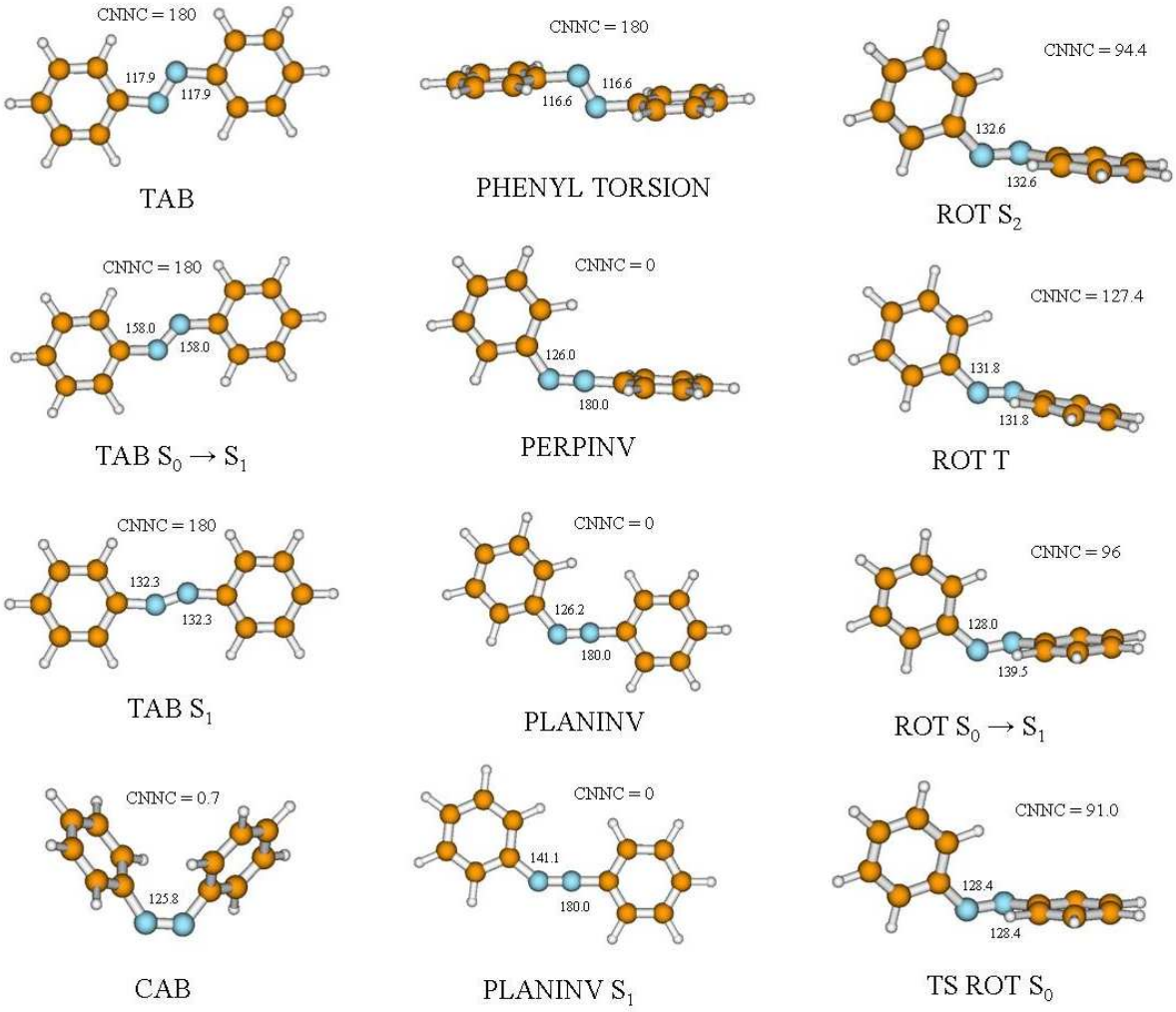

Figure 3.1: Optimized geometries in the ground, excited and transition states, indicated with S_N, considered in the reparameterization procedure, obtained with the CI of 82 determinants.

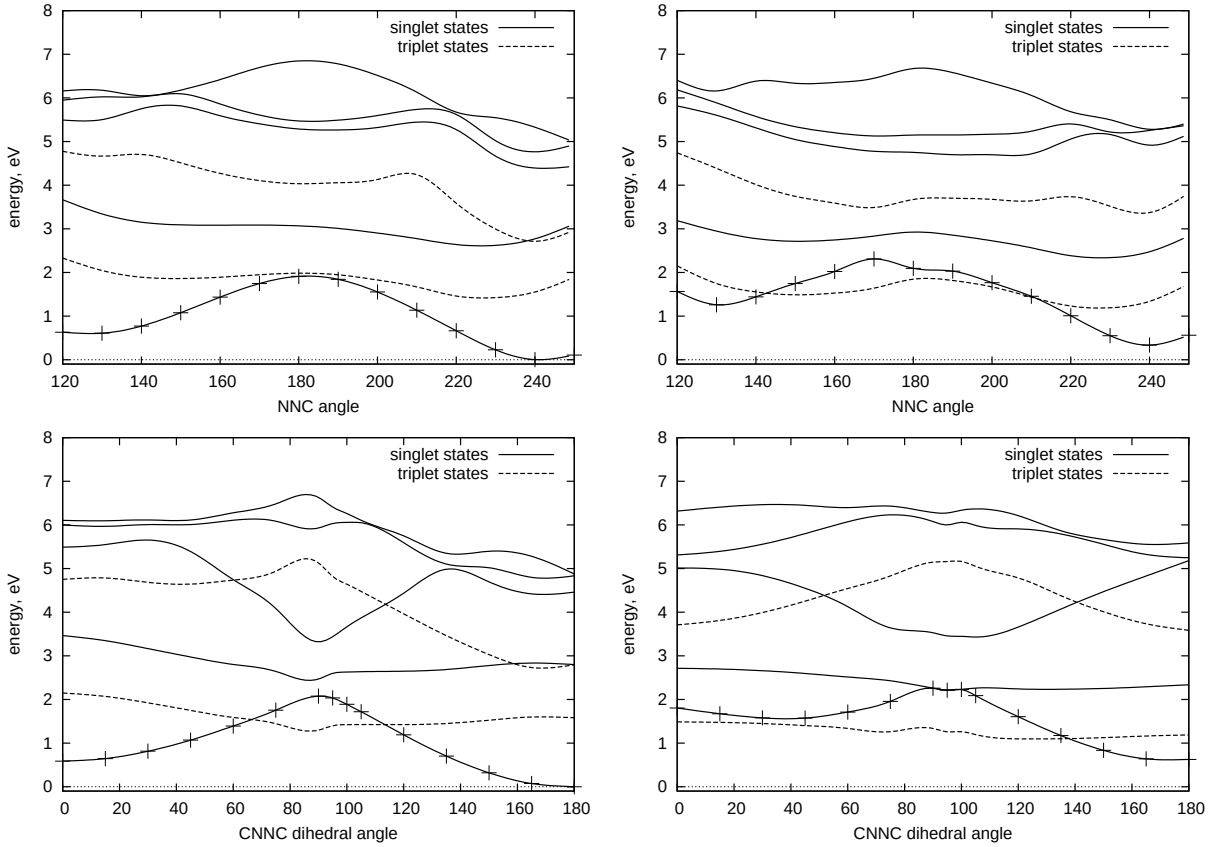

Figure 3.2: Potential curves for the inversion (upper panels) and rotation (lower panels) mechanisms, obtained with the CI with 82 determinants. Geometries optimized in S_0 and S_1 PES.

The spectra have been obtained by computing the transition energies ΔE and dipoles μ for the four excited states and for all the molecular geometries obtained in the Montecarlo run described in section 4.4 (red dots of Figure 4.2). The contribution of each Montecarlo geometry and electronic transition to the molar extinction coefficient ε ($M^{-1}\,cm^{-1}$) is represented by a gaussian, centered at the computed ΔE:

$$G(h\nu) = 10795 \cdot w\ \Delta E\ e^{-(h\nu-\Delta E)^2/w^2} \tag{3.14}$$

The gaussian is normalized so that its integrated area yields the oscillator strength, with the energies $h\nu$ and ΔE given in eV. The sum of all gaussians, divided by the number of Montecarlo points (about $6.8 \cdot 10^5$ for the TAB and about $3.8 \cdot 10^5$ for the CAB), yields the total spectrum. The gaussian width we used is $w = 0.05$ eV, much less than the total bandwidth, so that the latter is essentially due to the statistical distribution of geometries. In fact, the peaks are narrower than the experimental ones, probably because the classical Montecarlo sampling neglects the quantum uncertainty associated with the zero point vibrations, which is larger than the statistical one for the high frequency coordinates. For some of these modes, e.g. the N=N stretching, the excited state PESs differ noticeably from the ground state one, and this is a source of band broadening. Both the $n \rightarrow \pi^*$ and $\pi \rightarrow \pi^*$ oscillator strengths, collected in the Tables 3.8 and 3.9, are larger than the

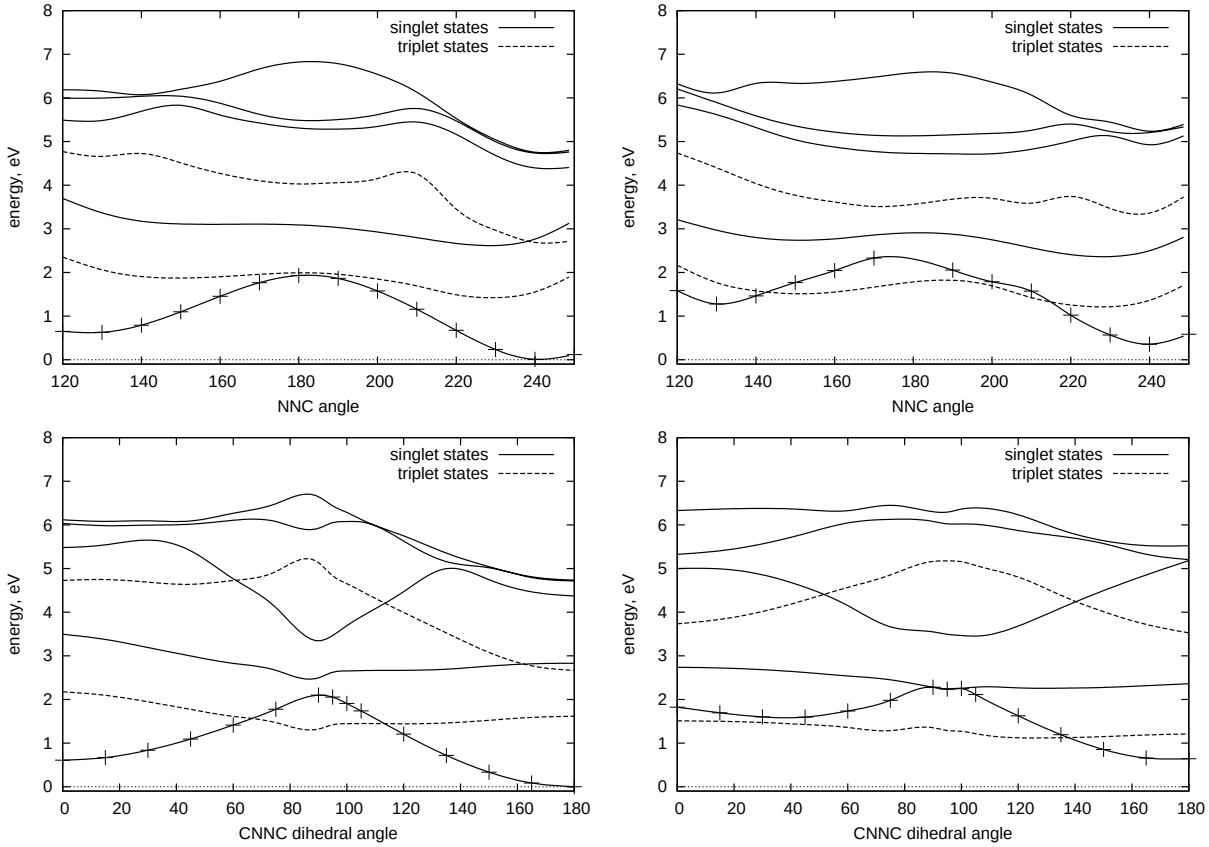

Figure 3.3: Potential curves for the inversion (upper panels) and rotation (lower panels) mechanisms, obtained with the CI with 94 determinants. Geometries optimized in S_0 and S_1 PES.

experimental ones, by a factor 1.3÷1.5 for the TAB and 0.9÷1.7. The combination of overestimated oscillator strengths and narrower bands results in much higher maxima of the molar extinction coefficient.

Table 3.8: Total oscillator strength and the corresponding values for each component for the $n \rightarrow \pi^*$ and $\pi \rightarrow \pi^*$ transitions of the TAB.

Transition	f_{tot}	f_x	f_y	f_z
$S_0 - S_1$	0.0129717971	0.0061244066	0.0068247863	0.0000226043
$S_0 - S_2$	1.0843463168	0.5652746949	0.5164666343	0.0026049876
$S_0 - S_3$	0.1152710088	0.0859683799	0.0246608865	0.0046417423
$S_0 - S_4$	0.0856060090	0.0633465963	0.0184441447	0.0038152680

In Figure 3.5 we also show the contributions of the three cartesian components of the transition dipole for the TAB. The body-fixed frame is defined as in chapter 2, i.e. the x axis corresponds to the N-N axis, the y axis also lies in the molecular plane and z is perpendicular to it. In the particular case of the $n-\pi^*$ transition, we can observe that the

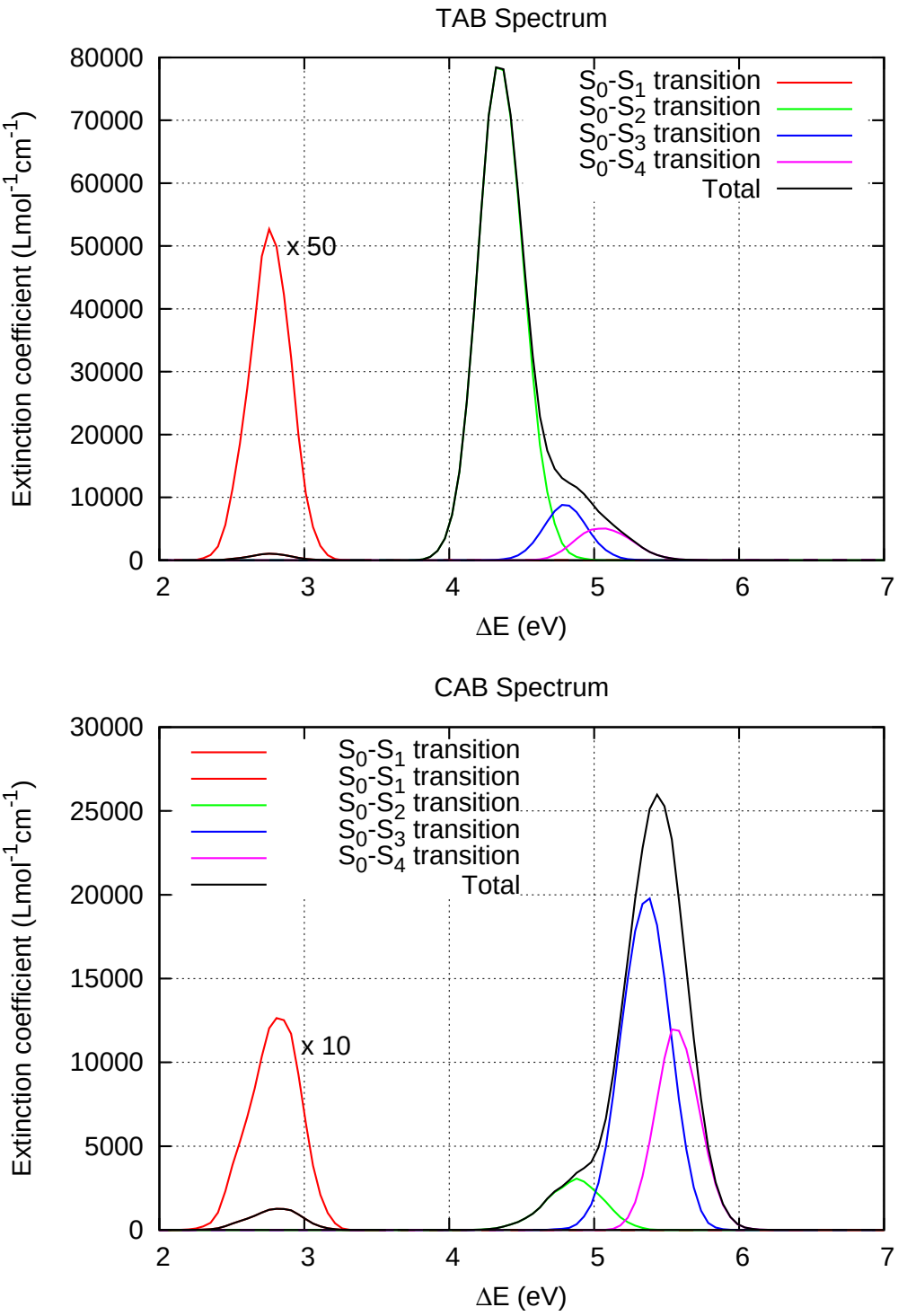

Figure 3.4: Absorption spectrum for the TAB (upper panel) and CAB (lower panel).

Table 3.9: Total oscillator strength and the corresponding values for each component for the $n \rightarrow \pi^*$ and $\pi \rightarrow \pi^*$ transitions of the CAB.

Transition	f_{tot}	f_x	f_y	f_z
$S_0 - S_1$	0.0194954631	0.0067440838	0.0123964214	0.0003549578
$S_0 - S_2$	0.0506645082	0.0321772985	0.0013647818	0.0171224279
$S_0 - S_3$	0.2884246416	0.2597786993	0.0145097154	0.0141362269
$S_0 - S_4$	0.1573833946	0.1306822630	0.0157568507	0.0109442809

x and y contributions to the oscillator strength are almost equal at all frequencies. Thus, the transition dipole moment forms an angle of about 45° with respect to the N=N axis, in sufficiently good agreement with the ab initio results. Moreover, the z component is very small and practically does not contribute to the total oscillator strength. The same holds for the strong $S_0 - S_2$ $\pi - \pi^*$ transition, while the less important $S_0 - S_3$ and $S_0 - S_4$ ones have dipoles approximately directed along the N-N axis (see Table 3.8). The $S_0 - S_1$ and $S_0 - S_2$ transition dipoles are perfectly parallel, and are overestimated by the same factor. This fact is consistent with the admixing of the $n - \pi^*$ and $\pi - \pi^*$ states at distorted geometries, already discussed in chapter 2. This borrowing mechanism seems to be well reproduced by the semiempirical calculations.

In Figure 3.6 we show the contributions of the three cartesian components of the transition dipole for the CAB. In this case the contributions of the x and y contributions are different, for both $n - \pi^*$ and $\pi - \pi^*$ bands. Again, the z component is very small in this case and its contribution to the total oscillator strength is very small. For the $\pi - \pi^*$ band the most important contribution comes from the S_0-S_3.

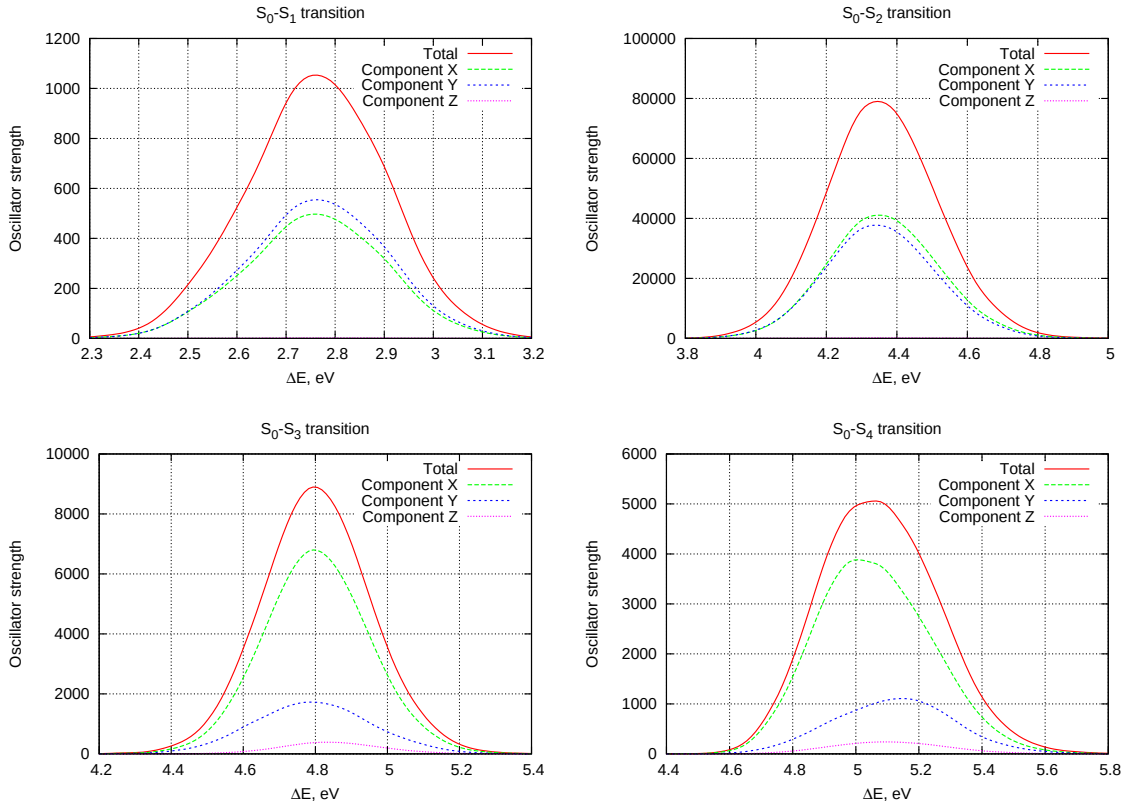

Figure 3.5: Oscillator strength of TAB for the $n - \pi^*$ and $\pi - \pi^*$ transition (namely, $S_0 \rightarrow S_1, S_0 \rightarrow S_2$, $S_0 \rightarrow S_3$ and $S_0 \rightarrow S_4$, respectively).

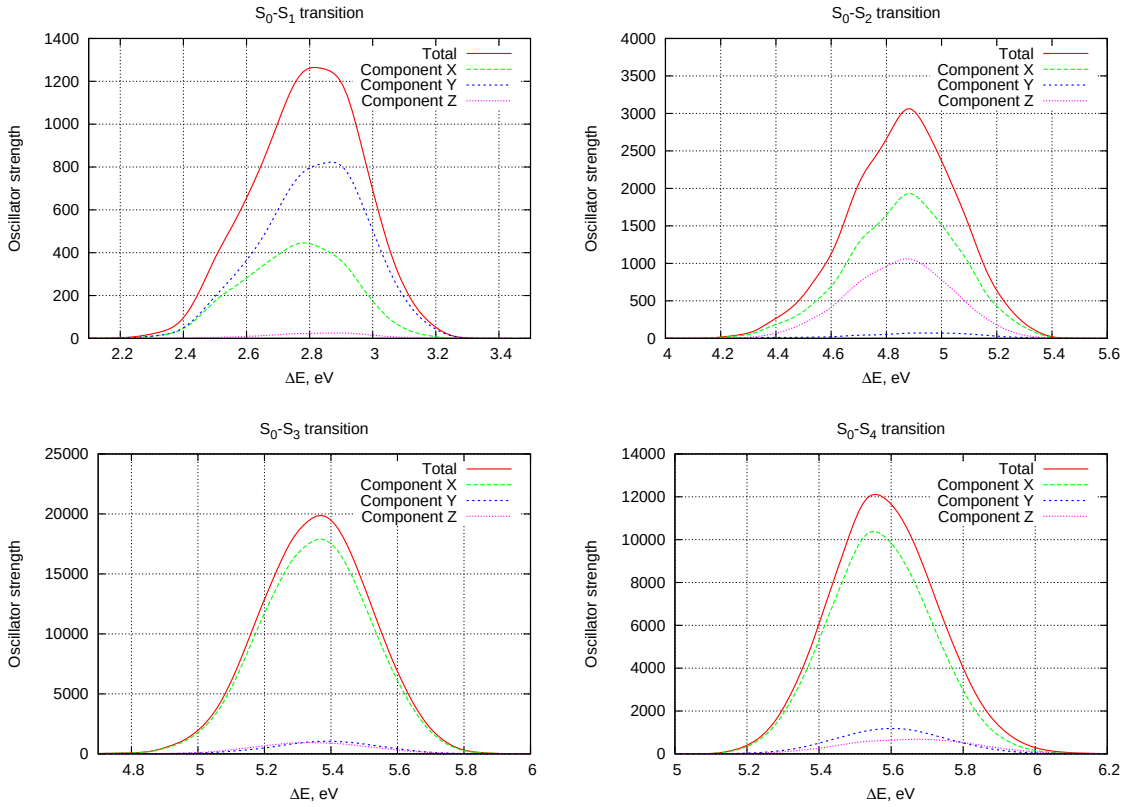

Figure 3.6: Oscillator strength of CAB for the $n - \pi^*$ and $\pi - \pi^*$ transition (namely, $S_0 \rightarrow S_1, S_0 \rightarrow S_2$, $S_0 \rightarrow S_3$ and $S_0 \rightarrow S_4$, respectively).

Chapter 4

Semiclassical dynamics of azobenzene

The simulation of photochemical reactions is an important tool to associate the theory to the experiments. They permit us to interpret reaction mechanisms and to individuate aspects that could not be observed in the experiments. In this way, it can be used to predict some behaviors in order to stimulate new research work in the laboratory. Most of the studies based on time dependent wavefunction calculations concern fast processes, where the electronic and nuclear dynamics are strongly coupled. In such physical situations, the Born-Oppenheimer approximation is not valid, especially when two potential energy surfaces are nearly degenerate or intersect each other. Therefore, in addition to the potential energy surfaces (PES), one needs to compute the nonadiabatic couplings that cause the radiationless transitions between different electronic states. PES and couplings can be computed and expressed as analytic functions of the internal coordinates, before performing the calculation of the dynamics. However, this preliminary step is particularly difficult when the PES depend in non-trivial ways on several coordinates, and when PES crossings must be represented. This time-consuming task can be avoided by using a direct strategy, i.e. by computing PES and couplings only when they are needed, namely at each time step during the integration of the dynamical equations. The direct option is especially convenient for fast dynamical processes, because the computational effort is directly proportional to the number of time steps, and, in trajectory methods, to the number of trajectories. This is the reason why we resort to semiempirical calculations of the electronic energies and wavefunctions. In fact, the computational cost of ab initio calculations of comparable accuracy for the excited states would be extremely high.

The simulation method we have applied is a semiclassical one, where the nuclear motion is treated classically and the electronic one is described by a time-dependent wavefunction. The surface hopping, in Tully's version [92, 93], represents the link between both physical descriptions. Many trajectories are usually run with the same or different initial conditions. Each trajectory, representing the time evolution of the classical degrees of freedom, evolves independently on a single electronic potential energy surfaces PES, with the possibility of occasional sudden hops to other surfaces. In the next section we will describe in detail the DTSH procedure (direct trajectories with surface hopping), by which we can study the time evolution of a physical system with a large number of nuclear degrees of freedom at a reasonably low computational cost.

4.1 Semiclassical dynamics

Molecular dynamics is considered as a set of simulation techniques used to study the dynamics of a physical system at molecular level. The motions of fast and slow degrees of freedom are partially separable (Born-Oppenheimer approximation), although the nonadiabatic couplings can be taken into account. In particular, the mixed quantum-classical or semiclassical dynamics is a class of methods where the slow (nuclear) motion is approximated with Newton's equations, while the fast one (electrons) is treated quantum mechanically. We shall indicate with Q the set of nuclear coordinates and with q the electronic ones. Once defined a newtonian trajectory $Q(t)$ in the nuclear configuration space, the electronic Hamiltonian $\hat{\mathcal{H}}_{el}(Q)$ is implicitly time dependent. We shall call its eigenstates $\psi_k(q;Q)$ and its eigenvalues $U_k(Q)$:

$$\hat{\mathcal{H}}_{el}(Q(t)) \ |\psi_k(Q(t))\rangle = U_k(Q(t)) \ |\psi_k(Q(t))\rangle \tag{4.1}$$

The time dependent Schrödinger equation (TDSE) can be written in the form:

$$i\frac{d}{dt}|\psi_{el}(t)\rangle = \hat{\mathcal{H}}_{el} \ |\psi_{el}(t)\rangle \tag{4.2}$$

We can expand the electronic wavefunction $\psi_{el}(t)$, in the basis of N_S adiabatic states $|\psi_l\rangle$:

$$|\psi_{el}(t)\rangle = \sum_l A_l(t) \ e^{-i\gamma_l(t)} \ |\psi_l(Q(t))\rangle \tag{4.3}$$

with

$$\gamma_l(t) = \int_0^t U_l(Q(t'))dt' \tag{4.4}$$

The probability to be in the state l at the time t is: $P_l(t) = |A_l(t)|^2$. The first derivative of $|\psi_{el}(t)\rangle$ with respect to time is

$$\frac{d}{dt}|\psi_{el}(t)\rangle = \sum_l \left[(\dot{A}_l - iU_lA_l)\,|\psi_l\rangle + A_l\left|\frac{d\psi_l}{dt}\right\rangle\right] e^{-i\gamma_l(t)} =$$
$$\sum_l \left[(\dot{A}_l - iU_lA_l)\,|\psi_l\rangle + A_l\sum_r \left|\frac{\partial\psi_l}{\partial Q_r}\right\rangle \dot{Q}_r\right] e^{-i\gamma_l(t)} \tag{4.5}$$

Substituting in the Eq. (4.2) and multiplying by $\langle\psi_K|$, we obtain:

$$\dot{A}_k = -\sum_{l(\neq k)} A_l(t)e^{i(\gamma_k-\gamma_l)}\sum_r \dot{Q}_r g_{kl}^{(r)} \tag{4.6}$$

where the $g_{kl}^{(r)}$ are the matrix elements of the dynamic coupling:

$$g_{kl}^{(r)} = \left\langle \psi_k \left| \frac{\partial}{\partial Q_r} \right| \psi_l \right\rangle \tag{4.7}$$

Then, the transition probability depends on the scalar product of the nuclear velocity vector, $\dot{Q}$, with the dynamic coupling vector, $\mathbf{g}_{kl}$. The couplings and the transition probabilities become large around the surface crossings (real or avoided). When the

surfaces are well separated (large $U_k - U_l$) the phase factors $exp[i(\gamma_k - \gamma_l)]$ are functions that oscillate very fast in the time, reducing in this way the transition probability.

The analytic solution of the set of coupled equations (4.6) is possible only in very simple cases. Generally, the coupled equations are solved numerically, by propagating the solution across small time steps. With the direct strategy, the electronic quantities U_k and $g_{kl}^{(r)}$ are obtained at each time step for the coordinates $Q(t)$.

The methods based on classical trajectories are appealing first of all because of their computational feasibility even for large molecular systems and because the results of such simulations are easily analyzed to yield information about the reaction mechanism and the nonadiabatic dynamics [94–96]. The mixing of classical mechanics for the nuclei and quantum mechanics for the electrons can be done in many different ways, due to the intrinsic arbitrariness of the semiclassical ansatz. In order to take into account both the QM uncertainty principle and the thermal distributions, one has to run many trajectories for each simulated experiment, with a suitable sampling of initial conditions (as we shall describe in the next sections).

4.2 Nuclear trajectories

The integration of classical trajectories is one of the oldest problems of numerical calculation applied to physics. As before, consider a system with the nuclear degrees of freedom Q. The potential energy surfaces $U_K(Q)$ and their gradients are obtained directly at each integration step of the nuclear trajectory by solving the time independent Schrödinger equation for the electrons with fixed nuclei, at a given level of approximation.

One of the simplest and most used methods to integrate the trajectories is the Verlet one. This algorithm updates the positions Q and the velocities $\dot{Q}$, from t to $t + \Delta t$, by finite difference formulas. Given the potential energy function $V(Q)$, it is possible to define the force $F_r = -\partial V/\partial Q_r$, and the acceleration $\ddot{Q}_r = F_r/m_r$, where m_r is the atomic mass associated to the coordinate Q_r. Employing the Newton equations, we can write the Taylor expansions:

$$Q(t + \Delta t) = Q(t) + \dot{Q}(t)\Delta t + \frac{\Delta t^2}{2}\ddot{Q}(t) + \frac{\Delta t^3}{6}\dddot{Q}(t) + O(\Delta t^4) \tag{4.8}$$

$$Q(t) = Q(t + \Delta t) - \dot{Q}(t + \Delta t)\Delta t + \frac{\Delta t^2}{2}\ddot{Q}(t + \Delta t) - \frac{\Delta t^3}{6}\dddot{Q}(t + \Delta t) + O(\Delta t^4) \tag{4.9}$$

Summing both equations:

$$\dot{Q}(t + \Delta t) = \dot{Q}(t) + \frac{\Delta t}{2}[\ddot{Q}(t) + \ddot{Q}(t + \Delta t)] + \frac{\Delta t^2}{6}[\dddot{Q}(t) - \dddot{Q}(t + \Delta t)] + O(\Delta t^3) \tag{4.10}$$

Introducing the first order approximation for the third derivatives:

$$\dddot{Q}(t) = \frac{\ddot{Q}(t) - \ddot{Q}(t - \Delta t)}{\Delta t} + O(\Delta t^2) \tag{4.11}$$

and similarly for $\dddot{Q}(t + \Delta t)$, the equations 4.8 and 4.10 become:

$$Q(t+\Delta t) = Q(t) + \dot{Q}(t)\Delta t + \Delta t^2 \left[\frac{2}{3}\ddot{Q}(t) - \frac{1}{6}\ddot{Q}(t-\Delta t)\right] + O(\Delta t^4) \tag{4.12}$$

$$\dot{Q}(t+\Delta t) = \dot{Q}(t) + \Delta t \left[\frac{5}{6}\ddot{Q}(t) + \frac{1}{3}\ddot{Q}(t+\Delta t) - \frac{1}{6}\ddot{Q}(t-\Delta t)\right] + O(\Delta t^3) \tag{4.13}$$

These equations define a version of Verlet's algorithm with an order of accuracy on $Q(t)$ of Δt^4 for each step, that is Δt^3 for a given time interval t, divided into $N = t/\Delta t$ time steps. The accuracy on the velocities $\dot{Q}(t)$ is of the order of Δt^2, for the same time interval.

4.3 Surface Hopping

Surface Hopping [66, 92–94, 96–102] is one of the basic approaches to the problem of combining classical and quantum mechanics for the study of nuclei and electrons. In this approach the molecule is considered in a given electronic state k at each time t. While we are in the adiabatic state $|\psi_k\rangle$ (the "current state"), the nuclear trajectory is governed by the associated potential energy surface (PES), $U_k(Q)$. In the other hand, each state l has a probability $P_l(t)$ to be occupied, generally different from zero. An increment in the probability $P_l(t)$ of any state different from the current one, can produce a transition ("Surface Hop") from $|\psi_k\rangle$ to $|\psi_l\rangle$. At a given time the system can be in any state, possibly different from the one with the highest probability P_l. The occurrence of surface hops is regulated by a stochastic algorithm proposed by Tully [92], with modifications that take into account the decoherence effects, put forward by our group [66]. Given the stochastic nature of the surface hopping method, in principle converged results can be obtained only if many trajectories are launched from a given starting point in the phase space.

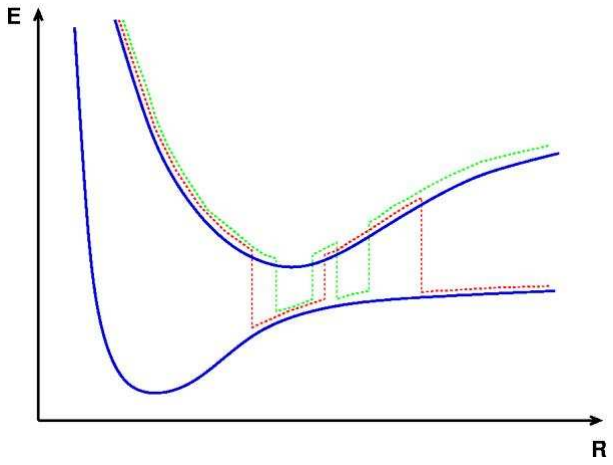

Figure 4.1: General surface hopping scheme.

We indicate with $\Pi_k(t) = N_k(t)/N_T$ the fraction of the total number of trajectories N_T that are on the surface U_k at time t. The probability function $P_k^{(j)}(t)$ is specific of the j-th trajectory, as any other dynamic quantity. The average over all the trajectories is indicated as $\overline{P}_k$:

$$\overline{P}_k(t) = \frac{1}{N_T} \sum_{j=1}^{N_T} P_k^{(j)}(t) \tag{4.14}$$

(for a sake of simplicity, in the following we shall drop the suffix (j) for trajectory-specific quantities).

Surface hopping is internally consistent if $\Pi_k(t)$ coincides with $\overline{P}_k(t)$ at each time t. This requirement can be easily satisfied, hopping at regular time intervals to a randomly chosen state, according to the probabilities $P_k(t)$. However, this procedure can be contradictory with the physics of the problem, because the hops could occur in regions of the phase space where the transition probability is almost vanishing.

The most popular method for mixed quantum-classical dynamics is Tully's "fewest switches" approach [92, 93], characterized by a good compromise between computational efficiency, conceptual simplicity and accuracy of results for medium or large sized molecular systems. In this algorithm the electronic density matrix is propagated coherently along the trajectory and the transition probability is evaluated taking into account the variation in time of the state probabilities $P_k(t)$. In this way the transitions only occur when they are needed, i.e., when the coupling among the electronic states is not negligible. Moreover, the number of state switches is minimized by imposing that, at each integration time step, the total flux of probability between any two states is obtained by one-way transitions [66].

From Eq. 4.7 it is possible to obtain an expression of the first derivative of $P_k(t)$ with respect to the time:

$$\dot{P}_k = \dot{A}_k A_k^* + A_k \dot{A}_k^* = -\sum_{l(\neq k)} B_{kl} \tag{4.15}$$

where

$$B_{kl} = 2\Re\left[A_l A_k^* e^{i(\gamma_k - \gamma_l)}\right] \sum_r \dot{Q}_r g_{kl}^{(r)} \tag{4.16}$$

(note that $B_{lk} = -B_{kl}$). If $|\psi_k\rangle$ is the current electronic state, its probability in a given time step will change as the sum of positive and negative contributions $B_{kl}\Delta t$. It is possible to ignore the negative contributions, and hop to other states with the hopping probability:

$$T(k \to l) = max\left\{0, \frac{B_{kl}\Delta t}{P_k}\right\} \tag{4.17}$$

To do this, a random number x is generated, with $0 \leq x \leq 1$: if

$$\sum_{l'(\neq k)}^{l-1} T(k \to l') < x \leq \sum_{l'(\neq k)}^{l} T(k \to l') \tag{4.18}$$

a hop to state $|\psi_l\rangle$ will occur. If $x > \sum_{l(\neq k)}^{N_S} T(k \to l)$, no hop occurs: for small Δt, this will be the most frequent case. If it is assumed that the functions $P_k(t)$ be the same for all the trajectories, this algorithm ensures that the equality $\Pi_k(t) = P_k(t)$ is conserved across a time step, as long as it be applied to a large number of trajectories. In fact, the variation of Π_k in the time Δt will be:

$$\Delta\Pi_k = \sum_{l(\neq k)} \Pi_k[T(l \to k) - T(k \to l)] = -\sum_{l(\neq k)} B_{kl}\Delta t = \Delta P_k \tag{4.19}$$

Unfortunately, even with the same initial conditions, two trajectories will not coincide, because they can hop at different times and therefore they travel, at least for a while, on different PES. Consequently, also their functions $P_k(t)$ will differ from each other, starting from the time of the first hop. The equality 4.19 is therefore not guaranteed. An important difference between the values Π_k and $\overline{P}_k$ can be considered as an indication of bad operation of the surface hopping algorithm.

After a jump from surface U_k to U_l the nuclear kinetic energy has to be changed from T to $T' = T + U_k - U_l$. This is usually accomplished by adjusting the nuclear momenta along the nonadiabatic coupling vector $\mathbf{g}_{kl}$. If $U_l - U_k > 0$ it may happen that there is not enough nuclear kinetic energy to compensate for the sudden variation of the potential electronic energy. In this case, the usual option is to give up the hop ("frustrated hops"), and this another reason why Π_k may differ from $\overline{P}_k$.

The internal incongruity of the surface hopping method, related to the inequality $\Pi_k \neq \overline{P}_k$, cannot be eliminated as long as it is assumed that the probabilities $P_k(t)$ are only determined by the TDSE. In formulating the TDSE, the molecule is represented by one point in the phase space, i.e. the same perfectly localized wavepacket on all states, only with different probability amplitudes. With non vanishing couplings and amplitudes, interference effects will be present for all the duration of the trajectory. This fact is at variance with the real behavior of the quantum wavepackets, that follow different trajectories according to the PES where they are. The interference is obtained only when the position of two packets in the phase space coincides, at least in an approximate way. Typically, this happens just after a nonadiabatic event has transferred part of the population from an electronic state to another one. After a short time (depending on the PES shape and the available kinetic energy), the wavepackets move far apart and do not interfere any more ("quantum decoherence"). In Appendix C we show an example.

The surface hopping method describes very well the fast transitions that occur when two PES are very near or crossing. The problems ("coherence" effect, difference between Π_k and $\overline{P}_k$, frustrated hops) usually occur when the energy difference between the PES is rather large. In order to deal with these problems, several corrections are proposed. Our group has adapted and tested a procedure, originally proposed by Truhlar et al [101,102] in a different context. The gist of this correction is to modify the coefficients A_k, calculated by the TDSE, and therefore the probabilities P_k, at each time step Δt. The probability of the current state k is incremented on the PES where the trajectory is evolving, at the expenses of the other ones:

$$\begin{aligned} A'_l &= A_l e^{-\frac{\Delta t}{\tau_{kl}}} \qquad \forall l \neq k \\ A'_k &= A_k \left[\frac{1 - \sum_{l \neq k} |A'_l|^2}{|A_k|^2} \right]^{1/2} \\ \tau_{kl} &= \frac{\hbar}{|E_k - E_l|} \left(1 + \frac{C}{E_{kin}} \right) \end{aligned} \tag{4.20}$$

where E_{kin} is the nuclear kinetic energy and C is an energetic constant with a reasonable value of 0.1 hartree [101]. This correction tends to equalize the average probabilities $\overline{P}_k$ and the distributions Π_k, and removes the interference effects for times larger than τ_{km} (few fs when the PESs are well separated in energy). When the PESs tend to cross, i.e. when the surface hopping works correctly, τ_{km} is very large and the corrections are negligible.

4.4 Initial conditions sampling

The surface hopping method, being based on a stochastic algorithm, can only work if a large number of trajectories is launched. The observables under study in photochemistry, for instance the population of the electronic states, will be calculated as averages over all the trajectories. In order to obtain a statistically reliable evaluation of a given quantity, one needs a number of trajectories that depends on the particular process under study. If N_T is the total number of trajectories and P is the probability of the event under study, the average number of "interesting" events will be $x = N_T P$ and the standard deviation is $\sigma = \sqrt{N_T P(1-P)}$. For a "reactive" event, $P = x/N_T$ is the quantum yield (Φ). In this case, the error on Φ is $\sqrt{P(1-P)/N_T}$. With a quantum yield of about 50%, one needs about 600 trajectories to have an error of 2%.

By running many trajectories, we also want to take into account the real distribution of initial conditions. In order to reproduce the thermal distribution of nuclear coordinates and momenta in the ground state PES, computed by the MOPAC program [91], we have applied the Montecarlo method. We have modified the code, in order to run the Montecarlo calculation using as variables the internal coordinates, rather than the cartesian ones. This choice turned out to be important for an effective sampling of the low frequency, large amplitude, motions, such as the torsion of the phenyl rings around the C-N bonds. The sampling of the initial conditions goes through the following steps:

- For each starting isomer, TAB and CAB, we have run 10^6 Montecarlo steps, considering a temperature of 300 K.
- From the accepted Montecarlo points, we select the initial geometries Q_i by a random algorithm based on successive bisections of the Montecarlo trajectory, in order to sample it in the most uniform way.
- To each of the selected geometries we associate a set of nuclear momenta P_i, randomly chosen according to the Boltzmann distribution of kinetic energies.
- Each phase space point (Q_i, P_i), defined in the last two steps, can give place to a number of trajectories (zero, one or more). A trajectory starts with a vertical transition (no change in Q_i and P_i) from the ground to an excited state k. The number of trajectories to be launched from the (Q_i, P_i) starting point depends on the computed transition probabilities, for the excited states that fall within a pre-defined transition energy window $\Delta E \pm \Delta\Delta E$. The choice of the starting excited state is again based on a stochastic algorithm, as described in the next three points.
- Transition energies ΔE_{0k} and dipoles μ_{0k} are computed at the geometry Q_i, and only the states with $\Delta E - \Delta\Delta E \leq \Delta E_{0k} \leq \Delta E + \Delta\Delta E$ are considered to be eligible, in order to simulate excitation with an approximately monochromatic light.
- We compute the quantity μ^2_{tot}, proportional to the total transition probability, as $\mu^2_{tot} = \sum_k \mu^2_{0k}$, where the sum runs only on the eligible states. Using a predefined reference parameter μ^2_{ref} we compute the maximum number of trajectories to be launched from the point (Q_i, P_i), by rounding μ^2_{tot}/μ^2_{ref} to the next integer N_{max}.
- We extract N_{max} random numbers x_j in the $[0, 1]$ interval, and for each x_j we start a trajectory on state k if $\sum_l^{k-1} \mu^2_{0l} < x_j N_{max} \mu^2_{ref} \leq \sum_l^k \mu^2_{0l}$. If $x_j N_{max} \mu^2_{ref} > \mu^2_{tot}$ the trajectory is not launched.

We have run separate simulations of the photodynamics that follows the excitation to S_1 ($n \rightarrow \pi^*$ transition) or to the higher excited states S_2, S_3 and S_4 ($\pi \rightarrow \pi^*$ transition). In the former case, the transition energy interval was chosen to be 2.5-3.1 eV for TAB and 2.6-3.2 eV for CAB. In fact, the average excitation energies were 2.8 eV for TAB and

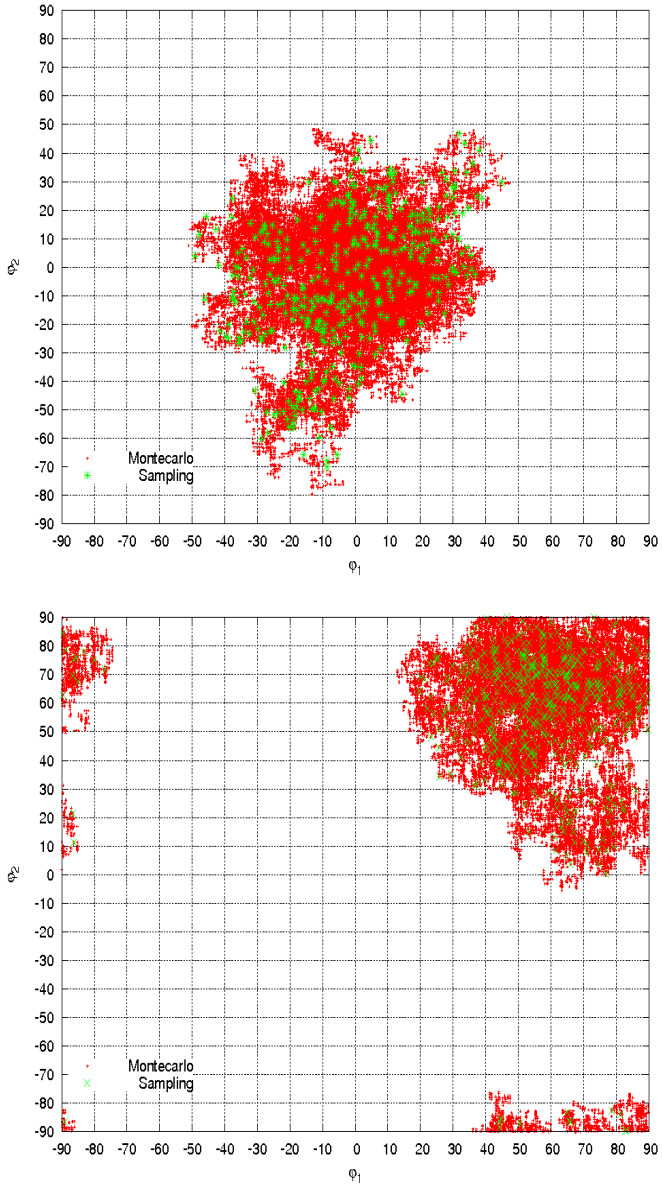

Figure 4.2: Red dots: Boltzmann distribution (Montecarlo) of the phenyl torsion angles of TAB (upper panel) and CAB (lower panel). Green dots: selected initial geometries for starting the trajectories in the S_1 state.

CAB. For the $\pi \rightarrow \pi^*$ band we imposed the ranges 4.0-5.0 eV for TAB and 4.7-5.7 eV for CAB, and we obtained the averages 4.4 eV and 5.4 eV, respectively. When exciting to the $\pi \rightarrow \pi^*$ band, the starting state can be S_2, S_3 or S_4: for TAB, S_2 has by far the largest fraction of trajectories, because it contributes most to the oscillator strength. For CAB, the most important contribution comes from the S_3 state, having the largest fraction of trajectories in this case.

Table 4.1: Sampling of the initial conditions for the simulations of the photodynamics in vacuo or with a Brownian representation of the solvent. The sampling is based on a Montecarlo run (CI space of 82 determinants). $N_{geo}(n)$ is the number of Montecarlo geometries from which n trajectories were launched (n=0,1,2 or more).

Excitation band	$n \to \pi^*$	$n \to \pi^*$	$\pi \to \pi^*$	$\pi \to \pi^*$
Starting isomer	TAB	CAB	TAB	CAB
ΔE, eV	2.8	2.9	4.5	5.2
$\Delta\Delta E$, eV	0.6	0.6	1.0	1.0
μ^2_{ref}, a.u.	0.30	0.45	16	5
Number of sampled geometries $= \sum_n N_{geo}(n)$	954	986	980	999
Number of trajectories, $N_T = \sum_n nN_{geo}(n)$	600	560	670	688
$N_{geo}(0)$	553	455	310	407
$N_{geo}(1)$	270	502	670	496
$N_{geo}(2)$	86	29	0	96
$N_{geo}(3) + N_{geo}(4) + N_{geo}(5) + \ldots$	46	0	0	0
Fraction of trajectories starting in S_1	1.00	1.00	0.00	0.00
Fraction of trajectories starting in S_2	0.00	0.00	0.90	0.09
Fraction of trajectories starting in S_3	0.00	0.00	0.07	0.65
Fraction of trajectories starting in S_4	0.00	0.00	0.03	0.26

As we show in Table 4.1, the reference squared transition dipole μ^2_{ref} has been chosen so that most of the phase space points that have been sampled are altogether discarded, or do originate one trajectory: only a minority of them originates two or more trajectories. In this way, we ensure a good spread of the initial geometries over the whole of the Montecarlo sample.

In Figure 4.2 we show the distribution of the phenyl torsion angles for the TAB and CAB isomers, obtained by the Montecarlo simulation (red dots) and the points selected to start a trajectory in the S_1 state (green dots). For TAB, since the $n \to \pi^*$ transition is forbidden at the equilibrium geometry ($\phi_1 = \phi_2 = 0$), the distribution of green points is distinctly less dense around the center of the plot.

4.5 Brownian dynamics simulations

4.5.1 Method and computational details

We have run a set of simulations with a simple representation of the frictional effect of the solvent, based on Brownian dynamics. While our ultimate goal is to introduce an explicit representation of the solvent molecules by the QM/MM strategy, we have deemed useful to evaluate how the solvent affects the photodynamics in this preliminary way. The simulations based on the Brownian dynamics also allow us to bring out the effects due to the transfer of energy from the solute (chromophore) to the solvent. Such "dynamic" effects in real systems are always mixed with the "static" ones, i.e. the state-specific

alterations of the PESs due to solute-solvent interactions.

The Brownian dynamics is realized by integrating the Langevin equation [103]:

$$\dot{P}_\alpha = -\gamma_\alpha P_\alpha - \frac{\partial E_K(\vec{R})}{\partial R_\alpha} + X_\alpha(t) \tag{4.21}$$

where $P_\alpha = m_\alpha \dot{R}_\alpha$ is the conjugated momentum of the R_α nuclear coordinate, m_α the associated mass and γ_α the friction coefficient. $X_\alpha(t)$ is a gaussian random white noise, with the properties: $\langle X_\alpha \rangle = 0$, $\langle X_\alpha(0) X_\beta(t) \rangle = 2 m_\alpha \gamma_\alpha k T \delta_{\alpha\beta} \delta(t)$.

The friction coefficients γ_α can be related to the molecular diffusion coefficients and therefore to the viscosity of the solvent. In fact, if the γ_α are chosen to match the diffusion coefficients, one obtains approximately the right effect on the slow modes, but overall the transfer of vibrational energy from solute to solvent is too fast. The high frequency modes are damped much more rapidly than found experimentally: while the vibrational relaxation times are of the order of some ps, the frictional times γ_α^{-1} are less than 1 ps even for solvents with low viscosity. In view of these considerations, in our simulations we have applied the friction and the white noise only to the carbon atoms of azobenzene. In this way, all fast modes involving the H and N atoms are not affected, while the motion of the phenyl rings is hampered by the viscosity. In order to choose the γ_C values for the carbon atoms, we have considered the diffusion coefficient of benzene in solvents with viscosity of about 1 mPa·s, such as ethanol or cyclehexane. With a diffusion coefficient $D = 2.0 \cdot 10^{-5}\ cm^2/s$ we get $\gamma_C = 8.7 \cdot 10^{12}\ s^{-1}$. Friction coefficients 10 times larger have been used to simulate a solvent of medium viscosity ($\eta \approx 10$).

In addition to the Brownian simulations, with two different values for the solvent viscosity, we have run simulations for the isolated azobenzene molecule (no solvent, regular Newtonian trajectories). The aim is to compare the results obtained in vacuo with those of our previous simulations using different semiempirical parameters, and with the results of the Brownian trajectories.

i We have executed four simulations, for the *trans* $\rightarrow$ *cis* and *cis* $\rightarrow$ *trans* photoisomerizations, with excitation energies in the $n \rightarrow \pi^*$ or in the $\pi \rightarrow \pi^*$ band. Each simulation involves about 600 trajectories, with the initial conditions sampled as described in the previous section. Five states have been taken into account, from S_0 to S_4. The maximum duration time of a trajectory is 5 ps, with Δt=0.1 fs. A trajectory is stopped when it has reverted to the ground state and it is near to the geometry of one of the two isomers. The criterium we adopted is the CNNC angle to be within $\pm 2^\circ$ of the values 0° for CAB and 180° for TAB. These specifications define a conventional "reaction time", t_R, that goes from the vertical excitation to the end of the trajectory. Moreover, we shall define the "reactive trajectories" as those that start near to the equilibrium geometry of one isomer and stop to the other one, and the "unreactive trajectories" as those that go back to the initial isomer. The fraction of the reactive trajectories is the calculated quantum yield Φ.

4.5.2 Quantum yields and mechanism

The results of the simulations for the three cases (in vacuo, with the low viscosity and with the medium one) are presented in Table 4.2 and in Figures from 4.3 to 4.8. In Table 4.2 we present the quantum yields for the *trans* $\rightarrow$ *cis* and *cis* $\rightarrow$ *trans* isomerizations. In Figures 4.3 and 4.4, we show the time evolution of the populations of the excited states (fraction of trajectories running on each PES). In Figures 4.5-4.8 we show the change

in time of the angles CNNC (dihedral angle), NNC_1 and NNC_2 for the different excited states, considering the "reactive trajectories" (when the isomerization occurs) and the "unreactive" ones (when the molecule returns to the initial isomer configuration).

Table 4.2: Quantum yields obtained in the simulations for the *trans* $\rightarrow$ *cis* and *cis* $\rightarrow$ *trans* processes, in vacuo and with solvent effects represented by the Brownian dynamics. Old results from ref. [21]. The experimental quantum yields only concern non polar solvents (see Table 1.1 and references therein)

.

	$n \rightarrow \pi^*$ transition	$\pi \rightarrow \pi^*$ transition
$\Phi_{trans \rightarrow cis}$ (old calculation - in vacuo)	0.33±0.03	0.15±0.02
$\Phi_{trans \rightarrow cis}$ (new calculation - in vacuo)	0.34±0.02	0.27±0.02
$\Phi_{trans \rightarrow cis}$ (new calculation - $\eta \approx 1$)	0.34±0.02	0.26±0.02
$\Phi_{trans \rightarrow cis}$ (new calculation - $\eta \approx 10$)	0.17±0.02	0.19±0.02
$\Phi_{trans \rightarrow cis}$ (experimental, $\eta < 3$)	0.21-0.28	0.09-0.13
$\Phi_{trans \rightarrow cis}$ (experimental, very high viscosity)	0.18	0.05
$\Phi_{cis \rightarrow trans}$ (old calculation - in vacuo)	0.61±0.03	0.48±0.03
$\Phi_{cis \rightarrow trans}$ (new calculation - in vacuo)	0.60±0.02	0.63±0.02
$\Phi_{cis \rightarrow trans}$ (new calculation - $\eta \approx 1$)	0.60±0.02	0.61±0.02
$\Phi_{cis \rightarrow trans}$ (new calculation - $\eta \approx 10$)	0.54±0.02	0.44±0.02
$\Phi_{cis \rightarrow trans}$ (experimental, $\eta < 3$)	0.40-0.56	0.40-0.44
$\Phi_{cis \rightarrow trans}$ (experimental, very high viscosity)	0.60	0.40

In the first place, the simulations show that the preferred reaction path is the torsion of the N=N double bond in all four cases (*cis* $\rightarrow$ *trans* or *trans* $\rightarrow$ *cis*, $n \rightarrow \pi^*$ or $\pi \rightarrow \pi^*$ excitation), in vacuo as in the two solvents (see figures 4.5-4.8). This is in agreement with our previous simulations [21]. Secondly, we note that the quantum yields here computed for the $n \rightarrow \pi^*$ excitation are in agreement with the experimental ones, and close to the results previously obtained for the isolated molecule [21]. However, for the $\pi \rightarrow \pi^*$ transition, the computed quantum yields are not substantially lower than the $n \rightarrow \pi^*$ ones, as one would expect. In the previous work, instead, the right ratio of $\pi \rightarrow \pi^*$ to $n \rightarrow \pi^*$ quantum yields had been obtained. The interpretation of this violation of Kasha's rule, offered in ref. [21], was based on the mechanism observed in the simulations. The first step is a fast $S_2 \rightarrow S_1$ conversion. The ensuing dynamics on the S_1 PES is characterized by a larger vibrational energy, and especially by a higher excitation of the NNC symmetric bending motion, with respect to the $n \rightarrow \pi^*$ case. As a result, the $S_1 - S_0$ conical intersection is reached more easily, and at CNNC angles closer to the starting point. Therefore, the radiationless decay of S_1 competes very effectively with the isomerization, resulting in lower quantum yields. The higher quantum yields obtained in the present simulations for the $\pi \rightarrow \pi^*$ excitation can be attributed to a poorer representation of the S_2 PES, obtained with the new parameterization. Although overall we have a better agreement with the target values, especially for the S_1 PES, the $S_1 - S_2$ energy gap is too large, at all geometries. As a consequence the decay of S_2 is too slow, and the CNNC twisting motion takes place in the S_2 PES, at least in part. This interpretation is confirmed by the comparison of the decay

times of $S_2 - S_4$ states, that are considered together because the interconversion among them is very fast (see Table 4.3). The lifetimes have been obtained by a fit of the curves shown in Figure 4.4, using the biexponential form: $w_1 exp(-t/\tau_1) + (1 - w_1) exp(-t/\tau_2)$. We have devised a way to correct the PESs in a state specific way, while preserving the consistence between PESs and wavefunctions. This correction will be applied to perform new simulations of the photodynamics following the $\pi \rightarrow \pi^*$ excitation. In this chapter, we shall focus on the $n \rightarrow \pi^*$ case.

Table 4.3: Decay times of the excited states, obtained by a fit of the populations $\Pi_k(t)$ with the biexponential form $w_1 exp(-t/\tau_1) + (1 - w_1) exp(-t/\tau_2)$. For the $\pi \rightarrow \pi^*$ excitation, we consider the sum of the populations of S_2, S_3 and S_4.

	$n \rightarrow \pi^*$ transition S_1 lifetimes			$\pi \rightarrow \pi^*$ transition $S_2 + S_3 + S_4$ lifetimes		
	w_1	τ_1 (fs)	τ_2 (fs)	w_1	τ_1 (fs)	τ_2 (fs)
TAB isomer (old calculation - in vacuo)	0.78	172.5	379.8	0.81	73.7	331.5
TAB isomer (new calculation - in vacuo)	1.00	196.9	-	0.47	82.0	455.0
TAB isomer (new calculation - $\eta \approx 1$)	1.00	488.1	-	0.29	60.8	364.2
TAB isomer (new calculation - $\eta \approx 10$)	1.00	2078.3	-	0.35	116.2	417.8
CAB isomer (old calculation - in vacuo)	0.96	34.5	264.1	0.25	21.7	107.1
CAB isomer (new calculation - in vacuo)	0.66	20.0	51.2	0.87	128.1	820.2
CAB isomer (new calculation - $\eta \approx 1$)	0.60	54.5	21.0	0.78	136.1	1021.3
CAB isomer (new calculation - $\eta \approx 10$)	0.35	29.8	99.2	0.77	391.8	1094.9

With the inclusion of the solvent effects, it is possible to observe the strong influence of the most viscous solvent on the population decay and on the quantum yield, shown in Tables 4.2 and 4.3 and in Figures 4.3 and 4.4. The decay of the excited states is slowed down in the presence of a solvent: the effect is moderate at low viscosity, and much larger at higher viscosity. To reach the $S_1 \rightarrow S_0$ crossing seam, the molecule must rotate around the N=N double bond (CNNC dihedral), or open symmetrically the NNC angles, or perform a combination of these two motions [21, 66]. Figures 4.5-4.8 show the CNNC and NNC angles, as functions of time, averaged over the reactive or the unreactive trajectories. In vacuo, the results are very similar to the previous ones [21], and the dominant reaction mechanism is the torsion of the N=N double bond. In solution, the torsional motion is slowed down by the solvent friction, and the NNC bending vibration is also damped, resulting in longer lifetimes. These effects are much more pronounced with the higher viscosity, and only in this case we also find significantly lower quantum yields. When exciting the TAB isomer, the dynamics is much more sensitive to the presence of a solvent and to its viscosity, then in the case of CAB: this is due to the shape of the excited state PESs, that are much steeper on the CAB than on the TAB side.

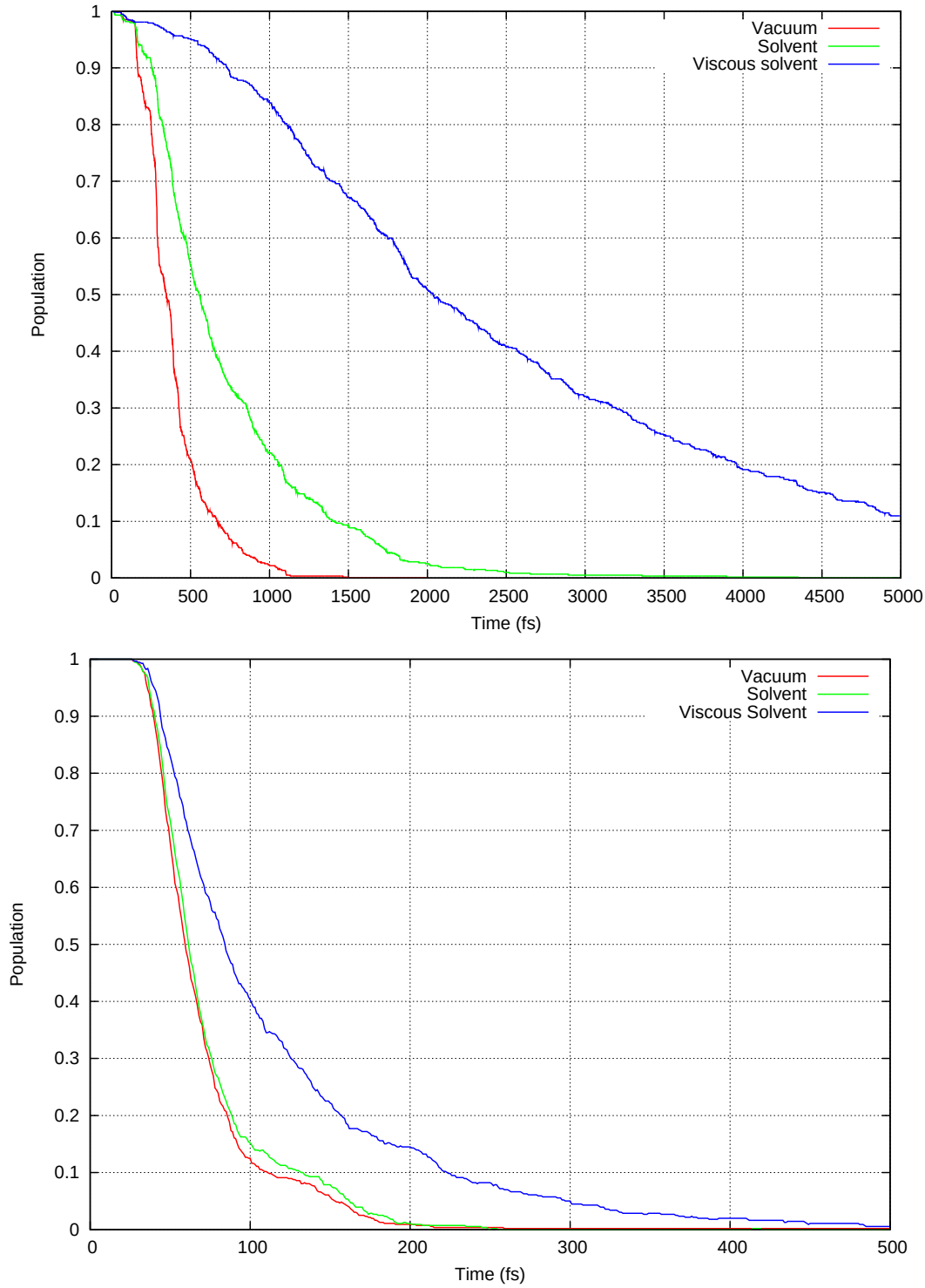

Figure 4.3: Time evolution of the population of the first excited state S_1, in the case of $n \rightarrow \pi^*$ excitation, starting from the TAB isomer (upper panel) and CAB isomer (lower panel), and considering three cases: in vacuo and in the two solvents, with low and medium viscosity.

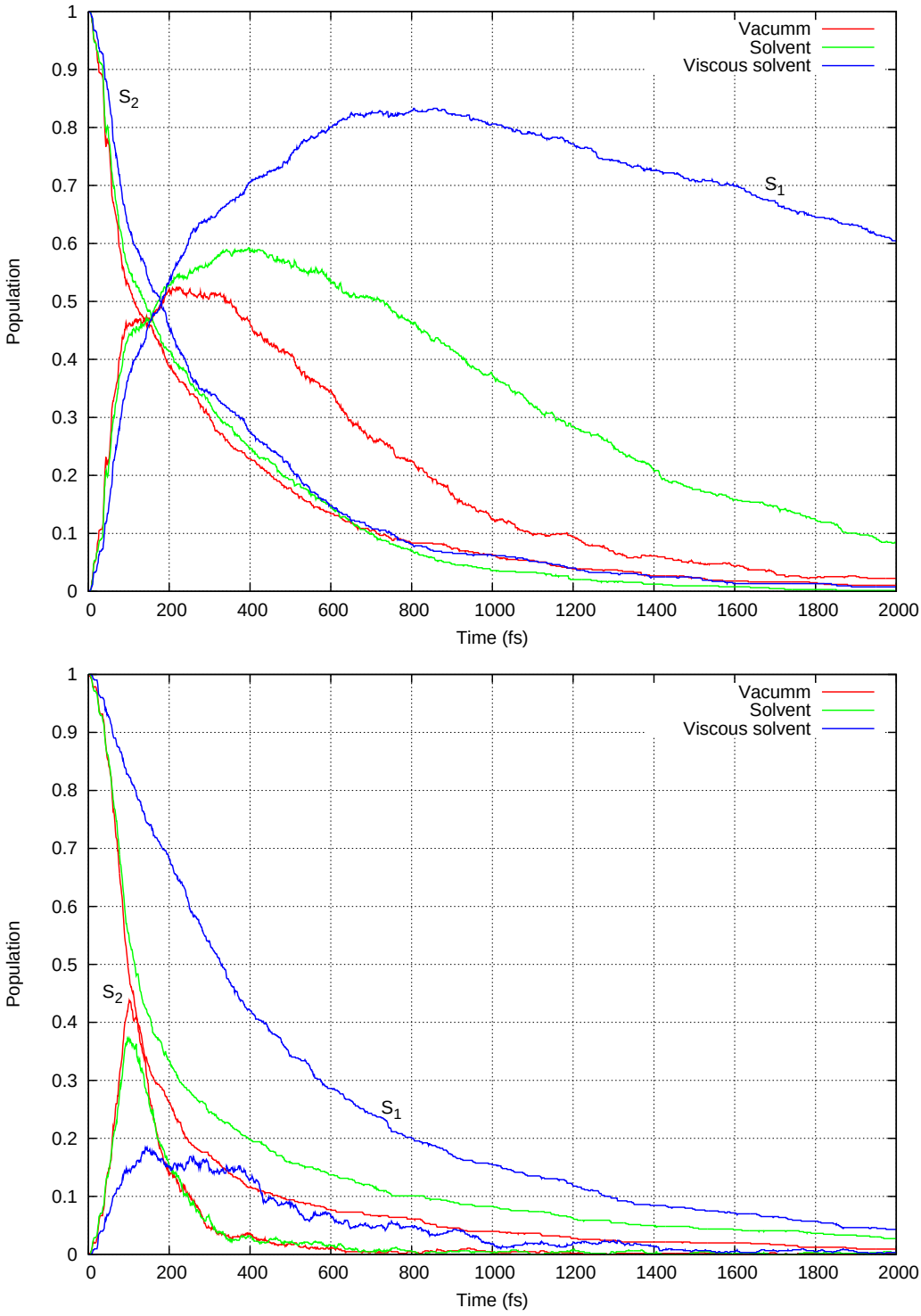

Figure 4.4: Time evolution of the excited state populations in the case of $\pi \rightarrow \pi^*$ excitation (sum of the populations of S_2, S_3 and S_4), starting from the TAB isomer (upper panel) and CAB isomer (lower panel), and considering three cases: in vacuo and in the two solvents, with low and medium viscosity.

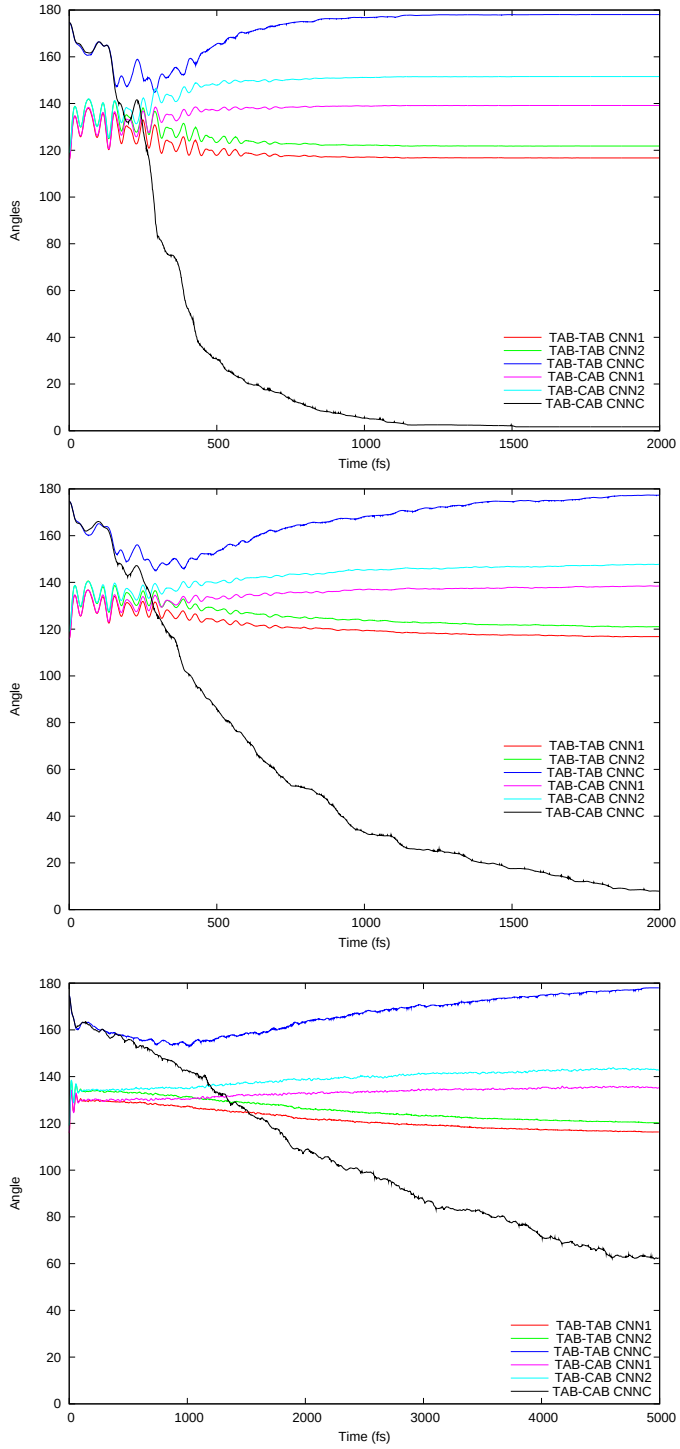

Figure 4.5: Time evolution of the angles CNNC, NNC_1 and NNC_2, averaged over the reactive and unreactive trajectories, in the case of $n \rightarrow \pi^*$ excitation of TAB and considering three cases: in vacuo and in the two solvents with low and medium viscosity (upper, medium and lower panel, respectively).

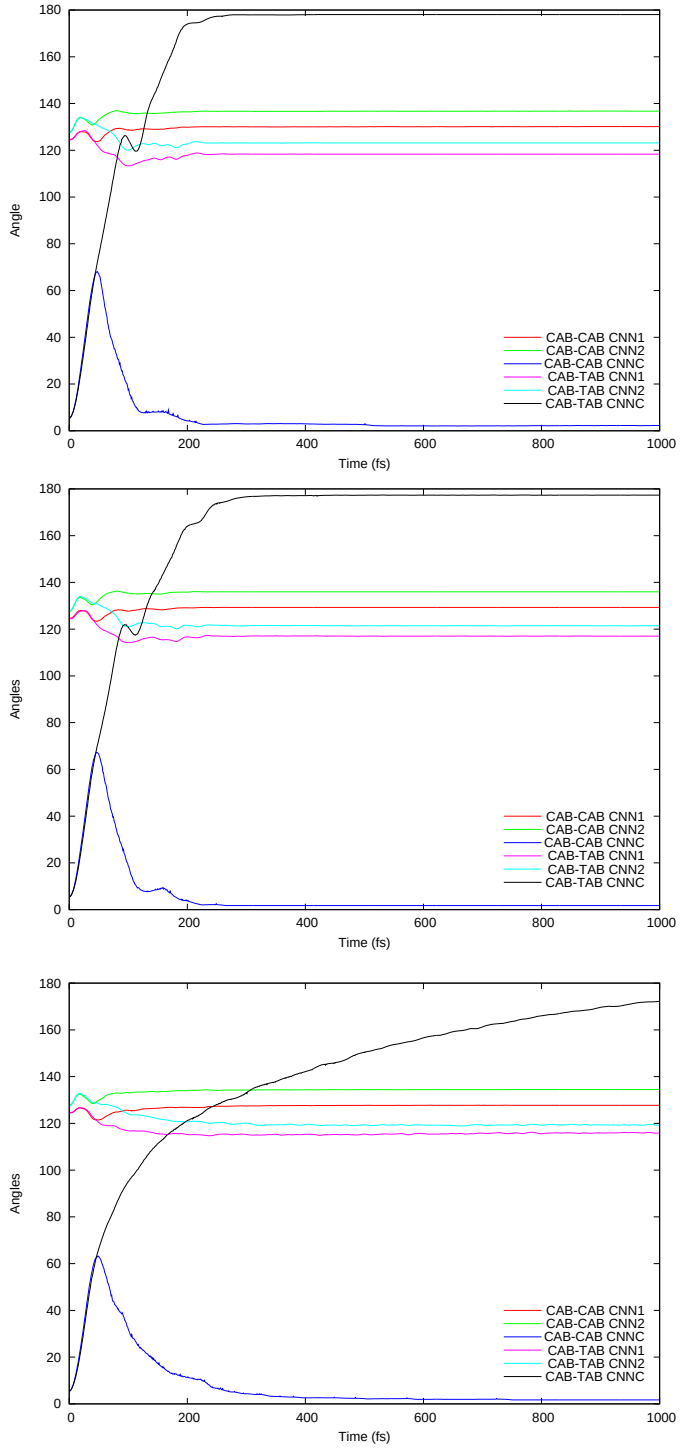

Figure 4.6: Time evolution of the angles CNNC, NNC_1 and NNC_2, averaged over the reactive and unreactive trajectories, in the case of $n \rightarrow \pi^*$ excitation of CAB and considering three cases: in vacuo and in the two solvents with low and medium viscosity (upper, medium and lower panel, respectively).

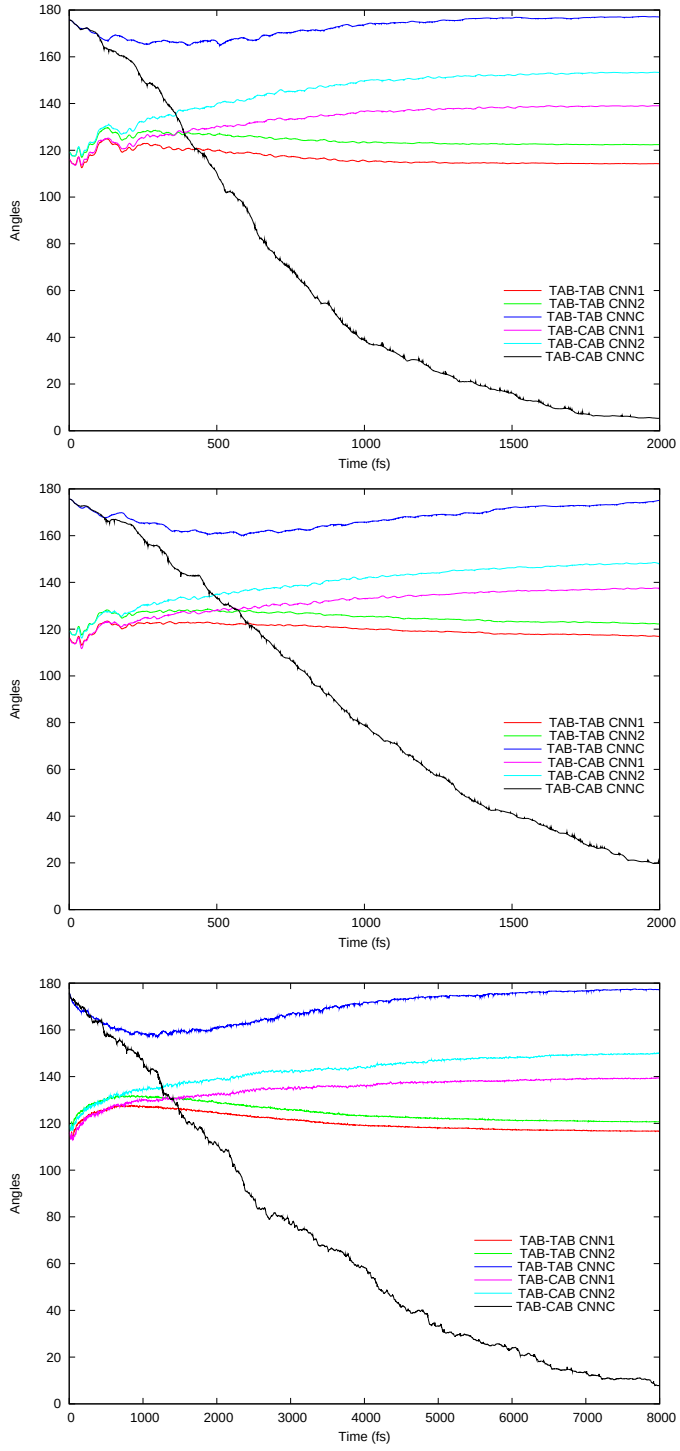

Figure 4.7: Time evolution of the angles CNNC, NNC_1 and NNC_2, averaged over the reactive and unreactive trajectories, in the case of $\pi \rightarrow \pi^*$ excitation of TAB and considering three cases: in vacuo and in the two solvents with low and medium viscosity (upper, medium and lower panel, respectively).

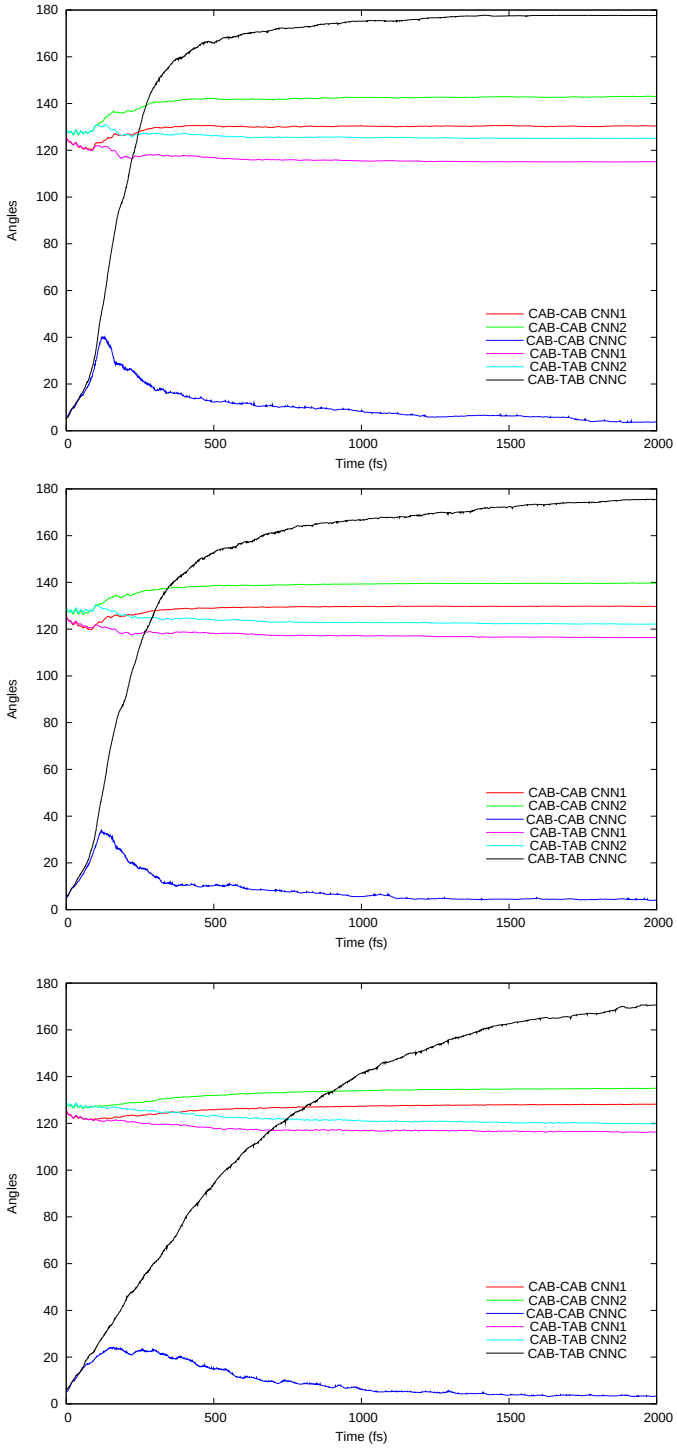

Figure 4.8: Time evolution of the angles CNNC, NNC_1 and NNC_2, averaged over the reactive and unreactive trajectories, in the case of $\pi \rightarrow \pi^*$ excitation of CAB and considering three cases: in vacuo and in the two solvents with low and medium viscosity (upper, medium and lower panel, respectively).

4.6 Photo-orientation of azobenzene.

An interesting aspect to be considered in this work is the phenomenon of molecular orientation induced by polarized light, because of the large amplitude motions that take place after the excitation. Induction of photochemical anisotropy in certain materials upon irradiation with polarized light (Weigert effect [104]) has been known since the beginning of this century. In the 1960s, this effect was widely studied in viscous solutions containing azo-dye molecules, which are known to undergo $cis \leftrightarrow trans$ photoisomerization upon light irradiation [105]. Recently, interest has arisen in the photoinduced anisotropy in azo-polymer films, and on applications in data storage and photo-modulable liquid crystal alignment, as well as in fundamental aspects of photo-orientation (Chapter 3 of ref. [106] and references therein).

Photo-orientation of azo-dye molecules occurs when these photochromic molecules are photo-selected by linearly polarized light of appropriate wavelength. The azo-dye molecules undergo successive cycles of excitation, internal dynamics in the excited states and then in the ground one, with or without $trans \leftrightarrow cis$ isomerization. Eventually, they align preferably with the transition dipole perpendicular to the polarization of the irradiating light. In solutions, photo-orientation can be neglected when rotational diffusion is fast enough to randomize induced molecular orientation. Small molecules diffuse rotationally in a few picoseconds in low-viscosity solutions. In solid polymer films, however, spontaneous molecular mobility can be strongly hindered, depending on temperature and pressure, and photo-orientation effects can be appreciable [106].

We are now able to relate the phenomenon of photo-orientation of azobenzene to the molecular photodynamics. The results obtained from the dynamics simulations provide information on the reorientation of a molecule, from the time of its excitation, to the time when it reaches again a stable configuration in the ground state (end of the trajectory). To extract this information, we must first define a body-fixed frame. This definition is given in detail in Appendix A, and it is valid for both isomers, even at distorted geometries. In all cases, the X axis corresponds to the N=N bond axis. For symmetric geometries, the Z axis coincides with the C_2 rotation axis, so it is perpendicular to the molecular plane of TAB. The CAB equilibrium geometry has no symmetry planes, but the CNNC atom are almost coplanar and the Z axis lies close to the $C_1N_1N_2$ and $N_1N_2C_2$ planes. Figure 4.9 shows the body-fixed frames for TAB and CAB. We shall call X_i, Y_i, Z_i the body-fixed frame of the initial geometry for a given trajectory, and X_f, Y_f, Z_f the final one. Each of the final axes can be expressed as a linear combination of the initial ones. For instance:

$$X_f = C_{xx}X_i + C_{xy}Y_i + C_{xz}Z_i \tag{4.22}$$

and in general:

$$\begin{pmatrix} X_f \\ Y_f \\ Z_f \end{pmatrix} = \begin{pmatrix} C_{xx} & C_{xy} & C_{xz} \\ C_{yx} & C_{yy} & C_{yz} \\ C_{zx} & C_{zy} & C_{zz} \end{pmatrix} \begin{pmatrix} X_i \\ Y_i \\ Z_i \end{pmatrix} \tag{4.23}$$

For each trajectory we obtain a different rotation matrix $\mathbf{C}$, which is related to the Euler angles of the rotation from the initial to the final molecular frame. A simulation provides a distribution of rotation matrices. It is convenient to represent such distributions by three dot density plots for each simulation, as in Figures 4.10 and 4.11. The coordinates of each dot in the plots are the final components of a given axis, that were initially null: for instance, for the X_f axis, we give the C_{xy} and C_{xz} components. In this way, we represent

pictorially the deviation of each axis from its original orientation. Dots of different colors are used for the reactive and the unreactive trajectories, i.e. to indicate the final orientation of CAB and TAB, respectively, when starting from TAB (and viceversa). In Figure 4.9 we also show three different views of the two isomers, corresponding to the initial orientation in each of the three dot density plots: the axis that is monitored in each plot points out of the paper in the corresponding view of the molecule.

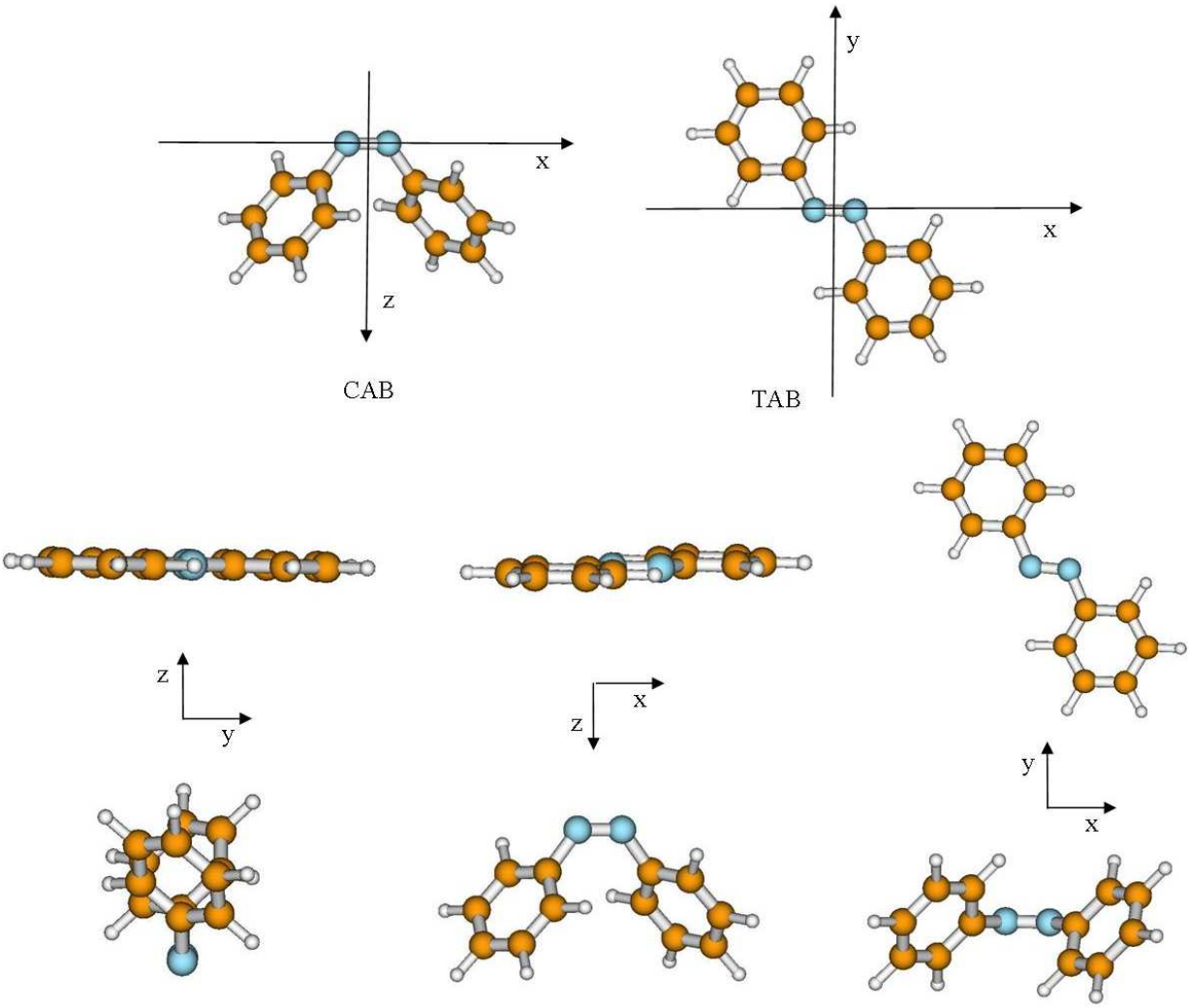

Figure 4.9: Body-fixed reference frames for the calculation of the orientation coefficients (top) and three views of TAB (center) and CAB (bottom), corresponding to the initial orientations in the dot density plots of Figures 4.10 and 4.11. The three orientations have one the three X, Y and Z axes pointing out of the paper, respectively.

Figure 4.10 shows the distribution of rotation coefficients obtained by excitation of TAB, for each of the three cases: in vacuo and in the two solvents of low and higher viscosity. Figure 4.11 shows the same for the excitation of CAB. It appears that the axes rotate into rather well defined preferential directions. To explain the observed behaviour, we recall that the pathway followed after excitation, by the reactive and the unreactive

trajectories alike, consists essentially in the torsion of the N=N double bond. Moreover, we apply the general principle that all atoms will be displaced as little as possible by the torsional motion. This is especially true for the atoms constituting the phenyl rings, that are relatively rigid and bulky groups. In vacuo, this is due to a mere inertial effect, but in a viscous solvent the friction hampers the large amplitude motions more effectively, and the spread of the distribution decreases. To minimize the displacements of the atoms, the torsion of the N=N bond is essentially performed by a rotation of the two halves of the molecule (the N-C_6H_5 groups) in opposite directions, around an axis that goes approximately through their centers of mass. With respect to this basic description, some refinements are necessary due to the bond length constraints, and because in S_1 the NNC angles tend to open more than in S_0. Of course, there is a certain degree of randomness in the overall rotation of the molecule, which is more likely to occur around the long axis, because it involves the smallest displacements of the atoms. For TAB, the long axis lies in the molecular plane, and is approximately the bisector of the fourth $(X, -Y)$ quadrant. For CAB, it is approximately parallel to the N=N bond (X axis).

In the case of the *trans* $\rightarrow$ *cis* isomerization, the above description of the molecular motion implies that the X axis is displaced in the negative Y direction, and the Y one in the positive X direction. However, the definition of the body-fixed frame is such that the sign of the Y and Z axes can change during the isomerization (see Appendix A), which corresponds to the formation of either one or the other enantiomeric conformation of CAB. Therefore, the positive and negative displacements are equally probable for the Y and Z axes. The rotation around the long axis adds a displacement of the Z axis along the bisector of the first and third quadrant of the XY plane, while X and Y acquire positive or negative Z components. The unreactive trajectories perform about half of the motion that leads to isomerization in the excited state, and then go back to the initial isomer in the ground state. Of course the two halves of this pathway do not coincide exactly, because of both random and systematic differences, the latter related to the shapes of the S_1 and S_0 PES. As a result, the rotation around the long molecular axis is more pronounced for the unreactive trajectories.

The *cis* $\rightarrow$ *trans* isomerization displaces the X and Y axes in the opposite direction, with respect to the *trans* $\rightarrow$ *cis* one. In this case, there is no ambiguity on the signs of the axes, because we always start with the same enantiomeric form of CAB. Moreover, all the random rotation effects are less pronounced than in the case of TAB excitation, because the photodynamics is faster and the molecular motion is better defined, thanks to the larger slope of the excited state PES. As a consequence, the final orientational distributions are less spread than in the TAB case, especially for the unreactive trajectories.

Finally, we have run a set of 300 brownian trajectories, each 3 ps long (Δt=0.1 ps) in the ground state of each isomer, with the two solvents of different viscosity. By taking two points along a trajectory, separated by a given time interval, we obtain the orientation coefficients for the rotational diffusion without excitation. The results with a time interval of 1 ps are shown in Figures 4.12 and 4.13. The faster rotational diffusion in the solvent of lower viscosity is apparent. With the more viscous solvent, the preferred axis of spontaneous rotation is also clear: for TAB, it lies in the $X - Y$ direction, and for CAB in the X direction, as previously noted.

Our results have been used in a successive work, which is not part of this thesis, where a stochastic model has been set up to simulate the development of anisotropy in a sample of azobenzene molecules. The main results of that work [107] are:

- In agreement with the experimental observations, the development of a strong anisotropy

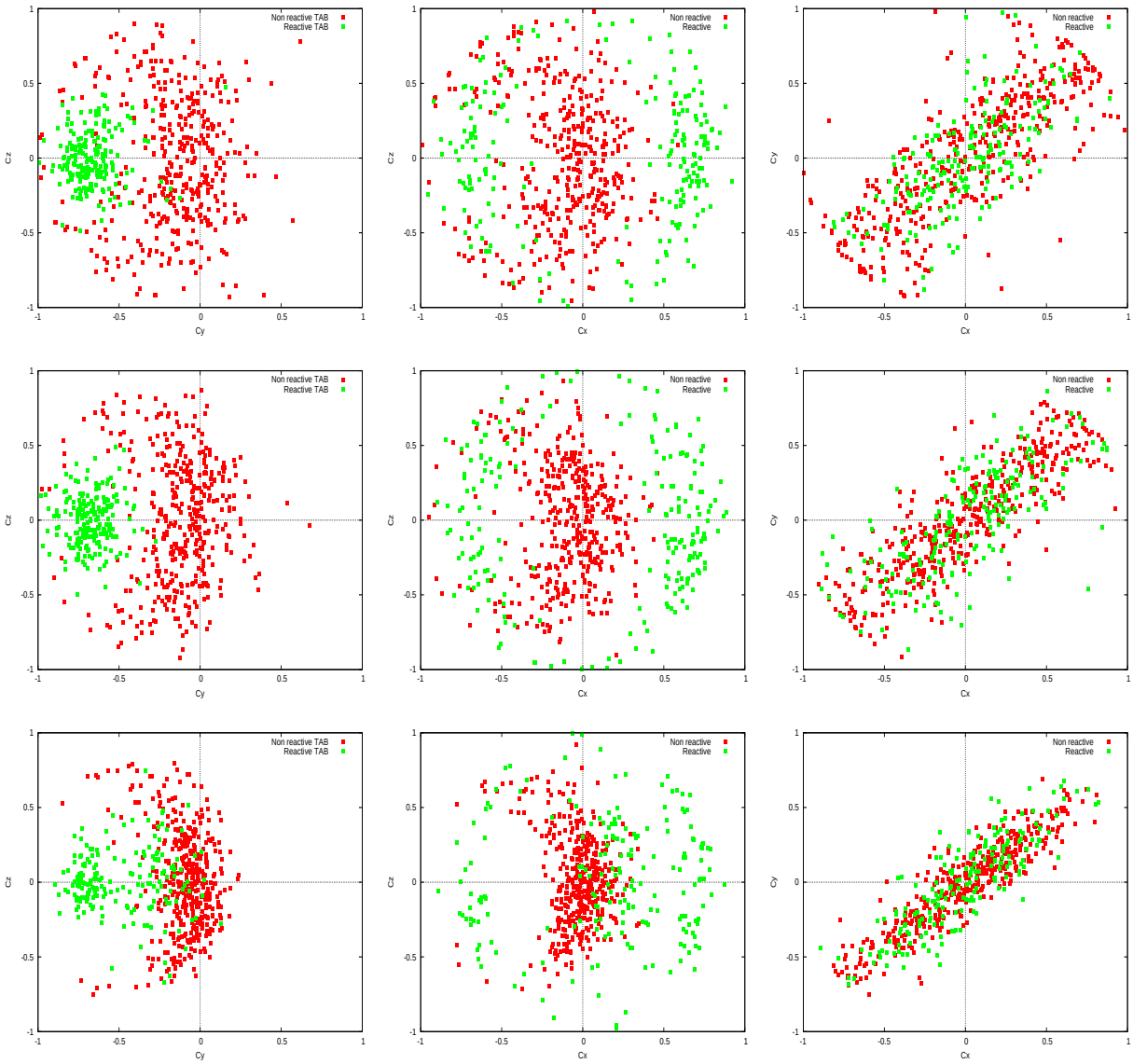

Figure 4.10: Orientation coefficients for the X axis (C_{xy} and C_{xz}), the Y axis (C_{yx} and C_{yz}) and the Z axis (C_{zx} and C_{zy}) of the TAB and CAB isomers, obtained by excitation of TAB, considering three cases: vacuum (upper panel), low viscosity solvent (middle panel) and medium viscosity solvent (lower panel). Green points: reactive trajectories; red points: unreactive trajectories.

can be induced, even with low irradiances, if the host matrix damps very effectively the rotational diffusion (polymers with low free volume). A solvent of medium viscosity would require very strong laser fields, in the Gw range.

- The photoisomerization process is not essential for the development of the anisotropy. In fact, our orientational distributions show that the unreactive trajectories are as effective in causing the reorientation of the chromophore as the reactive ones. Therefore, one may expect that, even in conditions where the quantum yields are considerably reduced,

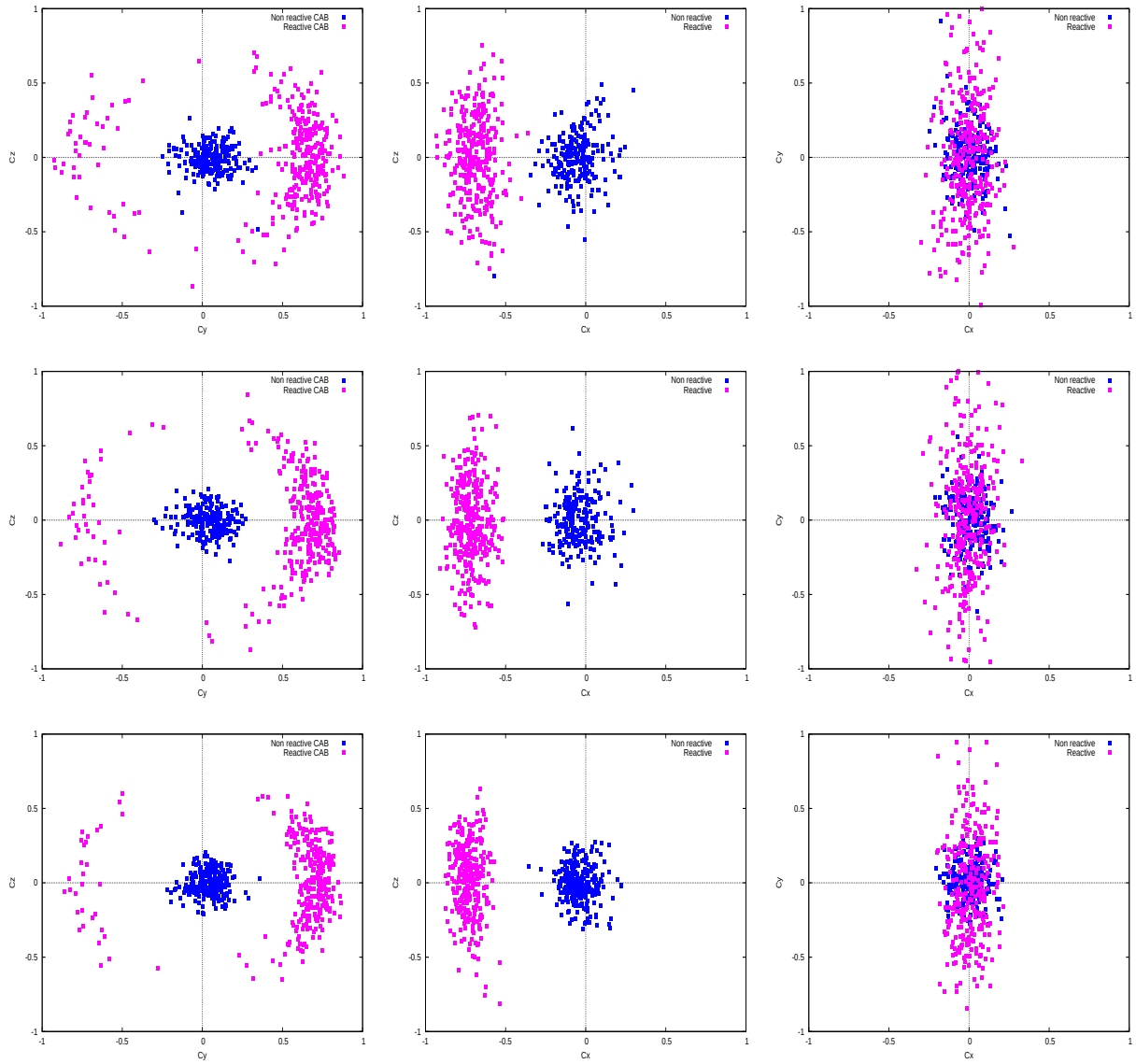

Figure 4.11: Orientation coefficients for the X axis (C_{xy} and C_{xz}), the Y axis (C_{yx} and C_{yz}) and the Z axis (C_{zx} and C_{zy}) of the TAB and CAB isomers, obtained by excitation of CAB, considering three cases: vacuum (upper panel), low viscosity solvent (middle panel) and medium viscosity solvent (lower panel). Purple points: reactive trajectories; blue points: unreactive trajectories.

the phenomenon of photoorientation can manifest itself. Moreover, even chromophores that do not isomerize may undergo the same phenomenon.

- The anisotropy of the sample has an important influence on the excitation rate. Since the orientation parameters of the two isomers are different (TAB being more easily oriented than CAB), the isomeric ratio in the photostationary state is widely different from the value one would obtain with an isotropic sample. This fact complicates the extraction of the quantum yields from the experimental data.

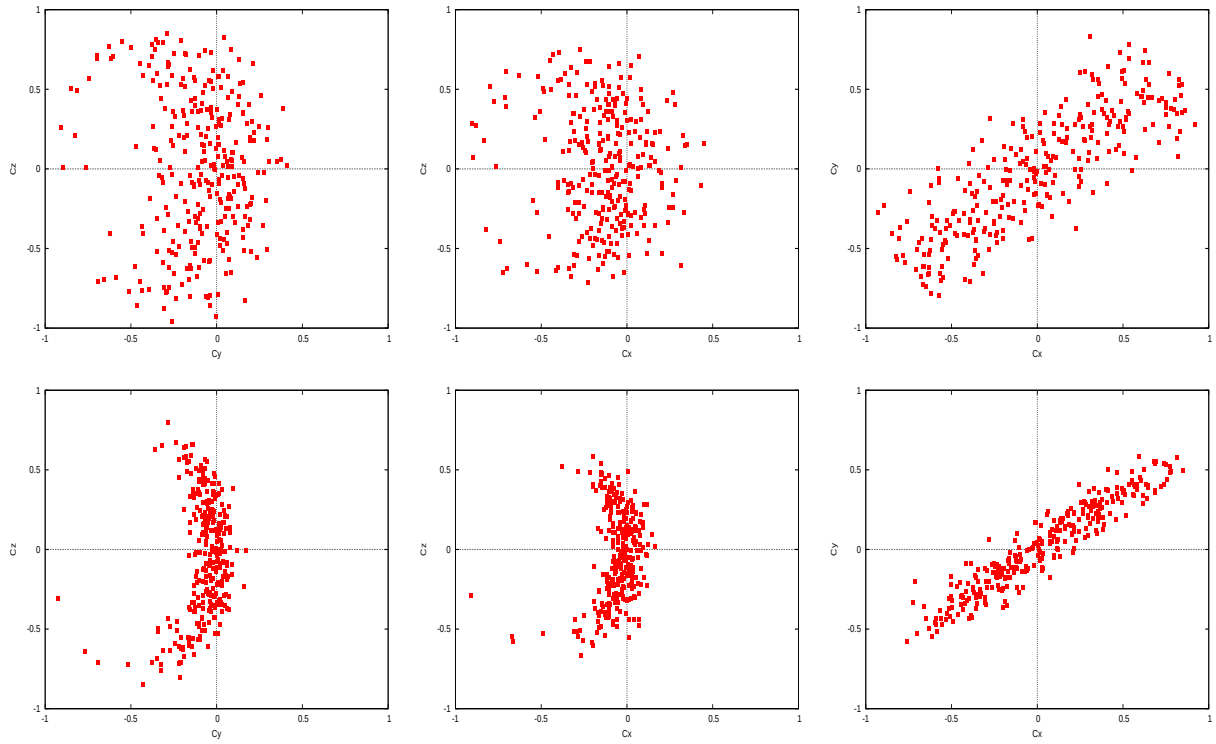

Figure 4.12: Orientation coefficients for the X axis (C_{xy} and C_{xz}), the Y axis (C_{yx} and C_{yz}) and the Z axis (C_{zx} and C_{zy}) of the TAB isomer, obtained by Brownian motion in the ground state for a time interval of 1 ps. Upper panel: low viscosity solvent; lower panel: medium viscosity solvent.

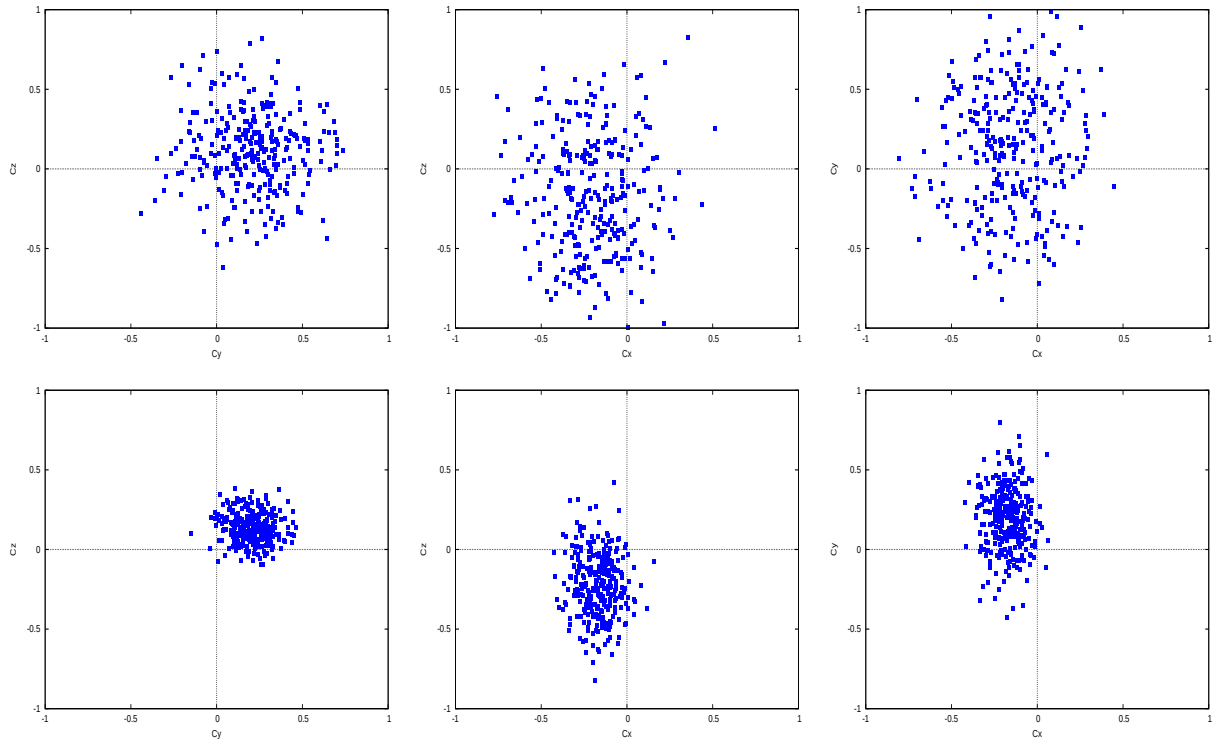

Figure 4.13: Orientation coefficients for the X axis (C_{xy} and C_{xz}), the Y axis (C_{yx} and C_{yz}) and the Z axis (C_{zx} and C_{zy}) of the CAB isomer, obtained by Brownian motion in the ground state for a time interval of 1 ps. Upper panel: low viscosity solvent; lower panel: medium viscosity solvent.

Part IV

INCLUSION OF THE SOLVENT EFFECTS

Chapter 5

Solute-solvent interaction potential

We want to remind that the main interest in our research work regards the simulations of the photoisomerization dynamics of azobenzene in solution in order to study the solvent effects on the excited states decay and on the quantum yields, as it has already been done for the isolated molecule [21, 38, 55]. As we have mentioned in Chapter 1, the most remarkable work related to the solvent effects on the photoisomerization of azobenzene is Diau's [6], who studied the variations of the fluorescence decay time and anisotropy due to solvent effects, for the $n \rightarrow \pi^*$ transition of azobenzene. As a non polar and low viscosity solvent they used n-hexane and as a polar and viscous one they used ethylene glycol. In their work, the authors show how the decay is slowed down and the fluorescence depolarization almost disappears, in the presence of a polar and viscous solvent. Thus, Diau hypothesizes two possible decay pathways: the symmetric NNC bending and the double bond N=N torsion. The first one would correspond to the fast decay and would not change the orientation of the transition dipole moment, while the second one would be slower and would cause the fluorescence depolarization.

The main aspects presented in this Chapter and in the next one are related to the interaction of azobenzene with solvents and to their influence on the photodynamics. Due to the size of the system (azobenzene embedded in a large cluster of solvent molecules), the simulations will be run by means of the QM/MM method [108,109] briefly described in Section 5.2. We are interested in three solvents: n-hexane, methanol and ethylene glycol, in order to span both the scale of polarities and that of viscosities. In a first stage, we have determined the solute-solvent interaction potential by ab initio calculations on the complexes of azobenzene with methane and methanol, i.e. the simplest representatives of hydrocarbons and alcohols. On the basis of such results, we have optimized the QM/MM parameters to be used for the dynamics.

5.1 Ab initio determination of the azobenzene-solvent interaction potential

The interaction forces between two molecular systems can be decomposed in a set of terms of different origin: repulsion forces (related to the superposition of electronic densities), dispersion forces (due to the correlation between electrons belonging to either system),

inductive forces (due to the polarization of the charge density of a molecule, induced by an electric field generated by the other one) and electrostatic forces (between charges or permanent multipoles). More specific and highly directional interactions, such as the hydrogen bonds, are partially accounted for by several terms of the kinds seen above. In our particular case, for the azobenzene-methane system, only the repulsion and dispersion terms are important. However, for the azobenzene-methanol system, also the electrostatic and inductive terms are important, and with the appropriate reciprocal orientations, a hydrogen bond is formed.

The interaction energies and optimal geometries of the azobenzene-solvent complexes will be obtained by MP2 calculations. The MP2 method is usually considered the simplest and fastest computational approach that provides a correct treatment of the dispersion interaction. As such, it is often used for systems of medium size, whenever dispersion plays an important role. Since we could not afford geometry optimizations with large basis sets, we have to deal with the Basis Set Superposition Error (BSSE). A brief account of the MP2 and BSSE theories is presented in the next section.

5.1.1 Møller-Plesset method and basis-set superposition error (BSSE)

In 1934, Møller and Plesset (MP) proposed a perturbation treatment of atoms and molecules in which the unperturbed wavefunction is the Hartree-Fock function [110]. The MP unperturbed Hamiltonian is taken as the sum of the one-electron Hartree-Fock operators $\hat{f_m}$ [111]:

$$\hat{\mathcal{H}}^{(0)} \equiv \sum_{m=1}^{n} \hat{f_m} \tag{5.1}$$

where the Fock operator is written as:

$$\hat{f}_m \equiv -\frac{1}{2}\nabla_m^2 - \sum_{\alpha} \frac{Z_\alpha}{r_{m\alpha}} + \sum_{j=1}^{n}[\hat{J}_j(m) - \hat{K}_j(m)] \tag{5.2}$$

Considering the ground state, the relative wave function for the unperturbated state, Φ_0, is represented by the Slater determinant of the n occupied spin-orbitals. This Slater determinant is an antisymmetrized product of the spin-orbitals, i.e. a sum of $n!$ terms, each term involving a different permutation of the electrons among the spin-orbitals. Thus, each term of the sum, and Φ_0 itself, are eigenfunctions of $\hat{\mathcal{H}}^{(0)}$:

$$\left[\hat{f}_{(1)} + ... + \hat{f}_{(n)}\right][u_1(1)..u_n(n)] = [\varepsilon_1(1) + ... + \varepsilon_n(n)][u_1(1)..u_n(n)] \tag{5.3}$$

$$\hat{\mathcal{H}}^{(0)}\Phi_0 = \left(\sum_{m=1}^{n} \epsilon_m\right)\Phi_0 \tag{5.4}$$

In these conditions, the perturbation operator can be written as the difference between the real electronic repulsion energy and the average potential used in the Hartree-Fock Hamiltonian:

$$\hat{\mathcal{H}}' = \hat{\mathcal{H}} - \hat{\mathcal{H}}^{(0)} = \sum_{l}^{n}\sum_{m>l}^{n}\frac{1}{r_{lm}} - \sum_{m=1}^{n}\sum_{j=1}^{n}[\hat{J}_j(m) - \hat{K}_j(m)] \tag{5.5}$$

The MP first order correction to the ground state energy is:

$$E_0^{(1)} = \left\langle \Phi_0 \left| \hat{\mathcal{H}}' \right| \Phi_0 \right\rangle \tag{5.6}$$

Thus,

$$\begin{aligned} E_0^{(0)} + E_0^{(1)} &= \left\langle \Phi_0 \left| \hat{\mathcal{H}}^{(0)} \right| \Phi_0 \right\rangle + \left\langle \Phi_0 \left| \hat{\mathcal{H}}' \right| \Phi_0 \right\rangle \\ &= \left\langle \Phi_0 \left| \hat{\mathcal{H}}^{(0)} + \hat{\mathcal{H}}' \right| \Phi_0 \right\rangle = \left\langle \Phi_0 \left| \hat{\mathcal{H}} \right| \Phi_0 \right\rangle = E_{HF} \end{aligned} \tag{5.7}$$

where E_{HF} is the Hartree-Fock energy. The first corrective term does not improve the accuracy of the result. Then, it is necessary to perform a second order development. The second order correction is calculated as:

$$E_0^{(2)} = \sum_{s \neq 0} \frac{\left\langle \Phi_s \left| \hat{\mathcal{H}}' \right| \Phi_0 \right\rangle^2}{E_0^{(0)} - E_s^{(0)}} \tag{5.8}$$

This term takes into account the interaction of the Hartree-Fock determinant Φ_0 with each excited determinant Φ_s. However, the Φ_s determinants that differ from Φ_0 by the excitation of one or more than two electrons, do not contribute to the sum ($\left\langle \Phi_s \left| \hat{\mathcal{H}}' \right| \Phi_0 \right\rangle = 0$). Consequently, the second order correction is obtained considering only the contributions of the doubly excited Φ_s determinants. The wave function that results from the $i \longrightarrow a$ and $j \longrightarrow b$ excitations can be indicated as $\Phi_s = \Phi_{ij}^{ab}$. Considering that $E_0^{(0)} - E_s^{(0)} = \varepsilon_i + \varepsilon_j - \varepsilon_a - \varepsilon_b$, the following expression is obtained:

$$E_0^{(2)} = \sum_{i=1}^{n} \sum_{j=i}^{n} \sum_{a=n+1}^{N} \sum_{b=a}^{N} \frac{\left\langle \Phi_{ij}^{ab} \left| \hat{\mathcal{H}}' \right| \Phi_0 \right\rangle^2}{\varepsilon_i + \varepsilon_j - \varepsilon_a - \varepsilon_b} \tag{5.9}$$

where N is the total number of spin-orbitals, and the first n are occupied. Consequently, in the second order correction, the expression for the total energy is:

$$E = E_{HF} + E_0^{(2)} = E_{HF} + \sum_{i=1}^{n} \sum_{j=i}^{n} \sum_{a=n+1}^{N} \sum_{b=a}^{N} \frac{\left\langle \Phi_{ij}^{ab} \left| \hat{\mathcal{H}}' \right| \Phi_0 \right\rangle^2}{\varepsilon_i + \varepsilon_j - \varepsilon_a - \varepsilon_b} \tag{5.10}$$

We examine now the problem of the Basis Set Superposition Error (BSSE), that affects practically all the ab initio methods in a similar way. In order to calculate the energy of a molecule with a method based on molecular orbitals it is necessary to choose a set of basis functions, most often centered on each atom of the system. Generally, a bigger basis produces better energy results. If we want to calculate the stabilization energy of a complex formed by two interacting units A and B, with respect to infinite separation, the standard procedure is to calculate the difference between the energy of the AB complex and that of the two separated partners A and B. In both calculations, one uses the same set of basis functions for each atom. The calculation for the two separated molecules can be substituted by a single one for the whole AB system, with a sufficiently large A-B distance (within the HF and MP2 methods the result does not change). Thus, the stabilization energy can be written as:

$$\Delta E = E_{AB}(\chi_A + \chi_B) - E_A(\chi_A) - E_B(\chi_B) \tag{5.11}$$

The computed energies depend on the basis set, therefore in eq. (5.11) we have indicated with χ_A the basis used to describe the fragment A and with χ_B that of the fragment B. With this method the interaction energy ΔE has a systematic negative error. As a matter of fact, at a short A-B distance each molecule (A or B) is described by a larger basis with respect to the one used at infinite distance, because the basis functions of the other molecule are available to improve variationally the wavefunction. Consequently, the complex is erroneously stabilized with respect to the two molecules at large distance. This error is called Basis Set Superposition Error (BSSE). The effect depends on the incompleteness of the basis set χ_A and on the ability of the basis functions χ_B to make up for it (and viceversa). Then, the BSSE decreases as a function of the A-B distance, and tends to zero for large basis sets, approaching completeness. The BSSE can be important for small interaction energies, as we shall see in the case of azobenzene-methane complex.

The counterpoise correction (CP) [112] permits, in a good approximation, to correct the BSSE. The energy at infinite distance is calculated as the sum of the energies computed separately for the A and B molecules, but the basis set used for each molecule also includes the basis functions of the other one, centered in the same positions as in the complex. The corrected interaction energy is then

$$\Delta E = E_{AB}(\chi_A + \chi_B) - E_A(\chi_A + \chi_B) - E_B(\chi_A + \chi_B) \tag{5.12}$$

The estimated BSSE is then

$$\delta E = E_A(\chi_A + \chi_B) - E_A(\chi_A) + E_B(\chi_A + \chi_B) - E_B(\chi_B) \leq 0 \tag{5.13}$$

5.1.2 Ab initio calculations

As we have mentioned at the beginning of this chapter, the first step is to obtain the interaction parameters between solute and solvent molecules by ab initio calculations. We shall focus on the interactions of the solvent molecule with the azo group, because we shall trust the standard force-fields to represent sufficiently well the interactions with the phenyl groups.

A direct minimization of the CP corrected energy for the azobenzene-solvent molecule complex has been discarded, because of convergence problems in the geometry optimization. For this reason, we have adopted the following procedure:

- Perform geometry optimizations for azobenzene and the solvent molecule at infinite distance and for their complex without counterpoise correction (CP).
- Carry out several "single point" calculations at different azobenzene-solvent distances, with the internal geometries and reciprocal orientations of the two molecules as optimized for the complex. The distance to be varied is that between a nitrogen atom of the azo group and the closest hydrogen of the solvent molecule (in methanol, the H atom of the OH group). In this step we take into account the CP correction, that depends mainly on the R(N-H) distance.
- Find the minimum of the CP corrected potential as a function of R(N-H), which is an approximation of the global minimum.

For the ab initio calculations, we have employed the cc-pVDZ basis set [113]. Moreover, we have carried out calculations with the cc-pVTZ basis set at the same geometries. In

Table 5.1: Scheme of the basis sets used for the calculation of the interaction potentials.

	cc-pVDZ		cc-pVTZ	
atoms	complete basis	contracted basis	complete basis	contracted basis
H	4s,1p	2s,1p	5s,2p,1d	3s,2p,1d
C,N	9s,4p,1d	3s,2p,1d	10s,5p,2d,1f	4s,3p,2d,1f

Table 5.1 we compare the composition of the two basis sets. Although the BSSE is much smaller with the larger basis, this procedure has not given satisfactory results, as we shall see in the next sections. Therefore, we have based the parameterization of the QM/MM potentials on the cc-pVDZ results.

In the next sections, we shall examine the results of the calculations of the interaction potentials of azobenzene with methanol and with methane. For clarity, Figure 5.1 shows the azobenzene-solvent complexes, with numbers indicating the most important atoms: to such numbers we shall refer in the following to designate the internal coordinates.

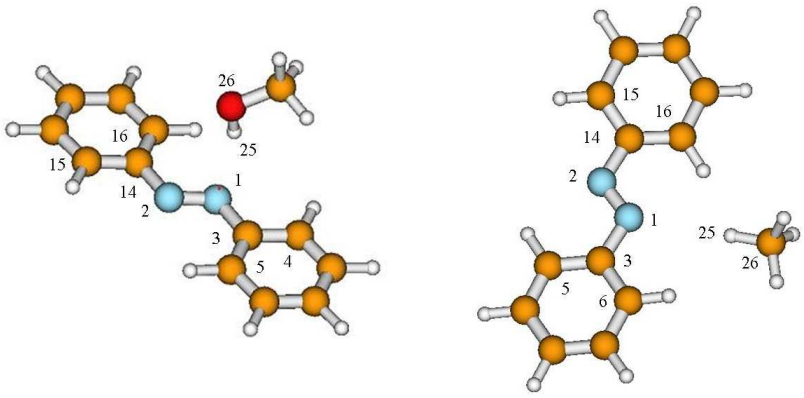

Figure 5.1: Azobenzene-methanol (left) and azobenzene-methane (right) complexes, with the numbering of the atoms related to the most important internal coordinates.

5.1.3 Ab initio results for the azobenzene-methanol interaction.

In the case of the azobenzene-methanol system, the interaction is dominated by the hydrogen bonding between the H atom of the alcohol and the N atoms of azobenzene. The ubiquitous repulsion and dispersion forces between other atoms or groups are also important.

First of all we have optimized the geometries of each molecule and isomer (TAB, CAB and methanol), with the MP2 method and the cc-pVDZ basis set. The energies of the "supermolecules" TAB + MeOH and CAB + MeOH at a very large R(N-H) distance have also been computed with the same internal coordinates, just to check that they coincide with the sum of the energies of the separated partners. Finally, we have carried out the optimization of the complexes *trans*-azobenzene-methanol (TAB-MeOH) and *cis*-

azobenzene-methanol (CAB-MeOH), without counterpoise correction, starting from the same geometry except that the R(N-H) is reduced to a reasonable H-bond value.

From the "free" optimization (without constraints) of the TAB-MeOH complex, we obtain a configuration with the H-O bond almost on the plane of the TAB, pointing towards one of the two N atoms of azobenzene (TAB-MeOH-Plan), where probably the interaction of H with the free electron pair of N is larger than in other orientations. For the CAB-MeOH complex we have also obtained a geometry with the H-O bond almost in the plane formed by $N_1C_3C_4$. Finally, we have performed another optimization for the TAB-MeOH complex, with the H-O bond perpendicular to the TAB plane (TAB-MeOH-Perp), in order to explore another approach of MeOH to the azo group. In this case we have applied the following constraints: $N_1X_1X_2$=90°, $N_2X_1X_2$=90°, $N_2X_1X_2N_2$=180°, $H_{25}N_2N_1X_2$=0° $C_3N_1N_2X_2$=90° and $C_{14}N_2N_1X_2$=90° (where X is a phantom atom, used to maintain the H-O bond of the methanol perpendicular to the TAB). Consequently, we have three configurations for the azobenzene-methanol complexes, shown in Figure 5.2. In the Tables 5.2 and 5.3 we show some important geometrical (distances N-H, angles and dihedrals) and energetic values, respectively, obtained from the above calculations. As a by-product, from the energies at large separation we also obtain the CAB-TAB energy difference, that amounts to 11.9 kcal/mol.

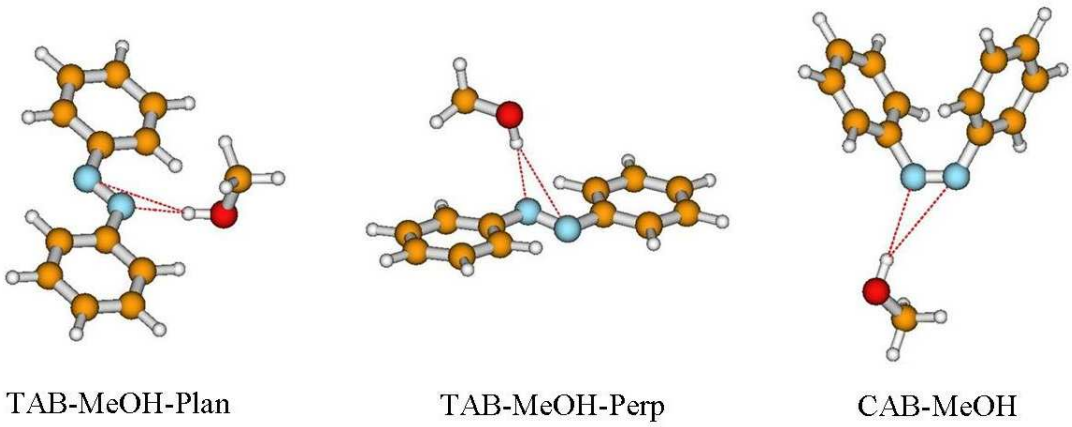

Figure 5.2: Optimized geometries for the complexes under study: TAB-MeOH-Plan, TAB-MeOH-Perp and CAB-MeOH. MP2 calculations, cc-pVDZ basis, no counterpoise correction.

The potential energy curves with the CP correction of the BSSE have been constructed by several single point calculations, varying the R(N-H) distance while keeping the other internal coordinates at their optimized values (the internal coordinates of the azobenzene and methanol and in particular the angles $H_{25}N_1N_2$, $H_{25}N_1N_2C_3$ with the values obtained by the ab initio calculations). These calculations have been repeated with the cc-pVDZ and the cc-pVTZ basis sets, both at the cc-pVDZ geometries: in fact, to optimize the geometries at the cc-pVTZ level was found computationally too demanding. The obtained energies are shown in Table 5.4. More detailed data about these results can be found in the Appendix D.

Figure 5.3 shows a portion of the potential energy curves for the different complexes and for both basis, with and without counterpoise correction. The lowest points of the

Table 5.2: Optimized geometrical parameters of the azobenzene-methanol complexes. MP2 calculations, cc-pVDZ basis, no counterpoise correction.

Coordinate	TAB-MeOH-Plan	TAB-MeOH-Perp	CAB-MeOH
$R_{N_1H_{25}}$ (Å)	1.927	2.096	2.817
$R_{N_2H_{25}}$ (Å)	2.982	2.900	1.998
$\angle N_2N_1C_3$ (Degrees)	113.6	113.4	120.8
$\angle N_1N_2C_{14}$ (Degrees)	115.1	113.4	121.9
$\angle C_3N_1N_2C_{14}$ (Degrees)	179.9	179.9	6.9
$\angle N_1N_2C_{14}C_{15}$ (Degrees)	-177.2	169.2	-135.8
$\angle N_1N_2C_{14}C_{16}$ (Degrees)	3.1	-12.8	51.7
$\angle N_2N_1C_3C_4$ (Degrees)	179.5	-161.0	-135.2
$\angle N_2N_1C_3C_5$ (Degrees)	-0.7	21.5	52.9
$\angle O_{26}N_1C_3C_4$ (Degrees)	-6.4	82.7	168.8
$\angle O_{26}N_1C_3C_5$ (Degrees)	173.4	-94.8	-3.0
$\angle O_{26}N_2C_{14}C_{15}$ (Degrees)	-173.1	120.7	2.3
$\angle O_{26}N_2C_{14}C_{16}$ (Degrees)	7.1	-61.2	-170.2

Table 5.3: Energies of the azobenzene-methanol complexes. MP2 calculations, cc-pVDZ basis, no counterpoise correction.

	TAB-MeOH-Plan	TAB-MeOH-Perp	CAB-MeOH
E_∞ (a.u.)[a]	-686.409592	-686.409592	-686.390564
E_{min}(a.u.)[b]	-686.427528	-686.417065	-686.407351
R_{min} (Å)[c]	1.93	2.10	2.00
ΔE(a.u.)[d]	-0.017936	-0.007473	-0.016787
ΔE(kcal/mol)	-11.25	-4.69	-10.53

[a]Energy at large distance, when the two molecules do not interact: R(N-H)=12Å
[b]Energy of the optimized complex
[c]Optimal R(N-H) distance
[d]Energy difference $E_{min} - E_\infty$

curves were fitted with a second order polynomial, to obtain the distance and energy of the potential curve minimum. For each complex and basis set, the corrected curve is above the non corrected one. Moreover, the optimal R(N-H) distance with CP correction is shifted to larger values with respect to the non corrected one. These features can be supported with the data presented in the Tables 5.3 and 5.4.

From the CP corrected cc-pVDZ results we observe that the TAB-MeOH-Plan complex is more stable than TAB-MeOH-Perp, i.e. the H-bond interaction with the lone pair of N is stronger than that with the π electrons of the azo group. Moreover, methanol binds to CAB slightly better than to TAB, because the lone pairs of the former do cooperate in

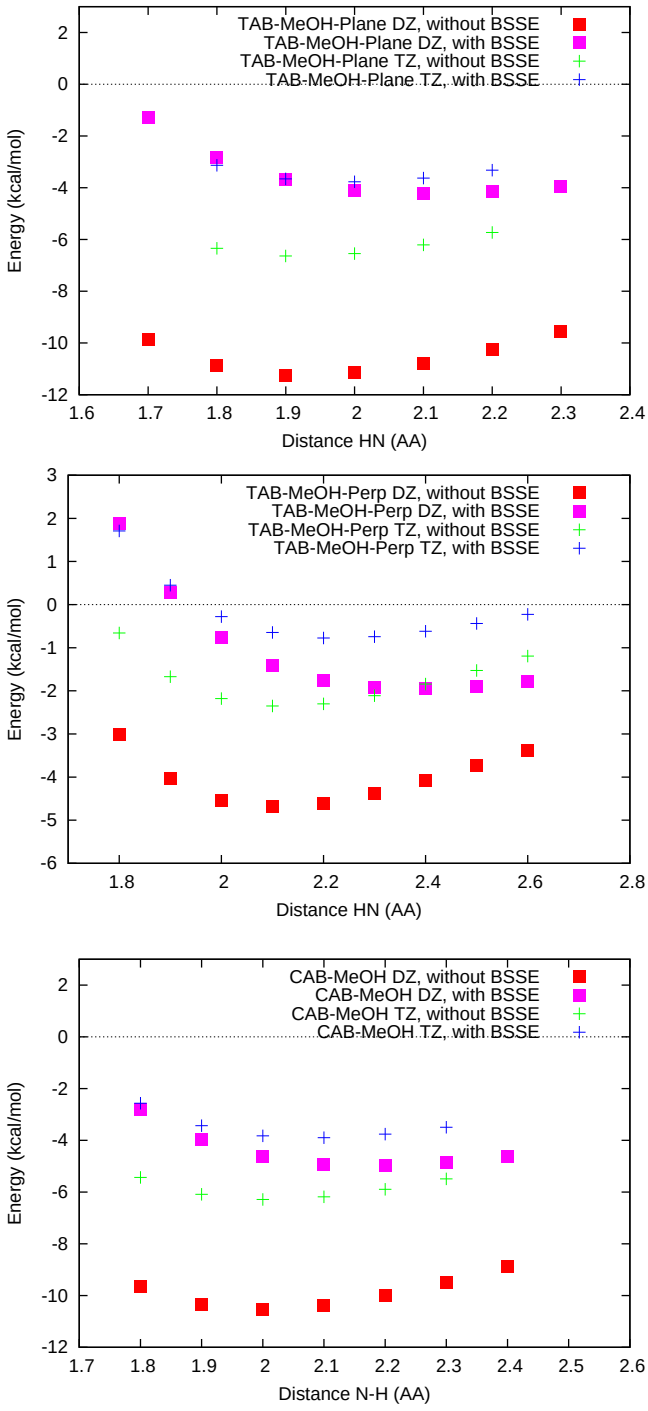

Figure 5.3: Comparison between the potential energy curves relative to the cc-pVDZ and cc-pVTZ basis, for the three complexes: TAB-MeOH-Plan (upper panel), TAB-MeOH-Perp (middle panel) and CAB-MeOH (lower panel), with and without the counterpoise correction.

Table 5.4: Energies of the azobenzene-methanol complexes. MP2 calculations, cc-pVDZ and cc-pVTZ basis sets, with counterpoise correction.

	TAB-MeOH-Plan	TAB-MeOH-Perp	CAB-MeOH
	cc-pVDZ basis		
E_∞(a.u.)[a]	-686.409592	-686.409592	-686.390564
E_{min}(a.u.)[b]	-686.416352	-686.412700	-686.398496
R_{min} (Å)[c]	2.11	2.38	2.18
ΔE(a.u.)[d]	-0.006760	-0.003108	-0.007932
ΔE(kcal/mol)	-4.24	-1.95	-4.98
	cc-pVTZ basis		
E_∞(a.u.)[a]	-687.073547	-687.073547	-687.055412
E_{min}(a.u.)[b]	-687.079562	-687.074784	-687.061636
R_{min} (Å)[c]	1.99	2.24	2.09
ΔE(a.u.)[d]	-0.006015	-0.001237	-0.006224
ΔE(kcal/mol)	-3.78	-0.78	-3.91

[a]Energy at large distance, when the two molecules do not interact: R(N-H)=12Å
[b]Energy of the complex, computed at R_{min}
[c]R(N-H) distance corresponding to the minimum of the CP corrected potential curve.
[d]Energy difference $E_{min} - E_\infty$

causing electrostatic and inductive effects, while those of TAB do not.

Considering the CP corrected cc-pVTZ results, we see that the depth of the minimum is slightly reduced for TAB-MeOH-Plan and CAB-MeOH, and much more so for TAB-MeOH-Perp. In fact, the stabilization energy of the latter complex at R(N-H) = 2.6 Å is almost vanishing. This is due, most probably, to the use of the cc-pVDZ geometry for the cc-pVDZ energy calculations. The geometries one would obtain with the two basis sets do not coincide, so the cc-pVTZ energies computed at cc-pVDZ geometries are higher than in the cc-pVTZ minimum. In the case of the TAB-MeOH-Perp complex this error is larger than at infinite R(N-H) distance, so the computed stabilization energy is too small. This artefact is even more apparent in the case of the azobenzene-methane complexes, and has prompted us to give up the use of the cc-pVTZ basis set.

5.1.4 Ab initio results for the azobenzene-methane interaction.

The azobenzene-methane interaction potential has been computed as part of a BS Thesis work, carried out in our research group [114]. Here we give a short account of the results. The procedure is similar to that followed in the case of methanol. Three complexes have been optimized: *cis*-azobenzene-methane (CAB-Met), *trans*-azobenzene-methane with one of the H-C bonds of the methane in the plane of the TAB (TAB-Met-Plan) and *trans*-azobenzene-methane with one of the H-C bonds perpendicular to the TAB plane (TAB-Met-Perp). The CAB-Met complex has been optimized without constraints, choosing a starting geometry with one of the H-C bonds of methane pointing towards one of the N atom of azobenzene and approximately in the C_{26}-N_1-N_2 plane. For the TAB-Met,

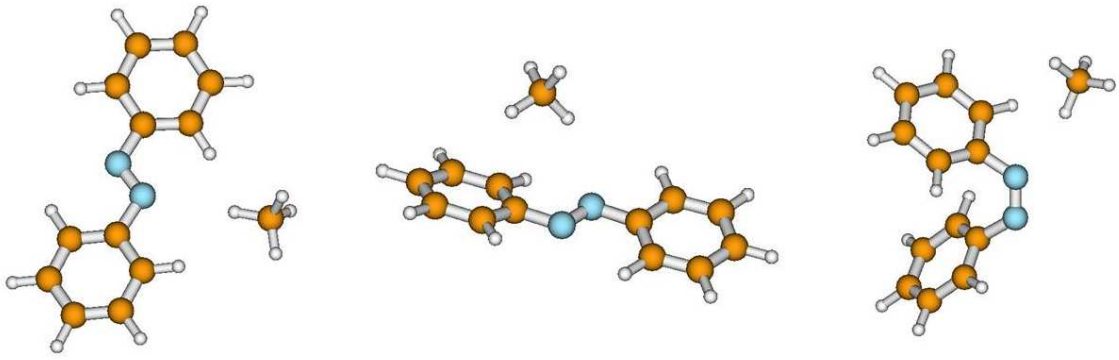

Figure 5.4: Optimized geometries for the complexes of azobenzene-methane: TAB-Met-Plan, TAB-Met-Perp and CAB-Met, by ab initio calculations.

the "free" optimization (without constraints) yields a perpendicular configuration of the complex, at variance with the methanol complex. The optimization of the configuration with the methane molecule in the plane of TAB needed the application of the following constraints on two dihedral angles: $H_{25}N_1N_2C_{14}$=0° and $C_{26}H_{25}N_1C_3$=0°. In Figure 5.4 we present the geometries obtained after the optimization.

The attractive forces involved in this system are very weak (induction and dispersion) and the gradients of the potential energy surfaces, along the coordinates that determine the relative position of the two molecules are very small, the minima are very shallow and the optimization converge with difficulty. The inductive effects due to the nitrogen lone pairs have some importance only when the CAB isomer is involved, because of the stronger electrostatic field generated by CAB with respect to TAB. As in the case of methanol, the optimizations of TAB+methane and CAB+methane at large distance have been carried out. Also in this case, we find a CAB/TAB energy difference of 11.9 kcal/mol. The results of the optimizations are shown in the Tables 5.5 and 5.6. More detailed data can be found in the Appendix E.

In this case, the TAB-Met-Perp complex is more stable than TAB-Met-Plan and very close to CAB-Met. In the TAB-Met-Perp and CAB-Met complexes the interaction between the two molecules involves the *azo*-group and one of two phenyl groups, unlike the case of TAB-Met-Plan, where the methane molecule is constrained to stay in the azobenzene plane. Apparently, the dispersive interaction with the phenyl ring makes the difference and explains why the CAB-Met and TAB-Met-Perp complexes are more stable than the TAB-Met-Plan one. In TAB-Met-Perp the methane molecule assumes a bridge position between both nitrogens of the double bond and interacts with the phenyl ring bonded to the N_2. The distorted conformation of CAB (with the phenyl groups out of the CNN plane) prevents the methane molecule to occupy an intermediate position between the two nitrogens. There is however a common characteristic between CAB-Met and TAB-Met-Perp: the methane molecule is on a plane that contains the axis of the nearest N-C bond and is perpendicular to the corresponding phenyl ring, in order to better interact with the π electrons.

Again, the energy values are affected by the BSSE. As we shall see, in the case of the

Table 5.5: Geometrical optimized parameters of the azobenzene-methane complexes. MP2 calculations, cc-pVDZ basis, no counterpoise correction.

Coordinate	TAB-Met-Plan	TAB-Met-Perp	CAB-Met
$R_{N_1H_{25}}$ (Å)	2.833	2.767	2.798
$R_{N_2H_{25}}$ (Å)	3.874	3.047	3.875
$\angle N_2N_1C_3$ (Degrees)	113.0	113.3	121.1
$\angle N_1N_2C_{14}$ (Degrees)	113.5	113.1	120.7
$\angle C_3N_1N_2C_{14}$ (Degrees)	-179.3	-179.2	7.3
$\angle N_1N_2C_{14}C_{15}$ (Degrees)	-167.8	-165.6	-134.5
$\angle N_1N_2C_{14}C_{16}$ (Degrees)	13.3	14.5	53.2
$\angle N_2N_1C_3C_4$ (Degrees)	-178.0	-175.5	-134.5
$\angle N_2N_1C_3C_5$ (Degrees)	2.2	4.8	54.7
$\angle C_{26}N_1C_3C_4$ (Degrees)	2.5	-77.9	79.3
$\angle C_{26}N_1C_3C_5$ (Degrees)	-177.3	102.4	-91.5
$\angle C_{26}N_2C_{14}C_{15}$ (Degrees)	-167.8	-102.1	-105.8
$\angle C_{26}N_2C_{14}C_{16}$ (Degrees)	13.3	78.0	81.9

Table 5.6: Energies of the azobenzene-methane complexes. MP2 calculations, cc-pVDZ and cc-pVTZ basis sets, with counterpoise correction.

	TAB-Met-Plan	TAB-Met-Perp	CAB-Met
E_∞ (a.u.)[a]	-611.381798	-611.381798	-611.362675
E_{min}(a.u.)[b]	-611.384152	-611.385575	-611.366359
r_{min} (Å)[c]	2.83	2.77	2.80
ΔE(a.u.)[d]	-0.002354	-0.003777	-0.003685
ΔE(kcal/mol)	-1.48	-2.37	-2.31

[a]Energy at large distance, when the two molecules do not interact: R(N-H)=12Å
[b]Energy of the optimized complex
[c]Optimal R(N-H) distance
[d]Energy difference $E_r - E_\infty$

methane complexes, the BSSE is of the same order of magnitude of the stabilization energy found in the geometry optimization without CP correction. Figure 5.5 shows the potential energy curves with and without CP correction, as functions of the R(N-H) distance. All the other internal coordinates maintain the values found with the optimization without counterpoise. Table 5.7 contains the CP corrected stabilization energies and optimal R(N-H) distances. Even with the CP correction, the TAB-Met-Perp and CAB-Met complexes have approximately the same stabilization energy, while TAB-Met-Plan is less stable.

We have also computed the energies corresponding to the minimum of the CP corrected cc-pVDZ curves, using the larger cc-pVTZ basis. For the two complexes with TAB,

TAB-Met-Perp and TAB-Met-Plan, the CP corrected cc-pVTZ energy is higher than the dissociation limit. This is due to the same artefact already discussed for the complexes with MeOH (inadequacy of the cc-pVDZ geometries for the cc-pVTZ calculations), so we have discarded the results obtained with this basis set.

Table 5.7: Energies of the azobenzene-methane complexes. MP2 calculations, cc-pVDZ basis set, with counterpoise correction.

	TAB-Met-Plan	TAB-Met-Perp	CAB-Met
E_∞(a.u.)[a]	-611.381798	-611.381798	-611.362675
E_{min}(a.u.)[b]	-611.382700	-611.383266	-611.364231
R_{min} (Å)[c]	3.18	3.08	3.03
ΔE(a.u.)[d]	-0.000902	-0.001468	-0.001556
ΔE(kcal/mol)	-0.57	-0.92	-0.98

[a]Energy at large distance, when the two molecules do not interact: R(N-H)=12Å
[b]Energy of the complex, computed at R_{min}
[c]R(N-H) distance corresponding to the minimum of the CP corrected curve
[d]Energy difference $E_{min} - E_\infty$

5.2 QM/MM Method

In order to carry out the simulations including an explicit representation of the solvent it is necessary to apply a method suitable for large systems, such as Molecular Mechanics. However, we need to describe quantum mechanically the chromophore, which is also, in our case, the reactive portion of the system. The QM/MM approach satisfies such requirements. This method was born from an idea of Warshel and Levitt [115], although some pioneering work was done in Pisa as early as in 1971 [116, 117].

In the QM/MM approaches, the electrons belonging to given portion of the system are described with a quantum mechanical (QM) method, and in our specific case, in a semiempirical way. It is the part of the system that one wants to study in detail, generally a reactive system or a system where the electronic structure is very important. It can be a molecule (like a solute in a solution), a group of molecules or a fragment of a big molecule. The other part of the system is the "environment". It does not participate directly in the chemical reaction, but it does interact with the reactive subsystem. This part is treated with a force field as in Molecular Mechanics (MM). This approach is very convenient when the chromophore or the reactive center constitutes a small part of the entire system. The MM subsystem can contain a certain number of solvent molecules, a solid surface, a natural or synthetic polymeric matrix or others molecules in condensate phase, and it can also contain chromophores with the condition that their excited states are not important for the process under study.

The electronic Hamiltonian of the global system can be partitioned into three terms: one related to the QM subsystem, $\hat{\mathcal{H}}_{QM}$; one represented by the force field for the MM atoms, $\hat{\mathcal{H}}_{MM}$; and the interaction between the two subsystems, $\hat{\mathcal{H}}_{QM/MM}$:

$$\hat{\mathcal{H}}_{el} = \hat{\mathcal{H}}_{QM} + \hat{\mathcal{H}}_{MM} + \hat{\mathcal{H}}_{QM/MM} \tag{5.14}$$

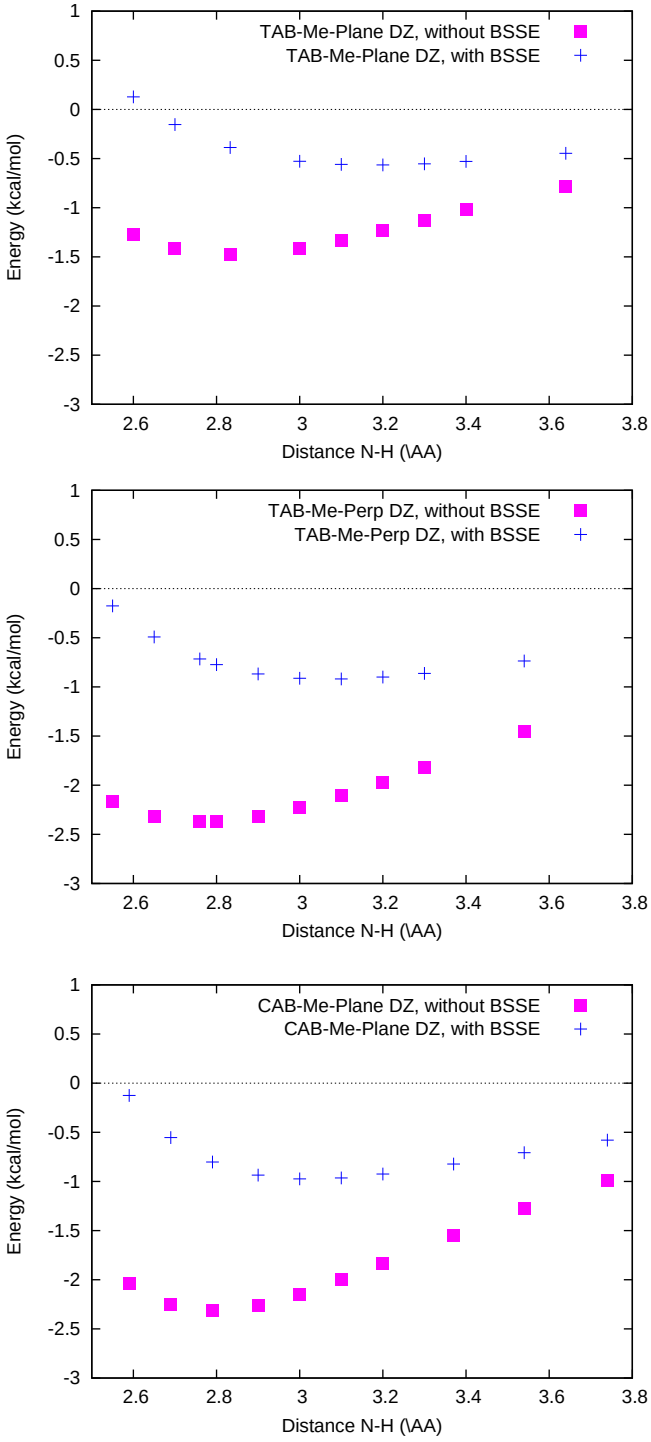

Figure 5.5: Potential energy curves relative to the cc-pVDZ basis, for the three complexes: TAB-Met-Plan (upper panel), TAB-Met-Perp (middle panel) and CAB-Met (lower panel), with and without CP correction.

The total energy of the system can also be divided into three terms:

$$U = U_{QM} + U_{MM} + U_{QM/MM} \tag{5.15}$$

Here U_{MM} can be identified with $\hat{\mathcal{H}}_{MM}$, while U_{QM} and $U_{QM/MM}$ are the expectation values of $\hat{\mathcal{H}}_{QM}$ e $\hat{\mathcal{H}}_{QM/MM}$, respectively. Thus, the total energy can be written as:

$$U_k = \left\langle \psi_k \left| \hat{\mathcal{H}}_{QM} + \hat{\mathcal{H}}_{QM/MM} \right| \psi_k \right\rangle + U_{MM} \tag{5.16}$$

In our formulation [108,109], $\hat{\mathcal{H}}_{QM}$ takes the expressions adopted in the semiempirical methods. U_{MM} is an energy obtained by a classical force field and it contains interaction terms between linked atoms, as well as purely electrostatic and repulsion/dispersion interactions between pairs of non bonded MM atoms. Some examples of this kind of force fields including OPLS [118–120], AMBER [121,122] and CHARMM [123]. A wide choice of functions of the internal coordinates can be used to describe the potential energy of a molecular system. Many force-fields are based on the general form

$$\begin{aligned} E_{MM}(\vec{R}_1, \vec{R}_2, ..., \vec{R}_N) = & \sum_{i_{bonds}=1}^{N_{bonds}} U_{bond}(i_{bonds}, |\vec{R}_a - \vec{R}_b|) \\ & + \sum_{i_{ang}=1}^{N_{ang}} U_{angles}(i_{ang}, \vec{R}_a, \vec{R}_b, \vec{R}_c) \\ & + \sum_{i_{dihed}=1}^{N_{dihed}} U_{dihed}(i_{dihed}, \vec{R}_a, \vec{R}_b, \vec{R}_c, \vec{R}_d) \\ & + \sum_{i=1}^{N-1} \sum_{j>i}^{N} U_{pairs}(i, j, |\vec{R}_a - \vec{R}_b|) \end{aligned} \tag{5.17}$$

where U_{bonds}, U_{ang}, U_{dihed} and U_{pairs} are the interaction terms depending on the length of the bonds, on the angles, on the dihedral angles and on the distance between non bonded atoms, respectively. The first three terms are treated as intramolecular interactions, while U_{pairs} depends on the distance between not bonded atoms of the same or of different molecules. N_{bonds}, N_{ang} and N_{dihed} are the numbers of the three kinds of intramolecular interactions and the collective indexes i_{bonds}, i_{ang} and i_{dihed} specify which a, b, c and d atoms are involved. The indexes i and j represents two non bonded atoms. The U_{pairs} interactions are repulsion/dispersion and Coulombic terms, the latter related to atomic charges. The interactions between bound atoms are considered in some MM force fields as Morse or harmonic terms depending on the bond length or bond angles, and truncated Fourier expansions for the dihedral angles (internal rotation). Frequently, the repulsion/dispersion terms are represented by Lennard-Jones potentials. In this work, the MM energy is computed through the TINKER program [124], that has been interfaced to MOPAC. The form of the force field and its parameters are those of the all-atom OPLS [118,125–127], i.e. OPLSAA.

The characteristic term for the QM/MM approach is $\hat{\mathcal{H}}_{QM/MM}$. It represents the interaction between MM atoms or groups of atoms and the electrons and nuclei of the QM subsystem. A simple expression for this term includes electrostatic interactions and

Lennard-Jones terms, related to repulsion-dispersion interactions [128]:

$$\hat{\mathcal{H}}_{QM/MM} = -\sum_{i,m} \frac{q_m}{R_{im}} + \sum_{\alpha,m} \frac{Z_\alpha q_m}{R_{\alpha m}} + \sum_{\alpha,m} \epsilon_{\alpha m} \left[\left(\frac{\sigma_{\alpha m}}{R_{\alpha m}} \right)^{12} - \left(\frac{\sigma_{\alpha m}}{R_{\alpha m}} \right)^{6} \right] \tag{5.18}$$

where q_m is the atomic charge on the n-th MM atom, Z_α is the core charge of the QM atom α, R_{im} and $R_{\alpha m}$ are the distances between a QM electron or nucleus and an MM atom, and $\epsilon_{\alpha m}$, $\sigma_{\alpha m}$ are the Lennard-Jones (LJ) parameters for the QM atom α interacting with the MM atom m. These pair LJ parameters reduce to atomic LJ parameters:

$$\epsilon_{\alpha m} = \sqrt{\epsilon_\alpha \epsilon_m} \tag{5.19}$$

$$\sigma_{\alpha m} = \sqrt{\sigma_\alpha \sigma_m} \tag{5.20}$$

The first electrostatic term is added to the QM Hamiltonian and it is treated in the same way as the electron-nucleus electrostatic interactions inside the QM region. We emphasize the importance of adding this term before diagonalizing the electronic Hamiltonian, because in this way the effect of the environment on electronic energies and wavefunctions is state-specific. This means that the environmental spectral shifts are treated correctly, and the conical intersections or the avoided crossings can be displaced both along the coordinate and along the energy axis. The last two terms in Eq. (5.18) are added to the computed electronic energies and cannot influence the electronic distributions, but may affect the PES and the dynamics of the system. The determination of the q_m, $\epsilon_{\alpha m}$ and $\sigma_{\alpha m}$ parameters is described in the next section.

5.3 QM/MM representation of the azobenzene-solvent interaction potential

As we have already stated, we shall apply the standard OPLS LJ parameters to the interactions between the MM atoms and the C and H atoms of the phenyl rings of azobenzene. We shall instead optimize the atomic Lennard-Jones parameters of the N azo atoms. Moreover, special terms have been added for the H atoms of the OH group. In fact, in OPLS these H atoms are not centers of LJ interactions. We have added LJ terms between such H atoms and the QM atoms, in order to add some flexibility to the intermolecular QM/MM potential. Finally, for the case of methanol only, we have divided all the MM atomic charges by the factor Q_{fac}, to be optimized. This amounts to dividing the two electrostatic terms in eq. (5.18) by Q_{fac}. The Q_{fac} factor is not applied to the MM force field, but only to the QM/MM hamiltonian.

The optimizations have been carried out by means of the SUPOPT program, that has been interfaced with MOPAC and TINKER. The target values are the R_{min} and ΔE, that characterize each of the three complexes of methanol or methane with azobenzene (CAB and TAB, the latter with a planar or perpendicular approach). These values were obtained by the CP corrected cc-pVTZ MP2 calculations, and are found in Tables 5.4 and 5.7. The reproduction of the target values requires a geometry optimization of the three complexes by the semiempirical QM/MM method. If the calculations are carried out with an active space of 12 electrons and 12 orbitals (82 determinants), two orbitals belonging respectively to the active and doubly occupied subspaces can switch, causing a discontinuity in the CI energies and wavefunctions. This problem manifests itself with convergence difficulties in

the optimization procedure. The problem was solved by increasing the active space to 14 electrons and 13 orbitals (94 determinants). Therefore, this is the CI space that will be used in the simulations of the photodynamics.

In the following two sections we shall present the results corresponding to two cases (as in the ab initio calculations): azobenzene-methanol and azobenzene-methane complexes.

5.3.1 Optimization of the QM/MM parameters. Azobenzene-methanol complex.

In this case, we optimize five parameters: ϵ_{N} and σ_{N} of the azo N atoms, ϵ_{H} and σ_{H} of the OH group, and the charge factor Q_{fac}. In the geometry optimizations, the starting point was taken from the ab initio results of Section 5.1.3.

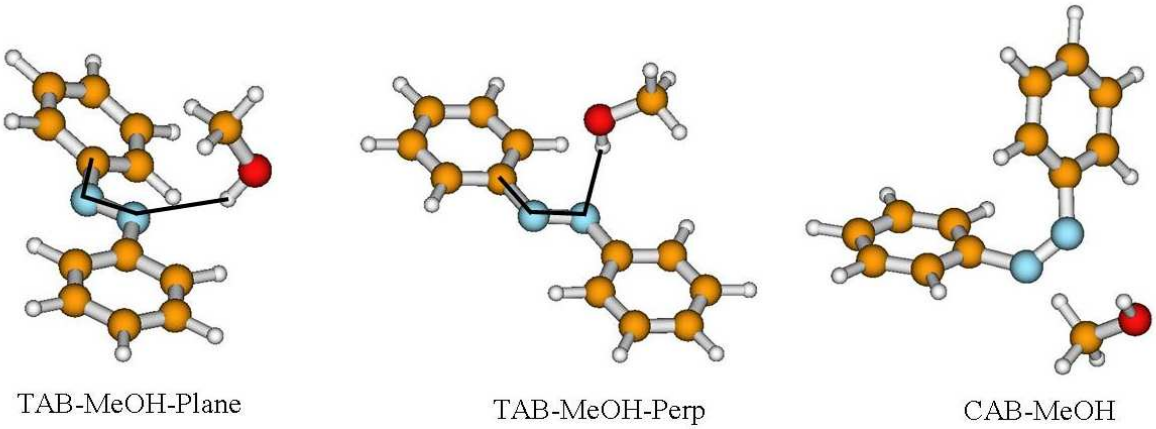

Figure 5.6: Optimized geometries for the azobenzene-methanol complexes, obtained by the semiempirical QM/MM method.

The azobenzene-methanol complex is very flexible: the minima are shallow, and different computational methods can be easily at variance as to the predicted energy orderings and the relative orientations of the two partners. Therefore, in optimizing the TAB-MeOH-Plan and TAB-MeOH-Perp complexes with the semiempirical QM/MM method, we have imposed some constraints, to compute R(N-H) distances and stabilization energies for geometrical configurations that are similar to the ab initio ones. In the case of TAB-MeOH-Plan, we have fixed the $H_{25}N_1N_2C_{14}$ dihedral angle at the value obtained from ab initio calculations, i.e. 3.11°. For the TAB-MeOH-Perp configuration we have fixed the angles $H_{25}N_1N_2$=90.0°, $H_{25}N_1N_2C_{14}$=90.0°, $O_{26}H_{25}N_1N_2$=0.0°, $C_{27}O_{26}H_{25}N_1$=180.0° and $O_{26}H_{25}N_1$=165.25° (the latter value taken from the ab initio results). Only for CAB-MeOH no constraints were applied.

In Figure 5.6 we show the configurations of the azobenzene-methanol complex obtained by the semiempirical QM/MM method, with the optimized parameters. For the TAB-MeOH-Plan and TAB-MeOH-Perp configurations we have shown the $H_{25}N_1N_2C_{14}$ dihedral angle, that distinguishes between the planar and perpendicular orientations.

Table 5.8 shows the target values and those obtained by the semiempirical QM/MM method with the best set of parameters, and the weights W_i. We can observe that we obtain better results for the CAB-MeOH complex than for the TAB-MeOH ones. Table

5.9 shows the optimized parameters. The charge factor Q_{fac} is rather large, i.e. the electrostatic interactions are considerably reduced with respect to using the original OPLS charges. As a consequence, the importance of the hydrogen bond is also reduced, by comparison with the dispersion interactions between the non-polar moieties (CH_3 and the phenyl rings). This shift of the balance is witnessed by a gradual change of the optimal geometries that are obtained with increasingly large Q_{fac} factors.

Table 5.8: Optimization of the QM/MM parameters for the azobenzene-methanol complex.

	Target value $V_{t,i}$	Semiempirical QM/MM value $V_{s,i}$	Error $V_{s,i}$-Vt,i	Relative error (%)	Weight W_i
			TAB-MeOH-Plan		
ΔE (kcal/mol)	4.2400	3.5392	-0.7008	16.529	1/2
R(N-H) (Å)	2.1100	2.2933	0.1833	8.687	1/2
			TAB-MeOH-Perp		
ΔE (kcal/mol)	1.9500	2.2616	0.3116	15.980	1/2
R(N-H) (Å)	2.3800	2.4923	0.1123	4.718	1/2
			CAB-MeOH		
ΔE (kcal/mol)	4.9800	5.0854	0.1054	2.117	1/2
R(N-H) (Å)	2.1800	2.1659	-0.0141	0.645	1/2

Table 5.9: Optimal QM/MM hamiltonian parameters for the azobenzene-methanol complex.

Parameter	Optimized value
ϵ_{N} (kcal/mol)	0.14898
σ_{N} (Å)	2.08149
ϵ_{H} (kcal/mol)	0.02889
σ_{H} (Å)	2.83696
Charge factor Q_{fac}	2.44069

5.3.2 Optimization of the QM/MM parameters. Azobenzene-methane complex

For the azobenzene-methane complexes the procedure is similar to the one followed in the previous section. In this case, we only optimize the ϵ_{N} and σ_{N} parameters of the azo N atoms. Since the electrostatic interactions are almost negligible, we have not optimized the charge factor, that keeps the standard value $Q_{fac} = 1$.

Again, the geometries used as starting point for these calculations are those obtained from the ab initio ones (described in the section 5.1.4). We found necessary to apply

some constraints in the geometry optimization of TAB-Met-Plan, in order to force the methane molecule to remain close to the TAB plane: we set $H_{25}N_1N_2C_{14}$=179.3° and $C_{26}H_{25}N_1N_2$=0.10° (ab initio results). In Figure 5.7 we show the configurations of the azobenzene-methane obtained after the optimization procedure, indicating the constrained $H_{25}N_1N_2C_{14}$ dihedral angle of TAB-Met-Plan.

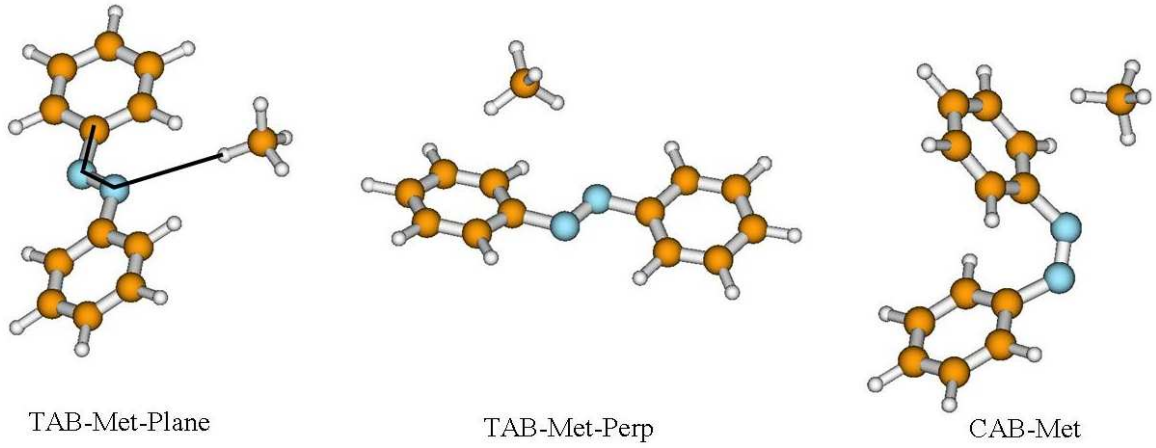

Figure 5.7: Optimized geometries for the azobenzene-methane complexes, obtained by the semiempirical QM/MM method.

Table 5.10 presents the target values and those obtained semiempirically with the best set of QM/MM parameters, and the weights W_i. Table 5.11 contains the optimized LJ parameters. From the results shown in both tables, it is apparent that the interaction of the azo group with non-polar molecules is weak. A non-polar solvent will affect the photodynamics because of the need to displace the solvent molecules when the solute performs large amplitude motions. Such inertial and viscosity effects will be essentially mediated by repulsive forces.

Table 5.10: Optimization of the QM/MM parameters for the azobenzene-methane complex.

	Target value $V_{t,i}$	Semiempirical QM/MM value $V_{s,i}$	Error $V_{s,i}$-Vt,i	Relative error (%)	Weight W_i
			TAB-Met-Plan		
ΔE (kcal/mol)	0.5700	0.7046	0.1346	23.616	1/2
R(N-H) (Å)	3.1800	3.1076	-0.0724	2.278	1/2
			TAB-Met-Perp		
ΔE (kcal/mol)	0.9200	0.9577	0.0377	4.098	1/2
R(N-H) (Å)	3.2814	3.0800	0.2014	6.539	1/2
			CAB-Met		
ΔE (kcal/mol)	0.9800	1.1215	0.1415	14.436	1/2
R(N-H) (Å)	3.0300	3.2792	0.2492	8.225	1/2

Table 5.11: Optimal QM/MM Lennard-Jones parameters for the azobenzene-methane complex.

Parameter	Optimized value
ϵ_{N} (kcal/mol)	0.00017892
σ_{N} (Å)	5.78167892

Chapter 6

Solvent effects on the semiclassical dynamics of azobenzene

As we have mentioned in the previous chapter, one of the most important aspects of this research work concerns the study of the solvent effects on the photodynamics of azobenzene, with focus on the quantum yields, the transient fluorescence, and its anisotropy. Previously (Chapter 5), we have obtained the interaction parameters for the azobenzene-solvent complexes, to be used on the dynamics calculations. by the QM/MM method. The first simulations we have run with this method concern the $n-\pi^*$ excitation, for which the most interesting experimental work has been carried out. The azobenzene molecule will be inserted in a large cluster of methanol or ethylene glycol. These two compounds have been chosen as examples of protic solvents, with low and high viscosity. Work in progress to perform simulations also in n-hexane, so as to reproduce Diau's experiments, that were done in this solvent and in EG. Moreover, we have repeated the simulations in vacuo with the CI space of 94 determinants, used in the QM/MM calculations.

For each simulation, the first steps are the preparation of the solvent sphere by molecular dynamics calculations, the inclusion of the solute molecule into the sphere, and the sampling of the initial conditions for the surface hopping trajectories. In running the surface hopping trajectory simulations, we have made use of new "stop conditions", different from those employed in the brownian simulations of the Chapter 4. These conditions require a trajectory to be integrated for a longer time after the decay to the ground state, in order to allow for the conversion of the hot ground state *cis* isomer into the *trans* one. The final results will be compared with those of the Brownian dynamics, and with the experimental data.

6.1 Molecular features of the solvents

The study of small functionalized organic molecules is a typical first step in the modeling of larger molecular systems. Among the variety of possible representatives of hydrogen bonded liquids composed of "small organic molecules", methanol and methylamine are the most widely studied ([129] and references therein).

Methanol is the simplest alcohol among a series of aliphatic alcohols, and is a close analog to water. Methanol molecules have both hydrophobic and hydrophilic groups.

They are able to form hydrogen bonds among themselves, which are responsible for many of the abnormal properties of bulk solvent. The presence of the methyl group induces significant differences between water and methanol. Since the first computer simulation of liquid methanol to determine the liquid structure were carried out by Jorgensen using the Monte Carlo method [130], much of the research effort has been devoted to examining the structural and dynamic properties of pure methanol and its aqueous solution [131]. Liquid methanol has been also the subject of many experimental studies. Extensive information on the structural dynamics, and spectroscopic properties of liquid methanol has been made available from various experimental techniques, including NMR, neutron scattering and X-ray diffraction ([132] and references therein). On the theoretical side, computer simulations have been performed to rationalize and elucidate the experimental data [133]. Liquid methanol has been also the subject of several detailed theoretical treatments [130, 134–136] in which the major emphasis was devoted to the analysis of the energetics of the system. In this direction, Jorgensen [130] has probably done the most complete attempt to obtain, by statistical mechanics simulation, structural and thermodynamics information on liquid methanol. One of the main conclusions he reached was that about 1.9 oxygen, on the average, are hydrogen bonded to another oxygen atom [137], as later confirmed by other studies [133, 138].

In the last 20 years the liquid structure of several monovalent alcohols such as methanol has been extensively studied by different methods, e.g. by neutron and x-ray diffraction, the Monte Carlo method, and molecular dynamics simulations [139–141]. However, liquid ethylene glycol (EG) is not well studied by these techniques. In general, 1,2-disubstituted ethanes (XCH_2CH_2Y) possess internal rotation, which results in the three rotameric dihedral angles: one about the C-C bond and one about each of the C-X and C-Y bonds [129]. The 1,2-disubstituted ethane most investigated by theoretical methods is the ethylene glycol (EG). Ethylene glycol (like the methanol) is one of the simplest polar molecules with internal degrees of freedom which may be regarded as a water analogue. This alcohol can form three-dimensional networks of hydrogen bonded molecules since each molecule has two proton donor hydroxyl groups and two oxygen atoms that can act as proton acceptors. Furthermore, one can imagine the EG molecule as two methanol molecules linked by the methyl groups and because each methanol molecule participates in two hydrogen bonds on average in the liquid phase [133, 138]. Then, provided the two subunits behave independently, one will expect a mean number of four hydrogen bonds per EG molecule. EG has one of the lowest ratios of weakly polar groups (methylene or methyl groups) vs polar groups (hydroxyl groups) in alcohols. Hence, the properties of this system will be dominated by hydrogen bonding interactions, and there may be competition between intermolecular and intramolecular H-bonds. This competition is not present either in water or in alkanols because only intermolecular hydrogen bonds can be formed in those cases.

6.2 Preparation of the solvent

The dynamics simulations in condensed phase require the preparation of a cluster of solvent molecules, which is done in several steps. For methanol, the OPLS-AA potential [118, 125–127] is adopted as the intermolecular interaction force field. The functional form for the OPLS-AA force fields are with harmonic terms for bond stretching and angle bending, Fourier series for torsional energetics, and Coulomb plus 12-6 Lennard-Jones potentials for the nonbonded interactions. Also, geometric combining rules for σ and ϵ

are used in the OPLS-AA force field. For the case of ethylene glycol we have applied a modified OPLS-AA force field, OPLS-AA-SEI-M (OPLS-AA Scaling Electrostatic Interaction Modified). This was an improvement proposed by Kony et al. [142] (OPLS-AA-SEI) and modified by de Oliveira et al. [143] for the study of thermodynamic properties of pure liquid EG. The modification includes new scaling factors for Lennard-Jones and Coulomb potentials, optimized to reproduce the heat of vaporization and density of the pure liquid as well as the average value of the O-C-C-O dihedral angle.

In both cases (methanol and ethylene glycol) we proceed as follows.

- A cubic box is filled with 1000 molecules, with the centers of mass arranged in a cubic crystal structure, and with a density considerably lower than the experimental one, in order to avoid strongly repulsive interactions. All the EG molecules are in their *trans* configuration. The initial configurations are shown in Figure 6.1.
- Molecular dynamics simulations are performed with constant NPT (P=1 atm and T=298K) and periodic boundary conditions, by means of the MOSCITO package [144]. The methanol simulation lasted about 2 ns, with a time step of 0.5 fs. For EG we did a first 5 ns run with fixed bond lengths and a time step of 1 fs, and then we continued for 1 ns without constraints and with a time step of 0.2 fs. Both simulations yield a disordered cube as shown in Figure 6.1.

Table 6.1: Physical and geometrical parameters of the solvent cubic cells and spherical clusters.

	methanol	ethylene glycol
Final cubic cell side length (Å)	41.17	45.41
Final ρ (g/cm^3)	0.761	1.099
Experimental ρ (g/cm^3)[a]	0.787	1.110
Radius of sphere (Å)	20.0	22.0
Molecules in the sphere	482	481
Molecules in the sphere with TAB	474	475
Molecules in the sphere with CAB	476	473

[a] P=1 atm and T=298K. References [145, 146] for methanol and [147, 148] for EG.

- The solvent properties are computed by averaging over the last 1000 ps of simulation. The final densities are in good agreement with experiment (see Table 6.1). The hydroxyl hydrogen-oxygen and oxygen-oxygen intermolecular radial distribution functions (RDF) are shown in Figure 6.2 (see Appendix F for general information about RDF). They are the usual way to describe the average structure of liquids, and in particular to evaluate the importance of hydrogen bonding [143]. For methanol, the RDF is in good agreement with that obtained experimentally [149]. The average number of H-bonds per molecule is 1.97: in half of them the molecule acts as an H donor, and in half it is an acceptor. In the case of EG, due to the complex spatial distribution of the molecules in the liquid phase, it is difficult to extract the RDF from neutron scattering and X-ray diffraction data. Therefore, in this case we just check that our results reproduce the theoretical ones of de Oliveira et al [143], considering the

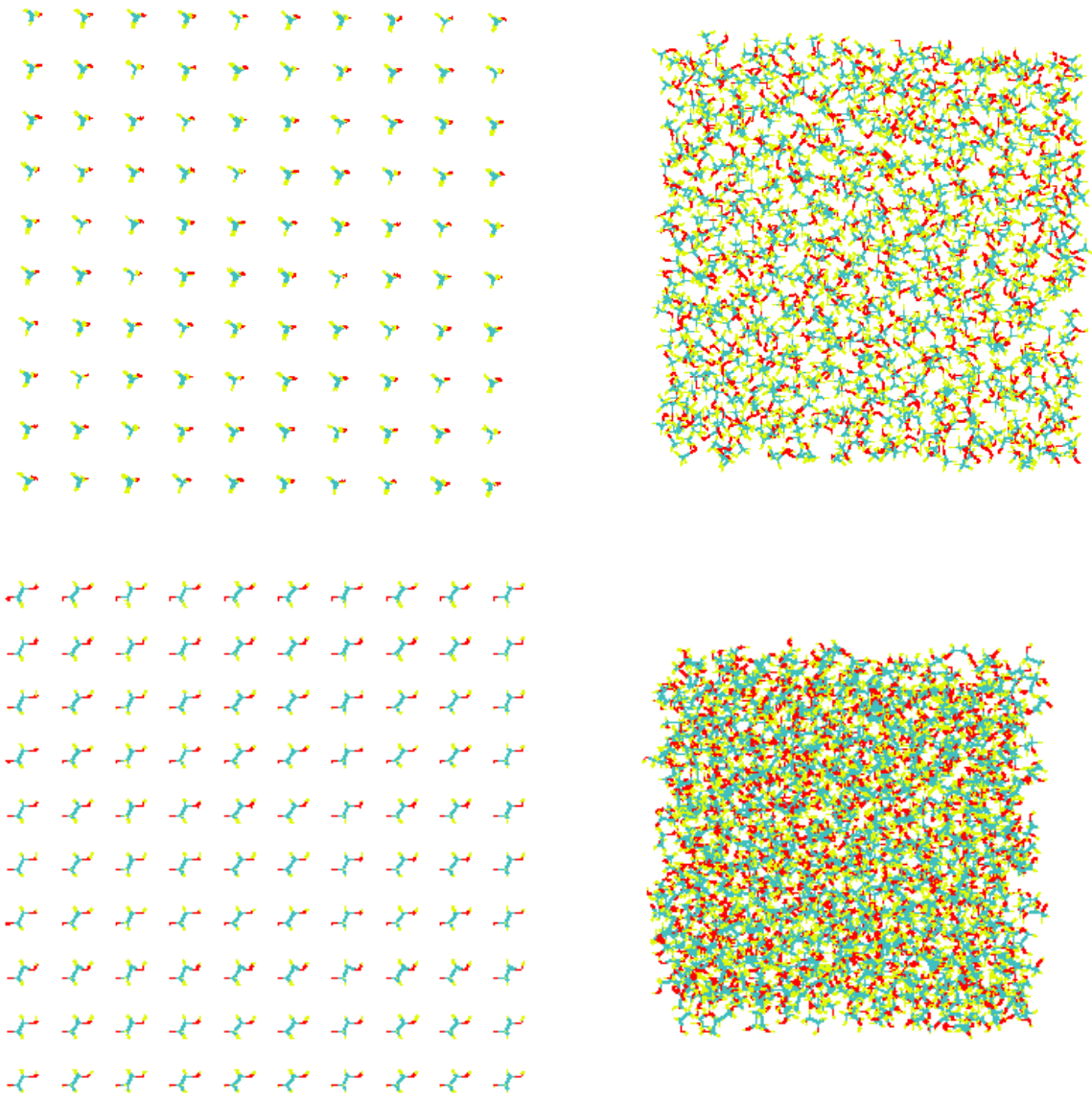

Figure 6.1: Initial and final configurations of the methanol (upper panels) and ethylene glycol (lower panels) cubic cells.

fact that we have employed their modified OPLSS-AA force field. The EG molecules form mainly intermolecular H-bonds, as shown by the RDF. In this case, the average number of H-bonds per molecule is 3.94: in average, each hydroxyl group would form 2.25 H-bonds. The two hydroxyl hydrogen atoms also have a tendency to approach the other oxygen atom of the same molecule. By monitoring the non-bonded H·O distances, we find 21.2% of the molecules with one H·O pair closer than 3.0 Å and

2.4% with both; if the threshold is raised to 3.5 Å, these percentages increase to 45.6% and 24.6%, respectively.

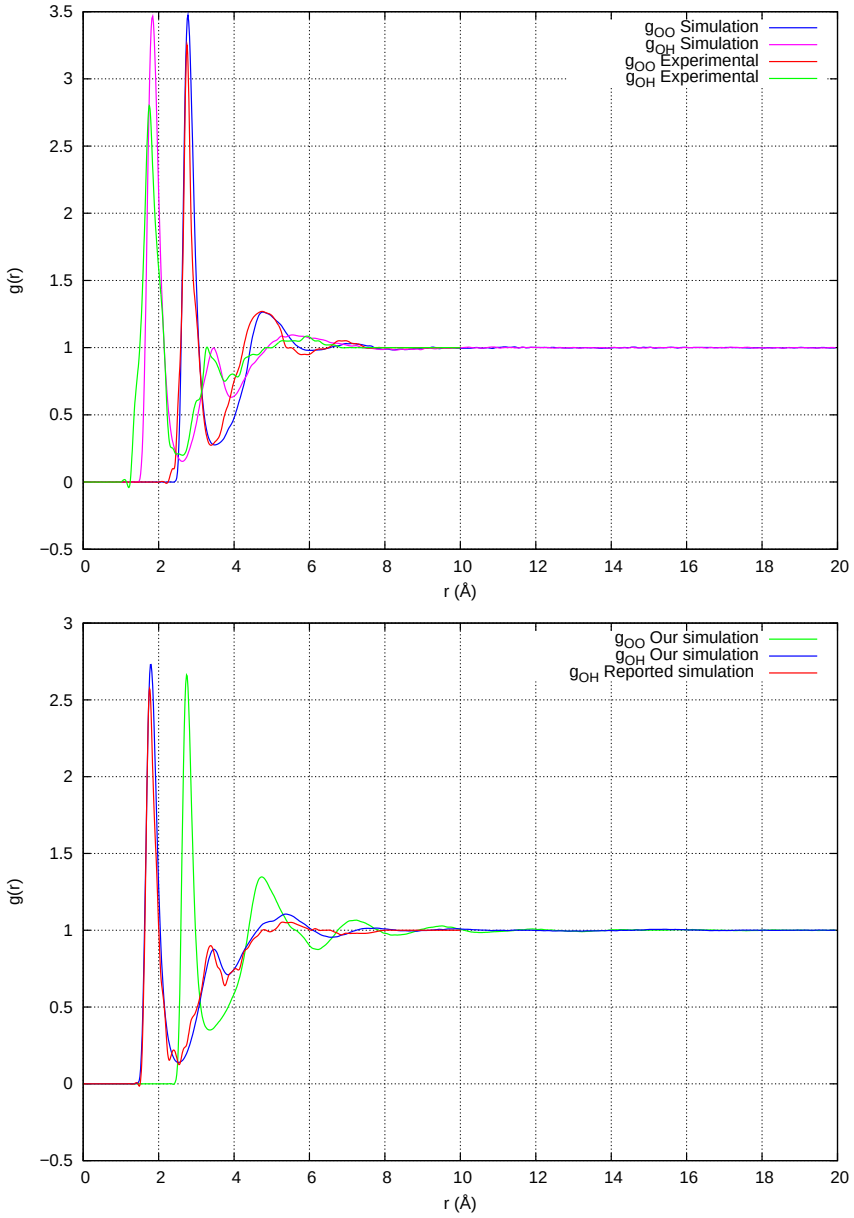

Figure 6.2: Radial Distribution Functions (RDF) for the oxygen-hydroxyl (H atom) and oxygen-oxygen site-site interactions. For methanol (upper graph) the experimental results [149] are also shown. For EG (lower graph), our results are compared with those of similar simulations by de Oliveira et al [143].

- From the cube obtained in the previous step, we cut a sphere of radius 20.0 Å for methanol and 22.0 Å for EG, including 482 and 481 molecules, respectively. In order to avoid that the molecules leaves the cluster, we have added an harmonic potential around the sphere, at a radius of 21.0 Å for methanol and 23.0 Å for EG.

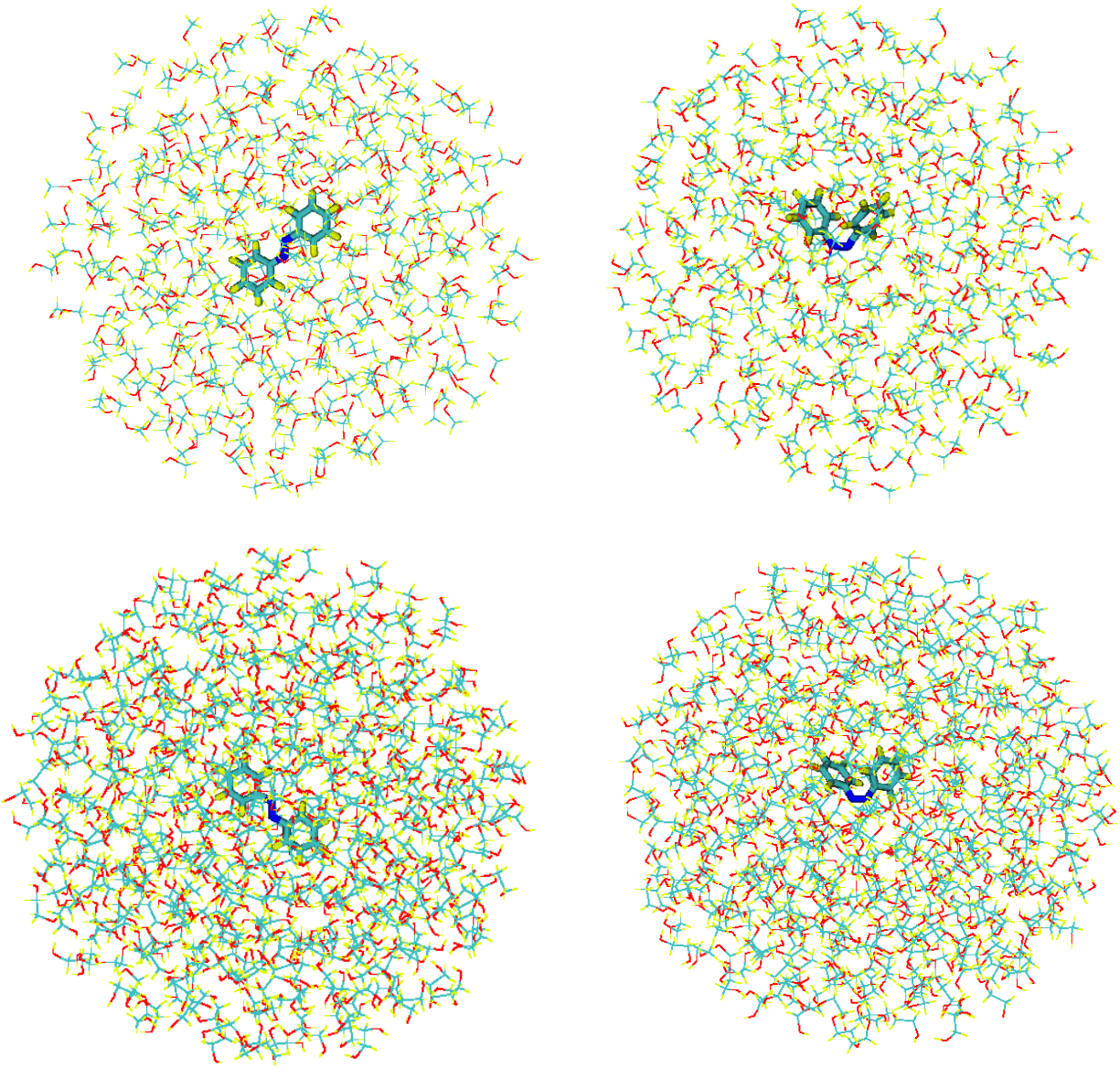

Figure 6.3: Configuration of the azobenzene+solvent systems, considering the insertion of an azobenzene molecule (both isomers) inside a solvent sphere of methanol (upper panels) and EG (lower panels).

- From the center of each sphere we take out a few solvent molecules, and we insert in the cavity an azobenzene molecule (CAB or TAB). This step is carried out by an algorithm implemented in the TINKER package [124] (see Figure 6.3).
- The azobenzene+solvent spherical clusters are equilibrated by QM/MM dynamics simulations using the MOPAC program. In a first stage, 25 ps of equilibration were performed by Brownian dynamics in the ground state. The RDFs for the distance between the azo N atoms and the hydroxyl H atoms show that there is very little

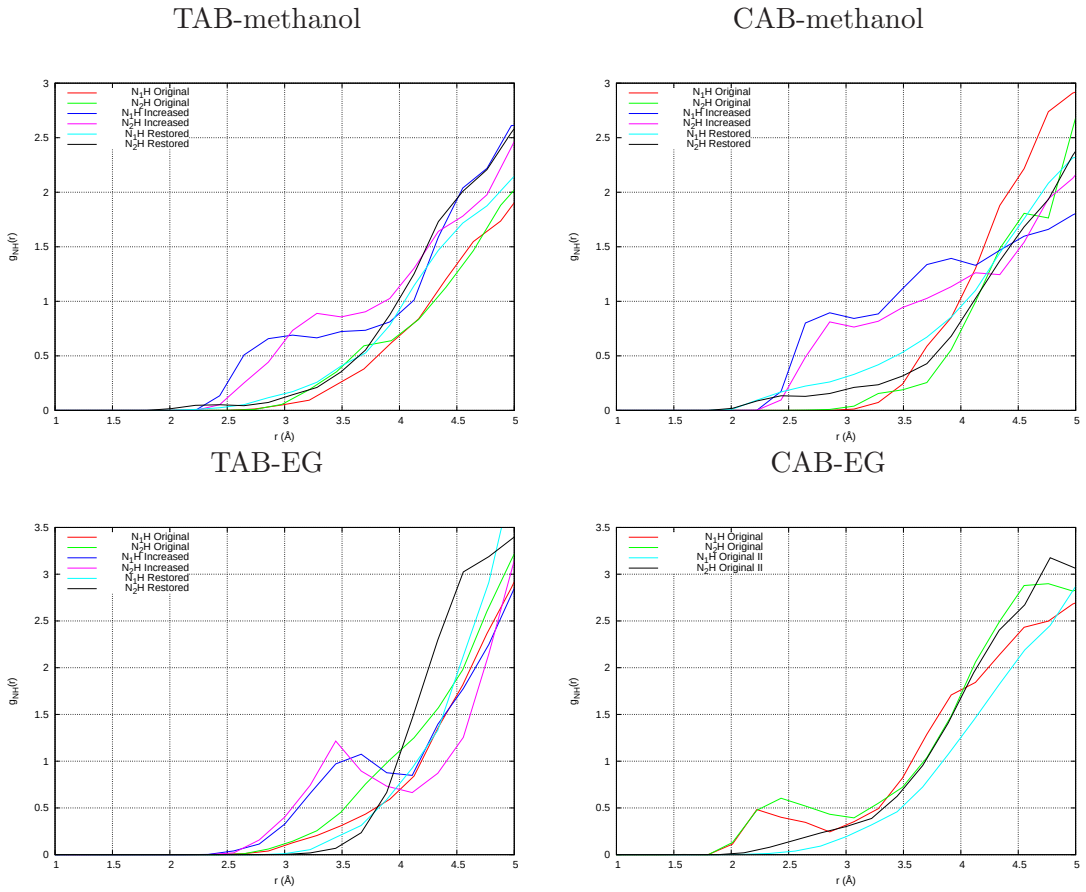

Figure 6.4: Radial Distribution Functions (RDF) for nitrogen-hydrogen site-site interactions for the azobenzene-methanol system (upper panels) and the azobenzene-EG one (lower panels). In each panel, three cases are shown: the first run, with the "original" value of the ϵ_{NH} parameter; the second run, with the "increased" value (ϵ_{NH}=1); the last run, again with the "original" or "restored" value of ϵ_{NH}.

H-bonding between azobenzene and the solvent molecules, at this stage (see Figure 6.4, where these results are labelled "original"). Only in the CAB-EG case did we find a significant peak in the RDF, at hydrogen bonding distance. We suspected that the absence of hydrogen bonding with azobenzene was due to the slowness of the rearrangement of the solvent structure. For this reason, in all cases except the CAB-EG one, we have increased the value of the ϵ_{NH} parameter from 0.0656086 (original value, obtained from the parameterization described in the Chapter 5) to 1.0000, i.e. we incremented by ∼15 times the original value. This change provokes a larger interaction between solvent and azobenzene and induces the formation of hydrogen bonds. With this change, 20 ps runs was performed, and the azo solvation peaks appeared in the RDFs (we shall label these results as "increased"). Subsequently, we reset the original ϵ_{NH} value and we executed 50 ps runs (results called "restored" in Figure 6.4). In these runs, all the solvation peaks of the RDFs vanished: both the CAB-EG one, that was present in the first 25 ps, and those artificially induced by increasing the strength of the interaction. Comparing the N···H-O and O···H-O

interactions we observe that the first one is lower than the last one: the largest N···H-O interaction energy obtained by us is that for the CAB-MeOH: 5.1 kcal (semiempirical calculation) and 4.98 kcal (ab initio calculation) vs 6.4 kcal of the O···H-O interaction in methanol. This fact could explain the preference of the solvent molecules to form hydrogen bond among them instead of with azobenzene.

- From the last run carried out in the previous step we have obtained the absorption spectra of the $n \rightarrow \pi^*$ transition of azobenzene in solution, considering both solvents (methanol and EG - Figure 6.5). We find that in solution the $\pi \rightarrow \pi^*$ band is less intense and red shifted with respect to the gas phase, especially for CAB. On the contrary, the $n \rightarrow \pi^*$ absorption is enhanced by the solvent effect, as found with other methods in Chapter 1.

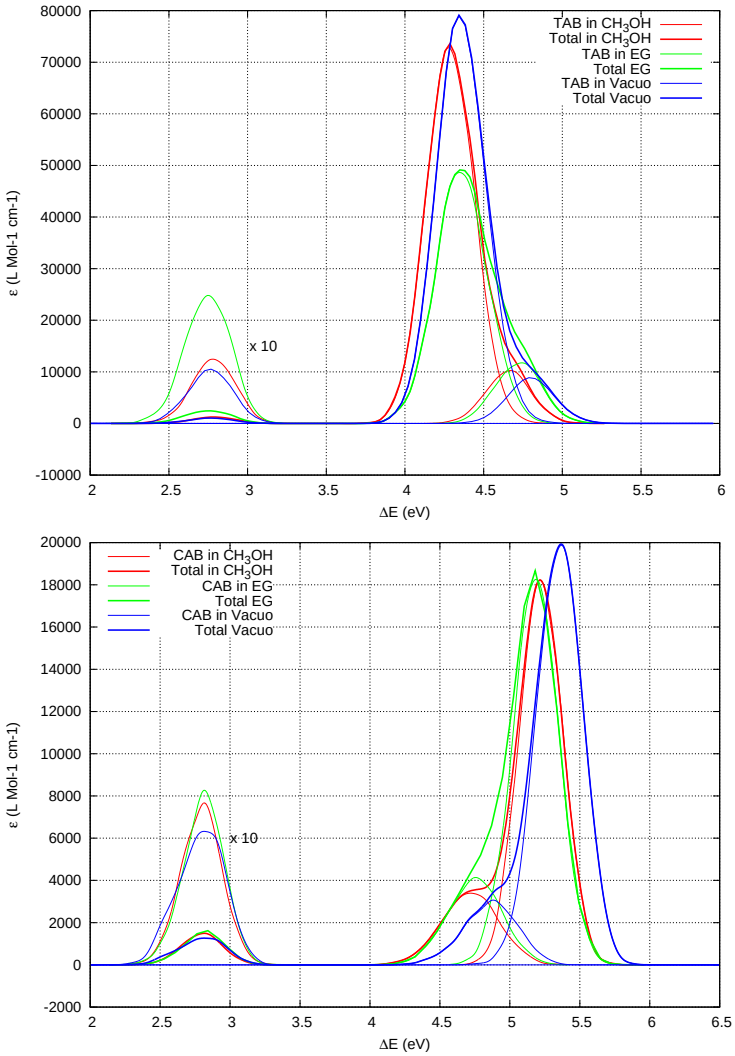

Figure 6.5: Absorption spectra of the azobenzene in vacuo and in solution (solvent=methanol and EG). TAB in the upper panel and CAB in the lower one. With thick lines we represent the total absorption, and with thin lines the contributions of each $S_0 \rightarrow S_n$ transition.

6.3 Initial and stop conditions

We have executed two simulations, for the *trans* → *cis* and *cis* → *trans* photoisomerizations, in each environment: in vacuo, in methanol and in EG. Each simulation involves about 600 trajectories). The sampling of the initial conditions is done essentially as described in section 4.4. There is a difference: the initial coordinates are sampled from the last 50 ps of Brownian dynamics in the ground state of each azobenzene-solvent cluster, instead of using the Montecarlo method. Also the nuclear momenta are taken from the Brownian trajectory, instead of being chosen independently from a Boltzmann distribution.

The transition energy interval to be used in the sampling procedure was 2.5-3.1 eV for TAB, both in vacuo and in methanol and 2.45-3.05 eV in EG, while for CAB it was 2.6-3.2 eV in vacuo and 2.5-3.1 eV in methanol and EG (see Table 6.2). In fact, the average excitation energies we obtain are 2.76 eV and 2.80 eV for TAB and for CAB, respectively, in vacuo; 2.79 eV for both isomers, in methanol; 2.74 eV and 2.80 eV, in EG. The reference squared transition dipole μ^2_{ref} has been chosen so that most trajectories start from different phase space points, as in section 4.4.

Table 6.2: Sampling of the initial conditions for the simulation of the photodynamics in vacuo, in methanol or in ethylene glycol. $n \rightarrow \pi^*$ excitation band, CI space of 94 determinants. $N_{geo}(n)$ is the number of Brownian geometries from which n trajectories were launched (n=0,1,2 or more).

Solvent	Vacuo		Methanol		EG	
Starting isomer	TAB	CAB	TAB	CAB	TAB	CAB
ΔE, eV	2.8	2.85	2.8	2.8	2.75	2.8
$\Delta\Delta E$, eV	0.6	0.6	0.6	0.6	0.6	0.6
μ^2_{ref}, a.u.	0.35	0.45	0.35	0.45	0.70	0.45
Number of sampled geometries $= \sum_n N_{geo}(n)$	1000	995	948	965	993	990
Number of trajectories, $N_T = \sum_n nN_{geo}(n)$	583	576	600	608	625	640
$N_{geo}(0)$	558	379	497	348	438	336
$N_{geo}(1)$	279	554	280	552	430	554
$N_{geo}(2)$	101	11	90	28	85	40
$N_{geo}(3) + N_{geo}(4) + N_{geo}(5) + \ldots$	31	0	42	0	8	2

As we have mentioned at the beginning of this Chapter, new stop conditions were applied with respect to the previous simulations. There are three necessary conditions to stop a trajectory, concerning respectively the electronic states, the molecular geometry and the time elapsed from the excitation. The molecule must be in the ground electronic state and its geometry must be sufficiently similar to that of a stable isomer: namely, the CNNC angle must be within ±5° of the values 0° for CAB and 180° for TAB, and both NNC angles must not exceed 150°.

Moreover, a trajectory is not stopped before a minimum time, that depends both on the starting isomer and on the final one. We have imposed this additional condition

because a previous investigation on the photodynamics of an azobenzene derivative [74] showed that a significant number of trajectories, after approaching the CAB equilibrium geometry in the ground state, can isomerize again to TAB. This hot ground state reaction is more likely in the $cis \rightarrow trans$ direction than in the $trans \rightarrow cis$ one, because CAB is less stable than TAB, and it is favoured by applying a pulling force tending to elongate the azobenzene moiety, which is a way to further destabilize the CAB isomer [74]. The process is made possible because of the large amount of vibrational energy that is available after the conversion to the ground state, in the modes that can lead to isomerization (mainly torsion of the N=N double bond and N-inversion). This condition only lasts for few picoseconds, because of the redistribution of the vibrational energy to other internal modes and, in condensed phase, to its transfer to the solvent. In fact, our previous simulations showed that the hot ground state reaction almost exclusively occurs during the first 1-2 picoseconds. Therefore, when the reactant is TAB, the minimum time is 1.0 ps if the final geometry is TAB (non reactive trajectory) and 2.5 ps for CAB (reactive trajectories). Starting from CAB, since the excited state decay and the photoisomerization dynamics are much faster, the minimum time is 1.0 ps for trajectories ending at TAB and 1.5 ps for those ending at CAB.

Moreover, in the particular case of the dynamics simulations of azobenzene in EG we have carried out calculations with a half of the trajectories with a maximum duration of the dynamics of 5 ps (Δt=0.1 fs), as in the other cases. However, we have observed that much of these trajectories stoped in the excited state and did not finished the dynamics. Then, we increased the maximum time to 15 ps (with the same Δt) for the other half of trajectories, in order to permit them to have time to continue their dynamics.

6.4 Quantum yields and mechanism

The results of the simulations for the three cases, in vacuo, in methanol and in EG, are presented in Tables 6.3 and 6.4 and in Figures from 6.6 to 6.11. We first observe that the small differences in the PES obtained with 82 or 94 determinants in the CI space have little effect on the dynamics: quantum yields and decay times for the isolated molecule remain practically the same. Therefore, it makes sense to compare the results obtained with the Brownian dynamics (82 determinant CI and no minimum time in the stop conditions) with those of the QM/MM simulations (94 determinant CI and more demanding stop conditions).

As we have seen, the new stop conditions impose a minimum time, besides more stringent requirements on the final geometry. Of course, they have no effect on the computed properties, with the exception of the quantum yields. Actually, very few trajectories go back to the starting isomer, and only in the isolated molecule simulations (see Figure 6.6). When TAB is excited, the trajectories that reach a cisoid geometry and then go back to TAB are only 3, that corresponds to a decrease of $\Phi_{trans \rightarrow cis}$ of 0.005. The trajectories that go from CAB to TAB and viceversa are 27, so $\Phi_{cis \rightarrow trans}$ is lowered by 0.047. The effect of such back-isomerizations is already included in the results of Table 6.3. The backward reaction cannot always be simply classified as a hot ground state process, because in some cases a short passage in the S_1 excited state occurs (see Figure 6.6). In our previous work on a derivative of azobenzene with two ethyl substituents in the $4, 4'$ positions [74], we found a more frequent occurrence of the back-isomerization, which decreases $\Phi_{trans \rightarrow cis}$ of 0.054, possibly due to kinematic effects (different distribution of masses). When a solvent is present, no back-isomerization is observed: apparently the

transfer of vibrational energy to the solvent is efficient enough to suppress this process.

Table 6.3: Quantum yields obtained in the simulations for the $trans \rightarrow cis$ and $cis \rightarrow trans$ processes, with $n \rightarrow \pi^*$ excitation. Previous simulations (see chapter 4): solvent effects represented by Brownian dynamics and CI space of 82 determinants. New simulations: explicit representation of the solvent and CI space of 94 determinants. Viscosity η in mPa·s.

	$\Phi_{trans \rightarrow cis}$	$\Phi_{cis \rightarrow trans}$
previous simulation, in vacuo	0.34±0.02	0.60±0.02
previous simulation, $\eta \approx 1$	0.34±0.02	0.60±0.02
previous simulation, $\eta \approx 10$	0.17±0.02	0.54±0.02
new simulation, in vacuo	0.33±0.02	0.57±0.02
new simulation, methanol, $\eta = 0.54$	0.27±0.02	0.58±0.02
new simulation, EG, $\eta = 16.1$	0.40±0.03	0.49±0.02
experimental, methanol, $\eta = 0.54$ [45, 50]	0.20-0.28	0.57-0.63
experimental, glycerol, $\eta = 934$ [44]	0.42	0.53

The computed quantum yields for the $trans \rightarrow cis$ and $cis \rightarrow trans$ reactions decrease slightly from the gas phase to the methanol solution, and in the latter case they compare very well with the experimental data obtained with exciting wavelengths between 405 and 436 nm [45, 50]. In EG, the computed $\Phi_{trans \rightarrow cis}$ is higher than in methanol, while $\Phi_{cis \rightarrow trans}$ undergoes a further decrease. These trends are again in agreement with the quantum yields measured in glycerol, which is much more viscous than EG [44]. The most striking difference with respect to the Brownian dynamics results concerns the $trans \rightarrow cis$ photoisomerization in a viscous solvent ($\eta \approx 10$ mPa·s), that should be comparable with EG ($\eta = 16.1$ mPa·s). The Brownian solvent hinders the photoisomerization quite effectively, while EG, when explicitly introduced in the QM/MM simulation, is less effective than methanol.

Our explanation of such results points mainly to the competition between the decay of the S_1 excited state and the isomerization reaction. The decay of S_1 occurs when the molecule can approach the $S_0 - S_1$ crossing, along the torsional coordinate (CNNC), possibly with the help of a symmetric opening of the NNC angles. Figure 6.9, that refers to TAB excitation, shows that the first $S_1 \rightarrow S_0$ surface hopping mainly occurs when the CNNC angle has covered most of the way from 180° to 90° (half-way to CAB). Hopping at CNNC angles in the 140° to 160° range is favoured by a the opening of the NNC angles, but very few hops can take place close to the starting CNNC angle of 180° (the viscous Brownian solvent is an exception to be discussed later on). As shown in figures 6.7 and 6.8, the isomerization follows essentially the torsional pathway, with the assistance of a simultaneous twist around the N-C bonds (see section 4.6). The NNC angles undergo a symmetric vibration, that goes on roughly until the CNNC angle has rotated by 90°. Since CAB rotates much faster than TAB, only the latter does show a well defined sequence of NNC bending oscillations. In fact, by means of resonant Raman spectroscopy Stuart et al [150] observed the NNC bending in TAB, whereas in CAB the most evident motion is the CNNC torsion.

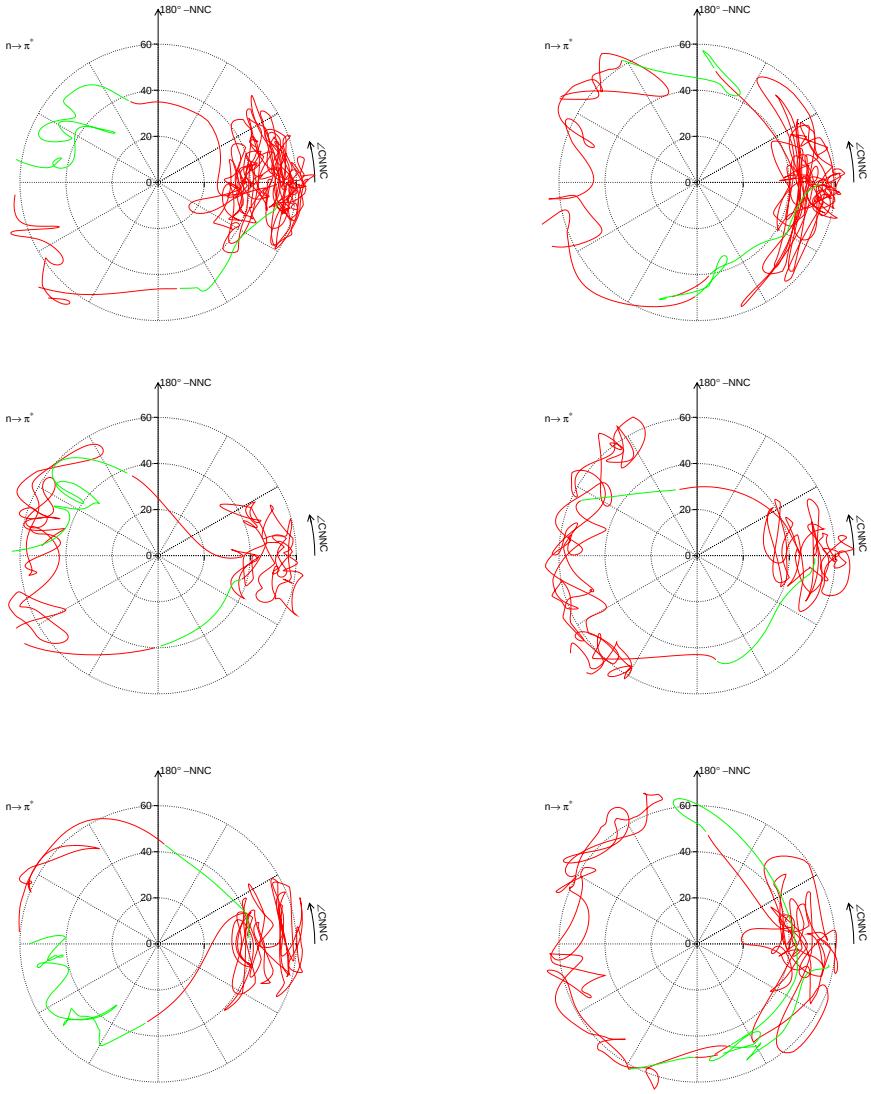

Figure 6.6: Some examples of trajectories that return to the initial isomeric conformation, starting from the TAB (left panels) and from the CAB (right panels), in the case of $n \rightarrow \pi^*$ excitation in vacuo.

The presence of a solvent slows down the torsion, and this effect is correlated with the solvent viscosity and is more pronounced for TAB than for CAB, as found both with the Brownian dynamics and with the explicit solvents. If the TAB molecule is trapped at a nearly planar geometry for a time of the order of one ps or more, as it may happen in the cage formed by ethylene glycol, the loss of vibrational energy to the solvent makes it difficult to reach the crossing seam. Moreover, smaller nuclear velocities also imply smaller nonadiabatic couplings, therefore both the nuclear kinetic energy and the energy gap $\Delta E(S_1 - S_0)$ at the time of the first surface hopping are smaller in EG than in vacuo or in methanol (see Figure 6.10). Therefore, when the torsion in EG eventually takes place, the transition to S_0 can only occur near the equilibrium geometry of S_1, that coincides

with the minimum of the crossing seam, at CNNC$\simeq 95°$. The suppression of the "early decay" at CNNC angles closer to 180° shifts the balance towards the isomerization and increases the quantum yield. This does not occur when starting from CAB, because of the larger slope of the S_1 PES and of the much faster dynamics.

As already noted, the Brownian dynamics fails to reproduce the behaviour found in EG. Although a true caging is not to be expected in this case, the torsional motion is substantially slowed down, as already noted in section 4.5.2. In figures 6.9 and 6.10 we see that many "early hops" occur in this case, without the assistance of the NNC symmetric bending and far from the crossing seam, i.e. with a large $\Delta E(S_1 - S_0)$. In order to hop at a geometry where the energy gap is large, a strong coupling is needed. The nonadiabatic couplings are the scalar products of the derivative matrix elements times the nuclear velocity vector. In the case of Brownian dynamics, the nuclear velocities are suddenly modified by the the random force $X_\alpha(t)$ of eq. (4.21), that keeps the kinetic energy at its Boltzmann average value against the effect of friction. With high viscosities, the application of the random force can produce large velocities that are rapidly damped because of the friction. With a friction coefficient γ and the time interval Δt between two successive applications of the random force, the damping factor of the velocity is $F = exp(-\gamma \Delta t)$ (in our case, $\Delta t = 1$ fs). As we see in figure 6.10, the surface hops with large $\Delta E(S_1 - S_0)$ are possible when also the nuclear kinetic energy is large. The occurrence of such "early hops" lowers the computed quantum yield and is an artifact of the Brownian dynamics with large friction coefficients, such that $F \ll 1$.

Table 6.4: Decay times of the S_1 excited state, obtained by a fit of the populations $\Pi_k(t)$ with the biexponential form $w_1 exp(-t/\tau_1) + (1 - w_1) exp(-t/\tau_2)$. $n \rightarrow \pi^*$ excitation. Previous simulations (see chapter 4): solvent effects represented by Brownian dynamics and CI space of 82 determinants. New simulations: explicit representation of the solvent and CI space of 94 determinants. Viscosity η in mPa·s.

	$n \rightarrow \pi^*$ transition S_1 lifetimes		
	w_1	τ_1 (fs)	τ_2 (fs)
TAB isomer, previous simulation, in vacuo	1.00	197	-
TAB isomer, previous simulation, $\eta \approx 1$	1.00	488	-
TAB isomer, previous simulation, $\eta \approx 10$	1.00	2078	-
TAB isomer, new simulation, in vacuo	1.00	120	317
TAB isomer, new simulation, methanol, $\eta = 0.54$	0.49	188	790
TAB isomer, new simulation, EG, $\eta = 16.1$	0.25	450	3021
CAB isomer, previous simulation, in vacuo	0.66	20	51
CAB isomer, previous simulation, $\eta \approx 1$	0.60	54	21
CAB isomer, previous simulation, $\eta \approx 10$	0.35	30	99
CAB isomer, new simulation, in vacuo	1.00	40	-
CAB isomer, new simulation, methanol, $\eta = 0.54$	1.00	28	-
CAB isomer, new simulation, EG, $\eta = 16.1$	1.00	94	-

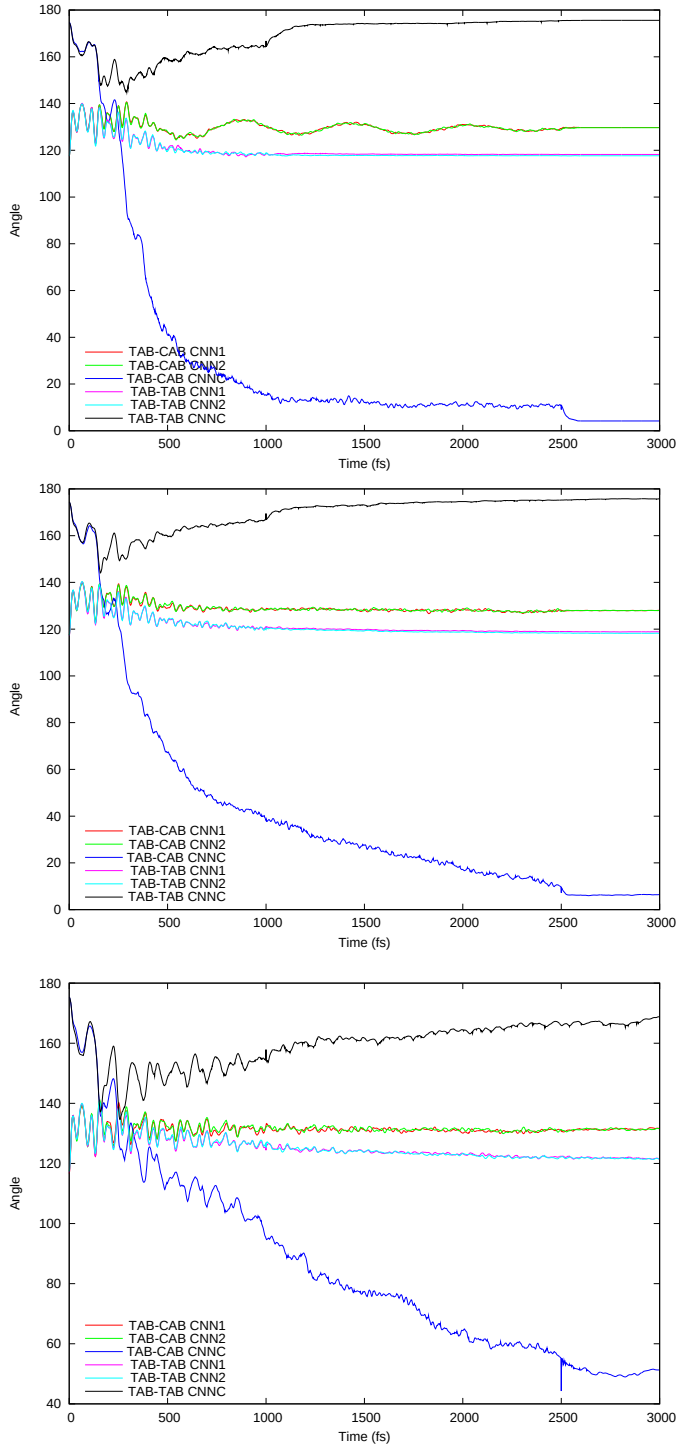

Figure 6.7: Time evolution of the angles CNNC, NNC_1 and NNC_2, averaged over the reactive and unreactive trajectories, in the case of $n \rightarrow \pi^*$ excitation of TAB and considering three cases: in vacuo and in the two solvents: methanol and ethylene glycol (upper, medium and lower panel, respectively).

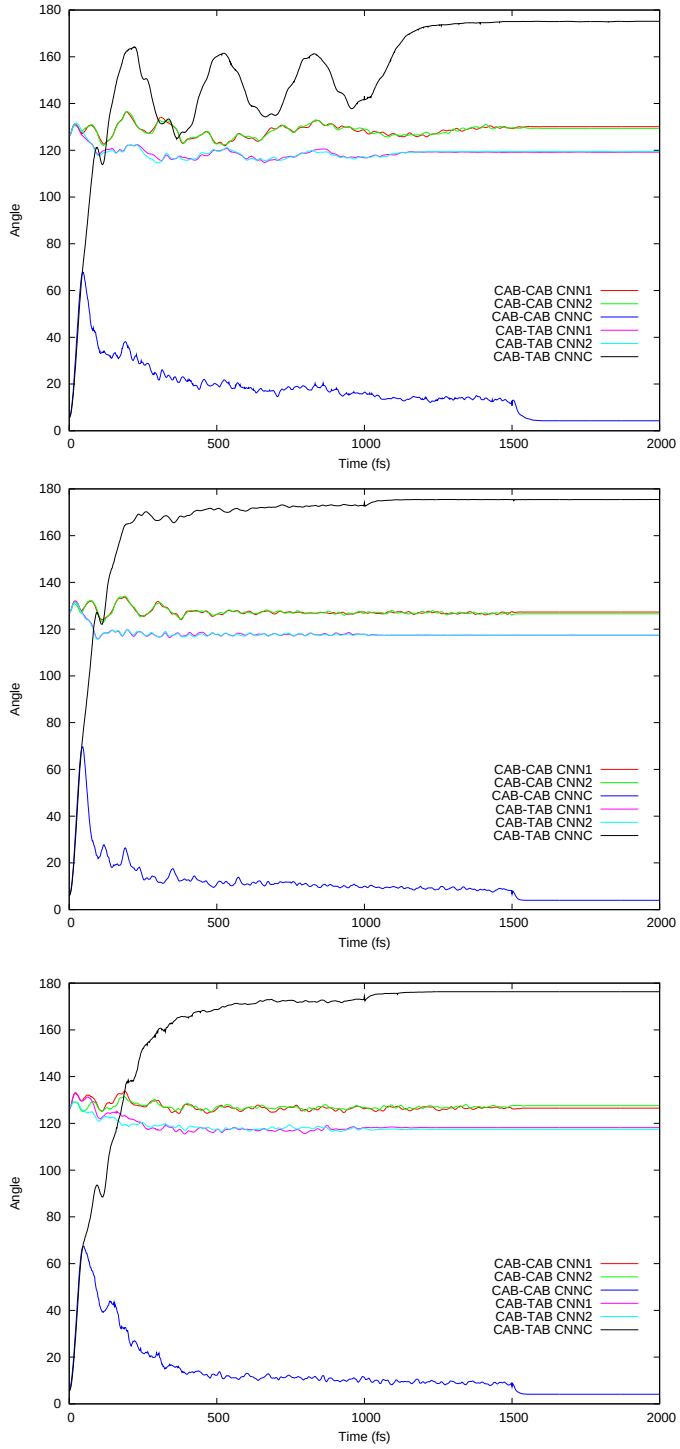

Figure 6.8: Time evolution of the angles CNNC, NNC_1 and NNC_2, averaged over the reactive and unreactive trajectories, in the case of $n \rightarrow \pi^*$ excitation of CAB and considering three cases: in vacuo and in the two solvents: methanol and ethylene glycol (upper, medium and lower panel, respectively).

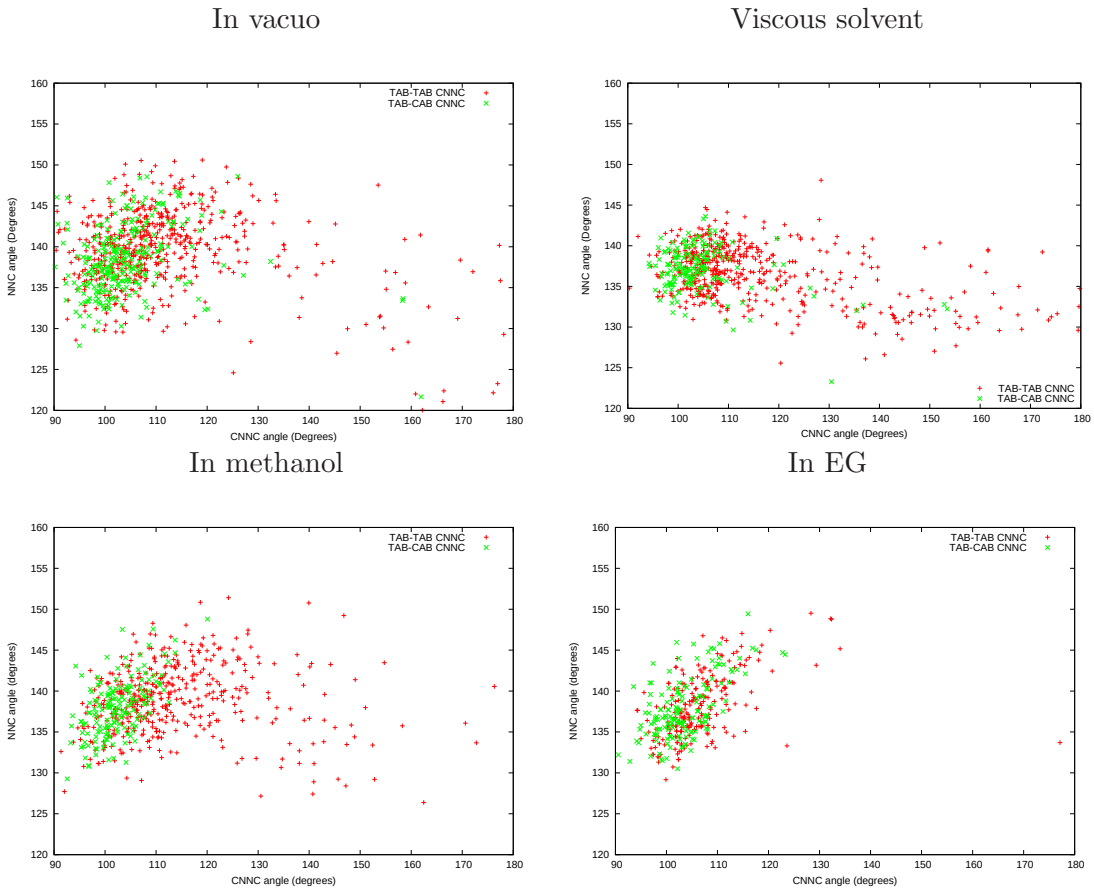

Figure 6.9: CNNC vs averaged NNC angles at the hopping step, for the reactive and unreactive trajectories, in the case of $n \rightarrow \pi^*$ excitation of TAB and considering four cases: in vacuo, in a viscous solvent, in methanol and in ethylene glycol.

The decay of the S_1 population for the isolated molecule is well fitted by a single exponential, as in our previous simulations [21, 56]. It is worth mentioning that the only time-resolved spectroscopy experiment performed up to now in gas phase on *trans*-azobenzene [8] also yields a single exponential decay (however, the excitation band was here the $\pi \rightarrow \pi^*$ one). The excited state decay is slowed down in methanol and much more in EG, in the same way as the CNNC torsional motion (see Figure 6.11 and Table 6.4). The decay becomes biexponential, in agreement with several experimental observations [3,4,19,62]. The fast component is 0.19 ps in methanol and 0.45 in EG, while the slow one is 0.8 ps and 3 ps in the two solvents, respectively. The results obtained in EG match the fluorescence decay times obtained by Diau and coworkers [6], for the two components that do not exhibit depolarization. The Brownian dynamics simulations fail to produce a biexponential decay, but do yield longer lifetimes than in vacuo.

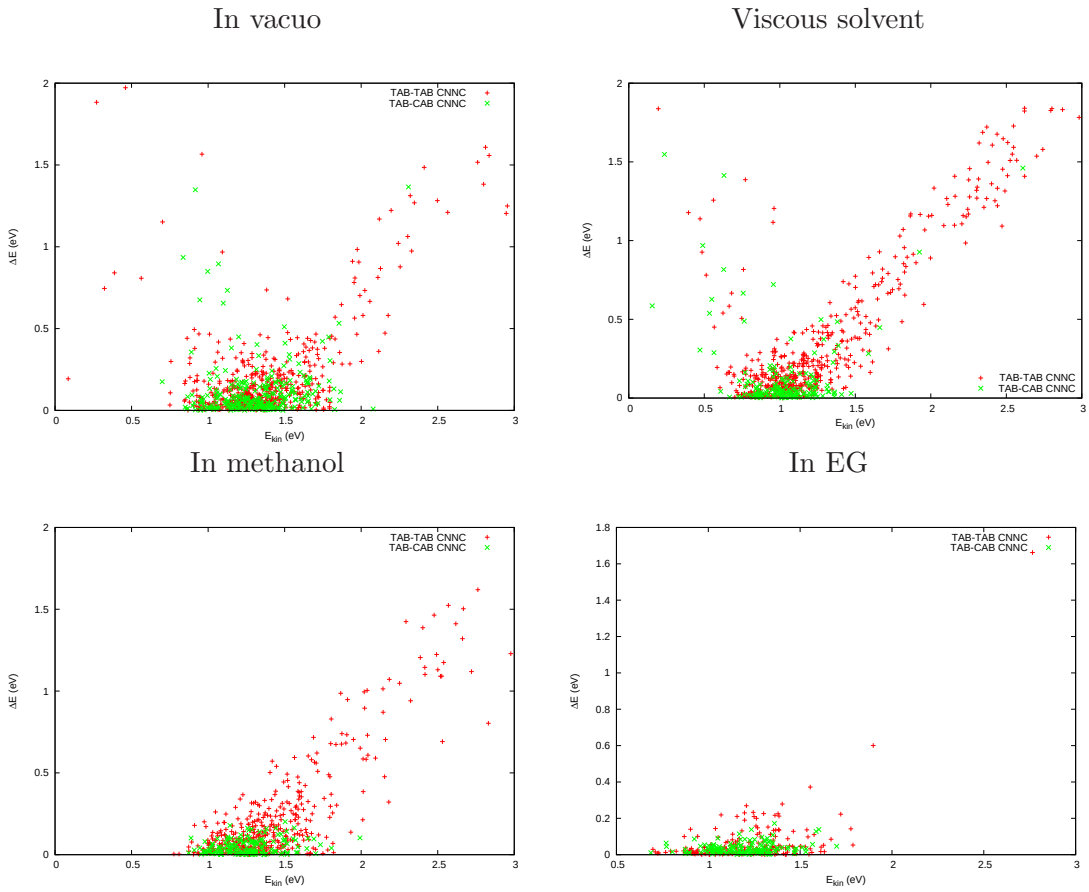

Figure 6.10: Kinetic energy vs $S_1 - S_0$ transition energy difference at the hopping step, for the reactive and unreactive trajectories, in the case of $n \rightarrow \pi^*$ excitation of TAB and considering four cases: in vacuo, in a viscous solvent, in methanol and in ethylene glycol.

6.5 The decay of the fluorescence and of its anisotropy.

The simulations also provide the $\Delta U_{kl} = U_l - U_k$ energy gaps and the associated transition dipole vectors μ_{kl} as functions of time, during the evolution of each trajectory in the excited PES. From these data we can compute the time-resolved fluorescence spectra, or the time-dependent fluorescence intensities observed at different wavelengths (two ways to represent essentially the same information). With the same data, we can also compute the time-dependent fluorescence anisotropy, thus having a complete reproduction of the experimental results by Diau's group and other authors [5, 6, 19, 61, 62, 150].

The rate of photon emission, averaged over all trajectories, is

$$I_{tot}(t) = \frac{4}{3N_T\hbar^4c^3}\sum_j \left[\sum_{l=0}^{k-1} \Delta U_{kl}^3 \mu_{kl}^2\right]^{(j)} \tag{6.1}$$

Here N_T is the total number of trajectories and k is the current state for the trajectory j, chosen according to the surface hopping algorithm. When exciting to S_1, the trajectories very seldom hop to higher states, so the fluorescence is almost exclusively due to the

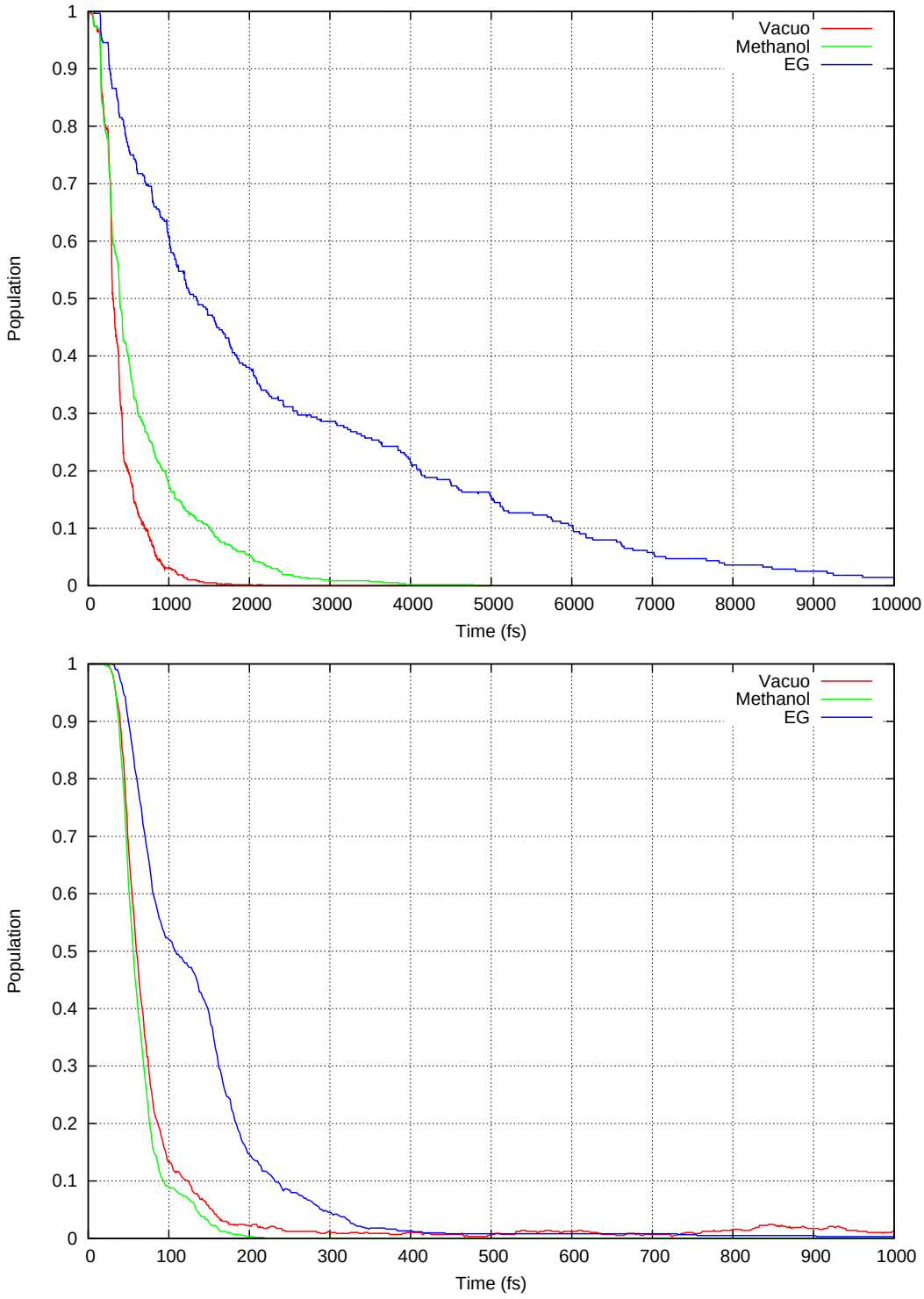

Figure 6.11: Time evolution of the population of the first excited state S_1, in the case of $n \rightarrow \pi^*$ excitation, starting from the TAB isomer (upper panel) and CAB isomer (lower panel), and considering three cases: in vacuo and in the two solvents: methanol and ethylene glycol.

$S_1 \rightarrow S_0$ transition. If we limit the sum (6.1) to energy differences contained in a small interval ($h\nu - \delta\nu < \Delta U_{kl} < h\nu + \delta\nu$), and we divide by $2\delta\nu$, we obtain the time dependent emission spectrum $I_{fr}(\nu, t)$. The spectrum can be expressed also as a function of wavelength. If ν is given in cm^{-1} and λ in nm, we have:

$$I_{wl}(\lambda, t) = \frac{10^7}{\lambda^2} I_{fr}(\nu, t) \tag{6.2}$$

The corresponding steady state spectra are obtained by integrating over time. For instance:

$$I_{wl}(\lambda) = \int_0^\infty I_{wl}(\lambda, t) dt \tag{6.3}$$

The analogous integral of $I_{tot}(t)$ is the fluorescence quantum yield:

$$\Phi_F = \int_0^\infty I_{tot}(t) dt \tag{6.4}$$

Notice that Φ_F is very small (see Table 6.5), which means the related transitions do not influence the overall dynamics appreciably. This is why we can compute the fluorescence transients "a posteriori", having neglected the fluorescence itself in the formulation of the nonadiabatic dynamics.

The computed steady state fluorescence is in semi-quantitative agreement with the experimental findings by Satzger et al [62], that operated in DMSO with the excitation wavelength $\lambda_{exc} = 488$, and by Stuart et al [150] in ethanol, with $\lambda_{exc} = 458$ nm (see Table 6.5 and Figure 6.12). We note that recording the very weak fluorescence of azobenzene is not easy and entails some operations that may give place to rather large errors, such as the substraction of the solvent background and, in the case of CAB, of the residual TAB contribution. This may explain part of the differences between the results of the two sets of experiments. The TAB and CAB spectra exhibit different features, that are well reproduced by our simulations and can be attributed to the shorter lifetime of CAB (Table 6.4). First of all the CAB quantum yield Φ_F is smaller, which makes its measurement even more uncertain. The factor of the Φ_F's is largest in EG, where also the computed lifetime of TAB is greatly increased. Secondly, the emission band of TAB features a substantial queue in the near IR, that is almost absent in CAB, because during the lifetime of TAB a larger degree of vibrational relaxation can take place. Also the Stokes shift, taken as the difference between the λ of maximum absorption and maximum emission, is larger for TAB than for CAB. The maximum emission wavelength λ_{max} also depends on the excitation wavelength λ_{exc}, as can be seen by comparing the two sets of experimental results, although other factors have probably contributed to the large discrepancy in the λ_{max} values. The λ_{max} used by both groups is on the long wavelength side of the absorption band, while the initial conditions do average over the whole band. Partly because of this, we get in all cases a shorter λ_{max}. Figure 6.12 shows the effect of the initial excitation energy. Taking as reference the average excitation energy ΔE, we computed the fluorescence spectra for the trajectories starting with ΔE in the upper or in the lower range. For TAB, this amounts to exciting with wavelengths centered at 433 nm (upper range) or 466 nm (lower range), and the corresponding emission maxima are at $\lambda_{max} = 669$ nm and 691 nm, respectively. For CAB, the same procedure yields the central λ_{exc} values of 427 nm and 462 nm, from which $\lambda_{max} = 440$ nm and 465 nm. The effect of the excitation wavelength is larger for CAB, again because of its shorter lifetime.

Table 6.5: Fluorescence quantum yields Φ_F and wavelengths of maximum intensity, λ_{max}.

	TAB		CAB	
	$\Phi_F \cdot 10^6$	λ_{max}, nm	$\Phi_F \cdot 10^6$	λ_{max}, nm
computed in vacuo	1.04	647	0.19	458
computed in methanol	1.74	669	0.18	458
computed in EG	9.56	742	0.26	458
exp. in DMSO, $\lambda_{exc} = 488$ nm [62]	3.2	640	0.5	600
exp. in ethanol, $\lambda_{exc} = 458$ nm [150]	11	530	1	520

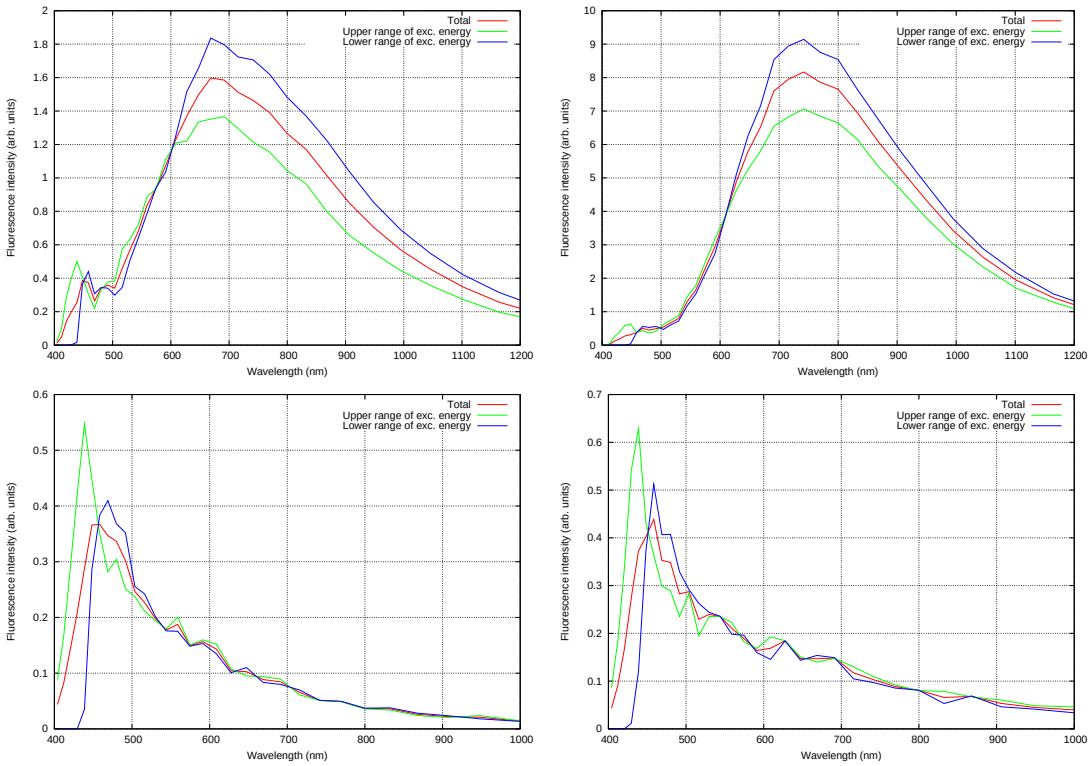

Figure 6.12: Steady state fluorescence spectra for TAB (upper panels) and CAB (lower panels) in methanol (left) and EG (right).

Figure 6.13 shows the computed time dependent fluorescence $I_{tot}(t)$ of TAB in methanol and in EG. The fast oscillation in the fluorescence intensity have a period of about 45 fs, i.e. a frequency of $\sim$750 cm^{-1}, the same as the symmetric NNC bending vibration (see Figure 6.7). Such oscillations cannot be observed in the experiments by Diau's group, because their excitation and detection pulses have a duration of about 100 fs. In the fitting of their data they use a gaussian convolution with a FWHM of 200 fs (slightly dependent on the emission wavelength [6, 19]). To compare with their transient

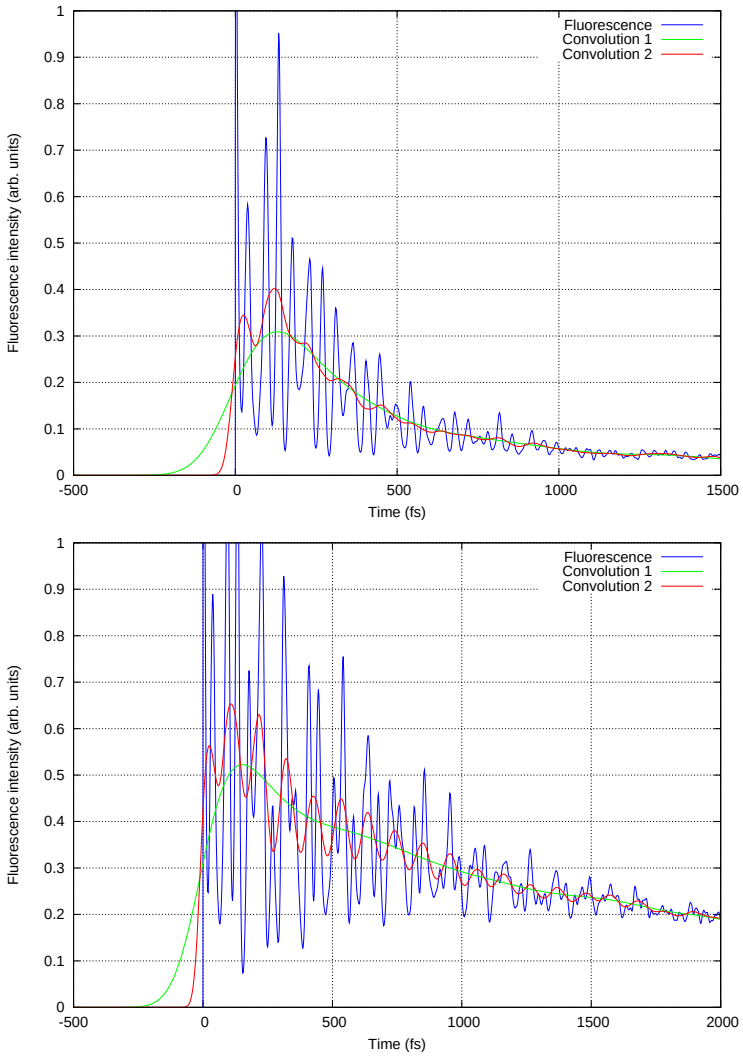

Figure 6.13: Fluorescence transient spectra of TAB in methanol and EG.

signals, we define a convoluted fluorescence intensity:

$$I_{tot,conv}(t) = \int_{-\infty}^{+\infty} I_{tot}(t-t')e^{-(t'/\tau)^2}dt' \tag{6.5}$$

where $I_{tot}(t-t')$ vanishes for $t-t'<0$. The gaussian width is related to the FWHM by FWHM$= 2\sqrt{ln2}\tau$. The convoluted signal with FWHM=200 fs, also shown in Figure 6.13, is very similar to those obtained by Diau's group (see Figure 1.3): no oscillations, a fast rise and a smooth decay of the fluorescence. We have also tried smaller gaussian widths, to show what could be observed with a better time resolution. In Figure 6.13 we also report the convoluted fluorescence with FWHM=50 fs. In this case the fast oscillations are still absent, but a slower and less pronounced oscillatory background is evidenced. This may be due to some other skeletal deformation, for instance concerning the NCC angles that define the relative orientation of the phenyl and azo groups.

Diau and coworkers not only measured the fluorescence intensity, but also the components $I_{\parallel}$ and $I_{\perp}$ with parallel and perpendicular polarization with respect to the exciting light. While the total intensity is $I_{\parallel} + 2I_{\perp}$, the ratio

$$R = \frac{I_{\parallel} - I_{\perp}}{I_{\parallel} + 2I_{\perp}} \tag{6.6}$$

is the fluorescence anisotropy. To compute the time-dependent fluorescence anisotropy and compare it with the experimental data, we consider for each trajectory the angle $\beta(t)$ between the $S_0 - S_1$ transition dipole at time $t = 0$ and the same vector at time t (more generally, the dipole vector for the absorption transition and the dipole vector for any transition contributing to the emission). The total parallel intensity is then

$$I_{\parallel,tot}(t) = \frac{4}{15N_T\hbar^4c^3} \sum_j \left[\sum_{l=0}^{k-1} \Delta U_{kl}^3 \mu_{kl}^2 (1 + 2cos^2\beta) \right]^{(j)} \tag{6.7}$$

and the perpendicular one is

$$I_{\perp,tot}(t) = \frac{4}{15N_T\hbar^4c^3} \sum_j \left[\sum_{l=0}^{k-1} \Delta U_{kl}^3 \mu_{kl}^2 (2 - cos^2\beta) \right]^{(j)} \tag{6.8}$$

Analogous equations hold for the frequency or wavelength dependent components, $I_{\parallel,fr}(\nu,t)$, $I_{\perp,fr}(\nu,t)$, $I_{\parallel,wl}(\lambda,t)$, and $I_{\perp,wl}(\lambda,t)$. From these quantities one obtains the related anisotropies R_{tot}, R_ν and R_λ.

In Figure 6.14 we show the total fluorescence of TAB and its $I_{\parallel,tot}(t)$ and $I_{\perp,tot}(t)$ components, after gaussian convolution with FWHM=200 fs. It will be noticed that, except for very short times, the decay of the total fluorescence is quite parallel to that of the S_1 population. The fluorescence anisotropy is plotted in the same figures without convolution, to show that it is not affected by the fast vibrations. At $t = 0$ the anisotropy has the maximum theoretical value of 2/5, and it decays much more slowly than the fluorescence intensity, especially in ethylene glycol, in good agreement with the measurements by Diau's group. They found that their data could be fitted by a two- or three-exponential decay, with gaussian convolution. One or two fast components of the decay of intensity are not associated with the depolarization, while the slow component entails a decay of both intensity and anisotropy with the same time constant τ_3 and weight W_3. The variable component of the anisotropy however does not vanish at the $t \to \infty$ limit, but converges to an asymptotic value R_∞. This is the expected behaviour if the depolarization is due to an internal motion rather than to the overall molecular rotation. In order to compare quantitatively our results to the experimental ones, we have fitted our intensity and anisotropy data essentially with the same formulas as in ref. [6]:

$$I_{tot}(t) = I_{tot}(0) \sum_i = 1,3 W_i e^{-t/\tau_i} \tag{6.9}$$

$$R_{tot}(t) = \frac{2}{5} + W_3 \left(\frac{2}{5} - R_\infty \right) e^{-t/\tau_3} \tag{6.10}$$

and similarly for the λ dependent quantities. Here τ_1 and τ_2 are the short lifetimes (not related to the depolarization), with their weights W_1 and W_2. In ref. [6] the experimental

data are fitted by varying the lifetimes and weights (with the constraint $W_1+W_2+W_3 = 1$), as well as three anisotropy parameters and the convolution FWHM. In fact, they find that the optimal FWHM is close to 200 fs in all cases, so we have assumed this value everywhere. Two of the anisotropy parameters (the third one being R_∞) can be assimilated to the initial anisotropy, and turn out to be about 2/5, so we have directly replaced them with this value in eq. (6.10).

Of course, the unconvoluted fluorescence intensities obtained by our simulations (see Figure 6.13) cannot be likened to a simple sum of three exponentials, but the gaussian convolutions of the two functions (Figures 1.3 and 6.14) are much more similar. Therefore, we compute the mean squared differences (MSD) between the gaussian convolutions (with FWHM=200 fs) of the simulations results for $I_{tot}(t)$ or $I_{wl}(\lambda, t)$, and of their counterparts given by eq. (6.9). The same is done for R_{tot} or $R_{wl}(\lambda, t)$, but here the FWHM is 40 fs: in fact, it is not strictly necessary to submit the anisotropy to a convolution, but this operation smooths away the noise in the simulation data and simplifies their numerical treatment. The MSD is minimized by varying the parameters. Since our aim is not to obtain the best fit, but rather to show that our data are compatible with the experimental findings, we shall adopt constant values for some parameters, choosing values close to those found in ref. [6]. The constant values are indicated with stars in Table 6.6.

We carried out several fits, both for the total fluorescence quantities $I_{tot}(t)$ and R_{tot}, for the emission wavelength dependent quantities $I_{wl}(\lambda, t)$ and $R_{wl}(\lambda, t)$, and, in the case of ethylene glycol, for selected intervals of the excitation wavelength (see Table 6.6). In vacuo, the fluorescence anisotropy decays in a non-exponential way, its deviation from the initial value of 2/5 increasing more than linearly with time. This may be expected from a free, rather than diffusional, motion (we remind that the anisotropy depends on the cosine of the angle by which the transition dipole vector has rotated). Both the overall rotation of the molecule, with an approximately constant angular velocity, or the internal torsional motions, are compatible with such feature. In this case, we have not fitted the anisotropy, but only the fluorescence intensity. The fitting can be done with a single exponential function, the lifetime being 0.27 ps.

With methanol as a solvent, we have obtained a satisfactory fitting by using the two exponentials with τ_1 and τ_3, as did Diau and coworkers for their low viscosity solvent, i.e. *n*-hexane. With ethylene glycol, we have included an additional time τ_2, but in this case τ_3 and w_3 have been fixed at the values obtained in ref. [6]. Since $w_3 = 0.03$, this term has little influence on the fitting of the fluorescence intensity, and our anisotropy is almost independent on time, except for a small decrease at the beginning. Actually, one can see a similar short time decrease, and even more pronounced, in the experimental data.

While our results for the TAB fluorescence agree very well with those of refs. [6,19], the interpretations partly differ. We recall that the decay of S_1, according to our simulations, cannot occur without a certain degree of torsion of the N=N double bond, but can be facilitated by the simultaneous symmetric NNC bending vibration. Diau and coworkers attributed the decay of fluorescence with depolarization to the torsion mechanism, and the decay without depolarization to another mechanism, possibly identifiable with the NNC symmetric bending. This was meant to explain the two- or three- exponential decay of fluorescence, and why the depolarization is much slower (actually, almost negligible) in a viscous solvent, where the torsional motion is hindered. Moreover, we observe that different lifetimes of the fluorescence decay and of its depolarization may be associated with any single mechanism. In fact, the depolarization can precede (never follow) the decay of the emitting state, so the lifetime of the former can be shorter. On the other hand, the

Table 6.6: Lifetimes and other parameters obtained by fitting fluorescence intensity and anisotropy data. Stars (*) indicate parameters that have not been varied in the fitting procedure. Times in ns and wavelengths in nm.

	λ_{exc}	λ_{flu}	τ_1 (W_1)	τ_2 (W_2)	τ_3 (W_3)	R_∞
computed in vacuo	no limit	no limit	0.25 (1.00*)			
computed in methanol	no limit	no limit	0.29 (0.62)		0.80 (0.38)	0.25*
	no limit	520±40	0.12 (0.76)		0.24* (0.24)	0.32*
	no limit	600±40	0.24 (0.95)		1.06 (0.05)	0.26*
	no limit	680±40	0.35 (0.89)		1.07 (0.11)	0.21*
computed in EG	no limit	no limit	0.28 (0.44)	2.40 (0.63)	22.0* (0.03*)	0.22*
	440±20	680±40	0.82 (0.77)	3.08 (0.20)	20.0* (0.03*)	0.21*
	480±20	680±40	0.42 (0.43)	2.13 (0.54)	24.0* (0.03*)	0.22*
exp. in *n*-hexane	440	520	0.15 (0.76)		0.6 (0.24)	0.32
	440	600	0.29 (0.69)		1.4 (0.31)	0.26
	440	680	0.33 (0.59)		1.7 (0.41)	0.21
exp. in EG	440	680	0.65 (0.75)	3.6 (0.22)	20. (0.03)	0.21
	480	680	0.35 (0.62)	3.1 (0.35)	24. (0.03)	0.22

depolarization (anisotropy loss) due to the dynamics associated with certain degrees of freedom can be very small. With our simulations, we have shown that torsion, although slower, is still the dominant mechanism in ethylene glycol, whereas other vibrational modes, including NNC bending, are damped down. The torsional motion does cause a change in the direction of the transition dipole vector, but most of the fluorescence emission takes place before this vector has deviated from its initial orientation, so very little depolarization is observed. Other contributions to the depolarization are due to different internal modes, and probably also to the transfer of energy to the closest solvent molecules, that excites their librational and vibrational motions. The solvent caging limits all the variations in the molecular orientation, much more if the solvent is associated, made of large molecules, and/or endowed with a small free volume, all these features being usually correlated with high viscosity. The multi-exponential behaviour of the fluorescence decay, which is a feature associated with the condensed phase, must be due to inhomogeneous effects, i.e. to the variety of situations (solvent cages, specific solute-solvent interactions) that are experienced by the azobenzene molecules at the time of excitation.

In this sense we have calculated the fluorescence intensity and anisotropy not only for the whole range of CNNC and NNC angles, but we have divided in two almost equal ranges in each case: a lower range and an upper range (considering approximately the same contribution to the total fluorescence intensity in both ranges). For the CNNC dihedral angle we have calculated the anisotropy below and above 150°. For the NNC angle we have done the calculations below and above 130°. Regarding the fluorescence intensity we observed almost the same contribution to the total intensity in each case. With respect to the anisotropy, we did not observe changes in the decay magnitude and in its general behavior, for any of the four limited ranges of the CNNC and NNC angles we have tried.

A calculation of the anisotropy, conserving the initial body-fixed frame of the molecule along the trajectory (as we have defined in the appendix A), produces an anisotropy with a small initial decrease, followed by a very stable value. These results permit us to support the explanation mentioned before where the decay in the fluorescence anisotropy can be then associated to the librational motion of the molecule inside a solvent cage.

Figure 6.15 shows the fluorescence transients obtained by excitation of CAB, including the anisotropy as a function of time. The decay is much faster than that of TAB, and only one or two oscillations can be observed. In solution the decay is slowed down, but not as much as in the case of TAB: the time scale in ethylene glycol expands by a factor of about 4 with respect to the isolated molecule, whereas in CAB there is not a significative change with the inclusion of solvent. The anisotropy decay, during the CAB fluorescence emission, is much more pronounced than that of TAB. Since the decay is not exponential, and no experimental determinations are available as yet, we have not attempted to evaluate the lifetimes through a convolution and fitting procedure.

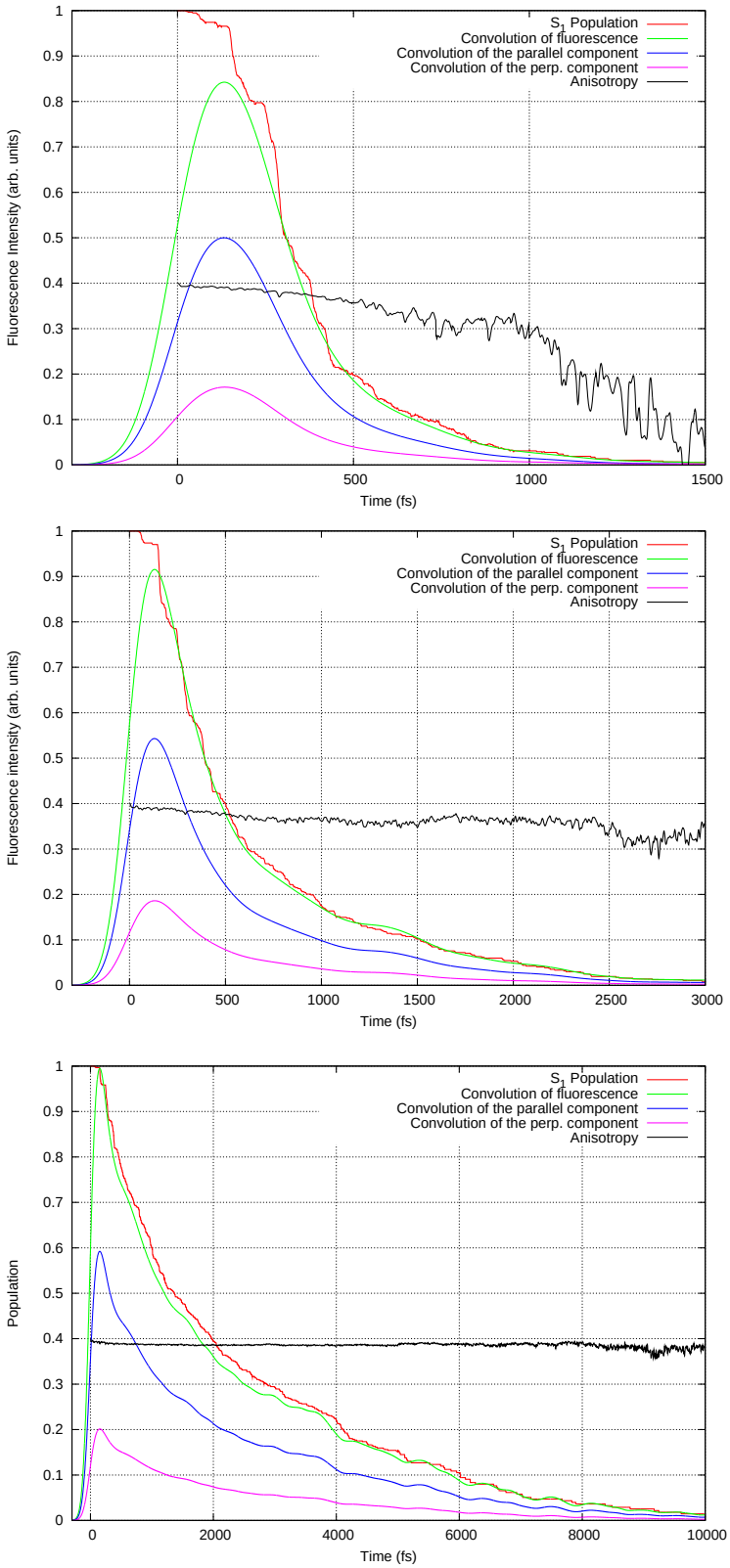

Figure 6.14: Total fluorescence intensity and perpendicular and parallel components of the signal after gaussian convolution, for TAB in vacuo (upper panel), methanol (middle panel) and EG (lower panel). The related anisotropy without convolution is also included.

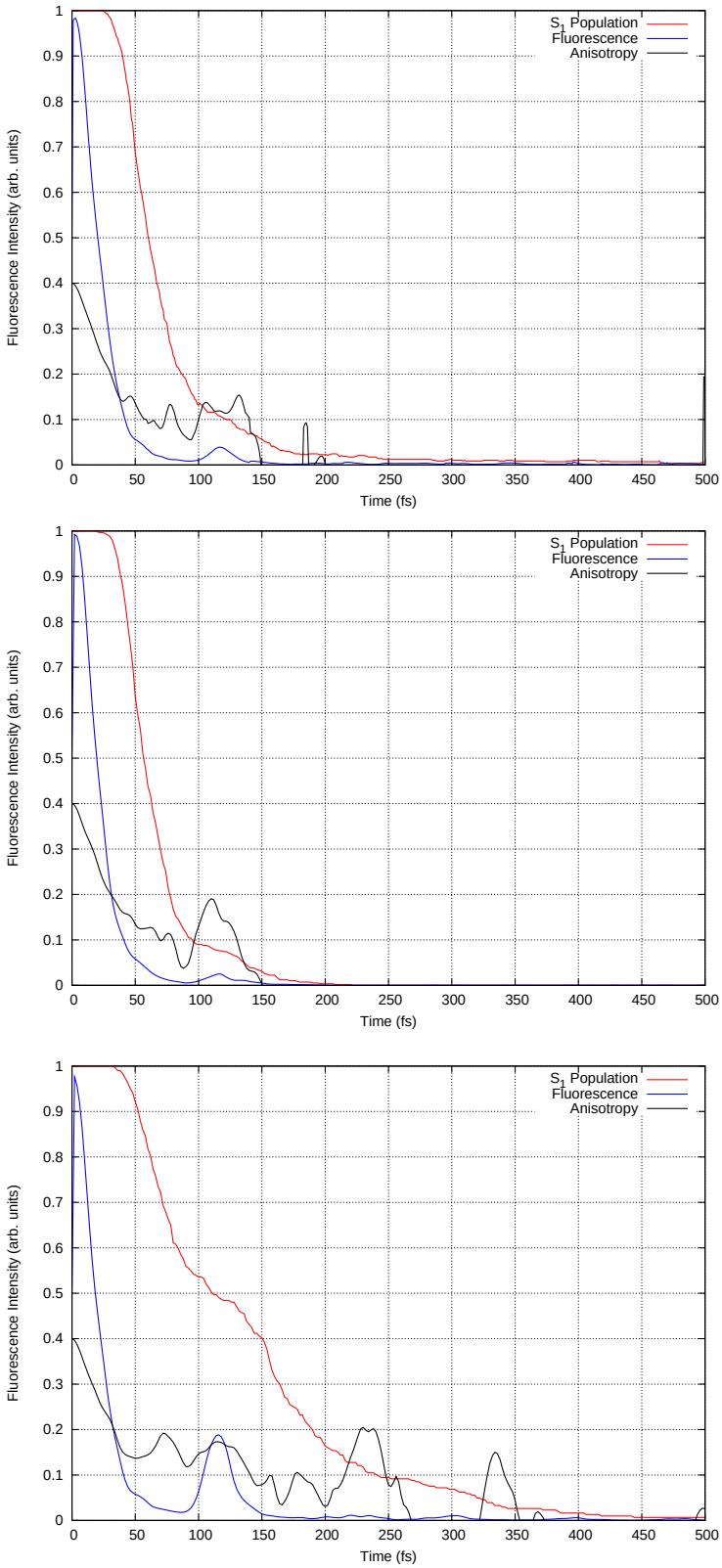

Figure 6.15: Total fluorescence intensity and perpendicular and parallel components of the signal after gaussian convolution, for CAB in vacuo (upper panel), methanol (middle panel) and EG (lower panel). The related anisotropy without convolution is also included.

Final Remarks

The main goal of this Thesis work is the theoretical study of the azobenzene photoisomerization in solution. This has been done by mixed quantum-classical simulations, using the surface hopping method. The electronic energies and wavefunctions are computed on the fly, by a semiempirical method modified by our group. The solvent effects have been introduced in a preliminary way by brownian dynamics, and then explicitly, with a QM/MM approach.

One of the guidelines of our work is a constant comparison with experimental results, first of all the photoisomerization quantum yields and the transient spectroscopy data. In the latter field, probably the best work has been done by Diau's group [6]. In their experiments they measure the fluorescence anisotropy of the $n \rightarrow \pi^*$ transition of *trans*-azobenzene in hexane and ethylene glycol solutions. They argue that the depolarization observed in hexane is probably due to the structural relaxation along the CNNC torsional pathway. However, in ethylene glycol this motion is hampered and the excited state decay, according to the authors, could be due to the in-plane symmetric NNC bending, that is another way to approach the $S_1 - S_0$ crossing seam.

As a first step in the study of the photophysics of *trans*-azobenzene, we have carried out an ab initio investigation of its $n \rightarrow \pi^*$ forbidden band. We have shown that the most effective coordinate in promoting this transition is the symmetric torsion of the phenyl groups. Other important coordinates are the antisymmetric phenyl torsion and the torsion of the N=N double bond. In order to determine the oscillator strength f we have taken into account the anharmonicity of the ground state PES and the non trivial dependence of the electronic transition dipole on the internal coordinates. The agreement of the computed f with the spectroscopic measurements confirms that *trans*-azobenzene is planar, even in solution, but the torsional potential of the phenyl rings is rather shallow. We have also tackled the problem of the direction of the transition dipole vector for the $n \rightarrow \pi^*$ transition, which is a basic preliminary question in the interpretation of experiments of fluorescence anisotropy and of the orientation of azobenzene samples in polarized light. The transition dipole vector turns out to lie essentially in the molecular plane, almost parallel to the N-C bonds and to the longest axis of the molecule. The dipole vector and the N-N axis form an angle of about 53°. This orientation is little affected by details of the calculation, changes in temperature, and solvation. Semiempirical calculations place the dipole moment vector at an angle of about 45° respect to the N=N axis, sufficiently close to the ab initio results.

Since we make direct use of semiempirical CI energies and wavefunctions in the trajectory surface hopping calculations, we have proceeded to a reparameterization of the semiempirical hamiltonian. In fact, the standard parameters (AM1, PM3 or others) are not suitable for CI calculations of the ground state, and much less for the excited states. Actually, a previous parameterization had already yielded good results in simulations of

the gas phase photodynamics. However, new ab initio results, that can be used as reference values, permit now to improve the accuracy of the parameterization. In addition, we have carried out an ab initio study of the interaction potentials between azobenzene and two simple molecules, methane and methanol, chosen as representatives of non-polar and of protic compounds, respectively. From these data, we have extracted the parameters for QM/MM calculations of azobenzene (the quantum mechanical system) interacting with solvent molecules that contain alkyl and hydroxyl groups. The solvent itself is represented by a Molecular Mechanics force-field (OPLS) and the QM/MM interactions are made of electrostatic and Lennard-Jones terms.

The solvent effects have been simulated in two ways. A preliminary set of simulations was based on Brownian dynamics, by integration of Langevin's equation. Two sets of friction coefficients were used, corresponding to solvents with viscosities of about 1 and 10 mPa·s, respectively. The main effort was put in a more realistic model of the solvent, obtained by the QM/MM method. In the QM/MM simulations, a large cluster of solvent molecules surrounds the azobenzene molecule. The first two solvents we have tried are methanol and ethylene glycol, chosen for their widely different viscosities (0.54 and 16.1 mPa·s, respectively). In particular, ethylene glycol is the viscous solvent used in Diau's time-resolved fluorescence experiments. Simulations were run for the $n \rightarrow \pi^*$ excitation of both *trans*- and *cis*-azobenzene, i.e. for the $trans \rightarrow cis$ and the $cis \rightarrow trans$ photoprocesses.

The results show that the preferred reaction path is the torsion of the N=N double bond for both photoisomerizations, both in vacuo and in all the solvents, including the implicit (Brownian) ones. With methanol, the $\Phi_{trans \rightarrow cis}$ and $\Phi_{cis \rightarrow trans}$ quantum yields for the $n \rightarrow \pi^*$ excitation are in good agreement with the experimental ones, and slightly lower than in vacuo. In ethylene glycol, $\Phi_{trans \rightarrow cis}$ increases, while $\Phi_{cis \rightarrow trans}$ further decreases, as found experimentally in the analogous solvent glycerol. The interpretation of such results draws on the competition between the $S_1 \rightarrow S_0$ internal conversion and the isomerization process. Both need a torsion of the N=N double bond (CNNC coordinate), but the decay of S_1 can take place with a moderate torsion, provided other internal vibrations (namely the symmetric NNC bending) allow to reach the crossing seam. When such an "early decay" occurs, the quantum yield is decreased. If the azobenzene molecule is kept close to the Franck-Condon region by the solvent cage for too long, the loss of vibrational energy to the solvent slows down the internal conversion, both by decreasing the nonadiabatic couplings and by making the crossing seam less accessible. This happens when exciting the *trans* isomer in ethylene glycol, with the consequent increase of the $\Phi_{trans \rightarrow cis}$ quantum yield. However, on the *cis* side, the slope of the excited PES is much larger, so all processes are accelerated, the $\Phi_{cis \rightarrow trans}$ quantum yield is larger, and does not increase in ethylene glycol. The enhancing of the $\Phi_{trans \rightarrow cis}$ quantum yield is not reproduced by the Brownian simulation, because of a well understood artifact associated with large friction coefficients.

With respect to the isolated molecule photodynamics, all solvents (Brownian or explicit) slow down the torsional motion and the excited state decay. In this respect, the viscous solvents are much more effective than the others, as found by Diau and coworkers. The explicit representation of the solvent also introduces a biexponential behaviour, which is apparent in all experiments performed in solution. The simulation of the fluorescence transients (intensity and anisotropy) shows a good agreement with the experimental data. However, the analysis of the mechanism partly differs from the interpretation previously put forward by Diau and coworkers. In fact, we find the decay of the S_1 state and of its

fluorescence is not due to two different mechanism, but to the N=N bond torsion alone, while the other internal modes only have an auxiliary role. In a viscous solvent, such as ethylene glycol, the torsional motion is slowed down, but is even more exclusively the decay and isomerization mechanism, because the vibrational energy contained in the other modes is transferred to the solvent.

Part V

APPENDIXES

Appendix A

Body axis frame

In this Appendix we specify the body fixed frame for the azobenzene molecule. We only consider four atoms, namely the C′-N′=N″-C″ group. The definition of the body fixed frame applies to any geometrical arrangement, except when all four atoms are collinear. However, we are particularly interested in geometries close to the *cis* and *trans* minima (CAB and TAB). The definitions of the axes are as follows (see also fig. A.1):
(1) The $\hat{x}$ axis coincides with the N′-N″ one, i.e. it is obtained by normalizing the $\vec{R}_{\mathrm{N'N''}} = R_{\mathrm{N''}} - R_{\mathrm{N'}}$ vector.
(2) We determine the $\vec{A}$ vector by orthogonalizing $\vec{R}_{\mathrm{N'C'}}$ with respect to $\hat{x}$ and by subsequent normalization. (3) Similarly, we determine $\vec{B}$ by orthogonalizing $\vec{R}_{\mathrm{N''C''}}$ with respect to $\hat{x}$ and by normalizing it. (4) We calculate $\vec{C} = \vec{A} + \vec{B}$.
(5) We calculate $\vec{C}' = \hat{x} \wedge (\vec{B} - \vec{A})$.
(6) The direction of the $\hat{z}$ axis is taken along $\vec{C}$ or $\vec{C}'$, choosing the one with the larger norm. We have $C > C'$ at cisoid geometries ($-\pi/2 < \angle\mathrm{CNNC} < \pi/2$), and $C < C'$ at the transoid ones.
(7) Obviously $\hat{y} = \hat{z} \wedge \hat{x}$.
The reason for defining both $\vec{C}$ and $\vec{C}'$ and choosing the longer one is that $\vec{C}$ vanishes at the *trans* geometry ($\vec{A} = -\vec{B}$ for $\theta = \angle\mathrm{CNNC} = 180°$), while $\vec{C}'$ vanishes at the *cis* geometry with θ=0 ($\vec{A} = \vec{B}$ for $\angle\mathrm{CNNC} = 0$).

Starting from TAB, θ may decrease from 180° to 0°, so that the molecule goes through the intermediate transoid and cisoid geometries of fig. A.1. In this case, one switches smoothly from the definition based on the $\vec{C}'$ vector to that based on the $\vec{C}$ one, when θ drops below 90°. If, on the opposite, θ increases towards 360°, we obtain a capsized CAB, in its enantiomeric form, with the $\hat{z}$ and $\hat{y}$ axes pointing in opposite directions with respect to the former case. Note that, along this pathway, the definition of the frame changes suddenly at $\theta = 270°$.

Of course the two pathways have the same probability to occur. This is why the plots of the final $\hat{y}$ and $\hat{z}$ axes show an approximate inversion symmetry: the same density of points is found for a given pair of cartesian components and for the same with opposite signs. Of course the symmetry would be exact only in the large number limit (infinite trajectories).

Figure A.1: Definition of the body-fixed frame. θ id the CNNC dihedral angle.

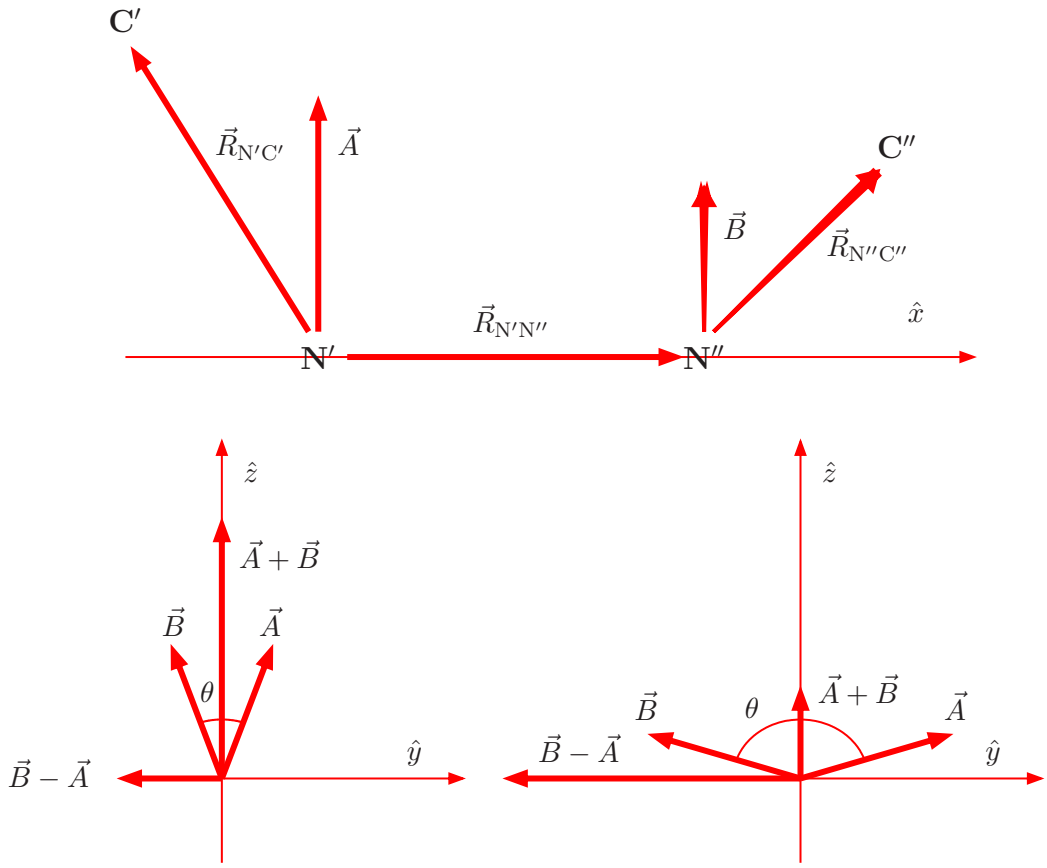

view along the N-N axis ($\hat{x}$)
cisoid geometry

view along the N-N axis ($\hat{x}$)
transoid geometry

Appendix B

Optimization methods

B.1 Simplex

Our group has developed a program adapted to the optimization calculations. This program is a strategy method to search the extreme value of a function independently of the gradient calculation. SUPOPT program can optimize the "aim" function following several minimization strategies like the Simplex method [151, 152], a genetic technique or "quasi-Newton" method with gradients calculated numerically. For the reparameterization of the semiempirical hamiltonian we have employed the Simplex Optimization Algorithm (SOA), because it does not require the calculation of the function gradient. We combined it with a Simulated Annealing (SA) technique (see the next section). The SA strategy is particularly indicated for nonlinear problems, where the "target" function has several relative minima. In the case of the optimization of the semiempirical parameters, in principle our interest is to reproduce as closely as possible the target values, i.e. to find the absolute minimum. However, it may be advisable to limit the changes with respect to the standard parameterization, i.e. to be content with a relative minimum closer to the starting point. In order to influence the final results and the rate of convergence, the functioning of the Simplex and Simulated Annealing algorithms can be controlled by choosing several options.

The SOA has a geometrical nature: a Simplex of order n corresponds to a shape of n dimensions constituted of $n+1$ vertices linked by segments or polygonal faces. Consider the optimization problem of a function of n variables $f(\mathbf{x})$; be $\mathbf{x}^1$ an initial estimated value of our minimum point x^*. We construct an initial Simplex of order n with the points $\mathbf{x}^1$, $\mathbf{x}^2$,...,$\mathbf{x}^{n+1}$, obtained from:

$$\mathbf{x}^{j+1} = \mathbf{x}^1 + h_j \mathbf{e}_j; j = 1, ..., n \tag{B.1}$$

where the $\mathbf{e}_j$ are the linearly independent versors and the h_j the path lengths of single directions. In the general SOA, we indicate:

$\mathbf{x}^h$ the vertex where the function has the higher value

$\mathbf{x}^s$ the vertex with the second higher value

$\mathbf{x}^l$ the vertex with the minimum value

$\mathbf{x}^c$ the centroid of all vertices excluding $\mathbf{x}^h$, namely

$$\mathbf{x}^c = \frac{1}{n}\sum_{j\neq h}^{n+1}\mathbf{x}^j \tag{B.2}$$

This algorithm proceeds as follow:

(1) Calculate the function $f(\mathbf{x})$ in the simplex vertices.
(2) After ordering the vertices as specified above, reflect $\mathbf{x}^h$, using a parameter α (Reflection)
$$\mathbf{x}^0 + \mathbf{x}^c = \alpha(\mathbf{x}^c + \mathbf{x}^h) \Rightarrow \mathbf{x}^0 = (1+\alpha)\mathbf{x}^c - \alpha\mathbf{x}^h \tag{B.3}$$
(3) If $f(\mathbf{x}^l) \leq f(\mathbf{x}^0) \leq f(\mathbf{x}^s)$, substitute $\mathbf{x}^h$ with $\mathbf{x}^0$ and return to step 2.
(4) If $f(\mathbf{x}^0) < f(\mathbf{x}^l)$, expand the Simplex using the expansion factor $\gamma > 1$ (Expansion), we find $\mathbf{x}^{00}$ such that:
$$\mathbf{x}^{00} = \gamma\mathbf{x}^0 + (1-\gamma)\mathbf{x}^c \tag{B.4}$$
and then evaluate $f(\mathbf{x}^{00})$: if $f(\mathbf{x}^{00}) < f(\mathbf{x}^l)$ substitute $\mathbf{x}^h$ with $\mathbf{x}^{00}$ and return to step 2; if $f(\mathbf{x}^{00}) \geq f(\mathbf{x}^l)$ substitute $\vec{x}^h$ with $\mathbf{x}^0$ and return to step 2.
(5) If $f(\mathbf{x}^0) > f(\mathbf{x}^s)$, contract the Simplex with a factor β with values between 0 and 1 (Contraction). There are two cases to be considered:
- if $f(\mathbf{x}^0) < f(\mathbf{x}^h)$, find $\mathbf{x}^{00}$ such that:
$$\mathbf{x}^{00} = \beta\mathbf{x}^0 + (1-\beta)\mathbf{x}^c \tag{B.5}$$
- if $f(\mathbf{x}^0) \geq f(\mathbf{x}^h)$ find $\mathbf{x}^{00}$ such that:
$$\mathbf{x}^{00} = \beta\mathbf{x}^h + (1-\beta)\mathbf{x}^c \tag{B.6}$$

In both cases there exists two further possibilities to be considered:
- if $f(\mathbf{x}^{00}) < f(\mathbf{x}^h)$ and $f(\mathbf{x}^{00}) < f(\mathbf{x}^0)$, substitute $\mathbf{x}^h$ with $\mathbf{x}^{00}$ and return to step 2;
- if $f(\mathbf{x}^0) < f(\mathbf{x}^h)$ or $f(\mathbf{x}^0) < f(\mathbf{x}^h)$, reduce the amplitude of Simplex halving the distances from x^l and return to step 2.

B.2 Simulated annealing

The Simulated Annealing (SA) is a strategy that allows to explore a large portion of the parameter space, before converging to a local minimum. When the function has several minima, it is not always desirable to remain in the local minimum nearest to the starting point, and deeper minima (possibly the absolute minimum) are looked for. To this aim, we have executed SOA optimizations with different starting points, and we have conjugated the SA strategy with the SOA. The latter option consists in adding a random quantity to each calculated value of the function. In this way, the SOA can accept an $\mathbf{x}$ point that would be discarded because the corresponding $f(\mathbf{x})$ is larger than the other f values previously found. In this way, the algorithm can escape a local minimum and possibly find another one. The random added values Δf follow a probability distribution $exp(-\Delta f/T)$, where T is a parameter choosen ad hoc. The "temperature" T is diminished by a factor R_T every N_T optimization steps, in order to decrease the effect of such random additions and to permit the accurate determination of the final minimum. When the search ends, the temperature is very small, and the optimizer reduces to the standard SOA. The initial

temperature T_0 and the R_T and N_T parameters are user-defined, and influence the range of variables to be explored and the rate of convergence of the algorithm.

The Simulated Annealing technique bears analogies with a heating/cooling cycle. Consider that the molecules of a liquid at a high temperature have a large probability of moving freely. Cooling slows down the atoms, so that they can aggregate in the most convenient ways, to produce low energy structures. If the cooling is fast, the liquid will freeze before finding the lowest energy structure, possibly giving place to an amorphous rather than to a crystalline solid. The essential features of this physical process are reproduced in the Simulated Annealing procedure.

Appendix C

Quantum decoherence

In the case of a full quantum calculation, the nuclear components of the wavefunction associated to different electronic states "wavepackets" evolve following different potential surfaces. Different wavepackets located in different regions of the nuclear phase space will have negligible overlap and therefore negligible interaction. Hence they will evolve independently.

A quantum wavepacket, by going through a strong coupling region, is split on two components, traveling on other electronic state. The two wave packets are initially coupled by the nonadiabatic terms of the Hamiltonian and keep exchianging population, but they end up evolving independently, as they travel into distant regions of the space of the nuclear coordinates and momenta [66]. The truly quantum mechanical time evolution therefore entails a progressive decoherence, which is practically irreversible in many-dimensional systems.

On the contrary, the semiclassical TDSE implies a fully coherent propagation of the electronic wave function due to the underlying assumption that the molecular geometry is described by a single point in the nuclear phase space (the same for all electronic states). Of the various procedures that can be used to introduce the decoherence in semiclassical schemes, we have adopted a simplified version of one put forward by Truhlar and co-workers [101, 102], in the framework of mean field methods, and briefly explained in the Section 4.3.

The lack of quantum decoherence in surface hopping can be easily understood considering a two state, one dimensional system. When a trajectory crosses a strong coupling region, a portion of the population go to the other state. This is similar to what happens in the full quantum case. However, when the trajectory leaves the coupling region, the electronic state populations keep the same values they had at the end of the coupling region. This behavior is different to the quantum one for the other state, where the wavepacket would has been evolved independently. Only part of the independence of the wavepackets is recovered averaging over all the trajectories. Moreover, if the trajectory pass again through the coupling region, the population of the other state (where the trajectory does not run) is still able to be transferred, modifying the hopping probabilities, and giving rise to the non physical effects.

Figure C.1 shows the populations averaged over 600 trajectories, including and not the quantum decoherence effects. We can note that when decoherence effects are included, Π_2 and P_2 are coincident.

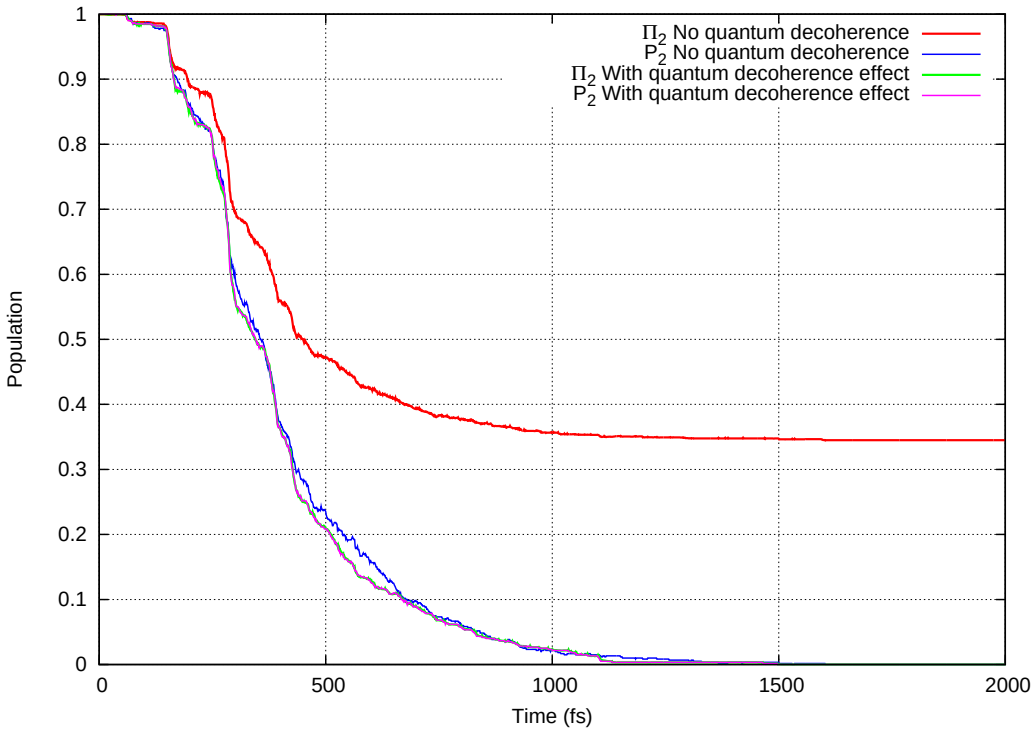

Figure C.1: Comparison of the time evolution of the excited state populations in the case of $n \rightarrow \pi^*$ excitation, starting from the TAB isomer, including or not the quantum decoherence effects.

Appendix D

Azobenzene-methanol: Tables of Results

Table D.1: TAB-MeOH-Plan: points of the potential energy curve relative to the cc-pVDZ basis (upper Table) and to the cc-pVTZ (lower Table), MP2 method.

$R_N - H(\mathring{A})$	E(ua)[a]	E_{cp}(ua)[b]	Contrib. CP(ua)[c]
1.7	-686.42532065649	-686.411639323369	0.013681333120
1.8	-686.42693188288	-686.414098930064	0.012832952815
1.9	-686.42750431312	-686.415486719261	0.012017593856
2.0	-686.42737749569	-686.416156362398	0.011221133292
2.1	-686.42678711694	-686.416348917379	0.010438199563
2.2	-686.42589826561	-686.416227777513	0.009670488095
2.3	-686.42482819852	-686.415905010732	0.008923187793

$R_N - H(\mathring{A})$	E(ua)[a]	E_{cp}(ua)[b]	Contrib. CP(ua)[c]
1.8	-687.08365349374	-687.078538001964	0.005115491778
1.9	-687.08412804704	-687.079375324486	0.004752722558
2.0	-687.08398020743	-687.079558726470	0.004421480960
2.1	-687.08344423747	-687.079325830783	0.004118406682
2.2	-687.08268086674	-687.078839632639	0.003841234100

[a] E is the non corrected MP2 energy
[b] E_{cp} is the energy corrected by the BSSE.
[c] Contrib. Cp is the counterpoise correction.

Table D.2: TAB-MeOH-Perp: points of the potential energy curve relative to the cc-pVDZ basis (upper Table) and to the cc-pVTZ (lower Table), MP2 method.

$R_N - H(\mathring{A})$	E(ua)[a]	E_{cp}(ua)[b]	Contrib. CP(ua)[c]
1.8	-686.41440539198	-686.406578579312	0.007826812672
1.9	-686.41603018979	-686.409155327482	0.006874862312
2.0	-686.41682669625	-686.410813148014	0.006013548237
2.1	-686.41706618905	-686.411827824183	0.005238364863
2.2	-686.41694144453	-686.412394144794	0.004547299740
2.3	-686.41658920408	-686.412650633186	0.003938570891
2.4	-686.41610515677	-686.412696933356	0.003408223413
2.5	-686.41555451385	-686.412605310169	0.002949203683
2.6	-686.41498035238	-686.412428057775	0.002552294607

$R_N - H(\mathring{A})$	E(ua)[a]	E_{cp}(ua)[b]	Contrib. CP(ua)[c]
1.8	-687.07459455108	-687.070826321621	0.003768229464
1.9	-687.07620887176	-687.072830015891	0.003378855864
2.0	-687.07702110650	-687.073989855011	0.003031251488
2.1	-687.07729416750	-687.074575585463	0.002718582034
2.2	-687.07721483157	-687.074778661563	0.002436170003
2.3	-687.07691398777	-687.074733574299	0.002180413472
2.4	-687.07648192626	-687.074533819397	0.001948106865
2.5	-687.07598013334	-687.074243629597	0.001736503746
2.6	-687.07545000269	-687.073906477940	0.001543524747

[a] E is the non corrected MP2 energy
[b] E_{cp} is the energy corrected by the BSSE.
[c] Contrib. Cp is the counterpoise correction.

Table D.3: CAB-MeOH: points of the potential energy curve relative to the cc-pVDZ basis, MP2 method.

$R_N - H(\mathring{A})$	E(ua)[a]	E_{cp}(ua)[b]	Contrib. CP(ua)[c]
1.8	-686.40596636125	-686.39502260352	0.010943757737
1.9	-686.40705334843	-686.39690062367	0.010152724755
2.0	-686.40735073218	-686.39794543172	0.009405300459
2.1	-686.40710913994	-686.39841398007	0.008695159869
2.2	-686.40651132022	-686.39848859740	0.008022722822
2.3	-686.40568928579	-686.39829942909	0.007389856697
2.4	-686.40473621496	-686.39794045301	0.006795761954

$R_N - H(\mathring{A})$	E(ua)[a]	E_{cp}(ua)[b]	Contrib. CP(ua)[c]
1.8	-687.06407345714	-687.059505318823	0.004568138321
1.9	-687.06511071403	-687.060887964734	0.004222749295
2.0	-687.06542870688	-687.061513017617	0.003915689261
2.1	-687.06526977310	-687.061627214265	0.003642558834
2.2	-687.06480635568	-687.061407211228	0.003399144455
2.3	-687.06415818830	-687.060977801149	0.003180387156

[a] E is the non corrected MP2 energy
[b] E_{cp} is the energy corrected by the BSSE.
[c] Contrib. Cp is the counterpoise correction.

Appendix E

Azobenzene-methane: Tables of Results

Table E.1: TAB-Met-Plan: points of the potential energy curve relative to the cc-pVDZ basis, MP2 method.

$R_N - H(\mathring{A})$	E(ua)[a]	E_{cp}(ua)[b]	Contrib. CP(ua)[c]
2.6	-611.38383009004	-611.381595089569	0.002235000467
2.7	-611.38406067462	-611.382045226638	0.002015447983
2.83291	-611.38415252133	-611.382416160570	0.001736360760
3.0	-611.38404854923	-611.382639394874	0.001409154353
3.1	-611.38391934090	-611.382689627992	0.001229712905
3.2	-611.38376434144	-611.382699208478	0.001065132960
3.3	-611.38359750243	-611.382680570354	0.000916932078
3.4	-611.38342869981	-611.382642847449	0.000785852364
3.64	-611.38305045872	-611.382511440881	0.000539017839

[a] E is the non corrected MP2 energy
[b] E_{cp} is the energy corrected by the BSSE.
[c] Contrib. Cp is the counterpoise correction.

Table E.2: TAB-Met-Perp: points of the potential energy curve relative to the cc-pVDZ basis, MP2 method.

$R_N - H(\mathring{A})$	E(ua)[a]	E_{cp}(ua)[b]	Contrib. CP(ua)[c]
2.55	-611.38524703472	-611.382079539518	0.003167495206
2.65	-611.38548749560	-611.382583008430	0.002904487165
2.75965	-611.38557407979	-611.382939789159	0.002634290631
2.8	-611.38556989953	-611.383030785627	0.002539113907
2.9	-611.38549559874	-611.383183149640	0.002312449102
3.0	-611.38535200548	-611.383253514014	0.002098491464
3.1	-611.38516144244	-611.383264525426	0.001896917014
3.2	-611.38494107566	-611.383233675475	0.001707400188
3.3	-611.38470404996	-611.383174448110	0.001529601850
3.54	-611.38412187068	-611.382972211868	0.001149658817

[a]E is the non corrected MP2 energy
[b]E_{cp} is the energy corrected by the BSSE.
[c]Contrib. Cp is the counterpoise correction.

Table E.3: CAB-Met: points of the potential energy curve relative to the cc-pVDZ basis, MP2 method.

$R_N - H(\mathring{A})$	E(ua)[a]	E_{cp}(ua)[b]	Contrib. CP(ua)[c]
2.59	-611.36592373206	-611.362874968326	0.003048763739
2.69	-611.36626440554	-611.363556788804	0.002707616737
2.79015	-611.36635898896	-611.363952609550	0.002406379414
2.9	-611.36627804595	-611.364165311896	0.002112734050
3.0	-611.36610009664	-611.364227671071	0.001872425570
3.1	-611.36586528391	-611.364211495911	0.001653787997
3.2	-611.36560195039	-611.364147663102	0.001454287291
3.37	-611.36513979064	-611.363985286450	0.001154504187
3.54	-611.36470281256	-611.363803023824	0.000899788732
3.74	-611.36425265144	-611.363599756256	0.000652895188

[a]E is the non corrected MP2 energy
[b]E_{cp} is the energy corrected by the BSSE.
[c]Contrib. Cp is the counterpoise correction.

Appendix F

Radial Distribution Function

The radial distribution function (RDF), $g(r)$, describes the way by the density of surrounding matter varies as a function of the distance from a particular point. The RDF takes into account the correlations in the distribution of molecules arising from the forces they exert on each other. Given a potential energy function, the RDF can be found via computer simulation methods like the Monte Carlo method.

It is defined in the following way [153, 154]. The RDF is defined by:

$$g(r) = \frac{\rho^{(2)}(0,r)}{\rho^2} \tag{F.1}$$

where $\rho = N/V$ is the density of a fluid of N particles in a container of volume V and $\rho^{(2)}(0,r)$ is the probability that a particle is at $\mathbf{r}$ when there is another particle at the origin of coordinates. The probability $P^{(2)}(R_1,R_2)$ that particle 1 is found at R_1 when particle 2 is at R_2, in a N particle system, is

$$P^{(2)}(R_1,R_2) = \frac{\int dr^{N-2} e^{-\beta U(R_1,R_2,r_3,\ldots,r_N}}{\int dr^N e^{U(r^N)}} \tag{F.2}$$

and the probability $\rho^{(2)}(0,r)$ that a particle (i.e., any particle) is found at R_1 when another one (i.e., any other one) is at R_2 is

$$\rho^{(2)}(R_1,R_2) = \frac{N!}{(N-2)!} P^{(2)}(R_1,R_2) = N(N-1)P^{(2)}(R_1,R_2) \tag{F.3}$$

In particular if a fluid where the interaction between particles can be neglected,

$$P^{(2)}(R_1,R_2) = \frac{1}{V^2} \tag{F.4}$$

or

$$\rho^{(2)}(R_1,R_2) = \frac{N(N-1)}{V^2} \approx \rho^2 \tag{F.5}$$

and g(r)=1. In an atomic fluid (e.g., liquid argon), $g(r_1,r_2) = g(r)$, where $r = |r_1 - r_2|$, since the fluid is uniform and isotropic. The presence of an atom at the origin of coordinates excludes other particles from all distances smaller than the radius of the first coordination shell where $g(r)$ has a maximum. The presence of the fisrt coordination shell tends to exclude particles that are closer than the radius of the second coordination shell, where

$g(r)$ has another maximum. This oscillatory form for $g(r)$ persist until r is larger that the range of correlations between the particles. At distances larger than the correlation length $g(r) = 1$, since $\rho^{(2)}(0, r) \approx \rho^2$ for uncorrelated particles. Therefore, $h(r) = g(r) - 1$ describes the deviation from the asymptotic limit of uncorrelated particles and the product $\rho g(r)$ describes the average density of particles at a density r from any particle in the fluid.

Note that $\rho g(r) 4\pi r^2 dr$ is the number of particles at a distance between r and $r + dr$ from any particle in the fluid. Therefore, the calculation of $g(r)$ involves averaging the number of particles at a distance r from any particle in the system and dividing that number by the element of volume $4\pi r^2 dr$.

By the way described before can be possible to determine the inter- and intra-molecular H-Bonds in alcohols like those used by us in this work. In the case of methanol and ethylene glycol, from the $g_{OH}(r)$ function it was possible to determine the intermolecular H-bonds by the folowing expression:

$$\bar{n}_{OH} = \alpha_{OH} \rho \int_0^{R_{min}} 4\pi r^2 g_{OH}(r) dr \tag{F.6}$$

where $\alpha_{OH} = 2*$number of OH groups of a molecule, ρ numberical density of OH groups and R_{min} is the distance of the first minimum in $g_{OH}(r)$.

In the other hand, for the intramolecular H-bonds in ethylene glycol molecule, we have calculate the distance between the OH groups in the same molecule, establishing the percent of one or two H-bonds possibly formed for the molecule, in base of the distance.

It is possible to measure $g(r)$ experimentally with neutron scattering or x-ray scattering diffraction data. In such an experiment, a sample is bombarded with neutrons or x-ray which then diffract in all directions. The average molecular density at each distance can be extracted according to Snells law: r=wavelength/sin(scattered angle), where r is the distance the neutron travelled during diffraction.

References

[1] H. Rau, in Photochromism. Molecules and Systems, edited by H. Durr and H. Bouas-Laurent (Elsevier, Amsterdam, 1990), pp. 165

[2] I.K. Lednev, T.-Q. Ye, R.E Hester and J.N. Moore, J. Phys. Chem. **100**, 13338 (1996).

[3] I.K. Lednev, T.-Q. Ye, P. Matousek, M. Towrie, P. Foggi, F.V.R. Neuwah, S. Umapathy, R.E Hester and J.N. Moore, Chem. Phys. Lett. **290**, 68 (1998).

[4] T. Nägele, R. Hoche, W. Zinth and J. Wachtveitl, Chem. Phys. Lett. **272**, 489 (1997).

[5] T. Fujino, S. Yu. Arzhantsev and T. Tahara, J. Phys. Chem. A **105**, 8123 (2001).

[6] C.-W. Chang, Y.-C. Lu, T.-T. Wang and E.W.-G. Diau, J. Am. Chem. Soc. **126**, 10109 (2004).

[7] P. Hamm, S.M. Ohline and W. Zith, J. Chem Phys. **106**, 519 (1997).

[8] T. Schultz, J. Quenneville, B. Levine, A. Toniolo, T. J. Martínez, S. Lochbrunner, M. Schmitt, J. P. Schaffer, M. Z. Zgierski and A. Stolow, J. Am. Chem. Soc. **125**, 8098 (2003).

[9] M. Asakawa, P. R. Ashton, V. Balzani, C. L. Brown, A. Credi, O. A. Matthews, S. P. Newton, F. M. Raymo, A. N. Shipway, N. Spencer, A. Quick, J. F. Stoddart, A. J. P. White and D. J. Williams, Chem. Eur. J. **5**, 860 (1999).

[10] A. Masumi and D. J. Williams, Chem. Eur. J. **5**, 860 (1999).

[11] A. N. Shipway and I. Willner, Acc. Chem. Res. **34**, 421 (2001).

[12] R. Ballardini, V. Balzani, A. Credi, M. T. Gandolfi and M. Venturi, Acc. Chem. Res. **34**, 445 (2001).

[13] C. Dugave and L. Demange, Chem. Rev. **103**, 2475 (2003).

[14] C. Cojocariu and P. Rochon, Pure Appl. Chem. **76**, 1479 (2004).

[15] K. G. Yager and C. J. Barrett, J. Photochem. Photobiol. A **182**, 250 (2006).

[16] T. Sasaki and J.M. Tour, Org. Lett. **10**, 897 (2008).

[17] N. Tamai and H. Miyasaka, Chem. Rev. **100**, 1875 (2000).

[18] T. Fujino and T. Tahara, J. Phys. Chem. A **104**, 4203 (2000).

[19] Y.-C. Lu, C.-W. Chang and E.W.-G. Diau, J. Chin. Chem. Soc. **49**, 693 (2002).

[20] H. Satzger, C. Root and M. Braun, J. Phys. Chem. **108A**, 6265 (2004).

[21] C. Ciminelli, G. Granucci and M. Persico, Chem. Eur. J. **10**, 2327 (2004).

[22] G. Granucci, M. Persico and A. Toniolo, J. Chem. Phys. **114**, 10608 (2001).

[23] J.J. De Lange, J.M. Robertson and I. Woodward, Proc. R. Soc. London, Ser. A **171**, 398 (1939).

[24] C.J. Brown, J. Acta Crystalogr. **21**, 146 (1966).

[25] A. Gruger, N. Le Calvé and P. Dizabo, J. Chim. Phys. **69**, 291 (1972).

[26] B. Kellerer, H.H. Hacker and J. Brandm*ü*ller, Indian J. Pure Appl. Phys. **9**, 903 (1971).

[27] M. Traettenberg, I. Hilmo and K. Hagen, J. Mol. Struct. **39**, 231 (1977).

[28] J. A. Bouwstra, A. Schouten and J. Kroon, Acta Crystallogr. C **39**, 1121 (1983).

[29] D.R. Armstrong, J. Clarkson and W.E. Smith, J. Phys. Chem. **99**, 17825 (1995).

[30] N. Biswas and S. Umapathy, J. Phys. Chem. A **101**, 5555 (1997).

[31] J. Harada, K. Ogawa and S. Tomoda, Acta Cryst. B **53**, 662 (1997).

[32] P. Cattaneo and M. Persico, PCCP **1**, 4739 (1999).

[33] N. Kurita, S. Tanaka and S. Itoh, J. Phys. Chem. A **104**, 8114 (2000).

[34] T. Ishikawa, T. Noro and T. Shoda, J. Chem. Phys. **115**, 7503 (2001).

[35] T. Tsuji, H. Takashima, H. Takeuchi, T. Egawa and S. Konaka, J. Phys. Chem. A **105**, 9347 (2001).

[36] P. C. Chen and Y. C. Chieh, J. Mol. Struct.: THEOCHEM **624**, 191 (2003).

[37] H. Fliegl, A. Köhn, C. Hättig and R. Ahlrichs, J. Am. Chem. Soc. **125**, 9821 (2003).

[38] A. Cembran, F. Bernardi, M. Garavelli, L. Gagliardi and G. Orlandi, J. Am. Chem. Soc. **126**, 3234 (2004).

[39] L. Briquet, D.P. Vercauteren, E.A. Perpète and D. Jaquemin, Chem. Phys. Lett. **417**, 190 (2006).

[40] A. Mostad and C. Romming, Acta Chem. Scand. **25**, 3561 (1971).

[41] M. Persico and P. Cattaneo, Phys. Chem. Chem. Phys. **1**, 4739 (1999).

[42] A. W. Adamson and R. Wachter, J. Am. Chem. Soc. **100**, 1298 (1978).

[43] G. Zimmermann, L.-Y. Chow and U.-J. Paik, J. Am. Chem. Soc. **80**, 3528 (1958).

[44] D. Gegiou, K. A. Muszkat and E. Fischer, J. Am. Chem. Soc. **90**, 12 (1968).

[45] J. Ronayette, R. Arnaud, P. Lebourgeois and J. Lemaire, Can. J. Chem. **52**, 1848 (1974).

[46] P. Bortolus and S. Monti, J. Phys. Chem. **83**, 648 (1979).

[47] H. Rau and E. Lüddecke, J. Am. Chem. Soc. **104**, 1616 (1982).

[48] N. Siampiringue, G. Guyot, S. Monti and P. Bortolus, J. Photochem. **37**, 185 (1987).

[49] H. Rau, J. Photochem. **26**, 221 (1984).

[50] G. Gauglitz and S. Hubig, J. Photochem. **30**, 121 (1985).

[51] A. Toniolo, C. Ciminelli, M. Persico and T.J. Martínez, J. Chem. Phys. **123**, 234308 (2005).

[52] H. Rau and S. Yu-Quan, J. Photochem. Photobiol. A **42**, 321 (1988).

[53] W. Horspool, in The Chemistry of the Hydrazo, Azo and Azoxy Groups, Volume 2, S. Patai ed., Wiley (2000)

[54] E.W.-G. Diau, J. Phys. Chem. A **108**, 950 (2004).

[55] L. Gagliardi, G. Orlandi, F. Bernardi, A. Cembran and M. Garavelli, Theor. Chem. Acc. **111**, 363 (2004).

[56] G. Granucci and M. Persico, Theor. Chem. Acc. **117**, 1131 (2007).

[57] J. Tomasi, B. Mennucci and R. Cammi, Chem. Rev. **105**, 2999 (2005).

[58] B. Mennucci, *"Continuum models for excited states"* in *"Continuum Solvation Models in Chemical Physics: from Theory to Applications"*, R. Cammi and B. Mennucci eds., Willey (2007), p.110.

[59] J.-Å. Anderson, R. Petterson and L. Tegnér, J. Photochem. **20**, 17 (1982).

[60] E. W.-G. Diau, Private communication

[61] W. S. Struve, Chem. Phys. Lett. **46**, 15 (1977).

[62] H. Satzger, S. Spörlein, C. Root, J. Wachtveitl, W. Zinth and P. Gilch, Chem. Phys. Lett. **372**, 216 (2003).

[63] S. S. B. Kim, R. B. Hommer and R. D. Cannon, Bull. Korean Chem. Soc. **27**, 255 (2006).

[64] C. Collaveri, G. Granucci, M. Persico and A. Toniolo, J. Chem. Phys. **115**, 1251 (2001).

[65] C. Ciminelli, G. Granucci and M. Persico, J. Chem. Phys. **123**, 174317 (2005).

[66] G. Granucci and M. Persico, J. Chem. Phys. **126**, 134114 (2007).

[67] W. Thiel, *"Modern Methods and Algorithms of Quantum Chemistry"* in Proceedings, Second Edition, J. Grotendorst (Ed.), John von Neumann Institute for Computing, Jülich, NIC Series, Vol. 3, ISBN 3-00-005834-6, pp.261-283, 2000

[68] M.J.S. Dewar and W. Thiel, J. Am. Chem. Soc. **99**, 4899 (1977).

[69] J.J.P. Stewart, J. Comput. Chem. **10**, 209 (1989).

[70] J.J.P. Stewart, J. Comput. Chem. **10**, 221 (1989).

[71] J.J.P. Stewart, J. Comput. Chem. **12**, 320 (1991).

[72] J.J.P. Stewart, J. Mol. Mod. **10**, 155 (2004).

[73] J. Stewart, MOPAC 2002, Fujitsu Limited, 1999, Tokyo

[74] L. Creatini, T. Cusati, G. Granucci and M. Persico, Chemical Physics **347**, 492 (2008).

[75] A. Biancalana, E. Campani, G. Di Domenico, G. Gorini, A. Iacoponi and G. Masetti, Spectrochim. Acta A **55**, 2883 (1999).

[76] P.-O. Åstrand, P.S. Ramanujam, S. Hvilsted, K.L. Bak and S.P.A. Sauer, J. Am. Chem. Soc. **122**, 3482 (2000).

[77] S. Monti, E. Giardini, P. Bortolus and E. Amouyal, Chem. Phys. Lett. **77**, 115 (1981).

[78] V.E. Shashoua, J. Am. Chem. Soc. **82**, 5505 (1960).

[79] R. Cimiraglia and H.-J. Hofmann, Chem. Phys. Lett. **217**, 430 (1994).

[80] M.L. Tiago, S. Ismail-Beigi and S.G. Louie, J. Chem. Phys. **122**, 094311 (2005).

[81] G. Füchsel, T. Klamroth, J. Dokić and P. Saalfrank, J. Phys. Chem. B **110**, 16337 (2006).

[82] T. Cusati, G. Granucci and M. Persico, J. Chem. Phys. **128**, 194312 (2008).

[83] G.S. Hartley, J. Chem. Soc. , 633 (1938).

[84] R.J.W. Le Fèvre and J. Northcott, J. Chem. Soc. , 944 (1949).

[85] R.J.W. Le Fèvre and J. Northcott, J. Chem. Soc. , 867 (1953).

[86] E.V. Brown and G.R. Granneman, J. Am. Chem. Soc. **97**, 621 (1975).

[87] J. Halpern, W.G. Brady and C.A. Winkler, Can. J. Res., Sect. B **28**, 140 (1950).

[88] A. Toniolo, comunicazione privata.

[89] A. Toniolo, A. L. Thompson and T. J. Martínez, Chem. Phys. **304**, 133 (2004).

[90] M.J.S. Dewar, J. Phys. Chem **89**, 2145 (1985).

[91] J. J. P. Stewart, *MOPAC 2000 and MOPAC 2002*, Fujitsu Limited, Tokio, Japan

[92] J. C. Tully, J. Chem. Phys. **93**, 1061 (1990).

[93] J. C. Tully, Int. J. Q. Chem. S. **25**, 299 (1991).

[94] J. C. Tully, Faraday Discuss. **110**, 407 (1998).

[95] M.S. Topaler, T.C. Allison, D.W. Schwenke and D.G. Truhlar, J. Chem. Phys. **109**, 3321 (1998).

[96] K. Drukker, J. Comput. Phys. **153**, 225 (1999).

[97] R. K. Preston and J. C. Tully, J. Chem. Phis. **54**, 4297 (1971).

[98] J. C. Tully and R. K. Preston, J. Chem. Phis. **55**, 562 (1971).

[99] D. S. Sholl and J. K. Tully, J. Chem. Phys. **109**, 7702 (1998).

[100] J.-Y. Fang and S.J. Hammes-Schiffer, J. Phys. Chem. A **103**, 9399 (1999).

[101] C. Zhu, S. Nangia, A.W. Jasper and D.G. Truhlar, J. Chem. Phys. **121**, 7658 (2004).

[102] C. Zhu, A. W. Jasper and D. G. Truhlar, J. Chem. Theory Comput. **1**, 527 (2005).

[103] P. Cattaneo, G. Granucci and M. Persico, J. Phys. Chem. A **103**, 3364 (1999).

[104] F. Weigert, Verh. Phys. Ges. **21**, 485 (1919).

[105] B. S. Neoport and O. V. Stolbova, Opt. Spectrosc. **10**, 146 (1961).

[106] Z. Sekkat, in *Photoreactive Organic Thin Films*, edited by Z. Sekkat and W. Knoll (Academic Press, USA, 2002)

[107] Valentina Cantatore, *Stochastic simulation of azobenzene orientation in a viscous matrix, irreadiated with polarized light*. Bs. Thesis, Universitá degli studi di Pisa, (2008)

[108] M. Persico, G. Granucci, S. Inglese, T. Laino and A. Toniolo, J. Mol. Struct. THEOCHEM **621**, 119 (2003).

[109] A. Toniolo, C. Ciminelli, G. Granucci, T. Laino and M. Persico, Theor. Chem. Acc. **111**, 270 (2004).

[110] I. N., Levine *Quantum Chemistry*, fifth edition, Prentice Hall (2000)

[111] M. Head-Gordon, J.A. Pople and M.J. Frisch, Chem. Phys. Lett. **153**, 503 (1988).

[112] S.F. Boys and F. Bernardi, Mol. Phys. **19**, 553 (1970).

[113] T.H Dunning, J. Chem. Phys. **90**, 1007 (1989).

[114] Francesca Martini, *Theoretical study of the interaction between the azobenzene and a non polar solvent*. Bs. Thesis, Universitá degli studi di Pisa, (2007)

[115] A. Warshel M. Levitt, J. Mol. Biol. **103**, 227 (1976).

[116] R. Bonaccorsi, C. Petrongolo, E. Scrocco and J. Tomasi, Theor. Chim. Acta **20**, 331 (1971).

[117] G. Alagona, R. Cimiraglia, E. Scrocco and J. Tomasi, Theor. Chim Acta **25**, 103 (1972).

[118] W. L. Jorgensen and J. Tirado-Rives, J. Am. Chem. Soc. **110**, 1657 (1988).

[119] W. L. Jorgensen, D. S. Maxwell and J. Tirado-Rives, J. Am. Chem. Soc. **117**, 11225 (1996).

[120] W. L. Jorgensen and N. A. McDonald, J. Mol. Struct.: THEOCHEM **424**, 145 (1998).

[121] W. D. Cornell, P. Cieplak, C. I. Bayly, I. R. Gould, K. M. Merz, D. M. Ferguson, D. C. Spellmeyer, T. Fox, J. W. Caldwell and P. A. Kollman, J. Am. Chem. Soc. **117**, 5179 (1995).

[122] D. A. Case, D. A. Pearlman, J. W. Caldwell, T. E. Cheatham III, J. Wang, W. S. Ross, C. L. Simmerling, T. A. Darden, K. M. Merz, R. V. Stanton, A. L. Cheng, J. J. Vincent, M. Crowley, V. Tsui, H. Gohlke, R. J. Radmer, Y. Duan, J. Pitera, I. Massova, G. L. Seibel, U. C. Singh, P. K. Weiner, P. A. Kollman, *AMBER 7*, University of California, San Francisco (2002)

[123] B. R. Brooks, R. E. Bruccoleri, B. D. Olafson, D. J. States, S. Swaminathan and M. Karplus, J. Comput. Chem. **4**, 187 (1983).

[124] J.W. Ponder, *TINKER 4.1* Washington University School of Medicine St. Louis, MO, 2004. (http://dasher.wustl.edu/tinker)

[125] W.L. Jorgensen and D.L. Severance, J. Am. Chem. Soc. **112**, 4768 (1990).

[126] W.L. Jorgensen, J.D. Madura and C.J. Swenson, J. Am. Chem. Soc. **106**, 6638 (1984).

[127] J. Åqvist, J. Phys. Chem. **94**, 8021 (1990).

[128] M. Field, P. A. Bash and M. Karplus, J. Comput. Chem. **11**, 700 (1990).

[129] A.V. Gubskaya and P.G. Kusalik, J. Phys. Chem. **108**, 7151 (2004).

[130] W.L. Jorgensen, J. Am. Chem. Soc. **102**, 543 (1980).

[131] W. Sun, Z. Chen and S.-Y. Huang, Fluid Phase Equil. **238**, 20 (2005).

[132] H. Yu, D.P. Geerke, H. Liu and W.F. Van Gunsteren, J. Comput. Chem **27**, 1494 (2006).

[133] B.M. Ladanyi and M.S. Skaf, Annu. Rev. Phys. Chem. **44**, 335 (1993).

[134] J.E. Del Bene, J. Chem. Phys. **55**, 4633 (1971).

[135] R.F. Nalewwajski, J. Mol. Struct. **40**, 247 (1977).

[136] Y.C. Tsé and M.D. Newton, J. Am. Chem. Soc. **99**, 611 (1977).

[137] M. Magini, G. Paschina and G. Piccaluga, J. Chem. Phys. **77**, 2051 (1982).

[138] J.A. Padró, L. Saiz and E. Guàrdia, J. Mol. Struct. **416**, 243 (1997).

[139] D.G. Montague, I.P. Gibson and J.C. Dore, Mol. Phys. **44**, 1435 (1981).

[140] D.G. Montague, I.P. Gibson and J.C. Dore, Mol. Phys. **47**, 1405 (1982).

[141] D.T. Bowron, J.L. Finney and A.K. Soper, Mol. Phys. **93**, 531 (1998).

[142] D. Kony, W. Damm, S. Stoll and W.F. Van Gunsteren, J. Comp. Chem. **23**, 1416 (2002).

[143] O.V. de Oliveira and L.C. Gomide Freitas, J. Mol. Struct.: THEOCHEM **728**, 179 (2005).

[144] MOSCITO 3.9, D. Paschek and A. Geiger, Departament of Physical Chemistry, University of Dortmund, (2000).

[145] R.C. Weast, *Handbook of Chemistry and Physics*; CRC: Boca Raton, FL. 1983

[146] R.C. Wilhoit and B.J. Zwolinski, J. Phys. Chem. Ref. Data, Suppl. **2**, (1973).

[147] Y. Marcus, *Ion solvation*, Ed. Wiley, New York, 1985

[148] J.A. Riddick, W.B. Bunger and T.K. Sakano, *Organic Solvents, Physical properties and Methods of Purification*, John Wiley & Sons, New York, 1986

[149] T. Yamaguchi, K. Hidaka and A.K. Soper, Mol. Phys. **97**, 603 (1999).

[150] C.M. Stuart, R.S. Frontiera and R.A. Mathies, J. Phys. Chem. A **111**, 12072 (2007).

[151] J. Nelder and R. Mead, The Computer Journal **7**, 308 (1965).

[152] W. H. Press, S. A. Teukolsky, W. T. Vetterling and B. P. Flannery, *"Numerical Recipes in Fortran 77"*, Cambridge U. P. (2001)

[153] D.A. McQuarrie, , *Statistical Mechanics*, Harper Collins Publishers, 1976

[154] S.A. Rice and P. Gray, , *Monographs in statistical physics. The statistical mechanics of simple liquids.*, Volume 8, John Wiley & Sons, USA, 1965

Alphabetic index

Acknowledgments

During this Thesis work there have been some people that have had an important role, people that have helped me not only at professional level but also at personal level and they have been close along this period. To these people I want to express sincere and special thanks:

* *In a first place I want to thank very much Maurizio Persico, my tutor, to have given me the opportunity to work with him in his group and in this way permits me to learn so much. I want to thank him for all the discussions that helped me to understand a lot of things, for all his help, for his immense patience and for all that has taught me not only at academic level but also at human and personal level. Professors like him are very few and I have had the fortune and the pleasure to work with him. I take advantage the opportunity to also thank his family to always have been nice and kind with me.*

* *To Giovanni Granucci, for all the inmense help that has given me in this period, overall with the computational and calculations aspects, for his patience, because without his help this thesis would not have been the same, for all the discussions that have allowed me to understand and to learn so much...Giovanni, thanks a lot!*

* *To the Galileo Galilei School, to have supported me by a grant that allowed me to complete one of most important aim, the Chemistry PhD at Pisa. life.*

* *To the professors Saulo A. Vázquez R. and Emilio Martínez Nuñez of the Chemical Physics Department of the Santiago de Compostela University, to give me the possibility to carry out part of my thesis work in their group, for their availability and simpathy. Particularly, I want to thank Saulo for his help in the correction and evaluation of the Thesis. Also I want to thank Ruben Meana-Pañeda, Juan José Pérez and Nicolas Ramos for their help along my stage at the USC.*

* *To the professors Ivo Cacelli, Alessandro Tani, Dario Pini and Benedetta Mennucci for their availability, for their help and sympathy given to me along these years working in the department.*

* *To Giacomo Prampolini and Luca De Gaetani for all their help not only with the Moscito and Mephan programs, for their availability to help me in whatever situation, giving me a hand always with a smile and a joke...Thanks a lot!*

* *To my parents, Orlando Cusati and Teresa Di Turi, because they have always supported me, to have believed in me in this time and for their life example, although the difficulties. To my brother Orlando to encourage me and for the jokes at the just moment. To my sister Patrizia, for what she has done for me and taught me in this period. Even if I don't tell you often I love you.*

* *To my aunt Antonieta Di Turi, for her words and her love, for her calls every weekend asking me about the thesis...Thanks aunt!... I always think of you.*

* *To my lovely sun, Alejandro Solís, one of the most important people of my life, for his support, to have believed in me, to always have been there although the distance and the time far one from the other one, to listen me, for his words, his advices, his encouragement and his love...Tus, this success is also your...It is not the same without you...I love you. I want to thank all his family for all their love and attention that always gave to me, because they have always been near although the distance. A special thanks to Mrs. Leonor Saldivia, for her love, her blessing and because she has always been as an aunt for me.*

* *To my best friend Yubisay Mendoza, because even the distance nor the time have canceled our friendship, to be a faithful and incondicional friend, to have listened to me always and to have been there without ever asking nothing, for our long conversations at the phone, for her words and suggestions...Yubi, you are the best friend that I can have. To Guillermo Garía and Diana D'Orazio to have always been near, for their love and friendship.*

* *To Gloria Spighi and Valentina Cantatore, for all the shared moments together, for the moments when we laught and the nice talks...to have made lighter this period.*

* *To Aurora Muñoz to have been a friend, always near in this period in which it has needed of someone that encourages us, for every time that she passed to the office to ask me about the thesis...thanks Aurora.*

* *To my special friends from Palermo: Sara Vaiana, Simone Mancuso, Giuseppe Riggi, Michela Chianello, Andrea Cannizzo, Sergio Severini (from Roma, even if a little palermitan), Aurelio Agliolo Gallitto, Marco Cannas, Benedetta Petta, Vito Mazzola, for their friendship, to be there, to remember me even if we are not together, for their emails, for their messagges to the cellular phone that given me a smile, for the help and the advices that have always given me, for all the moments shared together.*

* *To the Professor Antonino Messina of the Physical and Astronomical Sciences Department of the Palermo University, for all his help and advices. To Anna Napoli and her family to always have made me feel at home and in family.*

* *To the professors Mary Carmen Salazar and Antonio Hernández, for their support not only along my degree in Venezuela but also during my PhD here in Italy, to have believed in me and for their professional and human quality. I always remember you with love.*

* *To the people that I forget to mention in this moment, and that have had a direct or indirect influence on me, my PhD and my thesis, for their help and support.*

Ringraziamenti

Durante questo lavoro di tesi ci sono state delle persone che hanno avuto un ruolo importante, persone che mi hanno aiutato non solo a livello professionale ma anche personale e che mi sono state vicine lungo questo mio percorso. A queste persone voglio fare un ringraziamento sincero ed speciale:

* *In primo luogo voglio ringraziare molto Maurizio Persico, il mio relatore, per avermi dato l'opportunità di lavorare assieme a lui nel suo gruppo e permettermi di imparare tanto. Voglio ringraziarlo per tutte le discussioni che mi hanno aiutato a capire molte cose, per tutto il suo aiuto, per la sua immensa pazienza nei mie confronti e per tutto ciò che mi ha insegnato non solo a livello accademico ma anche a livello umano e personale. Professori come lui ce ne sono davvero pochi ed io ho avuto la fortuna e il piacere di lavorare al suo fianco. Approfitto l'opportunitá per ringraziare anche la sua famiglia, per essere stati sempre carini e gentili nei mie confronti.*

* *A Giovanni Granucci, per tutto l'immenso aiuto che mi ha i dato in questo periodo, sopratutto con gli aspetti computazionali e di calcolo, per la sua pazienza, perché senza il suo aiuto questa tesi non sarebbe stata la stessa, per tutte le discussioni che mi hanno permesso di capire e di imparare tanto...Giovanni, mille grazie!*

* *Alla Scuola Galileo Galilei, per avermi concesso la borsa di studio che mi ha permesso di portare a termine uno dei mie obbietivi che era quello di fare il Dottorato di Ricerca a Pisa.*

* *Ai professori Saulo A. Vázquez R. e Emilio Martínez Nuñez del Dipartimento di Chimca Fisica dell'Universitá di Santiago de Compostela (Spagna), per avermi dato la possibilità di portare avanti una parte del mio lavoro di tesi nel loro gruppo, per la loro disponibilità e simpatia. In particolare, voglio ringraziare Saulo per il suo aiuto nella correzione e valutazione di questo lavoro di tesi. Voglio anche ringraziare Ruben Meana-Pañeda, Juan José Pérez y Nicolas Ramos per il loro aiuto durante il periodo trascorso nella USC.*

* *Ai professori Ivo Cacelli, Alessandro Tani, Dario Pini e Benedetta Mennucci per la loro disponibilità, per il loro aiuto e la loro simpatia nei miei confronti lungo questi tre anni di lavoro nel dipartimento.*

* *A Giacomo Prampolini e Luca De Gaetani per tutto l'aiuto con i programmi Moscito e Mephan e non solo, per la loro disponibilità ad aiutarmi sempre in qualunque situazione, dandomi sempre una mano con un sorriso e una battuta...Mille grazie!*

* *Ai miei genitori, Orlando Cusati e Teresa Di Turi, perché mi hanno sempre appoggiata, per aver creduto in me in tutto questo tempo e per il loro essempio di vita, nonostante le difficoltà. A mio fratello Orlando per incoraggiarmi tutto questo tempo e per le sue battute nel momento giusto. A mia sorella Patrizia, per tutto quello che ha fatto per me e mi ha insegnato in questo periodo. Anche se non lo dico spesso, vi voglio tanto bene.*

* *A mia zia Antonieta Di Turi, per le sue parole e il suo affetto, per le sue chiamate ogni fine settimana chiedendomi come andava la tesi...Grazie zia..ti penso sempre.*

* *Al mio sole adorato, Alejandro Solís, una delle persone più importanti della mia vita, per il suo appoggio, per aver creduto in me, per essere stato sempre li nonostante la distanza ed il tempo lontani uno dall'altra, per ascoltarmi, per le sue parole, i suoi consigli, il suo incoraggiamento e il suo amore...Tus, questo successo è anche tuo...Ti amo...Inoltre, voglio ringraziare tutta la sua famiglia per il loro affetto e le attenzioni che hanno sempre avuto nei miei confronti, perche mi sono stati sempre vicini nonostante la distanze. Un ringraziamento speciale alla Sgra. Leonor Saldivia, per il suo affetto, le sue benedizioni e per essere sempre stata come una zia per me.*

* *Alla mia migliore amica Yubisay Mendoza, perché ne la distanza nel tempo sono riusciti a cancellare la nostra amicizia, per essere una amica fedele ed incondizionale, per avermi ascoltato sempre ed essere stata li senza chiedere mai niente, per le nostre lunghe chiacchere al telefono, per le sue parole e i suoi consigli...Yubi, sei la migliore amica che si possa avere. A Guillermo García e Diana D'Orazio per essermi stati vicini, per il loro afetto e la loro amicizia.*

* *A Gloria Spighi e Valentina Cantatore, per tutti i momenti condivisi assieme, per le risate e le piacevoli chiacchere che abbiamo avuto...insomma, per aver reso più leggero il mio percorso.*

* *A Aurora Muñoz per essere stata una amica, sempre vicino in questo periodo in cui si ha bisogno di qualcuno che ti incoraggi, per tutte le volte che si è avvicinata in ufficio a chiedermi come andava tutto...grazie Aurora.*

* *Ai miei amici palermitani più speciali: Sara Vaiana, Simone Mancuso, Giuseppe Riggi, Michela Chianello, Andrea Cannizzo, Sergio Severini (da Roma, ma anche lui un po siciliano), Aurelio Agliolo Gallitto, Marco Cannas, Benedetta Petta, Vito Mazzola per la loro amicizia, per essere li, per ricordarsi di me anche se non siamo più vicini, per i loro emails, per i mesaggi al telefonino che mi facevano sorridere, per l'aiuto e i consigli che sempre mi hanno dato, per tutti i momenti condivisi assieme...grazie picciotti!*

* *Al Professore Antonino Messina del Dipartimento di Scienze Fisiche ed Astronomiche dell'Università di Palermo, per tutto il suo aiuto e i suoi consigli. A Anna Napoli e la sua famiglia per avermi fatto sempre sentire a casa e in famiglia.*

* *Ai professori Mary Carmen Salazar e Antonio Hernández, per il loro appoggio non solo lungo la mia laurea in Venezuela ma anche durante il mio dottorato qua in*

Italia, per aver creduto in me e per la loro qualità umana e professionale...vi ricordo sempre con afetto.

* *A tutte quelle persone che mi dimentico di nominare e che in qualche modo mi hanno aiutato a rendere possibile il mio Dottorato e questa tesi.*

Agradecimientos

Durante este trabajo de tesis hubo personas que tuvieron un role importante, personas que me ayudaron no sólo a nivel profesional sino también a nivel personal y que estuvieron cerca a lo largo de este recorrido. A estas personas quiero expresar un muy especial y sincero agradecimiento:

* *En primer lugar quiero agradecer mucho a Maurizio Persico, mi tutor, por haberme dado la oportunidad de trabajar junto a él en su grupo y de este modo permitirme aprender tanto. Quiero agradecerle por todas las discusiones que me ayudaron a entender tantas cosas, por toda su ayuda, por su inmensa paciencia para conmigo y por todo lo que me ha enseñado no sólo a nivel académico sino también a nivel humano y personal. Profesores como él hay realmente pocos y yo tuve la suerte y el placer de trabajar a su lado. Quiero aprovechar la oportunidad para agradecer también a su familia, por haber sido siempre cariñosos y gentiles conmigo.*

* *A Giovanni Granucci, por toda su inmensa ayuda en este periodo, sobre todo con los aspectos computacionales y de cálculo, por su paciencia, porque sin su ayuda esta tesis no hubiese sido la misma, por todas las discusiones que me ayudaron a entender y a aprender tanto...Giovanni, un millón de gracias.*

* *A la Escuela Galileo Galilei, por haberme otorgado la beca que me permitió llevar a cabo una de mis metas que era la de obtener el Doctorado en Química en Pisa.*

* *A los profesores Saulo A. Vázquez R. y Emilio Martínez Nuñez, del Departamento de Química Física de la Universidad de Santiago de Compostela (España), por haberme dado la posibilidad de llevar a cabo parte de mi trabajo de tesis en su grupo, por su disponibilidad y simpatía. En particular quiero agradecer a Saulo por su ayuda en la corrección y evaluación de este trabajo de tesis. También quiero agradecer a Ruben Meana-Pañeda, Juan José Pérez y Nicolas Ramos por la ayuda que me brindaron durante mi estadía en la USC.*

* *A los profesores Ivo Cacelli, Alessandro Tani, Dario Pini y Benedetta Mennucci por su disponibilidad, por su ayuda y su simpatía hacia mi durante estos tres años de trabajo en el departamento.*

* *A Giacomo Prampolini y Luca De Gaetani por toda su ayuda no sólo con los programas Moscito y Mephan, por su disponibilidad a ayudarme siempre en cualquier*

situación, brindándome siempre una mano con una sonrisa y una broma...Muchas gracias!

* *A mis padres, Orlando Cusati y Teresa Di Turi, porque me han apoyado siempre, por haber creído en mi en todo este tiempo y por su ejemplo de vida, a pesar de las dificultades. A mi hermano Orlando por haberme apoyado en todo este tiempo y por sus bromas en el momento justo. A mi hermana Patrizia, por todo lo que hizo por mi y por lo que me enseñó en este periodo. Aunque no se los diga a menudo, los quiero mucho.*

* *A mi tía Antonieta Di Turi, por sus palabras y su cariño, por las llamadas de los fines de semana preguntándome por la tesis...Gracias tía...pienso siempre en ti.*

* *A mi sol adorado, Alejandro Solís, una de las personas más importantes de mi vida, por su apoyo, por haber creído en mi, por haber estado siempre allí, a pesar de la distancia y el tiempo lejos uno del otro, por escucharme, por sus palabras, sus consejos, por darme siempre ánimos y por su amor...Tus, este logro también es tuyo...No es lo mismo sin ti...Te amo. Además, quiero agradecer a toda su familia por todo el cariño y las atenciones que siempre han tenido hacia mi, porque han estado siempre cerca a pesar de la distancia. Un agradecimiento especial a la Sra. Leonor Saldivia, por su cariño, sus bendiciones y por haber sido siempre como una tía para mi.*

* *A mi mejor amiga Yubisay Mendoza, porque ni la distancia ni el tiempo han logrado borrar nuestra amistad, por ser una amiga fiel e incondicional, por haberme escuchado siempre y haber estado allí sin perdir nunca nada a cambio, por nuestras largas conversaciones al teléfono, por sus palabras y sus consejos...Yubi, eres la mejor amiga que se pueda tener. A Guillermo Gracía y Diana D'Orazio por estar siempre pendientes de mi, por su cariño y su amistad.*

* *A Gloria Spighi y Valentina Cantatore, por todos los momentos que compartimos juntas, por los momentos en que reímos juntas y por las conversaciones agradables que tuvimos...en fin, por haber hecho más ligero mi camino.*

* *A Aurora Muñoz per haber sido una amiga, siempre cerca en este periodo en el que uno necesita a alguien que le de ánimos, por todas las veces que se acercó a la oficina para preguntarme como andaba todo...gracias Aurora.*

* *A mis amigos palermitanos más especiales: Sara Vaiana, Simone Mancuso, Giuseppe Riggi, Michela Chianello, Andrea Cannizzo, Sergio Severini (de Roma, pero un poco siciliano), Aurelio Agliolo Gallitto, Marco Cannas, Benedetta Petta, Vito Mazzola por su amistad, por estar allí, por recordase de mi a pesar de que no estemos juntos, por sus emails, por los mensajes al celular que me hacían sonreir, por la ayuda y los consejos que siempre me han dado, por todos los momentos que compartimos juntos.*

* *Al Profesor Antonino Messina del Departamento de Ciencias Físicas y Astronómicas de la Universidad de Palermo, por toda su ayuda y sus consejos. A Anna Napoli y su familia por haberme hecho sentir siempre como en casa y en familia.*

* *A los profesores Mary Carmen Salazar y Antonio Hernández, por su apoyo no sólo a lo largo de mi carrera en Venezuela, sino también durante mi Doctorado aquí en Italia, por haber creído en mi y por su calidad humana y profesional...Los recuerdo siempre con afecto.*

* *A todas aquellas personas que se me olvida mencionar y que de alguna u otra manera me ayudaron a hacer posible la realización de este Doctorado y de esta tesis.*